The Modelling of Particle Resuspension in a Turbulent Boundary Layer

by

Fan Zhang

A Dissertation Submitted for the Degree of
Doctor of Philosophy

School of Mechanical and System Engineering
Newcastle University
and
Laboratoire de Mécanique des Fluides et d'Acoustique
Ecole Centrale de Lyon

November 2011

Dedicated to my mother, Jingjie Liu,
and my father, Lusheng Zhang.

Acknowledgements

Knowledge is in the end based on acknowledgement.

– Ludwig Wittgenstein

Oddly, I must first thank my Master's supervisor, David Swailes. When I told him I was considering a PhD, without hesitation he told me to talk to Mike Reeks. I have never received more sage advice. When I first started this thesis was clearly outside of my capabilities, but I believed in its virtue because Mike did. Nobody else on earth could have planted this seed in my head and help it come to fruition, so I thank him deeply from my heart. Mike is also an amazing person. When he is around, you can always cheer up. Academic work numbers aside, he also enlightens me on having a light-hearted attitude about life.

I am also very grateful to my second supervisor, Martin Kissane. He offered me a great deal of help on revising the reports and this thesis (plus he also translated the abstract to French version for me). He turned me from a rookie in nuclear safety area to a semipro. The period when I was in Cadarache, we almost spent all the lunchtimes together. I am so glad to have such a nice mate to share opinions on all sorts of topics and we also have the same taste in movies.

I must also sincerely thank my third supervisor, Richard Perkins, who not only set me an example of preciseness and patient, but also had been looking after me like one's elder after I had my first operation in Lyon. I am deeply indebted. I also thank him for revising the thesis.

I sincerely thank my friend Chunyu Jin (Newcastle University) for the LES data and Faouzi Laadhari (Ecole Centrale de Lyon) for the DNS data. I also thank Yuri Sergeev, David Swailes, Ian Potts, Peter Van Dijk and Yasmine Ammar for their patient replies on my boring questions. I sincerely thank Hansmartin Friess and Flavio Parozzi for their help of providing useful reports and videos.

I thank the IRSN (Institut de Radioprotection et de Sûreté Nucléaire) for financial support of this PhD. I also thank the secretaries and managers (Caroline Theuret, Marie-Claire Kallend, Didier Vola, etc.) of Building 702 in IRSN for all the help they provided to me. I also thank the staff (Sonia Wilson, Julie Sleightholme, Ann Pattison, Nicola Davison, Derek Simm, Ken Madden etc.) of the School office in Newcastle University for their help on my Visa and other requests.

I sincerely thank all the examiners in the Jury (Mike Fairweather, George Yadigaroglu, David Swailes, Michel Lance, Yannis Drossinos, Jean-Pierre Minier and Denis Boulaud) for their precious time on revising my thesis and attending my thesis defend in Lyon from all round of Europe.

I think my girlfriend, Xinyue Cui, for caring and encouraging me all the time. It was quite sad that I did not spend enough time with her because this joint PhD basically turned me into a member of guerrilla that moved to different places frequently.

My mother is a very smart person. She could have become very successful in her career, but she chose to become a great mother of her son and a back supporter of her husband. My father is a workaholic. In my memory, he was like always working, working and working. They receive my deepest gratitude and love for their dedication and the many years of support during my studies that provided the foundation for this work. I hope I am able to give one-tenth as much as I received.

Abstract

The work presented concerns the way small particles attached to a surface are resuspended when exposed to a turbulent flow. Of particular concern to this work is the remobilization of radioactive particles as a consequence of potential nuclear accidents. In this particular case the focus is on small particles, < 5 microns in diameter, where the principal force holding such particles onto a surface arises from van der Waals inter-molecular forces. Given its suitable treatment of the microphysics of small particles, it was decided here to aim to develop improved versions of the Rock'n'Roll (R'n'R) model; the R'n'R model is based on a statistical approach to resuspension involving the rocking and rolling of a particle about surface asperities induced by the moments of the fluctuating drag forces acting on the particle close to the surface.

Firstly, a force (moment) balance model has been modified by including the distribution of the aerodynamic force instead of considering only its mean value. It was also possible to improve the representation of the adhesive-force distribution where it is customary to include a substantial reduction factor to take account of surface roughness.

The R'n'R model is significantly improved by using realistic statistical fluctuations of both the stream-wise fluid velocity and acceleration close to the wall obtained from Large Eddy Simulation (LES) and Direct Numerical Simulation (DNS) of turbulent channel flow; in the standard model a major assumption is that these obey a Gaussian distribution. The flow conditions are translated into the moments of the drag force acting on the particle attached to the surface (using O'Neill's formula for the aerodynamic drag forces in terms of the local flow velocities). In so doing the influence of highly non-Gaussian forces (associated with the sweeping and ejection events in a turbulent boundary layer) on the resuspension rate has been examined along with the sensitivity of the fluctuation statistics to LES and DNS. We have found most importantly that the statistics of both fluctuating forces and its derivative (normalized on their rms values) are noticeably independent of the normalized distance from the wall, y^+ within the viscous sublayer ($y^+ < 6$) – if this were not the case then modelling fluctuations with different particle sizes would be far more complex.

In particular as a result of the analysis of our DNS/LES data 3 distinct features of the modified R'n'R model have emerged as playing an important part in the resuspension. The first is the typical forcing frequency ω due to the turbulent (fluctuating) aerodynamic drag forces acting on the particle attached to a surface (in the modified R'n'R model based on the DNS results ($y^+ = 0.1$) it is a factor of 4 > the value in the original model based on Hall's measurements of the lift force). This naturally has a significant effect of increasing the fraction resuspended for very short times (ωt ~< 1)

and is the controlling influence over the entire range of times from short to long term resuspension. The second is the value of the ratio of the root-mean-square (rms) drag force to its mean value which in the modified model is nearly twice (1.8) than that in the original. This feature of the model is largely responsible for the greater fraction resuspended after times ~ 1s (times which are sufficient to include the transition period from short term resuspension to long term resuspension rates ($\sim t^{-1}$). The third feature introduces changes in the resuspension because the distribution of aerodynamic drag forces in the modified model is distinctly non-Gaussian behaving more like a Rayleigh distribution. This means that the distribution of the drag force decays much more slowly in the wings of the distribution than the equivalent Gaussian (with the same rms) so that for very large values of the adhesive force / rms drag force ~ 8 (at the extreme end of the DNS measurements), the resuspension rate constant is a factor of 30 larger than that for an equivalent Gaussian model. Thus although the fraction of particles resuspended is very small in these instances, the differences between the modified and original models can be very large. This is particularly important when we consider resuspension from multilayer deposits.

When we consider these influences in the context of a broad range of adhesive forces due to surface roughness, we find that in general, the modified model gives around 10% more for the fraction of particle resuspension fraction than the original R'n'R model (for an initial log normal distribution of adhesive forces), however the difference could become significant (3 to 7 times greater depending on the range of values of the adhesive-force spread factor) when the friction velocity is small (i.e., smaller resuspension fraction). As for the short-term resuspension rate, the difference between the modified and original model becomes significant when this is dominated by the typical forcing frequency (ω^+ is 0.0413 for the original model, 0.08553 for LES approach and 0.127143 for DNS for y^+ = 6). The sensitivity to the adhesive-force spread factor has also been studied and the results indicate that the modified model removes particles much more easily than the original model in conditions of small friction velocity and a smoother surface (i.e., small spread factor). Finally in this phase of the work, the correlation between the distribution of the fluctuating force and its derivative has been checked for both LES and DNS statistics. The results demonstrate that this correlation has a very slight effect on particle resuspension compared with the result from the uncorrelated curve-fitted model.

In view of recent numerical data for lift and drag forces in turbulent boundary layers (Lee & Balachandar), the lift and drag we have considered and the impact of these data on predictions made by the non-Gaussian R'n'R model are compared with those based on O'Neill formula. The results indicate that, in terms of the long-term resuspension fraction, the difference is minor. It is concluded that as the particle size decreases the L&B method will lead to less-and-less long-term resuspension.

Finally the ultimate model that has been developed in this work is a hybrid version of the R'n'R model adapted for application to multilayer deposits based on the Friess and Yadigaroglu multilayer

approach. The deposit is modelled in several overlying layers where the coverage effect (masking) of the deposit layers has been studied; in the first instance a monodisperse deposit with a coverage ratio factor was modelled where this was subsequently replaced by the more general case of a polydisperse deposit with a particle size distribution. The results indicate that, in general, as the number of modelled layers increases the resuspension fraction of the whole deposit after a certain time decreases significantly. In other words, it takes a much longer time to resuspend a thicker deposit. Taking account of the particle size distribution slightly increases the short-term resuspension. However, this change decreases the long-term resuspension significantly. The model results have been compared with data from the STORM SR11 test (ISP-40) and the BISE experiments. In general, both comparisons indicate that with smaller spread of the adhesive force distribution (i.e., the range of adhesive force distribution is narrower) the new multilayer model agrees very well with the experimental data. It can be inferred that multilayer deposits lead to much narrower distributions of adhesive force.

Résumé

Les travaux présentés traitent la manière dont de fines particules déposées sur une surface sont remises en suspension lorsqu'elles sont soumises à un écoulement turbulent. Le domaine d'application spécifique de ce travail concerne la remobilisation de particules radioactives qui peut se produire pendant des accidents nucléaires. Dans ce cas particulier l'intérêt doit se focaliser sur de petites particules, de diamètre inférieur à 5 microns, pour lesquelles la force principale les retenant sur une surface est due aux forces intermoléculaires de van der Waals. Etant donné son traitement approprié de la microphysique de petites particules, l'objectif choisi pour les recherches actuelles était le développement de versions améliorées du modèle Rock'n'Roll (R'n'R); le modèle R'n'R se base sur une approche statistique de la remise en suspension qui intègre le balancement et le roulement d'une particule par rapport à des aspérités d'une surface, balancement et roulement qui sont induits par les moments des forces de traînée fluctuantes près de la surface qui agissent sur la particule.

Dans un premier temps, un modèle de bilan des forces (moments) a été modifié en incluant la distribution de la force aérodynamique au lieu de considérer uniquement sa valeur moyenne. Il a été également possible d'améliorer la représentation de la distribution de la force d'adhérence alors qu'habituellement cette distribution intègre un facteur de réduction important afin de tenir compte de la rugosité de la surface.

Le modèle R'n'R est amélioré de manière importante en remplaçant l'hypothèse d'une distribution gaussienne des fluctuations statistiques de la vitesse et de l'accélération du fluide dans le sens du courant près de la paroi par des statistiques réalistes qui sont générées avec les techniques de simulations aux grandes échelles (LES) ou de simulations numériques directes (DNS) pour un écoulement turbulent dans un tuyau. Les conditions d'écoulement sont traduites en moments de la force de traînée agissant sur la particule attachée à la surface en appliquant la formule d'O'Neill pour les forces de traînée aérodynamiques en fonction des vitesses d'écoulement locales. De cette manière, l'influence de forces fortement non-gaussiennes (associées aux événements de balayage et d'éjection dans une couche limite turbulente) sur le taux de resuspension a été examinée ainsi que la sensibilité des statistiques de fluctuation selon leur origine LES ou DNS. Nous avons principalement trouvé que les statistiques de la force fluctuante et de sa dérivée (tous les deux normalisés par rapport à la racine de la moyenne du carré – ou RMC - de leurs valeurs respectives) sont sensiblement indépendantes de la distance normalisée depuis la paroi, y^+, à l'intérieur de la sous-couche visqueuse (c'est-à-dire, $y^+ < 6$) – si ceci n'était pas le cas la modélisation des fluctuations pour des particules de tailles différentes serait beaucoup plus complexe.

En particulier du fait des analyses de nos résultats DNS/LES, trois aspects distincts du modèle R'n'R modifié ont émergé comme jouant un rôle important dans la remise en suspension. Le premier est la fréquence typique ω due aux forces de traînée aérodynamique turbulentes agissant sur la particule déposée sur une surface (dans le modèle R'n'R modifié utilisant les résultats de la DNS (y^+ = 0,1), celle-ci est 4 fois supérieure à la valeur dans le modèle standard qui se base sur les mesures de Hall de la force de portance). Ceci a bien entendu un effet significatif en augmentant la fraction remise en suspension pour les délais très courts (ωt ~< 1) et constitue l'influence déterminante pour la gamme temporelle entière de remise en suspension à court jusqu'au long terme. Le deuxième est la valeur du rapport de la RMC de force de traînée à sa valeur moyenne qui, dans le modèle modifié, est presque deux fois (1,8) fois supérieur que dans le modèle standard. Cet aspect du modèle est largement responsable de la fraction remise en suspension plus importante au-delà de 1s environ (un délai suffisamment long pour intégrer la phase de transition entre le taux de remise en suspension à court terme et celui à long terme (qui varie comme $1/t$). Le troisième aspect introduit des modifications de la remise en suspension à cause de la distribution des forces de traînée aérodynamiques qui est nettement non gaussienne dans le modèle modifié; en pratique cette distribution se rapproche plutôt d'une distribution de Rayleigh. Cette différence signifie que, dans les zones extrêmes de la distribution, la force de traînée s'estompe beaucoup plus lentement qu'avec la distribution gaussienne équivalente (ayant la même RMC) de sorte que, pour les valeurs très grandes du rapport {force d'adhérence / RMC de la force de traînée} ~8 (à la limite extrême des résultats de la DNS), la constante du taux de resuspension initial est 30 fois supérieure à celle du modèle gaussien équivalent. Ainsi, bien que la fraction de particules remise en suspension soit très faible dans ces conditions, les différences entre les modèles standard et modifié peuvent être très grandes. Ceci est particulièrement important à la considération de la resuspension depuis les dépôts de particules multicouches.

Lorsqu'on considère ces influences dans le contexte d'une étendue large de forces d'adhérence due à la rugosité d'une surface, on trouve en général que le modèle modifié produit une fraction de resuspension de particules environ 10% plus élevée que le modèle R'n'R standard (pour une distribution initialement lognormale des forces d'adhérence), cependant cette différence peut devenir plus significative (3 à 7 fois plus élevée en fonction de la gamme des valeurs du facteur d'étendue de la force d'adhérence) lorsque la vitesse de frottement est faible (c'est-à-dire, fraction de resuspension faible). Quant au taux de resuspension à court terme, la différence entre le modèle modifié et le modèle standard devient significative lorsque ce taux est dominé par la fréquence typique de bourrasque (ω^+ égale 0,0413 pour le modèle gaussien, 0,08553 pour l'approche LES et 0,127143 pour celle de la DNS à y^+ = 6). La sensibilité au facteur d'étendue de la distribution de la force d'adhérence a été également étudiée et ces résultats indiquent que le modèle modifié conduit à remettre en suspension des particules beaucoup plus facilement que le modèle standard sous conditions de vitesse de frottement faible et de surface plus lisse (c'est-à-dire, facteur d'étendue de la distribution plus petit). Pour terminer cette phase des travaux, la

corrélation entre la distribution de la force fluctuante et de sa dérivée a été vérifiée pour les statistiques de la LES et de la DNS. Les résultats démontrent que cette corrélation a un effet très faible sur la remise en suspension de particules comparé aux résultats du modèle à distribution ajustée et non-corrélée.

A la lumière de données d'études numériques récentes des forces de portance et de traînée dans des couches limites turbulentes (Lee et Balachandar), l'impact de ces forces sur les résultats produits par le modèle R'n'R modifié utilisant la formule de O'Neil a été investigué. Les résultats indiquent que, en termes de la fraction remise en suspension à long-terme, la différence est mineure. La conclusion est que lorsque la taille de particule décroit la méthode de L&B conduira à de moins en moins de resuspension à long terme.

Enfin l'ultime modèle qui a été développé dans le cadre de ces recherches est une version hybride du modèle R'n'R adaptée au cas de dépôts multicouches et qui se base sur l'approche multicouche de Friess et Yadigaroglu. Le dépôt est modélisé en plusieurs couches qui se recouvrent et l'effet de masquage des couches du dépôt a été étudié; dans un premier temps un dépôt monodispersé incluant un facteur du ratio de masquage est modélisé puis, par la suite, celui-ci est remplacé par le cas plus général d'un dépôt polydispersé associé à une distribution de tailles de particules. Les résultats indiquent, en général, une décroissance significative suite à un certain laps de temps de la fraction remise en suspension de l'ensemble du dépôt lorsque le nombre de couches modélisées augmente. Autrement dit, il faut beaucoup plus de temps pour remettre en suspension un dépôt plus épais. La prise en compte de la distribution de taille de particules augmente légèrement la remise en suspension à court terme. Cependant, cette modification diminue de manière significative la remise en suspension à long terme. Les résultats du modèle multicouche ont été comparés à des données expérimentales provenant de l'essai SR11 du programme STORM (l'ISP-40) et des expériences BISE. En général, les deux comparaisons indiquent qu'avec une étendue réduite de la distribution de la force d'adhérence (c'est-à-dire, la distribution de la force d'adhérence est plus étroite) la nouvelle modélisation multicouche s'accorde très bien avec les données expérimentales. Il est possible d'inférer que les dépôts multicouches conduisent à des distributions de force d'adhérence sensiblement plus étroites.

Table of Contents

List of Figures

List of Tables

Nomenclature

Latin Alphabet

A, B	constants
B_f	reduction factor of the derivative of the fluctuating aerodynamic force
C_C	correlation coefficient
C_D	drag coefficient
D	particle diameter
D_m	mass mean diameter of deposit particles
E_1	particle Young's modulus
E_2	substrate Young's modulus
$E^+(\omega^+)$	universal energy spectrum
$\hat{E}_L(\omega)$	normalized energy spectrum of the fluctuating lift force
F	total aerodynamic force
F_A	added mass force
F_{AR}	adhesive restoring force
F_a	adhesive force on smooth surface
F_{ad}	adhesive force on rough surface
$F_{a\tau}$	tangential pull-off force
F_B	Basset force
F_b	buoyancy force
F_C	cohesive force
F_D	drag force
F_{DS}	drag force near surface
F_F	Faxen force
F_G	gravitational force
F_{il}	inertial lift force on a sphere particle in a linear shear flow close to a flat wall
F_L	lift force
F_{LA}	mean lift force obtain by Leighton and Acrivos
F_{lp}	lift force of the particle on the plane in uniform flow
F_M	Magnus force
F_P	net pressure force
F_R	particle resuspended fraction
F_{pf}	pressed (attractive) force between two spheres

F_r	ratio of adhesive force to the removal force
F_{Sl}	Saffman lift force
F_{ssD}	steady-state drag force
F_τ	shear stress force
$\langle F_D \rangle$	mean drag force
$\langle F_L \rangle$	mean lift force
G	shear rate
$G()$	Gaussian distribution
H	material property constant
H_0	equilibrium distance between particles (normally 0.3nm)
H_c	Hamaker constant
I	particle inertia
K	composite Young's modulus
K(u,v)	rate constant of two particles coagulation with volume u and v
L	number of layers
L	representative length of a body in the flow
L_n	quantity layer number
L_w	representative distance away from the wall
L_{large}	mean distance between two large-scale asperities
$L(\mu, \sigma)$	log-normal distribution with mean and standard μ and deviation σ
M	mass load/moment
M_0	initial mass load
M_a	adhesion moment
M_D	moment of drag force
N	number of points, cells or data
N_{ijk}	discrete pdf of exposed particles $n(t)$
$N(F,t)$	number density of particle on the surface at time t
$N_0(F)$	initial adhesive force distribution function
P	pull-off force
P_0	force acting on the particle,
P_1	apparent Hertzian force
$P(\mu)$	Poisson distribution with mean μ
$P()$	joint distribution / a distribution
$\langle PE \rangle$	average potential energy of a particle in a wall
Q	height of the surface adhesive potential well
Re	Reynolds number
Re_p	particle Reynolds number
Re_r	shear rate Reynolds number
Re_s	particle slip Reynolds number
Re_ω	particle rotation Reynolds number

$R(v)$	rate constant of particles deposition with volume v on the surface
S	representative area of an object
S_B	maximum spring extension
$S(v)$	source rate of the particle
U	representative magnitude of the flow velocity
U_c	characteristic flow velocity
V_i	total volume of the *i*th layer
V_p	particle volume
V_s	particle slip velocity
$\overline{V}_{pi}$	average single particle volume in *i*th layer
$W(v,y)$	distribution function of particle velocity and displacement
a	displacement between two asperities
$a(F)$	exponential removal rate
a_{rms}	asperity root mean square value
d_{50}	mass-median diameter of the particles
f	fluctuating component of a force F
f_{Ai}	particle occupied area fraction in *i*th layer
f_a	normalized adhesive force
$f_c(t)$	fraction of particle resuspension as a function of time
f_{dh}	fluctuating component of aerodynamic force at detachment point
f_{fric}	friction factor
$f_L(t)$	fluctuating lift force
f_R	particle fraction remaining
$f_R(t)$	particle fraction remaining at time t
f_{rms}	Coefficient of rms fluctuating force
$f_r(t)_L$	particle resuspension fraction at time t for L layers deposit
f_{Vi}	particle volume fraction
f^*	Fanning friction factor
$\sqrt{\langle f^2 \rangle}$	root mean square force
$<f_L^2>$	mean square fluctuating lift force
h	Characteristic height
g	standard gravity
g_n	gravitational component of acceleration acting normal to the surface
g_t	gravitational component of acceleration acting tangential to the surface
i,j,k	index
k	numerical constant dependent upon the shape of the potential
k_{pw}	ratio of particle radius to particle distance from the wall
k_r	Nikuradse roughness length
m	particle mass

m_D	fluctuating component of drag moment
$m(t)$	remaining mass per unit wall surface area as a function of time
m_0	initial mass
$n(t)$	normalized particle concentration
$n(z)$	atomic density
$n(\xi,t)$	pdf of the exposed particles with a statistical variable at time t
$n(\mathrm{v},t)$	number concentration of particles with volume v and time t
$\overline{n}_i$	average number of particles in ith layer
p	resuspension rate constant
$p(\xi)$	resuspension rate constant as a function of a statistical variable
p_c	resuspension probability per unit time
p_f	fluid pressure
p_G	resuspension rate constant from Gaussian model
p_{nG}	resuspension rate constant from non-Gaussian model
r	particle radius
r_a	asperity radius
r_c	contact radius
r_e	equilibrium radius
r_i	sphere radius
r_{fine}	mean asperity radius
r_a'	normalized asperity radius
r_{ab}'	normalized asperity radius when drag moment balanced with adhesive moment
$\overline{r}$	geometric mean of the particle size distribution
$\overline{r}_i$	average particle radius in ith layer
$\overline{r}_a'$	geometric mean of the normalized asperity radius
r^+	dimensionless particle radius (normalized by friction velocity / kinematic viscosity)
S	sticking probability
$\mathbf{u}$	fluid velocity vector
$\mathbf{u}_0$	initial fluid velocity
u_i^+	dimensionless fluid velocities
u_τ	wall friction velocity
$u_{\tau 50}$	friction velocity to resuspend 50% of particles
v	particle velocity
$\mathbf{v}$	particle velocity vector
$\mathbf{v}_0$	initial particle velocity
v_i^+	dimensionless particle velocities
$\langle v^2 \rangle$	mean square velocity
t^+	dimensionless time
x_B	maximum x-direction displacement

y	displacement normal to the wall
y_B	maximum vertical displacement
y^+	dimensionless distance normal to the wall.
$\langle y^2 \rangle$	mean square displacement
z_1	normalized fluctuating aerodynamic force
z_2	normalized derivative of the fluctuating aerodynamic force
z_a	normalized adhesive force
z_S	normalized fluctuating aerodynamic force from Stokes method
$\dot{z}_S$	normalized derivative of fluctuating aerodynamic force from Stokes method
z_{LB}	normalized fluctuating aerodynamic force from Lee and Balachandar method
$\dot{z}_{LB}$	normalized derivative of fluctuating aerodynamic force from L&B method
z_{dh}	normalized fluctuating component of aerodynamic force at detachment point

Greek Alphabet

Γ	couple of a system
Γ'	fluctuating component of the couple
Λ	particle resuspension rate
$\Lambda(t)$	particle resuspension rate as a function of time
$\Lambda_i(t)$	particle resuspension rate of ith layer as a function of time
Φ_r	resuspension mass flux
α	constant
β	damping constant in RRH model
β_θ	damping constant in R'n'R model
γ	surface energy per unit contact area
δ	step function
ε	stiffness of the system
η	resonance contribution factor
θ	angle of small oscillation / new variable
κ	elastic constant
λ	collision shape factor
μ_f	fluid viscosity
ν_1	particle Poisson's ratio
ν_2	substrate Poisson's ratio
ν_f	fluid kinematic viscosity
ξ	statistical variable or number of variables
ξ_1	long-term resuspension rate constant 1

ξ_2	long-term resuspension rate constant 2
ρ_f	density of the continuous phase material (fluid)
ρ_p	density of the particle
ρ_{fine}	mean surface density
ς	porosity
σ_a'	adhesive spread factor
σ_r	geometric standard deviation of particle size distribution
τ	shear stress
τ_w	wall shear stress
τ_f	fluid time scale
τ_f^+	dimensionless fluid time scale in turbulent boundary layer
τ_p^+	dimensionless particle response time in turbulent boundary layer
$\varphi()$	probability distribution
$\varphi(r_a')$	distribution of the normalized asperity radius
$\varphi_t(r_a')$	truncated distribution of the normalized asperity radius
x	aerodynamic shape factor
ψ	a random function
$\psi(r)$	particle size distribution
ω	natural frequency in RRH model
ω_0	typical natural frequency
ω_p	particle rotation
ω_θ	natural frequency in R'n'R model
ω^+	normalized natural frequency / Coefficient of typical forcing frequency

Chapter 1
Introduction

And the continuity of our science has not been affected by all these turbulent happenings, as the older theories have always been included as limiting cases in the new ones.

- Max Born

1.1 Nuclear Accidents

During nuclear accidents, the severity of the consequences is governed by the quantities and forms of radioactive substances (including actinides from the fuel, products of the actinide fission reactions and activated structural material) released into the environment. This release is mainly influenced by the formation, deposition (i.e., retention) and resuspension (i.e., remobilization) of aerosols in the primary system and containment building. Therefore, aerosol resuspension can become an important contribution to the severity of accidents. With different reactor technologies, the causes of deposition and resuspension are different. There are three main reactors that will be introduced below: pressurized-water reactor (PWR); high-temperature reactor (HTR) and International thermonuclear experimental reactor (ITER).

1.1.1 Pressurized Water Reactor

In PWRs, there are three different barriers between fuel and environment. Firstly, there are thousands of fuel rods making up the core and the fuel is contained as pellets in the fuel rods with metal cladding (the first barrier). The core is inside a reactor vessel (which is part of the primary system, the second barrier) which is inside a containment building (the third and final barrier). All these barriers reduce the risk of radioactivity release to the environment.

Accidents can be caused by equipment failure or human errors. Different well-defined sequences arise from accident scenarios that include station blackout (e.g. primary pumps stop working, back-up power fails, etc.), transient sequences (severe over-reactivity of the core occurs when boric acid in the primary coolant is suddenly diluted by pure water), loss of the

primary coolant by leakage, and rupture of one or several steam generator tubes (Hocke *et al.*, 1995).

All of the above scenarios, coupled to other failures or events, can lead to the core meltdown and consequently, the emission of various highly-toxic fission products (FPs) such as isotopes of Kr, Xe, I, Cs, Sb, Ce, Te, Ba, etc. Some of these products initially in vapour state can result in aerosol particles by homogeneous and/or heterogeneous nucleation where these aerosol particles will undergo agglomeration and other processes (Zoulalian & Albiol, 1995).

The liquid or solid particles deposit by various mechanisms onto the reactor vessel internals and the coolant pipework and, subsequently, can be resuspended if one of the following events occurs (Parozzi, 1992):

- core quenching due to the delayed intervention of Emergency core cooling system (ECCS);
- slumping of the (partially) molten core into the pool of water remaining in the vessel bottom;
- forced depressurization of the reactor coolant system (RCS) after or during the melting period;
- fast depressurization due to pipework or vessel failure after or during the melting period.

Since the radioactive particles are released into the containment building and deposit on the walls and the floor, in the same manner, particles can be resuspended here because of:

- Hydrogen deflagration;
- Steam explosion by vessel melt-through and corium contact with underlying water;
- Fast depressurization due to the containment failure;
- Fast depressurization due to the containment venting.

Compared to steam explosion, hydrogen deflagration is a more important phenomenon from a safety point of view since, given the later time that deflagration can occur, high contamination levels can be achieved in the containment atmosphere at a relatively late time in the accident.

1.1.2 High Temperature Reactor

In HTRs, fuel materials are contained either in graphite rods or inside graphite pebbles. Graphite dust will be generated during the normal reactor operation and pebble-to-pebble friction and will deposit inside the primary system; it will then become radioactive due to the sorption of FPs. This radioactive dust is the major problem in accidents. In the case of a depressurized loss-of-flow accident (e.g., large pipework leak), a significant amount of radioactive dusts will be resuspended from the primary system inside surface due to the fast depressurization and will be released into the confinement building and then be filtered before release to the environment. Therefore,

resuspension of deposited particles become a key issue in HTR safety analyses (e.g., see Stempniewicz & Komen, 2006).

1.1.3 International Thermonuclear Experiment Reactor

ITER is to be the first large-scale fusion reactor. The fuel (tritium gas) will be heated to the plasma phase by the tokomak-based technology comprising, of most interest here, the 'donut' shaped vacuum vessel (VV) which is surrounded by water pipes for cooling. Metallic dust will be generated in the VV during normal operation due to the contact with and radiation of the plasma onto structural surfaces where this dust will deposit inside the VV.

If a LOVA (Loss of vacuum accident) event occurs, an external flow which may be air or steam may burst into the inside of vacuum vessel causing fast pressurization (Takase, 2001). Furthermore, hydrogen will be generated from the reaction of steam with metallic dust (either resuspended or on the hot surfaces) with the risk of causing a hydrogen explosion after condensation of the steam (Iseli, 2001). During the accidents, the radioactive dust will be resuspended from the inside surface of the VV due to the external turbulent flow or the hydrogen explosion and must be dealt with by confining measures if it is not to be released into the environment.

1.2 Aerosol Physics

Aerosols are suspensions of small particles in gases. They are formed by disintegration (fragmentation) of solids or liquids or by condensation of gases to liquid or solid particles. They may also result from the resuspension of powdered material or the breakup of agglomerates. The size of aerosols varies from 1nm to 100 μm (Friedlander, 2000) where raindrops, e.g., are much larger (diameter around 1 mm). Heat and mass transport to the particles, as well as their interaction with radiation, are strongly affected by size and shape. Liquid aerosols, due to surface tension, are almost always spherical, but solid aerosols can occur in many different shapes varying from spherical to fibrous (needle-like forms). They can be chain-like agglomerates, or can be amorphous clumps (Williams & Loyalka, 1991).

1.2.1 Nuclear Aerosols

The aerosol characteristics in three different reactors will be described in this section. The interested reader is referred to Allelein et al. (2009) for details of our current level of knowledge and analytical capabilities with respect to nuclear aerosols (the reference concerns PWRs but is of much more general validity).

1.2.1.1 Pressurized Water Reactor

In a reactor accident, aerosols may range in size from 0.01μm to 20μm. Aerosol concentrations in accident analyses are typically less than 100g/m^3 and usually more than 1g/m^3. Kissane (2008) concluded that the typical aerosol composition for PWRs is seen to be a mixture of roughly one third metals (Ag and/or Cd, 15-40%), one third metal-oxide content (SnO and, potentially, UO_2 and ZrO_2) and one third FPs covering a diversity of compounds (from metals to oxides to salts, e.g., RbI, to ternary compounds). Concerning particle shape, relatively compact particles without branching chain-like structures appear to be typical in the RCS.

1.2.1.2 High Temperature Reactor

In the HTR context, Kissane (2009) has reviewed information on this technology. Operating experience with HTRs showed that three types of carbonaceous dust arose: graphite from mechanical mechanisms in the core; carbon from decomposition of hydrocarbons (oil contamination) and carbon from decarburization of steel alloys. Indeed, one can consider four types of dust since the graphite from the core is generated from both the high-purity highly-graphitized filler and the partially-graphitized binder of the fuel elements/pebbles.

Concerning the quantity of carbonaceous dust, information from HTR experience may well not be directly relevant with respect to modern designs since materials (alloys, graphites) and conditions have changed: decarburization-generated (if any) and graphite-abrasion-generated dusts are likely to be different; hydrocarbon contamination can be ruled out. Nevertheless, given that knowledge for this important parameter is very scarce, extrapolation from HTR experience is useful. It seems that in a 400MWt pebble-bed HTR abrasion-generated carbonaceous dust can be anticipated to be in the range 30–100 kg yr^{-1}; dust in a prismatic-core HTR can be expected to be far less.

Concerning the size of carbonaceous dust, for the same reasons just stated above, information on dust size from HTR experience may well not be of direct use with respect to modern designs. Furthermore, it turns out to be reasonable to assume that the partially-graphitized binder is the major source of carbonaceous dust. From only two reliable sources of relevant data, dust size (diameter) is expected to be in the 1-5μm range.

1.2.1.3 International Thermonuclear Experiment Reactor

The basic safety concern with ITER is the prevention of events leading to the release of tritium, activated dust and activated corrosion products. It can be expected that in ITER the interaction of plasma with structural walls of the tokomak and the diverter will generate hundreds of kilograms of tungsten, beryllium and/or carbon dust (Chuyanov and Topilski, 2006; Ciattaglia, 2010). These particles will have a characteristic diameter <100μm with a considerable fraction <10μm. Hypothetical accidents have been identified and investigated for ITER (Taylor, 2007). In particular,

interaction of hot dust with water in the case of a water-ingress accident (i.e., failure of the first-wall cooling loop inside the vacuum vessel) will produce hydrogen and risk producing an explosion. Air ingress into the vacuum vessel could also potentially lead to a dust explosion. Such explosions could damage the machine and would present a danger to the public if the release of radioactivity (mainly due to the accumulated contamination in the dust) from the VV is not mitigated. The current strategy to cope with the risk of dust and hydrogen explosions is based on administrative limits on accumulation of dust within the ITER vacuum vessel.

1.2.2 Aerosol Mechanism

The General dynamic equation (GDE) is the fundamental description for modelling industrial and atmospheric aerosol processes. According to Friedlander (2000), without considering the spatial effect, the equation is obtained as shown below.

$$\frac{\partial n(v,t)}{\partial t} = \left[\frac{\partial n(v,t)}{\partial t}\right]_{coag} - R(v)n(v,t) + S(v) \qquad [1.1]$$

Where,

n(v,t) is the number concentration of particles with volume *v* at time *t*

the first term on the right is the rate of production of particles with volume v by coagulation

R(v) is the removal-rate constant of particles with volume *v*, i.e., deposition

S(v) is the source rate of the particles with volume *v*.

The coagulation term in Eq.[1.1] can be presented as shown below.

$$\left[\frac{\partial n(v,t)}{\partial t}\right]_{coag} = \frac{1}{2}\int_0^v K(u, v-u)n(u)n(v-u)du - n(v)\int_0^\infty K(u,v)n(u)du \qquad [1.2]$$

where *K(u,v)* is the rate constant of two particles coagulating one with volume *u* and the other *v*. Concerning Eq.[1.2], the first integral on the right hand side is the rate of coagulation of the particles with volume *u* and *v-u* to form a particle of volume *v*, i.e., a creation term for this size. The second integral is the rate of coagulation of the particles of volume *v* with particles of any volume to form a particle that is no longer in the *v* to *v+dv* volume interval.

1.2.2.1 Particle Coagulation

'Coagulation' describes the process of fusion or adhesion of two particles when they touch. The 'collision' takes place due to the relative velocity between the aerosol particles. The relative velocity can be affected by the following phenomena: Brownian motion, gravitational settling and turbulent effects (Williams & Loyalka, 1991).

- *Brownian motion*

The simultaneous random walk of a large number of particles suspended in the fluid due to the random impact of molecules on their surfaces arising from thermal energy leads to collisions causing, therefore, coagulation.

- *Gravitational settling*

The larger particles settling under the force of gravity will sweep up the smaller particles. If two particles are within a certain distance of each other the faster one (if it is above) has the possibility of colliding with the slower one, thereby causing coagulation.

- *Turbulence effects*

There are two independent mechanisms, turbulent inertia and turbulent diffusion. The former one means that the particles are expelled from turbulent eddies due to the large difference in the densities of the particles and the fluid and then impact with other particles. The latter one is that the particles are carried by the turbulent eddies when the particles are relatively small and then contact other particles.

More explanations are given in Williams & Loyalka (1991) and Friedlander (2000). There is a summary of all the formulas of particle coagulation in Allelein et al (2009).

1.2.2.2 Particle Deposition

Aerosol particles do not remain stationary. They can move because of gravity, temperature and concentration gradients, random diffusion, aerodynamic forces or the force exerted by electrical fields or radiation. There are various reasons causing particles deposition which include sedimentation, impaction, diffusion and different phoretic mechanisms. Some of them will be described below. More explanation, formulas and experiments are provided in Zoulalian & Albiol (1995) and Allelein et al. (2009).

- *Deposition by Sedimentation*

This phenomenon results from the action of gravity on a particle counteracted by the friction force (drag). Practically, sedimentation becomes an important phenomenon when large particles (several microns) are carried in a horizontal pipe by low-velocity flow and it often becomes dominant within containment where the average velocity of the fluid is practically zero, particles size increases (agglomeration) and temperature gradients are low.

- *Deposition by Impaction*

In the presence of a gaseous flow submitted to a velocity variation or a direction change, the liquid/solid particles, due to higher inertia, can follow a different path from that of the fluid phase. On the other hand, smaller and lighter particles with low inertia follow closely the fluid path. Consequently, a particle can encounter a surface which represents an obstruction in its path; the

particles will hit the obstruction and remain there if the adhesive force is larger than the bouncing force.

- *Deposition by Laminar and Turbulent Diffusion*

Velocity and momentum gradients appear in a viscous fluid. Gradients enhance the migration of aerosols to low velocity zones and consequently the trapping of aerosols on the wall where, in the limit, flow is stagnant. This deposition process resulting from a velocity gradient is also called viscophoretic deposition. In laminar flow, this phenomenon is dependent on fluid properties and particle size where, in normal conditions, being driven by Brownian motion it is only be appreciable in the case of submicronic particles. In turbulent flow, eddies enhance the mixing and dispersive transport of particles having most impact on supramicron particles. In a turbulent flow near a surface, i.e., within the viscous boundary layer, particles reach this layer by turbulent transport then other mechanisms such as Brownian motion lead to transport to the wall. It must be noted that, in the case of highly turbulent flows, there exists an additional projection mechanism where eddies can impart sufficient momentum to (larger) particles for them to be able to coast their way through the boundary layer onto walls. This inertial impaction phenomenon is significant when the stopping distance is non-negligible compared to the thickness of the boundary layers.

- *Deposition by Thermophoresis*

A solid particle within a gaseous flow where there exist temperature gradients is subjected to a force because the particle momentum flux is not nil due to the temperature gradient and the gas molecule impactions on the particle which are not symmetrical (higher on the side facing higher temperatures). If the wall temperature is lower than in the bulk of the gas, the particles tend to move towards the wall and finally deposit there. This phenomenon is called thermophoresis. Since thermophoretic deposition is linked to temperature gradients, it is only significant in spaces where the distance between particles and the wall is small.

- *Deposition by Diffusiophoresis*

Diffusiophoresis is particle movement by entrainment in the flux of a condensing vapour (Stefan flow) such as steam. This effect arises because the gas impinging on one side of the particle imparts more momentum than that impinging on the other side. The particles are carried by the condensing vapour towards to the cold wall and deposit. This phenomenon always appears simultaneously with thermophoretic deposition.

- *Electrophoretic Deposition*

Generally speaking, the electric charge of an aerosol is never nil following impact with molecules. Charged particles can be drawn to a wall due to the electric force (which can, in certain cases, be very superior to gravity) and be trapped on the wall. Even for a “neutral” aerosol there may be a charge balance of positive and negative particles; this balance can be destroyed by generating positive or negative ions in the medium, such as in a strong electric field or near a radioactive

source. Nuclear aerosols tend to be charged due to transporting radioactive isotopes that emit β and α radiation carrying away electric charge.

1.2.2.3 Particle Resuspension

In reactors, particles deposited on surfaces can become resuspended by an aerodynamically-generated lift and drag forces due to the incidents already described above. The basic nature of the resuspension process is understood but it is not possible with today's models to predict reliably when and to what extent the process occurs (see Chapter 2).

Many parameters need to be considered in the resuspension process such as particle size, flow conditions and the adhesion strength between particles and wall. Surface roughness is a significant parameter in adhesive force. Resuspension is a random process. Particles are not immediately resuspended by a certain flow but by irregular bursts. In turbulent flow, small particles are resuspended in the boundary layer due to the occasional bursts of turbulent eddies. Resuspension is a key precursor to dust explosions (cf. ITER above). In nuclear accidents, resuspension can have considerable impact on the progression of the accident and radiation releases (Williams & Loyalka, 1991).

1.3 Objectives and Outline

1.3.1 Objectives

The underlying objective of this research is to develop, validate and apply a physical model for the resuspension of particles from multilayer deposits that can account for the resuspension of clusters of particles from a bed of particles of variable size and shape. It was not expected that a final model taking account of an arbitrary deposit in arbitrary conditions would be developed but that very substantial progress would be made towards this objective. The practical application will be that of assessing resuspension of particles in a range of accident scenarios for PWRs as well as other reactor technologies such as ITER. It will be seen that progress has been made with a hybrid development of the Rock'n'Roll (Reeks & Hall, 2001) model suited to application to multilayer deposits.

The resuspension of a particle from a multilayer deposit depends on the interaction of two processes: the aerodynamic forces tending to remove the particle from the bed and the various forces (essentially due to particle-particle interactions) that resist resuspension. To some extent, these two effects can be decoupled and studied separately. The aerodynamic forces acting on a particle will depend mainly on the turbulent flow and will be largely independent of the nature of the surface so that results obtained for an isolated particle on a smooth wall can be applied to an

exposed particle sitting at the surface of a multilayer deposit. The form of the particle resistance to resuspension that is assumed in the Rock'n'Roll model might also be expected to apply to exposed particles on a multilayer deposit. But there are also good physical reasons for believing that other effects might occur in the resuspension of particles from a multilayer model that are not present in the resuspension of an isolated particle from a smooth wall. For example, the micro- and macro-scale roughness of the multilayer deposit will have some influence on the turbulent structure of the near-wall boundary layer, thus modifying the aerodynamic forces acting on the particle. And the presence of a wide range of particle sizes within the multilayer deposit can result in additional resistance forces caused by interaction between the particles. An important consequence of this interaction is that the resistance to resuspension can vary in time – the largest particles will tend to disappear first, leaving a high concentration of small particles in the surface layer. These small particles might then act as 'cement', locking in the larger particles in the lower layers, and thus modifying the threshold for particle erosion. In such a situation the Rock'n'Roll model might no longer be a reliable or relevant model for the intervening physical processes.

There remain some physical uncertainties in the basic Rock'n'Roll model, notably concerning the validity of the assumptions made in modelling the aerodynamic forces on a particle at the surface. It was decided, therefore, that since the Rock'n'Roll model will form the basis of a model for resuspension from a multilayer deposit, the first priority of this research would be to improve the modelling of the turbulence-induced aerodynamic forces on an isolated particle. It was thought that investigating how the presence of layers of particles might modify the turbulence and the aerodynamic forces exerted on the particle might also be achieved. Some account of how the resistance to resuspension is modified for particles at the surface of a multilayer deposit was also a possibility. The results from these possibilities could then be used to develop a simpler engineering model for resuspension from multilayer deposits.

Detailed objectives begin with improving the Rock'n'Roll model for the resuspension of particles from surfaces with less than a mono-layer coverage. Simulations will be required of the stochastic properties of the turbulent forces generated on particles due to the turbulent structures generated in the boundary layer (sweeping and bursting mechanisms). In particular, the examination of the sensitivity or otherwise of the Gaussian assumption used in earlier stochastic models for resuspension must be verified. This data will be used to construct a model for resuspension rate that takes account of the non-Gaussian nature of the turbulent fluctuations (in particular the turbulent induced shear force). It will be important to see how, for instance, the spectrum of the turbulent-fluctuation strain rates is coupled to the induced aerodynamic forces. These forces will be calculated using various models for the lift and drag based on the local instantaneous strain rate and fluid velocity. Then, the intention was to develop a mechanistic model for resuspension of particles of variable sizes (and perhaps shapes) from multilayer deposits accounting for the resuspension of particles in clusters. A detailed model must deal with detailed mechanisms for

release of clusters under the actions of turbulent drag and lift forces and their couples and the cohesive forces binding the deposit together.

1.3.2 Outline

There are six chapters in this thesis. The present Chapter is the introduction which describes the background of severe nuclear accidents and aerosol issues in different types of reactors as well as the objective of this research. Chapter 2 is a literature review which presents the previous theories on forces acting on particles when they are near the boundary layer, classical resuspension models and previous resuspension experiments. The previous classical resuspension models are summarized in three parts: 1) models based on force balance, 2) models based on energy accumulation, 3) multilayer-deposit resuspension. Modifications of resuspension models rendering them physically more acceptable will be demonstrated in Chapter 3 and Chapter 4, i.e., Chapter 3: modification of a typical force-balance model (the fluctuating aerodynamic forces will be considered); Chapter 4: modification of an energy-accumulation model (the statistics of fluid fluctuations will be modified based on Large Eddy Simulation and Direct Numerical Simulation data). In Chapter 5, a multilayer resuspension model based on energy accumulation will be developed, tested and discussed. Finally, Chapter 6 leads to the final conclusions and future possibilities.

Chapter 2
Literature Review

....I was standing on the shoulders of giants.

- Isaac Newton

In reality when a particle is sitting on the wall in a fluid flow (see Figure 2.1 below), the aerodynamic forces - such as drag, lift, etc. - are tending to remove the particle from the surface whereas the adhesive force, gravitational force, etc. tend to hold the particle on the surface and resisting particle resuspension. In this section, the boundary layer condition and different forces acting on particles will be introduced, and then the classical resuspension models will be particularly reviewed; finally the resuspension experiments will be discussed.

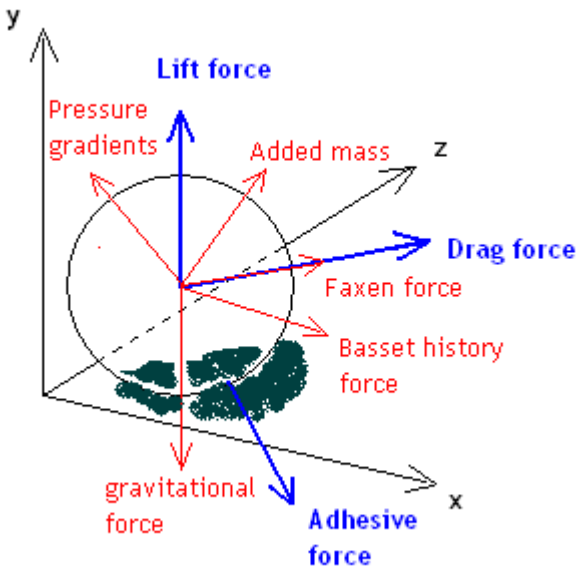

Figure 2.1 - Forces on particle

2.1 Boundary Layer and Forces

2.1.1 Boundary Layer

A boundary layer is a relatively thin layer of fluid close to a solid boundary in which the fluid velocity changes rather rapidly with distance from the boundary. As we know, due to the effect of viscosity, the fluid in contact with a solid surface must move at the same velocity as the surface (the 'no-slip' condition). If the wall is stationary, the fluid velocity must therefore fall to zero at the wall. Therefore, there will be a velocity transition between the near wall region and the boundary. At large Reynolds numbers this transition takes place in a thin layer near to the wall and Prandtl (1904) named this layer *the boundary layer*. A boundary layer is not a static phenomenon but dynamic. The thickness of a boundary layer (there are several ways of defining the boundary layer thickness: the height from the solid surface where 99% of free stream speed is first encountered or on the basis of momentum, etc.) varies with streamwise position on the boundary. The boundary layer may be laminar or turbulent which depends on the Reynolds number but viscous forces dominate very near the wall even in the turbulent case.

Consider a flow with velocity U past an object with typical length scale L (for a circular pipe, this is the diameter of the pipe and for a flat plate the distance from leading edge), a relative Reynolds number is defined as $Re = UL/\nu_f$, where ν_f is the kinematic viscosity of the fluid. The Reynolds number characterizes the relative strength of viscous and inertial forces and it is the key parameter used in defining whether a flow is likely to be turbulent. For low values of Re, viscous forces dominate the flow and it tends to be laminar. For larger values, a point (typically $Re = 4 \times 10^3$ for circular pipe and $Re = 5 \times 10^5$ for flat plate) is reached where a transition occurs in which the fluctuations are amplified. Beyond this point, the flow tends to be a fully turbulent state.

2.1.1.1 Laminar Boundary Layer

In a laminar boundary layer, any mass or momentum exchange takes place only between adjacent layers and the shear stress associated is able to be predicted by molecular viscosity. More details on laminar boundary layer are provided in Batchelor (1967). In the present thesis, particles resuspension is only considered in turbulent boundary layer.

2.1.1.2 Turbulent Boundary Layer

In a turbulent boundary layer, turbulent eddies rather than molecular viscosities are responsible for the exchange of mass, momentum and energy (except for the very thin viscous layer adjacent to the surface), and thus take place on a much bigger scale than for the laminar boundary layer. It is convenient to transform the variables to dimensionless form with respect to the wall variables.

$$u_\tau = \sqrt{\frac{\tau_w}{\rho_f}}, \quad u_i^+ = \frac{\bar{u}_i}{u_\tau}, \quad y^+ = \frac{u_\tau y}{v_f}, \quad v_i^+ = \frac{\bar{v}_i}{u_\tau}, \quad t^+ = \frac{u_\tau^2 t}{v_f} \qquad [2.1]$$

u_τ is the wall friction velocity, τ_w is the wall shear stress, ρ_f is the density of the continuous phase, v_f is the kinematic viscosity of the continuous phase, u_i^+ are the dimensionless fluid velocities (note that $\bar{u}_i$ is the time averaged fluid velocity), v_i^+ are the dimensionless particle velocities, t^+ is the dimensionless time and y^+ is the dimensionless distance normal to the wall (Schlichting, 2000).

In the case of smooth surfaces, the friction velocity can be evaluated as a function of the Fanning friction factor *f** and the fluid characteristic velocity *U* (cross sectional average velocity which is averaged over the cross sectional area and mass flow rate); In TRAP-MELT2, *f** is computed from an empirical correlation with Reynolds number (Parozzi & Masnaghetti, 1990).

$$u_\tau = U\sqrt{\frac{f^*}{2}} = U\sqrt{\frac{0.0014 + 0.125Re^{-0.32}}{2}} \qquad [2.2]$$

Close to the wall in the viscous sublayer ($0 < y^+ \leq 5$) viscous forces dominate and the dimensionless velocity varies linearly with distance from the wall:

$$u_x^+ \propto y^+$$

Further away from the wall ($y^+ > 70$), momentum transfer is dominated by turbulent eddies, and the velocity profile is logarithmic (but note that the log regime does not extend indefinitely):

$$u_x^+ = \frac{1}{\kappa}\ln y^+ + 5$$

In between those two layers, there is a transition region – the buffer region – where the velocity evolves from a linear to a logarithmic profile. Varies forms have been proposed for the velocity distribution in this region; recently, Gersten and Herwig (1992) suggested:

$$u_x^+ = \frac{1}{\Lambda}\left[\frac{1}{3}\ln\frac{\Lambda y^+ + 1}{\sqrt{(\Lambda y^+)^2 - \Lambda y^+ + 1}} + \frac{1}{\sqrt{3}}\left(\arctan\frac{2\Lambda y^+ - 1}{\sqrt{3}} + \frac{\pi}{6}\right)\right] + \frac{1}{4\kappa}\ln(1 + 0.00143\kappa y^{+4}) \qquad [2.3]$$

where $\kappa = 0.41$ and $\Lambda = 0.127$. The complete profile is plotted in Figure 2.2.

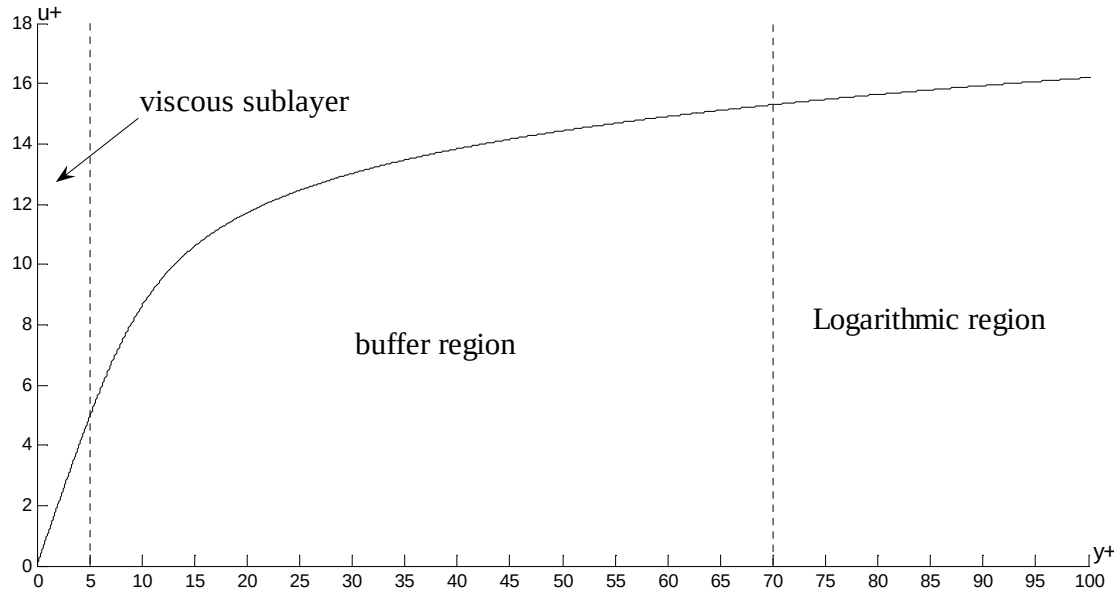

Figure 2.2 - Dimensionless fluid mean velocity in the turbulent boundary layer

In the viscous sublayer ($y^+ < 5$), the mean flow shows a linear profile where the shear rate is given by $G = u_\tau^2 / v_f$. Therefore, the shear rate Reynolds number becomes $Re_r = u_\tau r / v_f$.

In the case of a rough surface, the measurements of Nikuradse (1932, 1933) give

$$u_x^+ = 2.5 \ln \frac{y}{k_r} + 8.48 \qquad [2.4]$$

where k_r is the Nikuradse roughness length (depends on material, e.g. 0.06 for coated steel, 0.16 for coated cast iron, 0.3-3.0 for reinforced concrete, etc).

There is no analytical solution for the profiles of turbulent quantities such as fluctuating velocities and Reynolds stress, but various authors have attempted to fit equations to measured data. In this way, Kallio and Reeks (1989) obtained the following profiles for the root mean square of fluctuating streamwise velocity and the dimensionless timescale of the fluid fluctuation (see Figure 2.3):

$$u'_{rms} = \frac{0.005 y^{+2}}{1 + 0.002923 (y^+)^{2.218}} \qquad 0 < y^+ < 200$$

$$\tau_f^+ = \begin{cases} 10 & 0 \le y^+ \le 5 \\ 7.122 + 0.5731 y^+ - 0.00129 y^{+2} & 5 < y^+ < 200 \end{cases} \qquad [2.5]$$

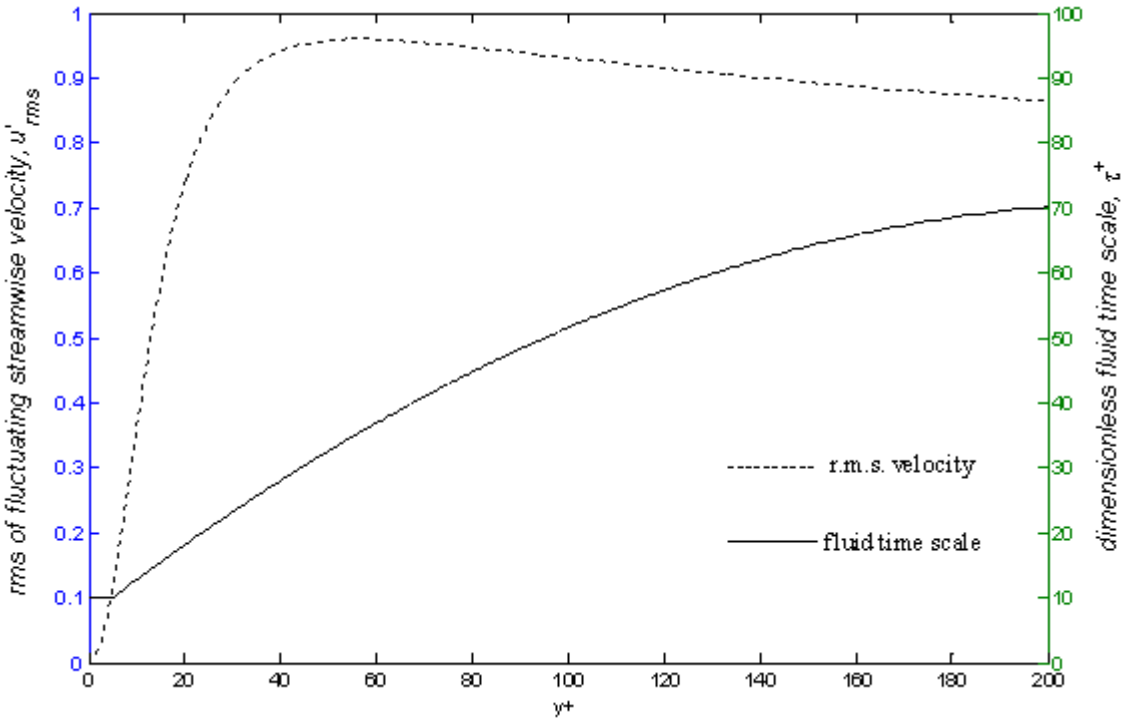

Figure 2.3 - rms of fluctuating velocity and fluid time scale vs. y^+ (Kallio & Reeks, 1989)

Although there is strong activity in the near-wall region as shown by Townsend (1956), the important feature this region reveals in the turbulence dynamics was first demonstrated by Kline *et al*. (1967). They demonstrated an experiment to visualize the flow in a low-speed water channel by using hydrogen bubbles which were generated by an electric wire. This technique revealed the presence of low-speed streaks (shown in Figure 2.4, the wire is located parallel to a flat plate and normal to the direction of flow; the flow is from left to right of the pictures). Intermittently, the streaks begin to oscillate and then break up in a fairly violent motion, also called a 'burst' (shown in Figure 2.5, the wire is located normal to the plate on the left of the pictures; the flow is from left to right of the pictures).

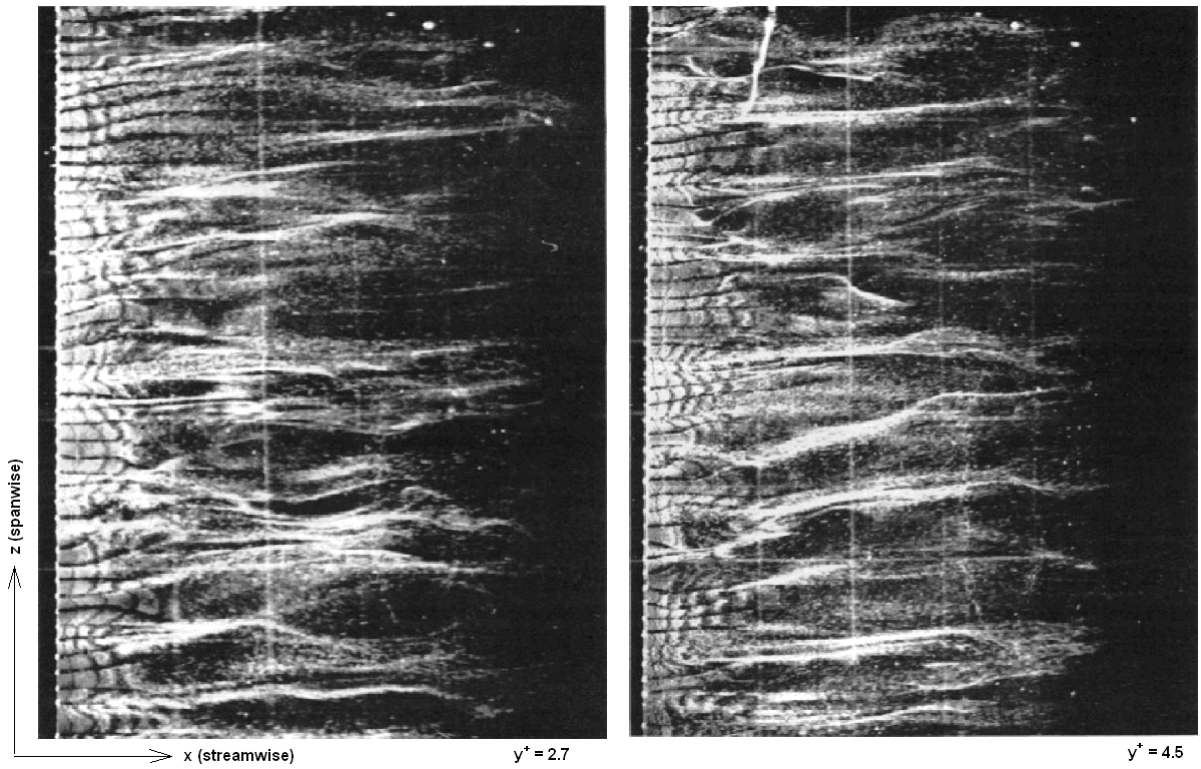

Figure 2.4 - Near-wall structure of a turbulent boundary layer (top view) (Kline *et al.*, 1967)

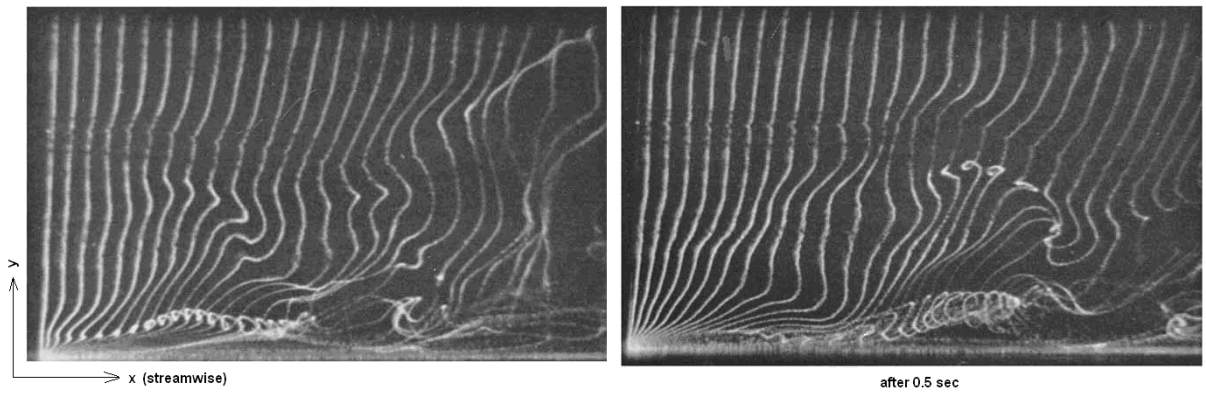

Figure 2.5 - Near-wall structure of a turbulent boundary layer (side view) (Kim *et al.*, 1971)

Figure 2.6 sketches the formation and breakup of the streak in the bursting process. Kim *et al.* described that the total bursting process is a continuous chain of events leading from a relatively quiescent wall flow to the formation of relatively large and relatively chaotic fluctuations. The process, in the cases observed, is of an on-off or intermittent character. They also showed that much of the turbulence production (about 70% of the total) was associated with the bursting.

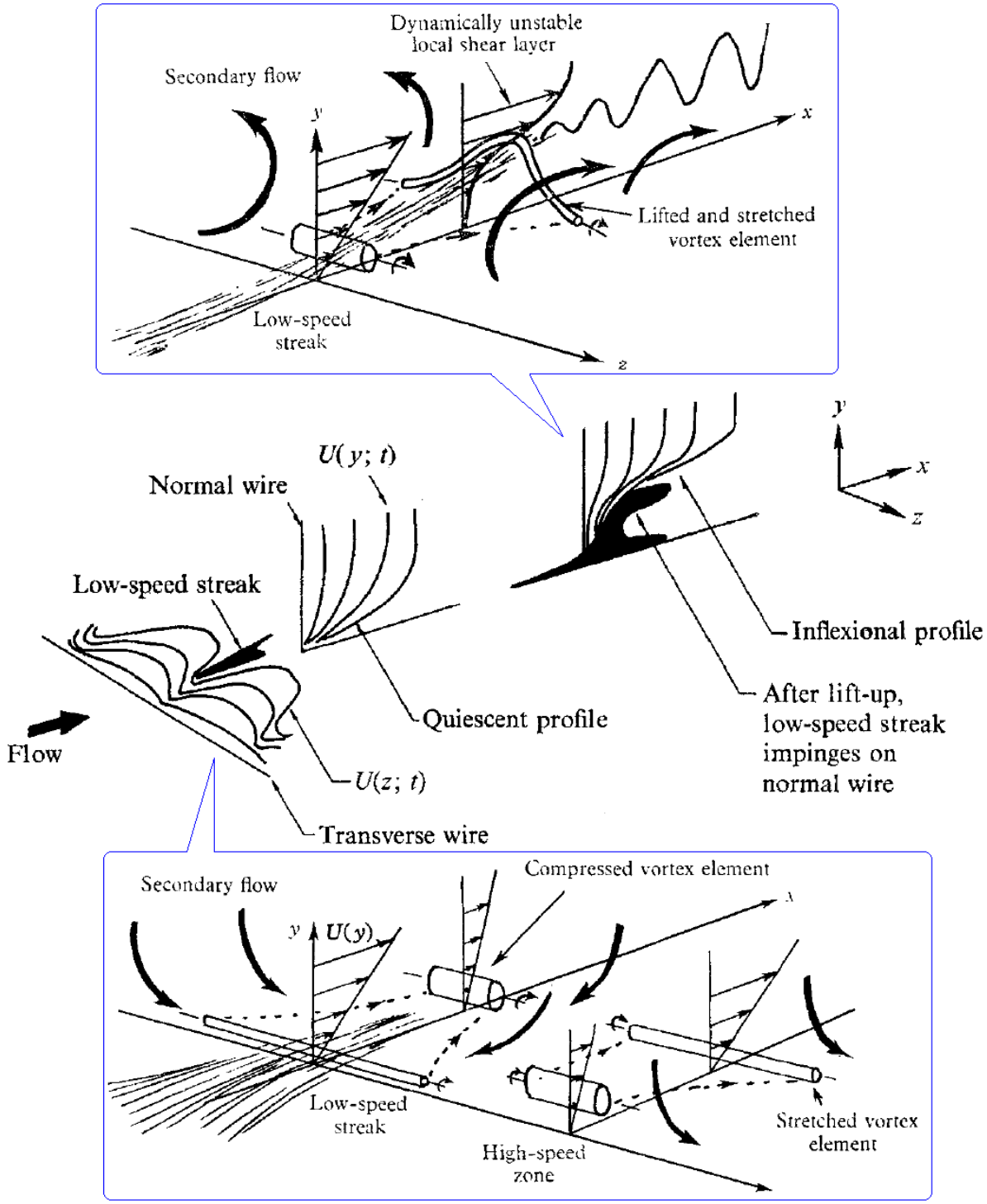

Figure 2.6 - Mechanics of streak formation and breakup (Kline *et al.*, 1967; Kim *et al.*, 1971)

In Kim *et al.* (1971) model, the first stage of bursting is considered as the lifting of a low-speed streak from the wall. As the low-speed streak moves downstream it also gradually moves away from the wall. The observed secondary (streamwise) vorticity embodied in a low-speed high-speed streak pair initially is very low. As a result, the low-speed streak at first moves away from the wall very slowly over a very long streamwise extent. One might say that its outward motion, away from the wall, is then the cumulative effect over long distances (or times) of a small streamwise vorticity.

However, once the low-speed streak has reached some critical distance from the wall, it appears to turn much more sharply outward, away from the wall, but still moving downstream. This more rapid outward motion is referred as ‘low-speed-streak lifting’ or, for brevity, ‘streak lifting’. The use of the words ‘critical distance’ should not be interpreted as sharply defined single distance; there is, in fact, a distribution of critical values when measured over a large number of streak-lifting processes.

2.1.2 Forces Acting on a Particle

When a particle is moving in a flow, different forces are generated from either the fluid properties such as viscosity or the properties of the particle itself (density, radius, etc.). In this section, the aerodynamic forces will be described in detail.

2.1.2.1 Drag Force and Faxen Force

Suppose the particle is moving in a uniform pressure field when there is no acceleration, the drag force acting on the particle is defined as the steady-state drag force.

$$F_{ssD} = \frac{1}{2}\rho_f C_D S|\mathbf{u}-\mathbf{v}|(\mathbf{u}-\mathbf{v}) \qquad [2.6]$$

ρ_f is the density of the flow, C_D is the drag coefficient which varies with particle Reynolds number (Re_p). S is the representative area (cross section perpendicular to the flow) of the particle. **u** and **v** are fluid and particle velocity vector, respectively. Re_p is defined as below.

$$Re_p = \frac{2\rho_f r|\mathbf{u}-\mathbf{v}|}{\mu_f} \qquad [2.7]$$

r is the radius of the particle (assumed as sphere), μ_f is the fluid viscosity. The relationship between Re_p and C_D is shown in Figure 2.7. At critical Reynolds number (Re_p ~ 3 x 10^5), there is a dramatic decrease in the drag coefficient since the boundary layer becomes turbulent.

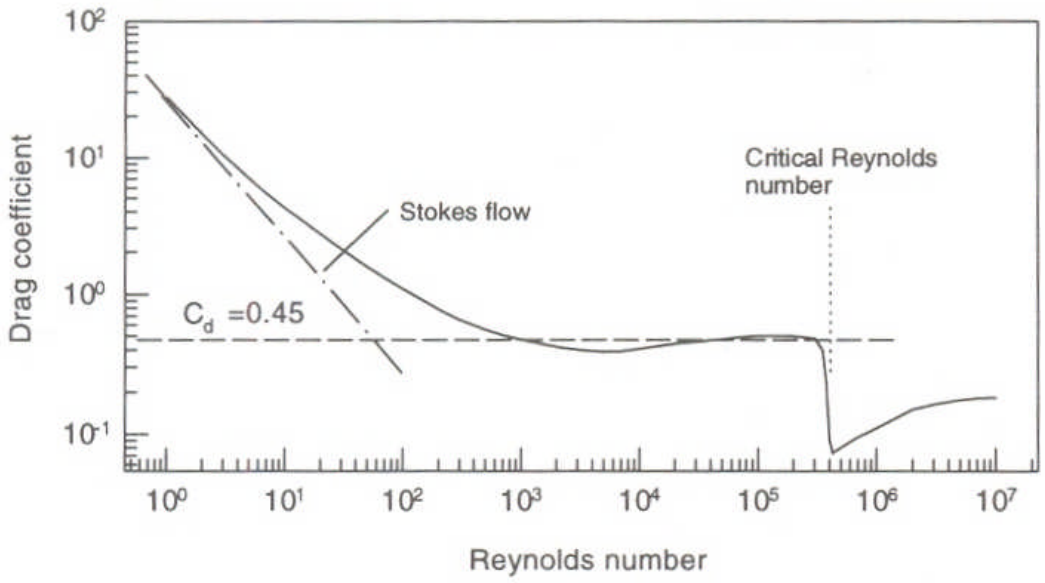

Figure 2.7 - Drag coefficient vs. Particle Reynolds number (Crowe *et al.*, 1998)

When Re_p < 1, C_D becomes the classical Stokes drag coefficient (C_D = 24/Re_p). Stokes was the first to derive an expression for the drag force on a small spherical particle falling in a viscous fluid.

$$F_D = 6\pi\mu_f r(\mathbf{u}-\mathbf{v}) \qquad [2.8]$$

O'Neill (1968) derived that the drag force on a spherical particle near a surface in uniform linear shear flow is approximately 1.7 greater than the Stokes drag force.

$$F_{DS} = 32.06\mu_f r(\mathbf{u} - \mathbf{v}) \qquad [2.9]$$

It can also be written as

$$F_{DS} = 32.06\mu_f r^2 G$$

where G is the shear rate. For a dimensionless distance from a surface smaller than $y^+ = 5$, the shear rate can be written as u_τ^2/v_f , u_τ is wall friction velocity and v_f is the fluid kinematic viscosity.

The Stokes drag force is based on a uniform free stream velocity; for non-uniform flow field an additional force was derived by Happel & Brenner (1973) which is called the Faxen force.

$$F_F = \pi\mu_f r^3 \nabla^2 \mathbf{u} \qquad [2.10]$$

Dandy and Dwyer (1990) performed 3D numerical simulations of a non-rotating sphere in a steady linear shear flow for a wide range of particle Reynolds numbers ($0.1 \le Re_p \le 100$) and dimensionless shear rates. Their simulations showed that the drag force on a spherical particle in a shear flow is almost the same as that in a uniform flow, in other words, the effect of shear on the drag force is very weak.

Hontanon *et al*. (2000) derived the expressions of the drag force on a spherical particle near the wall in turbulent pipe flow, including corrections due to both inertial and wall effects.

$$F_x^{drag+} = 6\pi Re_p(u_x^+ - v_x^+)\left[1 + \frac{2^{2/3}}{6} Re_p{}^{2/3}(u_x^+ - v_x^+)^{2/3}\right]\left(1 - \frac{9}{16}k_{pw} + \frac{1}{8}k_{pw}{}^3 - \frac{45}{256}k_{pw}{}^4 + \frac{1}{16}k_{pw}{}^5\right)$$

$$F_y^{drag+} = 6\pi Re_p(u_y^+ - v_y^+)\left[1 + \frac{2^{2/3}}{6} Re_p{}^{2/3}(u_y^+ - v_y^+)^{2/3}\right]\left(1 - \frac{9}{8}k_{pw} + \frac{1}{2}k_{pw}{}^3\right)^{-1} \qquad [2.11]$$

where u_x^+, u_y^+ are the fluid velocities in the streamwise and normal directions, v_x^+, v_y^+ are the particle velocities in the streamwise and normal directions and k_{pw} is the ratio of particle radius to particle distance from the wall.

In this thesis, the drag force will be calculated by simply using the O'Neill (1968) method. Also there is an alternative method calculating drag force from local velocity gradients (Lee and Balachandar, 2010) which will be introduced in Chapter 4.1.7 (p148)

2.1.2.2 Lift Force and Magnus Force

The Magnus force is caused by particle rotation. Due to the velocity difference between the two sides of the particle, there is a pressure difference across the particle surface. Rubinow & Keller

(1961) derived an analytical expression for the Magnus lift force on a spinning sphere, for the condition Re_p ~ 1.

$$F_M = \frac{1}{8}\pi\rho_f D^3 \left[\left(\frac{1}{2}\nabla\times\mathbf{u} - \omega_p\right)\times(\mathbf{u}-\mathbf{v})\right] \quad [2.12]$$

Lift force is the force generated due to particle inertia and shear rate, which causes the particle to travel normally to the flow direction (perpendicular to the direction of the drag). There are three important parameters of the Reynolds numbers associated with the shear rate (Re_r), the particle slip (Re_s) and the particle rotation (Re_ω).

$$Re_r = Gr^2/v_f, \quad Re_s = V_s r/v_f, \quad Re_\omega = \omega_p r^2/v_f \quad [2.13]$$

where G is the velocity gradient or shear rate, V_s is the particle slip velocity, v_f is the fluid kinematic viscosity, and ω_p is the particle rotation.

When a particle is moving in a shear flow ($Re_p \ll 1$), due to the pressure distribution induced by velocity gradient, a force is generated by the pressure gradient normal to the velocity streamline. This is so called the Saffman lift force (Saffman, 1965), which is valid only for the strong shear regime ($Re_r^{1/2} \gg Re_s$).

$$F_{Sl} = 6.46r^2\sqrt{\mu_f\rho_f}\,\frac{(\mathbf{u}-\mathbf{v})\times(\nabla\times\mathbf{u})}{\sqrt{|\nabla\times\mathbf{u}|}} \quad [2.14]$$

This solution, as noted by Saffman, is not valid for the particle near the wall surface.

According to Goren (1970), the lift force acting on a particle in contact with a plane in uniform flow depends on fluid viscosity, particle radius and a constant characterizing velocity gradient of the fluid velocity normal to the plane. The constant gradient based on Laufer's (1954) result is estimated proportional to fluid kinematic viscosity and wall friction velocity. Then the lift force of the particle on the plane in uniform flow is obtained by

$$F_{lp} = 0.608\rho_f v_f^{\,2}\left(\frac{r u_\tau}{v_f}\right)^3 \quad [2.15]$$

However, this model was considered in the case of creeping flow only and the flow direction was normal to the surface.

For a sphere resting on a flat surface in wall-bounded shear flow under conditions of small particle Reynolds numbers, Leighton and Acrivos (1985) showed the mean lift force in terms of the shear rate is equal to u_τ^2/v_f in the viscous sublayer ($y^+ < 5$). Therefore, the mean lift force acting in the boundary layer is derived as

$$F_{LA} = 0.576\rho_f v_f^{\,2}\left(\frac{D u_\tau}{v_f}\right)^4 \quad [2.16]$$

However, their solution is only strictly valid when the shear Reynolds number is much less than one.

Cherukat and McLaughlin (1994) derived a simplified equation for the inertial lift force on a spherical particle in a linear shear flow very close to a flat wall (i.e., the ratio of particle radius to particle distance from the wall, $k_{pw} \approx 1$) which interpolates smoothly between the Saffman and the Leighton-Acrivos limit. It is considered to be the best analytical result to calculate the lift force on a sphere in wall-bounded shear flow (Lazaridis *et al.*, 1998).

$$\begin{aligned} F_{il} = &\left(1.7716 + 0.2160k_{pw} - 0.7292{k_{pw}}^2 + 0.4854{k_{pw}}^3\right)Re \\ &-\left(3.2397 / k_{pw} + 1.1450 + 2.0840k_{pw} - 0.9059{k_{pw}}^2\right)Re_r \\ &+\left(2.0069 + 1.0575k_{pw} - 2.4007{k_{pw}}^2 + 1.3174{k_{pw}}^3\right){Re_r}^2 / Re \end{aligned} \quad [2.17]$$

There is a major assumption for all the lift force theories above, which is that both the shear rate Reynolds number and slip Reynolds number are much smaller than unity ($Re_r \ll 1$, $Re_s \ll 1$).

None of the above theories can be extrapolated to the situation where larger particle Reynolds numbers are considered and also they are not valid for the spherical particles near the surface in the sublayer region. Hall (1988) then produced an experiment to measure the lift force on the particles in the viscous sublayer and derived a correlation of mean lift force by fitting to the experimental data.

$$\left\langle F_L \right\rangle = 20.9\rho_f {v_f}^2 \left(\frac{ru_\tau}{v_f}\right)^{2.31} \quad [2.18]$$

which is valid over the range ($1.8 < ru_\tau / v_f < 70$). This model will be applied for the mean lift force in this thesis.

2.1.2.3 Pressure Gradient and Buoyancy Force

The local pressure gradient generates a force in the opposite direction of the pressure gradient. The net pressure force and shear stress force are given by:

$$F_P = -V_p \nabla p_f, \quad F_\tau = V_p \nabla \cdot \tau_{ij} \quad [2.19]$$

where V_p is the particle volume, τ_{ij} is the shear stress tensor and p_f is the fluid pressure.

Sometimes, in the case of bubbly flow, the buoyancy effect becomes important. The corresponding buoyancy force is known as Archimedes principle.

$$F_b = (\rho_p - \rho_f) g V_p \quad [2.20]$$

where ρ_p is the particle density.

However, pressure gradient and buoyancy force is very small for solid particles compared to drag and lift. Therefore, they are not considered in this thesis.

2.1.2.4 Added Mass Force and Basset Force

The added mass force, also known as the virtual mass force, is a result of the fluid around the particle being accelerated with the particle. Essentially, it just expresses the fact that in order to accelerate the particle, the fluid also needs to be accelerated: the fluid in front of the particle has to get out of the way, and the fluid behind has to follow the particle. Balancing the work done in accelerating inviscid and incompressible fluid surrounding the particle, the added mass force is obtained

$$F_A = \frac{1}{2}\rho_f V_p \left(\frac{D\mathbf{u}}{Dt} - \frac{d\mathbf{v}}{dt} \right) \qquad [2.21]$$

The Basset force, also called the Basset history force, is the force associated with past movements of the particle. The Basset term takes account of viscous effects - it describes the force due to the lagging boundary layer development with changing relative velocity. The Basset force depends on the acceleration history up to the present time. Reeks and McKee (1984) modified the expression for the Basset force to include the case when there is an initial fluid and particle velocity.

$$F_B = 6r^2\sqrt{\pi\rho_f\mu_f}\left[\int_0^t \frac{\dot{\mathbf{u}} - \dot{\mathbf{v}}}{\sqrt{t-s}}\,ds + \frac{\mathbf{u}_0 - \mathbf{v}_0}{\sqrt{t}}\right] \qquad [2.22]$$

where $\mathbf{u}_0$ and $\mathbf{v}_0$ are the initial fluid velocity and particle velocity, respectively.

In this thesis, the added mass and Basset force are not considered due to their small contributions to the aerodynamic force for small solid particles in gas flow.

2.1.2.5 Adhesive Force and Surface Roughness

Adhesive forces include intermolecular forces such as van der Waals interactions, various chemical and hydrogen bonds, and sintering effects such as diffusion, condensation and diffusive mixing (Krupp, 1967). Surface roughness also plays an important role in adhesion since the adhesion of small particles on rough surfaces is mainly determined by the geometrical features of the surface-particle system (Katainen *et al.*, 2006).

Hertz (1896) was the first person who investigated the contact between two smooth elastic bodies and demonstrated that the contact radius (distance between the centres of the mass of two bodies) between two spheres is a function of the sphere radii and the force acting on them.

$$r_c^{\,3} = \frac{3}{4}\pi(k_1 + k_2)\frac{r_1 r_2}{r_1 + r_2}F_{pf} \qquad [2.23]$$

where r_c is the contact radius, k_1 and k_2 are elastic constants for each sphere, r_1 and r_2 are sphere radii, and F_{pf} is the pressed force (interaction force) between spheres. Based on Hertz's contact equation, Johnson *et al.* (1971) (JKR) demonstrated that the pull-off force between the solid elastic spheres in contact is determined by the surface energy:

$$P = \frac{3}{2}\pi\gamma\frac{r_1 r_2}{r_1 + r_2} \quad [2.24]$$

where γ is the surface energy per unit contact area. Based on the JKR theory, the element of the normal force of adhesion to the surface for a perfectly smooth contact surface and a spherical particle of radius is:

$$F_a = \frac{3}{2}\pi\gamma r \quad [2.25]$$

where γ is the surface energy, (0.56J/m^2 for aluminium, for example). This simple model will be applied for the adhesive force of particle sitting on perfect smooth surface in this thesis.

Schaefer et al. (1995) investigated the surface force interactions between individual 8 μm diameter spheres and atomically-flat substrates and concluded that by including the surface asperities of the substrates, the measured pull-off forces are a factor of 3 smaller than that expected from the JKR predictions. Deladi *et al.* (2002) presented a 3D adhesion model based on JKR theory, which is capable of estimating adhesive forces between two arbitrary surfaces taking into account van der Waals forces, normal forces, elastic and plastic deformation of the contacting asperities.

Recently, surface energy and pull-off forces for particles in contact with a rough surface have been measured using Atomic Force Microscopy (AFM). The basic principles of this technique are well described in Binnig *et al.* (1986). Measurements of pull-off force obtained using this method are provided by Beach *et al.* (2002) and Drelich *et al.* (2004). George and Goddard (2006) describe the use of this technique to measure surface energy of rough surfaces. Several approaches have been developed for describing the effect of surface roughness on adhesion, and Eichenlaub *et al.* (2004) compare three of these – representation by hemispherical asperities, by fractals, and by Fourier transforms (Cooper et al., 2001) – using results from AFM. However, the details are not included here since this is not important to the rest of this study.

Van der Waals and cohesive force

The Van der Waals force is the principal interaction force between particles caused by general molecular attraction. It is related to the Hamaker constant (H_c) which is determined by the number and static polarizability of the atom particles. Ranade (1987) stated that the effect of roughness on Van der Waals force is highly dependent on the nature of the roughness and that the molecular interactions are usually active over a distance of several nanometres across the interface between the particle and the substrate. Recent models simulating adhesive force between a small spherical particle and a rough surface are based on the idea that the asperities can be modelled as hemispherical caps on a smooth substrate. Rabinovich *et al.* (2000) modified Rumpf's model (Rumpf, 1990) - commonly used in modelling adhesive force between a spherical particle and nanoscale surface roughness - by replacing asperity radius with the asperity root mean square (rms) roughness (rms value of the asperity radii) since the asperity radius is not easily measured; they proposed:

$$F_{ad} = \frac{H_c r}{6H_0^2}\left[\frac{1}{1+r/1.48a_{rms}} + \frac{1}{(1+1.48a_{rms}/H_0)^2}\right] \quad [2.26]$$

where H_c is the Hamaker constant, H_0 is the equilibrium distance (closest approach between surface, approximately 0.3nm), r is the particle radius and a_{rms} is the asperity rms value. Rabinovich *et al.* (2000) concluded that their model is more accurate than previous models. The experimental adhesion force was predicted within 50% of experimental values using their method whereas previous models underestimated adhesion by a factor of 10-50.

The cohesive force is defined as the adhesive force between particles and is generated by the same physical processes as those responsible for the van der Waals force, but the cohesive force depends on the contact geometry between the particles. Alloul-Marmor (2002) noted that the contact forces between particles in a bed are much more complicated to evaluate than the equivalent forces for particles on a surface, because of the widely-varying contact conditions or deposit structure.

Other forces

There can be an electrostatic interaction between particles, or particles and a surface caused by the difference in the work function of contact potential between two materials or by the electric charge on the particle or the surface. Bowling (1988) concludes that for particles less than 25 μm (radius), the Van der Waals force predominates over the electrostatic force.

If a liquid film is present, capillary forces can have an important effect; in dry conditions it might be expected that this force will not be significant, but if the aerosol particles have absorbed liquid, then a liquid film can be present on the surface of the particle. The force is linearly proportional to the radius of curvature of the liquid film, and this will generally scale on particle radius.

The frictional force is due to the sliding and rolling resistance and is related to the particle weight. However, in the multilayer deposit the frictional force is also affected by other forces (adhesion, particles interaction force, etc.).

2.1.2.6 Gravitational Force

The gravitational force for a spherical particle with radius r and material density ρ_p is given by:

$$F_G = \frac{4}{3}\pi r^3 \rho_p g \quad [2.27]$$

This force is generally only important for aerosol particles radii larger than 50μm, whilst for particle radii smaller than 25μm it becomes negligible.

2.2 Resuspension Experiments

2.2.1 General Experiments

Many experiments have been performed to investigate different aspects of the resuspension of small particles by a turbulent flow, and Table 2.1 (taken from Alloul-Marmor, 2002) provides a summary of most (if not all) of the relevant experiments. These experiments can be divided into two main groups – those aimed at improving the detailed understanding of specific physical processes involved in the resuspension of a small particle from a clean surface, and those designed to provide data concerning the collective resuspension of a large number of particles from a deposit. Often these latter experiments have been performed in conditions that are as close as possible to those that might occur in a real resuspension event in a nuclear circuit.

Data from both types of experiment have been used in the development and validation of resuspension models, but the very wide range of conditions and experimental techniques that have been used makes it difficult in some cases to obtain general agreement on the influence of certain parameters and effects.

It should also be emphasized that the conditions in a real resuspension event in a nuclear circuit are likely to be so extreme (temperature, velocities, radioactivity...) that it is not possible to envisage simulating them directly in an experiment. So the only way of extrapolating from laboratory experiments to these extreme conditions is with models which reproduce the basic physical processes correctly.

For the work presented in this thesis, the most useful resuspension experiment is that of Reeks and Hall (2001), partly because this was used to validate the Rock'n'Roll model, but also since the experiment provided direct measurements of particle adhesion. Detailed information about Hall's experiment is included in Chapter 4.1.4 (p129). Therefore, the parameters of adhesive force distribution, especially if it is assumed to be lognormal, could be useful for the comparison of the modified models. Also Biasi's correlation (Biasi *et al.*, 2001) between particle size and the statistical distribution of adhesive forces which was derived by tuning to results from several experiments (Braaten, STORM and ORNL, see next section) will be also widely applied here in the unmodified- and modified-model calculations.

Author	Year	Installation / Measurement Technology	Surface	Deposit of Particles	dp(µm)	Std	Parameters of flow	Measured value	Objective of experimental study and *observations*
Wright and Pattison	1984	Circular tubes 2.33×7.62 cm	Polished steel	Multilayer of Mg, Zn, TiO_2, FeO_2	0.1 - 1	---	Up to 120 m/s		Study of influence of parameters on reentrainment in multilayer deposits
Braaten *et al.*	1988	Wind tunnel 1×1×2.5 m / Optical system	Glass	Monolayer of Lycopodium	28	1.07	V (m/s) = 6,0 ; 7,5 ; 9,0 I <1 %	Concentration of resuspended particles as a function of time	Identification of coherent structures *2 events of Resuspension:* - *Ejection-sweeping* - *Macro-sweeping*
Wen and Kasper	1989	Tubes 1.25 to 25 mm / CNC and LPC	Polished steel, Electropolished steel, Rough steel	Monolayer of Dust Inconnu Latex	>0.01 >0.2 0.4 to 1	Polyd.	Volume flowrate (10^4 m^3/s) = 1.25 1.67 7.5	Concentration of resuspended particles as a function of time	Validation of the kinetic model of molecular desorption (Wen and Kasper, 1989) for the long-term (between 10 h and 100 h) *Observation of systematic departure from the 1 / Δ t law*
Wen *et al.*	1989	Tube 5 mm/ CNC and LPC	Pure steel	Monolayer of Latex	> 0.01	Polyd.	Re = 12400 155000	Concentration of particles Resuspension as a function of time	Validation of the model of Wen and Kasper (1989) for short term (< 1 min)
Fromentin	1989	Tunnel PARESS 25×25×350 cm / Gravitational weight	Stainless steel sample 10×30 cm^2	Multilayer of SnO2 Fe203 Sn Si	0.4 2 4 4.3	2.8 2 2 2	V (m/s) = 5 to 25	Flux of resuspension as a function of time	Study of resuspension a multiplayer deposit - Elaboration of a semi-empirical correlation *Observation of a reduction if the resuspension flux as a function of time*
Braaten *et al*	1990	Wind tunnel 1×1×2.5 m / Optical system	Glass (microscopic plate)	Dispersed monolayer of Lycopodium	28	1.07	V (m/s) = 6.0 ; 7.5 ; 9.0 I <1 %	Fraction resuspension as a function of time	Measurement of the adhesion force - Validation of the resuspension model based on a Monte-Carlo algorithm (Braaten *et al.*, 1990)
Tsai *et al.*	1991	Hard disk of computer / Calculations	Smooth disk of SiO_2	Monolayer of SiO_2 sphèrical and smooth	0.01 to 0.12		V (m/s) = 0.3 to 0.9	Critical linear velocity of resuspension	Validation of the resuspension model of critical moments *Highlighted the influence of the size of particles, energy of surface and parameters of membership on the critical velocity of detachment of particles*
Taheri and Bragg	1992	Injector 24×12 mm / Microscopic counting	Glass plate	Monolayer of Glass marbles	20 35	1.04 1.8	V (m/s) = 5 to 87	Percentage of particles resuspended as a function of the free velocity and friction velocity	Study of resuspension and of the critical velocity of detachment *Description of the lognormal distribution of the adhesive forces*
Wu *et al.*	1992	Blower 1×1×9 m / Microscope and camera	---	Monolayer of Uranine Polymer Lycopodium Pollen	5 to 42	Monod.	V (m/s) = 4 to 8 I~2 %	Resuspension and rebound fraction, Resuspension rate as a function of time	Phenomena of rebound and of resuspension of particles Description of the 2 regimes of resuspension: <1 min, strong rate ; followed by a weaker rate *Description of the influence of the velocity of flow, of the size of particles, of humidity and of roughness of surface*
Fairchild and Tillery	1992	Hemispheric channel 20×15 cm / Gravitational weight	Steel	Monolayer of Aluminium spheres	0.8 7.0	2.4 1.6	V (m/s) = 5 to 22	Rate of resuspension Vertical flux of resuspension	Effect of particles in saltation (100 to 200 µm) on resuspension of particles <10 µm Increase of Resuspension with the size of particles in saltation
Nicholson	1993	Wind tunnel 1×1×19.25 m / Isokinetic probe and optical microscope	Concrete Grass	Silica marbles	4.1 9.6 17.5 22.1	0.8 1.9 2.7 3.2	V (m/s) = 3.0 ; 5.0 ; 6.5 3.0 ; 4.5 ; 8.0	Rate of resuspension as a function of time	Influence study of the surface, particle sizes, air velocity and the type of resuspension surface *Variation of the rate: 1/Δt*

Braaten	1994	Wind tunnel 0.5×0.5×6 m / Optical system (microscopic counting)	Glass (microscopic plate)	Dispersed monolayer of Ni marbles Lycopodium Glass marbles Pollen	18 28 20 34	Polyd 1.07 Polyd	I <1 % V (m/s) = 9.6 to 15.1 5.9 to 11.0 13.5 to 19.6 5.4 to 10.9	Fractional resuspension as a function of adhesives forces and of velocity	Study of characteristics of resuspension of monolayer deposits *Determination of the entrainment velocity as a function of the flow velocity*
Foucault	1994	Tunnel 0.5×0.47×5.7m / Capture by sound and laser system	Polished or rough Steel	Natural bed of Polystyrene PVC Silica gel Glass marbles	80 to 2000 2 to 250 3 to 60 80 to 520	Tend to Monod Monod. Monod. Monod.	V (m/s) = 1 to 25	Critical lift-off velocity Mass of recovered particles	Phenomenon of takeoff and of saltation particles in a turbulent boundary layer– Validation of the lift-off model (Foucault, 1994)
Giess *et al*	1994 1997	Aerodynamic tunnel / Isokinetic probe	Palouse of different height	Silica spheres	dae = 1 ; 5 ; 10 et 20	Monod.	V (m/s) = 3.0 ; 5.0 et to 7.8	Resuspension rate and accumulative resuspension fraction as a function of time	Influence of the roughness of the surface, the speed of the wind, the stability of the speed and the time of exposure on resuspension *Description of the dependence of the rate as a function of time*
Matsusaka and Masuda	1996	Canal rectangulaire 3×10×400 mm / Electrostatic method	---	Fly ash agglomerates	3,0 10-30	2.14	V (m/s) = 10 to 40 Acc (m/s2) = 0.01 to 0.6	Resuspension flux and Mass resuspended per unit surface area as a function of velocity and time	Study of a entrainment in a stable and accelerated flow – Validation of the model of Matsusaka and Masuda (1996) *Description of the influence of acceleration on reentrainment*
Hummel *et al*	1998	Circular wind tunnel STORM 63 mm×5 m /	Steel with roughness of 0.8 µm	Multilayer SnO_2	dae= 0.8 0.7 0.7	 1.8 2.7 2.3	V (m/s) = 58 to 127 89 to 109 78	Rate of resuspension	After a deposition stage, the study of resuspension of a multilayer deposit Study of influence of the temperature and of the gas flow velocity on resuspension
Tsai and Chiou	1999	Wind tunnel 5×5×20 cm /Suction on filters – TSI DustTrak	Flat plate	Road dust	< 44	---	V (m/s) = 0 to 15	Emission factor	Critical velocity of reentrainment and entrainment in an accelerated flow *Description of the influence of acceleration on the emission factor*
Phares *et al.*	2000	Channel of breadth 1.27 mm / Camera	Glass plate	Spheres of fluorescent ammonium	8.4 to 15.7 6.6 to 13.5	Monod. Monod.	Re inconnu	Effectiveness of resuspension	*Description of the influence of the size of particles and properties of the surface on the resuspension* Development of a kinetic model of detachment taking into account these observations
Reeks and Hall	2001	Tunnel 5×0.2×0.02 m / Photograph	Polished steel	Dispersed polystyrene and monolayer aluminium	12.2 23 13	1.15 1.17 1.85	u_τ (m/s) = 0.1 to 10	Fractional resuspension after 1 s Adhesive forces	Comparison with RRH (Reeks *et al* ., 1989) and Rock'n'Roll models (Reeks and Hall, 2001) *Closer experimental results of the Rock'n'Roll model*
Gotoh *et al*	2001	Rectangular section 2×40×400 mm / Camera at the microscopic scale	Glass plate	Graphite Particles spheres of polyethylene	10-55	Polyd.	V (m/s) = 9.9 to 39.6 Re =2600 to 10000	Instantaneous and integrated resuspension fractions as a function of Δt	Effect of the numbers of particles per unit surface area on the resuspended fraction

Table 2.1 - List of experimental studies of particle resuspension (Alloul-Marmor, 2002)

2.2.2 Experiments in Nuclear Area

Parozzi *et al*. (1995) reviewed several nuclear based resuspension experiments in detail:

- The Marviken Experimental Intermediate Program (Ström, 1986) which investigated the possible effect of the resuspension mechanism on the aerosol deposition in pipes and concluded that no resuspension effect had influenced the tests previously performed;.
- The LWR Aerosol Containment Experiments (LACE) (Rahn, 1988) which focused on providing a representative database for thermal-hydraulic and aerosol codes in the scenarios of containment failures;
- PARESS (PArticle RESuspension Study) (Fromentin, 1989) which gave preliminary indications about the main characteristics of the resuspension phenomenology although it did not produce data bases representative of RCS (Reactor Coolant System) conditions because of the lack of accurate measurements of the initial mass in RCS condition;
- AEA Winfrith Experiments (Benson & Bowsher, 1988) which confirmed the importance of the physical resuspension process in severe accident analyses although the conditions of those tests were again quite far from LWR accident conditions;
- Oak Ridge Experiments (Wright & Pattison, 1994) which is the most systematic experimental approach to dry aerosol resuspension within the RCS and the results showed that the resuspension became significant at high velocity (~ 60m/s);
- STORM Program (Simplified Tests on Resuspension Mechanisms) (Agrati *et al.*, 1991)

The STORM programme (SD test series for deposition and SR test series for gas-flow-induced resuspension) carried out at the Joint Research Centre Ispra (Bujan *et al.*, 2008) was conceived to provide data for the development and validation of models for deposition and resuspension in severe accident conditions. In particular, the experiments were designed to investigate two processes considered to be important in the primary cooling circuit – thermophoretic deposition and mechanical resuspension. The resuspension tests can be subdivided into four phases: (1) heat-up phase, (2) temperature stabilization phase, (3) aerosol deposition phase, (4) and aerosol resuspension phase. In test SR11 for example, the test section is a straight pipe 5.0055 meter long, with 63 mm internal diameter; the aerosol used was tin oxide (SnO_2) and in the resuspension phase, pure nitrogen was used as the carrier gas (Castelo *et al.*, 1999). The test was performed over two consecutive days, with the deposition phase in the first day and the resuspension phase in the second day. The resuspension phase was subdivided in 6 periods, with stepwise increases of the N_2 carrier gas flow from 450 to 805 kg/h at 370 °C. Detail information on the STORM SR11 – ISP40 is presented in Chapter 5.2.1 (p184).

It is worth noting here that the ASTEC/Sophaeros code developed by IRSN is designed to predict the transport of fission products in the RCS of a LWR during severe accidents (more information about the Sophaeros code in Chapter 5.2.1, p184) where this includes aerosol mechanisms; in fact, either a force-balance model can be activated for resuspension or the R'n'R model. This code has been

used to simulate the STORM experiments (see Figure 2.8) but it does not agree particularly well with the measurements, even after modifications – FB1 refers to the force balance model with the cohesive force coefficient = 1.0×10^{-6} N/m; FB2 refers to the force balance model with the coefficient of 1.0×10^{-5} N/m; RnR1 refers to the Rock'n'Roll model with an imposed maximum time step of 1s; RnR2 refers to the Rock'n'Roll model with the imposed maximum time step of 30s.

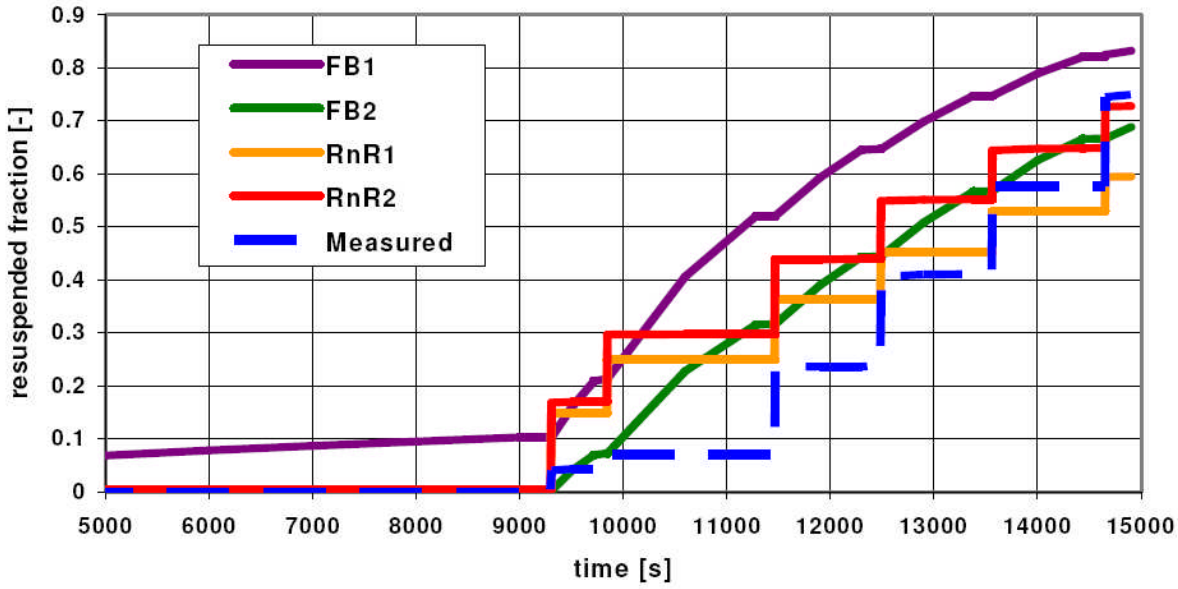

Figure 2.8 - Comparison between model predictions and STORM SR11 test (Bujan *et al.*, 2008)

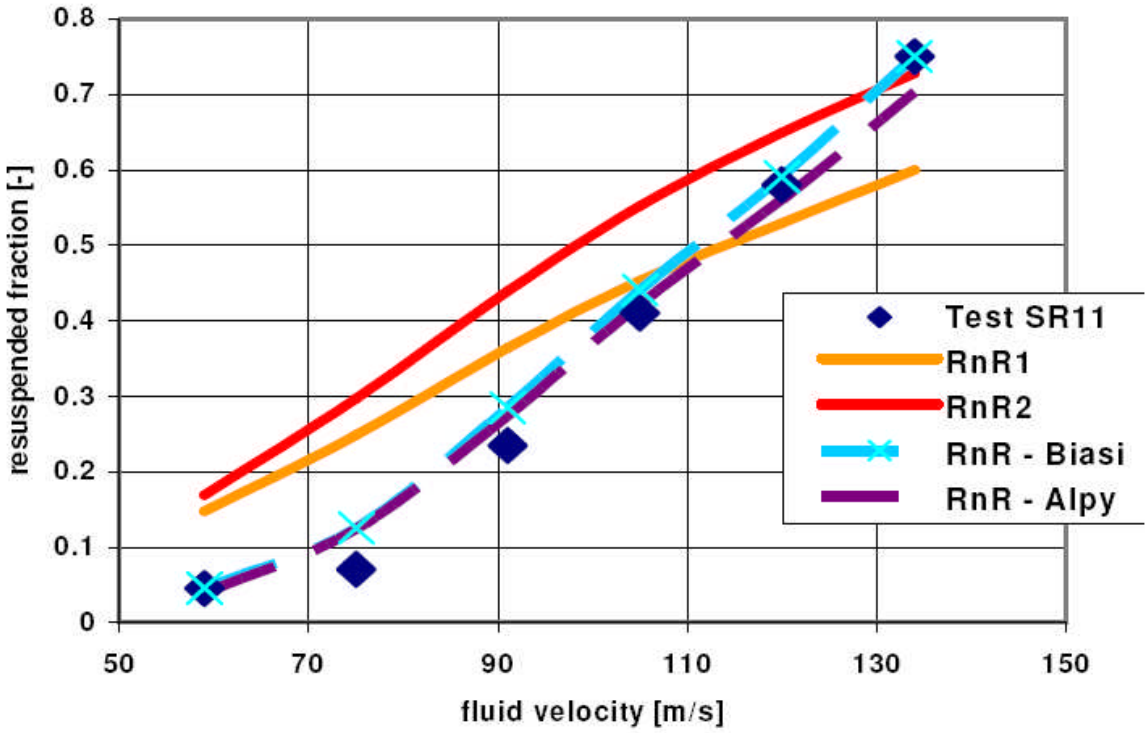

Figure 2.9 - Comparison between model predictions and STORM SR11 test (Bujan *et al.*, 2008)

In particular, the experiments show that resuspension occurs almost instantaneously when the conditions change, and then drops to zero, whereas the models FB1 and FB2 show a steady increase in resuspension fraction during periods of constant conditions. The R'n'R model reproduces the stepwise intermittent behaviour observed in the experiments, but also over-estimates the fraction resuspended.

If the R'n'R model is modified, using the adhesive force correlation developed by Biasi *et al.* (2001), then it agrees much more closely with the data (Figure 2.9), but this is hardly surprising, since the STORM data set was one of those used to develop this correlation in the first place.

2.2.3 Experiments on Multilayer Deposits

Only a few experiments have been performed using multilayer deposits. The PARESS experiment (Fromentin, 1989) includes two steps:

- Deposition phase in which particles (Fe_2O_3, Sn, Si and NaCl) are generated with an AMMD (Aerodynamic Mass Median Diameter) between 2 and 4.3μm and STD (Geometric Standard Deviation) is around 2;
- Resuspension phase in which the mean velocity of the flow could be selected from 5 to 20 m/s.

Fromentin determined a fraction of resuspended particles which he expressed in terms of the mean flux, calculated from the difference between the mass of the deposit before and after resuspension. From these experimental data, Fromentin established a relationship between resuspended flux, the exposure time and the friction velocity near the surface. He also concluded that the resuspended flux was approximately proportional to the surface friction velocity. Also, the study described that the mechanical resuspension of dry particles reveals two distinct aspects: erosion and denudation. If erosion occurs, the dust is removed steadily layer by layer, while if denudation occurs, the deposit is suddenly lifted and holes are produced on the deposited surface.

Alloul-Marmor (2002) produced a resuspension experiment (BISE) for cone structured multilayer deposit, which will be presented in detail in Chapter 5.2.2 (p189).

Raunio (2008) produced a resuspension experiment funded by VTT (Technical research center of Finland). In the VTT experiment, the N_2 flow is controlled by critical orifices which were designed to give 100 l/min at a pressure 1.8 bar and normal temperature. The gas has a density of 1.194 kg/m^3, and a kinematic viscosity of 1.47×10^{-5} m^2/s. In a deposition phase, the nickel particles were deposited on a glass surface. Deposited particle size is not measured whereas the AMMD of particles in the gas flow is measured as 1.8μm with GSD 1.4 (GMD is around 0.4294μm). During the experiment the flow rate was progressively increased and the commutative fraction of particles resuspended was measured for each new value of the friction velocity (0 ~ 3.2m/s). The experimental data showed that there are only approximately 50% of the particles resuspended after about 100 minutes. Raunio concluded that their resuspension results suffered from large uncertainties and are largely inconclusive.

In this thesis, the data of STORM SR11 test and the BISE experiment will be applied for the comparison to the multilayer model results.

2.3 Classical Resuspension Models

The reentrainment phenomenon has long been studied. For a liquid surface, the adhesive force acting on a particle is much greater than on the solid surface and the particle is very hard to remove. In this case, particle reentrainment is assumed to be negligible. On a dry solid surface, apart from resuspension there is a rebound or bounce-off process during deposition. When a particle strikes a surface, due to the momentum of the particle and mechanical properties of both the particle and surface, it can bounce off the surface. For given physical properties, the physics of rebound shows that a particle would rebound from a surface as long as the particle speed or kinetic energy is above some critical level and that it will prevent resuspension from taking place. A brief review on rebound process is discussed by Paw U and Braaten (1995). In this thesis, the bounce-off process is not considered. We deal with a simplified situation where the resuspension process occurs after a deposition phase with particles that have been deposited on a surface being resuspended by gas flow sweeping over the surface.

The particle resuspension is usually indicated in terms of resuspension rate (Λ) and resuspension mass flux (Φ_r). According to Fauske (1984), for an initial mass load of M_0 particles deposited on the surface with area S, and if ΔM is the mass of the particles resuspended during a time interval Δt, the resuspension rate and mass flux are defined as

$$\Lambda = \lim_{\Delta t \to 0} \frac{\Delta M / S}{(M_0 / S)\Delta t} = \frac{1}{M_0}\frac{dM}{dt}$$
$$\Phi_r = \Lambda \frac{M_0}{S} = \frac{1}{S}\frac{dM}{dt} \qquad [2.28]$$

Over the years, many studies have been devoted to the construction of theoretical models for simulating and predicting resuspension properties which have been divided into two categories: one is based on a balance of forces which concerns the resultant force from aerodynamic and adhesive forces acting on a particle and the other is based on energy accumulation that describes particle removal in terms of accumulation of kinetic energy from the flow.

Early scientific research on resuspension, such as Chepil (1959) and Bagnold (1960), was concerned with soil grains and settled-dust transport into atmosphere. Corn and Stein (1965) studied the re-entrainment of spherical glass particles and fly ash from metal surfaces by high speed air flow (e.g., 20m/s to 30m/s) and indicated that one main difficulty of predicting particle re-entrainment on the surface is the influence of particle adhesion. Concerning the nuclear industry, Romney and Wallace (1977) concluded that resuspension of contaminated particles in the environment can lead to re-deposition and formation of foliar clusters, which contributes significant plutonium level in vegetation. Ziskind *et al*. (1995) mentioned that experimental measurements of resuspension indicate that particle removal from a surface is not instantaneous but takes place over a period of

time. Thus, it is assumed that resuspension has a statistical origin associated with the turbulent flow character.

Hereafter, the classical models based on a force balance approach are reviewed and discussed in Chapter 2.2.1 (p35) and those based on energy accumulation are reviewed and discussed in Chapter 2.2.2 (p47).

2.3.1 Models Based on Force Balance

The force-balance model is based on a simple concept where particle resuspension is assumed to take place instantaneously when the aerodynamic forces exceed the surface adhesive force. Three types of force balance model have been developed - statistical models, kinetic models and Lagrangian models – and they will be reviewed separately.

2.3.1.1 Statistical Models

Cleaver and Yates (1973) developed the first isolated-particle resuspension model to combine the statistical character of turbulent bursting with particle resuspension by using the visual observations on burst distribution in space and time. Although it is statistical in nature, it retains the essential character of a force-balance model. The resuspension depends on both the lift force caused by burst flow and the adhesive force from the surface, as shown below.

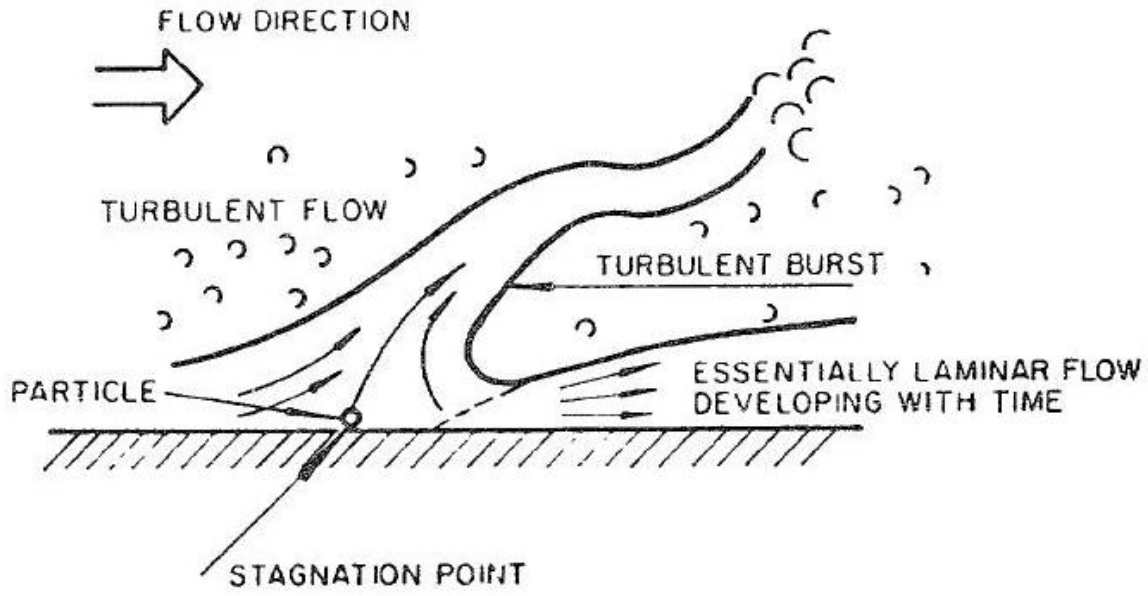

Figure 2.10 - Schematic diagram of turbulent burst in the wall region (Cleaver & Yates, 1973)

The burst is modelled by Cleaver and Yates as an axisymmetric stagnation-point flow and the lift force acting on a particle is proportional to $\rho_f v_f^2 (Du_\tau / v_f)^3$ (given by Eq.[2.15])

$$F_L = 0.608 \rho_f v_f^{\,2} \left(\frac{r u_\tau}{v_f} \right)^3$$

In their model, particle resuspension can occur if the lift force is greater than the adhesive force leading to the criterion (Eq.[2.29]). Following Zimon (1964) they assumed that all types of adhesive forces are proportional to the particle diameter. Therefore, particle resuspension occurs (in other words, the lift force is greater than adhesive force) when

$$\frac{\rho_f v_f^2}{r}\left(\frac{r u_\tau}{v_f}\right)^3 > const. \quad \Rightarrow \quad \tau_w r^{4/3} > B \qquad [2.29]$$

where τ_w is the wall shear stress and B is a constant.

Ziskind *et al.* (1997) analysed particle detachment from a surface by considering the aerodynamic and adhesion force (or moment). By using the JKR adhesion model (Johnson *et al.*, 1971), they defined the conditions of particle resuspension from a perfect smooth surface which is similar to Eq.[2.29] and from a two-asperity rough surface.

$$\begin{aligned} &\tau_w r^{4/3} > \frac{\gamma^{4/3}}{5.37\kappa^{1/3}} \qquad \text{smooth surface} \\ &\tau_w r^3 > \frac{\gamma r_a^2}{35.7} \qquad \text{rough surface} \end{aligned} \qquad [2.30]$$

where κ is elastic constant of the particle, γ is the surface energy and r_a is the asperity radius.

The aerodynamic force for resuspending the particles is provided by turbulent burst; based on an analysis of experimental data, Cleaver and Yates suggested that a typical burst diameter is of the order of $20v_f/u_\tau$ and that bursts are separated by a distance of about s $630v_f/u_\tau$ in the streamwise direction, and $135v_f/u_\tau$ in the cross-stream direction, as shown in Figure 2.11.

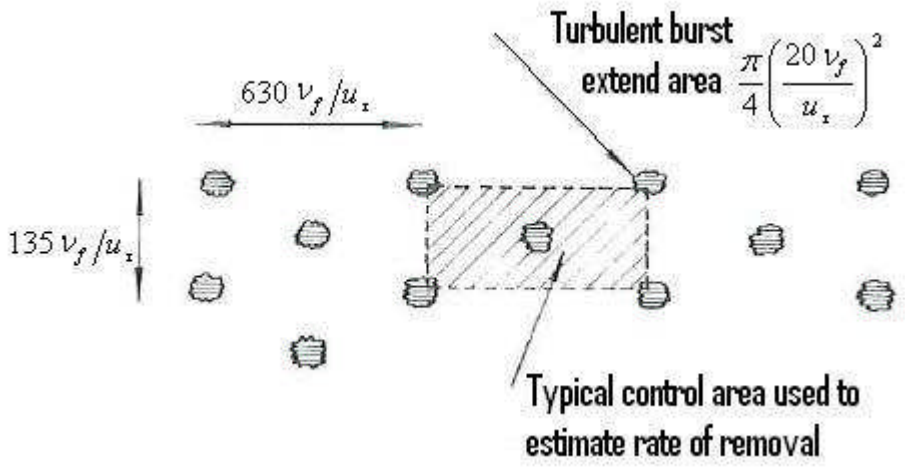

Figure 2.11 - Turbulent burst distribution on the surface (Cleaver & Yates, 1973)

The mean time period between bursts is approximately $75v_f/u_\tau^2$. Assuming that some fraction a of the particles exposed to a turbulent burst on the surface of the deposit are removed, in other words all the particles in an area of $a(\pi/4)(20v_f/u_\tau)^2$ will be removed from the surface in any one burst, the fraction of the particles resuspended as a function of time is given by

$$f_c(t) = 1 - \left(1 - \frac{a(\pi/4)(20v_f/u_\tau)^2}{630v_f/u_\tau \times 135v_f/u_\tau}\right)^{(u_\tau^2/75v_f)t} = 1 - \left(1 - \frac{a}{270}\right)^{(u_\tau^2/75v_f)t} \qquad [2.31]$$

The initial resuspension rate defined at the moment when the surface is first exposed to a turbulent burst is given by

$$\Lambda(0) = \left.\frac{df_c}{dt}\right|_{t=0} = -\frac{u_\tau^{\,2}}{75 v_f}\ln\left(1-\frac{a}{270}\right) \qquad [2.32]$$

Cleaver and Yates assume that the constant a is approximately of the order 1/100. Their model recognises the importance of the rms (root mean square) lift force in particle resuspension, but it does not give consideration of this quantity in the turbulent burst.

Phillips (1980) followed the study and extended the resuspension conditions to four regimes (see Figure 2.12):

a) Large particle regime, the hydrodynamic force balances with net weight, which leads

$\tau_w = 700r$ (for air) and $\tau_w = 1680r$ (for water): $\tau_w \propto r^1$

b) Intermediate regime, net weight balances with turbulent lift force, which leads

$\tau_w = 0.047$ (for air) and $\tau_w = 0.13$ (for water): $\tau_w \propto r^0$

c) Small particle regime, adhesion force balances with turbulent lift force, which leads

$\tau_w r^{4/3} = 5\times10^{-8}$ (for air): $\tau_w \propto r^{-4/3}$

d) Unrealised regime, drag force balances with adhesion force, which leads

$\tau_w r = 3.8\times10^{-7}$ (for air): $\tau_w \propto r^{-1}$

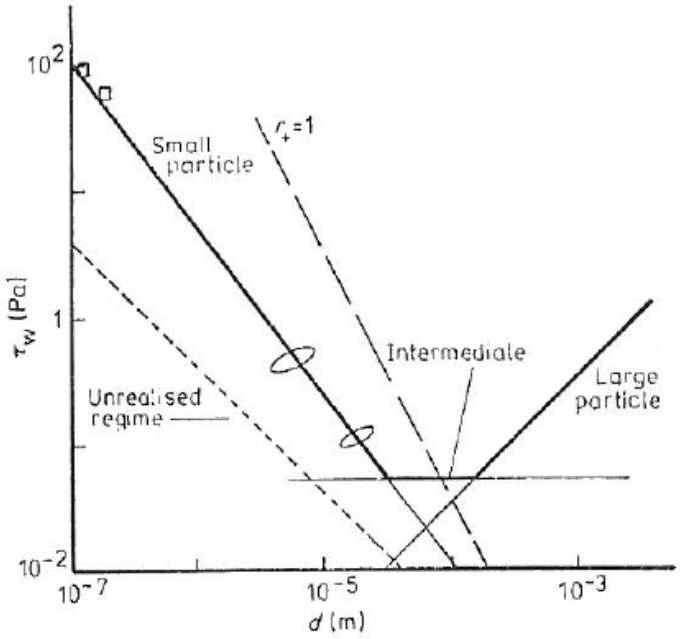

Figure 2.12 - Four limiting regimes of resuspension (Phillips, 1980)

Phillips concluded that there are two major weaknesses of this type of models: the first is that the lift force is specified without a mechanism for its operation, and the second is that a distinction has to be made between water and air as carrying fluid.

Braaten *et al*. (1990) developed a Monte-Carlo particle resuspension model which is capable of simulating the unsteady nature of resuspension and compared the results with those obtained from a resuspension experiment using Lycopodium particles (count-median diameter 27.8 μm). They considered the random nature of turbulent-burst effect and used an approximate mean time ($300\nu_f/u_\tau^2$) between bursts. For each time step, Braaten *et al*. generate a random number from unique probability distribution to calculate surface fluid force; if it is larger than the minimum required for resuspension, a fraction of particles removed is determined by a particle adhesion function (which is given by a log-normal distribution) and compared to the current cumulative removal fraction. If the calculated fraction removed is larger than the current cumulative removal fraction, the latter is replaced.

Braaten *et al*. concluded that the fraction of particles removed from the wall in a turbulent boundary layer with a constant streamwise velocity as a function of time was found to be governed by two regimes which both can be fitted to exponential functions. The first occurs in the first few minutes (nearly 60% particles removed in first 5 minutes) and then the fraction becomes a constant value around 60% - 70%.

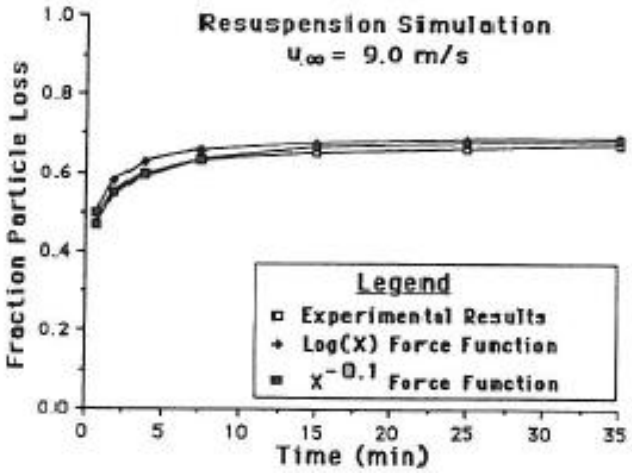

Figure 2.13 - Fraction of particle removed vs. time (Braaten *et al.*, 1990)

2.3.1.2 Kinetic Models

Wen and Kasper (1989) demonstrated a kinetic model of particle reentrainment which is possible to calculate particle concentration as a function of time. The model describes resuspension as a first order reaction, similar to molecular desorption from a heterogeneous surface with a certain rate constant. They defined a dimensionless variable F_r which is the ratio of adhesive force to the removal force and the first order rate constant for molecular desorption from a uniform surface which is identical to the one used in chemical kinetics and assumed as

$$a(F_r) = Ae^{-F_r} \qquad [2.33]$$

where A is a constant. Then the number density of particles on the surface at time t is given by

$$N(F_r,t) = N_0(F_r)e^{-a(F_r)t} \quad [2.34]$$

$N_0(F_r)$ is the initial distribution function of the force ratio which could be assumed as a log-normal distribution. Then the normalized particle concentration in the gas generated by resuspension from a unit surface element is derived.

$$n(t) = \int_0^\infty N_0(F_r)a(F_r)e^{-a(F_r)t}dF_r \quad [2.35]$$

Their model showed a good agreement with experimental data (particle size around 0.5 ~ 0.6 μm) and also explained observed systematic deviation of the data from the 1/t decay as showed in Figure 2.14. They believed that the derivations could be accounted for the correction of 1/t law. The results shown that for short times ($t < 4/A$):

$$n(t) \propto \frac{1-e^{-At}}{t}$$

and for long times ($t > \frac{4}{A}e^{F_{r-max}}$):

$$n(t) \propto \frac{\exp(-At/e^{F_{r-max}})}{t}$$

where $F_{r\text{-}max}$ is the maximum value of the ratio. The empirical constants are tuned to adjust the model results to coincide with experiment data. Hall (1989) pointed that these derivations could be caused by the sensitivity of the 1/t relationship to perturbations of the flow rate.

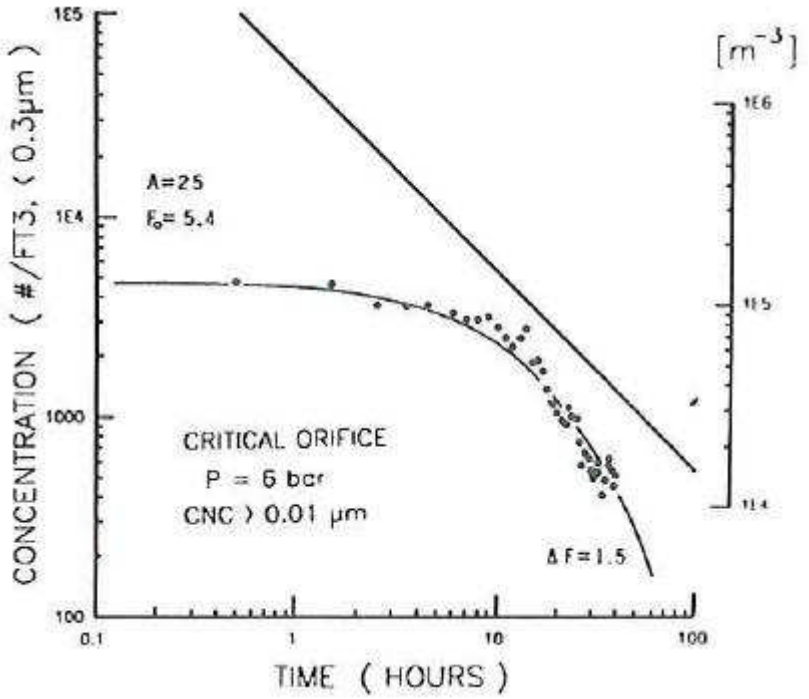

Figure 2.14 - Resuspension particle concentration vs. time (Wen & Kasper, 1989)

Matsusaka and Masuda (1996) studied the resuspension of aggregates from a fine powder layer in an accelerated flow and presented a new model to explain the time dependence of the resuspension of aggregates. An experiment is also provided by resuspending fly-ash particles (mass median diameter ~ 3 μm) in air flow. The experimental results showed that the distribution of adhesive strength (wall shear stress which calculated from the mass flux) was approximated by a log-normal distribution.

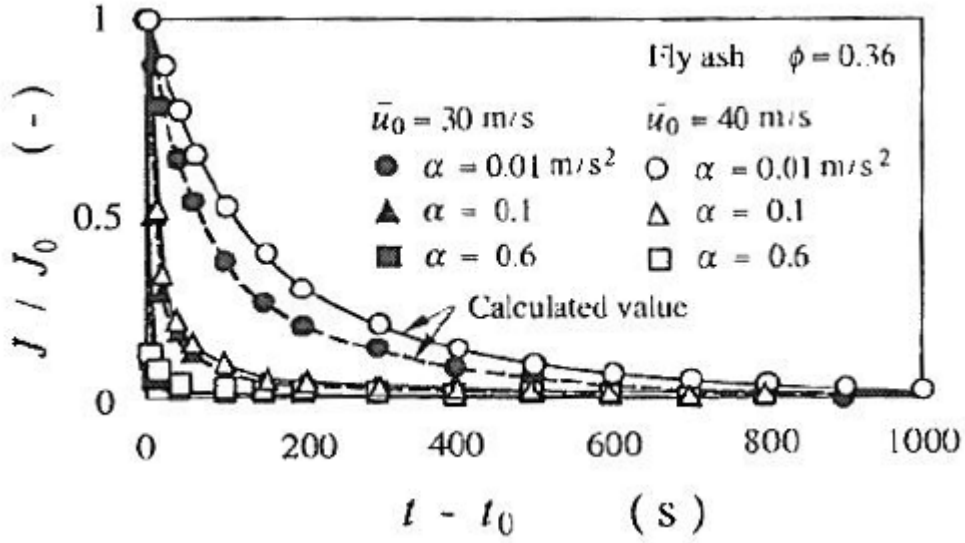

Figure 2.15 - Resuspension flux with different flow acceleration (Matsusaka & Masuda, 1996)

The resuspension phenomena is described as consisting of two types, the short delay resuspension (due to small fluctuation in the shear flow) and long delay resuspension (due to large fluctuation caused by turbulent burst), where the resuspension flux of both cases is approximated by simple exponential functions. It is also shown that the resuspension flux increased in an accelerated flow with elapsed time being approximately proportional to flow acceleration α (shown in Figure 2.15).

Parozzi and Tagliaferri (2000) derived a correlation model assuming that the resuspension rate depends on the resultant force *F(r)* acting on the deposited particles. The model is capable of handling only the average behaviour of each particle size bin. The resultant force is calculated as the algebraic sum of aerodynamic forces (drag and lift force) and adhesive forces (gravity, cohesive and frictional force).

$$F(r) = F_{drag} + F_{lift} - (F_{gravity} + F_{cohesive} + F_{friction}) \quad [2.36]$$

The resuspension rate is defined as:

$$\Lambda(r) = A[F(r)]^{B} \quad [2.37]$$

where *A* and *B* are empirical coefficients to fit the experimental date, *F(r)* is the resulting force acting on the particles with particle radius *r*.

The drag force is set equal to the product of shear stress and the particle streamwise projected area (Parozzi *et al.*, 1995) and the lift force is similar to Eq.[2.15] with some coefficients adjusted,

$$F_{drag} = \tau\pi r^2 x^{2/3}$$
$$F_{lift} = 4.21 x \rho_f v_f^{\,2} \left(\frac{2 r u_\tau}{v_f} \right)^{2.31} \qquad [2.38]$$

where τ is the shear stress at the wall, x is the aerodynamic shape factor normally set to 1 for densely-packed and spherical particles and 3 for porous particles in the model. Gravity is only important for large particles (D > 100μm) and becomes negligible for small particles (D < 10 ~ 50μm).

The cohesive force is caused by intermolecular attraction and is expressed according to Brockmann (1985). The friction is assumed to be proportional to the adhesive force and gravity.

$$F_{cohesive} = 2H r \lambda$$
$$F_{friction} = 0.2\left[2Hr\lambda + \frac{4\pi}{3} r^3 \lambda^3 \rho_p g \right] \qquad [2.39]$$

where H is a constant depending on material properties (experiment data confirmed H is of a order $1x10^{-7}$ N/m for single layer and $1x10^{-6}$ N/m after ten layers), λ is collision shape factor and set to 1 and ρ_p is particle density.

The empirical constants used for resuspension rate in Eq.[2.37] were estimated using data from several experiments (Wurelingen, STORM and Oak Ridge); these gave A = 0.4037 and B = 0.6003 for the case $F(r)$ < $3.06x10^{-4}$ μN, and A = 90.28 and B = 1.269 for the case $F(r)$ ≥ $3.06x10^{-4}$ μN; the resulting model predictions are compared with the data in Figure 2.16.

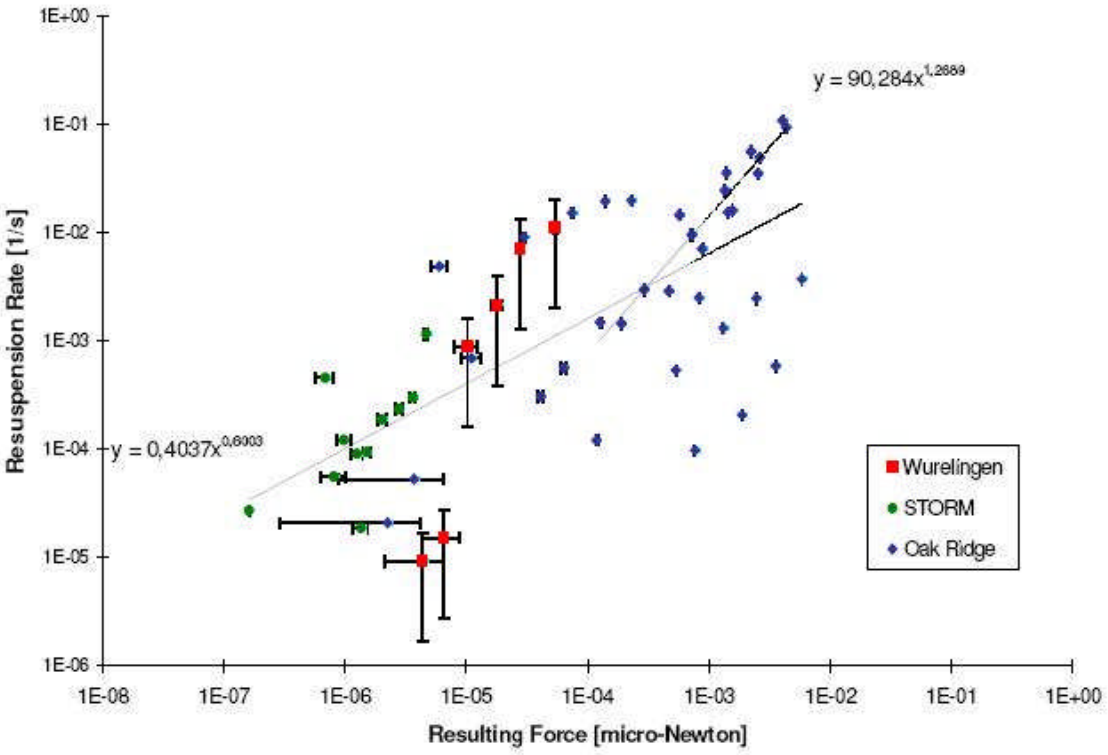

Figure 2.16 - Distribution of resuspension rate vs. resultant force (Parozzi & Tagliaferri, 2000)

It is not apparent from Figure 2.16 that the Parozzi and Tagliaferri model captures all the data sufficiently. However, the proposed correlation does not reflect the experimental data very well. Indeed, Parozzi and Tagliaferri concluded that this model is only applicable to the homogeneous layer which means the deposit is thin (< 1mm) and not packed. The development of the model for heterogeneous layers would require taking into account the packing and agglomeration of the deposited particles' packing and agglomeration.

2.3.1.3 Lagrangian Models

Hontañón *et al.* (2000) developed a force-balance resuspension model by using a 2D Lagrangian particle tracking method, which calculates the trajectory of the particles within the viscous sublayer of turbulent pipe flow. The model is conceived to deal with small particles (up to a few microns) so the gravitational force is neglected. The drag force for a small particle close to a wall is given by Eq.[2.11] and the lift force used in the model is that derived by Cherukat and McLaughlin (1994) (Eq.[2.17]). The particles are assumed to be hard smooth spheres, sitting on a rough surface consisting of asperities with the same radius of curvature, and a height distribution given by a polynomial approximation.

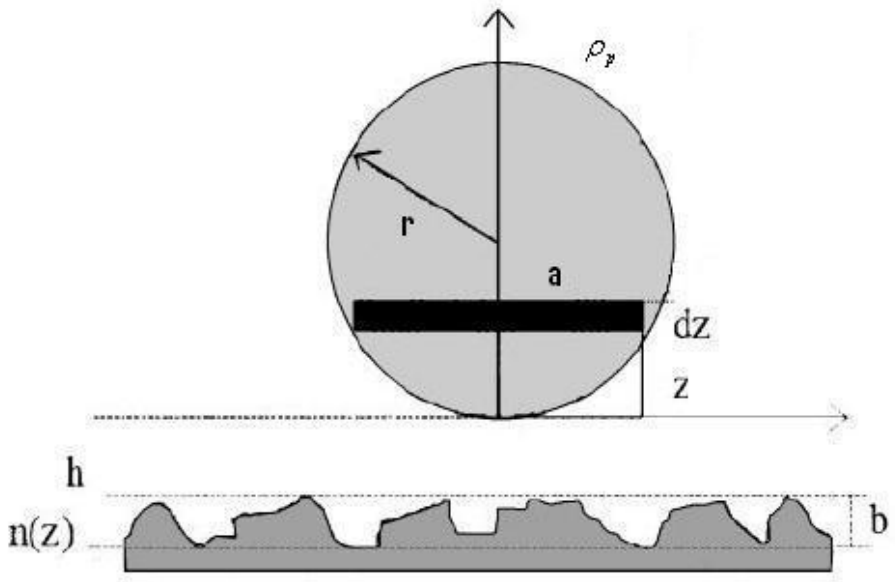

Figure 2.17 - Interaction of a particle with a rough surface (Hontañón *et al.*, 2000)

The adhesive force acting on the particle is derived using the Lennard-Jones (LJ) potential (Lennard-Jones, 1931) to describe the intermolecular interaction of the particles and surface. The equation includes both the attractive and repulsive terms and is shown below.

$$F_{adhesive} = \pi\rho_p \int_0^{2r} z(2r-z)\left[2\pi\int_0^{\infty} ydy \int_{h+z-b}^{h+z} \frac{-6A}{a^7} n(z)dz\right]dz + \pi\rho_p \int_0^{2r} z(2r-z)\left[2\pi\int_0^{\infty} ydy \int_{h+z-b}^{h+z} \frac{12B}{a^{13}} n(z)dz\right]dz \quad [2.40]$$

where *A*, *B* are coefficients related to LJ parameters, *n(z)* is atomic density which is expressed in terms of a polynomial distribution, and the other parameters are as defined in Figure 2.17 above.

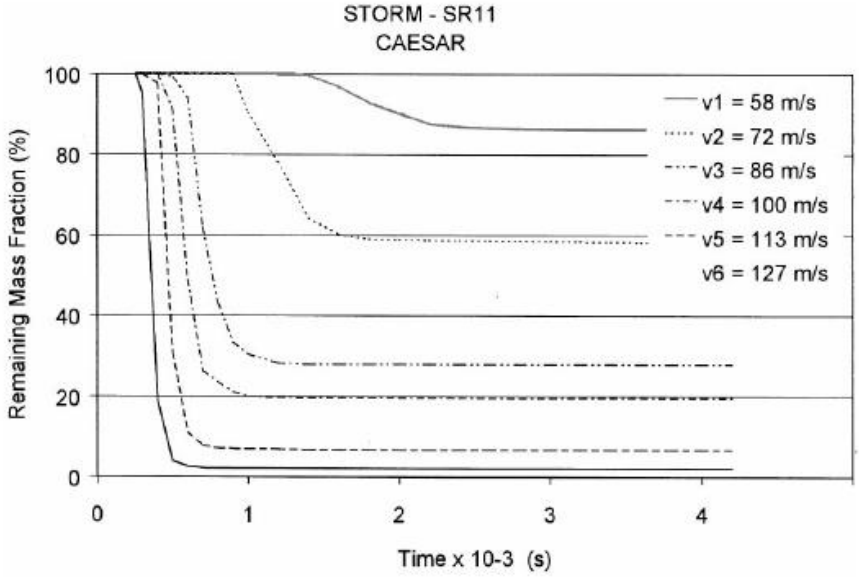

Figure 2.18 - Remaining mass fraction vs. time prediction (CÆSAR model) (Hontanon *et al.*, 2000)

The model was used to simulate resuspension in the STORM (details on STORM are provided in Chapter 2.2.2, p29) experiment conditions; typical results from those simulations are shown in Figure 2.18. There is an initial phase, lasting a few milliseconds, in which most of the material is resuspended, and then the resuspension rate falls very rapidly. This agrees qualitatively with experimental observations, but the initial resuspension rate is higher than that measured in the experiments. One possible explanation for this is that this is a single layer model, in which all the particles are exposed to the flow immediately and it does not include cohesion between particles.

Guingo and Minier (2008) proposed a new model aiming at simulating the resuspension of spherical particles in turbulent air flow using stochastic Lagrangian methods. In the model, particles are considered to be resuspended when the drag moment exceeds the adhesion moment. The drag force is taken as 1.7 times the Stokes drag (see Eq.[2.9]). In this model the surface of the wall consists of a mixture of large and small scale roughness elements, and the adhesive force then depends on the size of the particle relative to the size of the roughness elements and the spacing between them. There different cases are possible, as illustrated in Figure 2.19.

i, Case A: small particles

In this case, the wall is considered as smooth. According to the JKR theory, the adhesive force is given as Eq.[2.25]

$$F_a = 3\pi r\gamma \qquad [2.41]$$

where γ is the surface energy.

ii, Case B: mid-size particles

The particle is large enough to be in contact with several small asperities; to evaluate the number of these asperities, the contact radius (r_c) needs to be defined using the JKR theory.

$$r_c = \left(\frac{12\pi\gamma r^2}{K}\right)^{1/3} \qquad [2.42]$$

where K is the composite Young's modulus defined by

$$K = \frac{4}{3}\left(\frac{1-v_1^2}{E_1} + \frac{1-v_2^2}{E_2}\right)^{-1} \qquad [2.43]$$

v_1, v_2 are Poisson's ratio for the particle and the substrate, respectively, and E_1, E_2 are Young's moduli.

If the mean asperity radius is denoted for the small scale roughness by r_{fine}, and the surface density of the small scale elements by ρ_{fine}, then the adhesive force is similar to that given by Eq.[2.26].

$$F_a = P(\rho_{fine}\pi r_c^2)\frac{H_c L(r_{fine})}{6H_0^2} \qquad [2.44]$$

where P is generated from a Poisson distribution, L is generated from a log-normal distribution with the standard deviation equal to the mean, H_c is the Hamaker constant and H_0 is the equilibrium distance (0.3nm), i.e., the particle-surface gap.

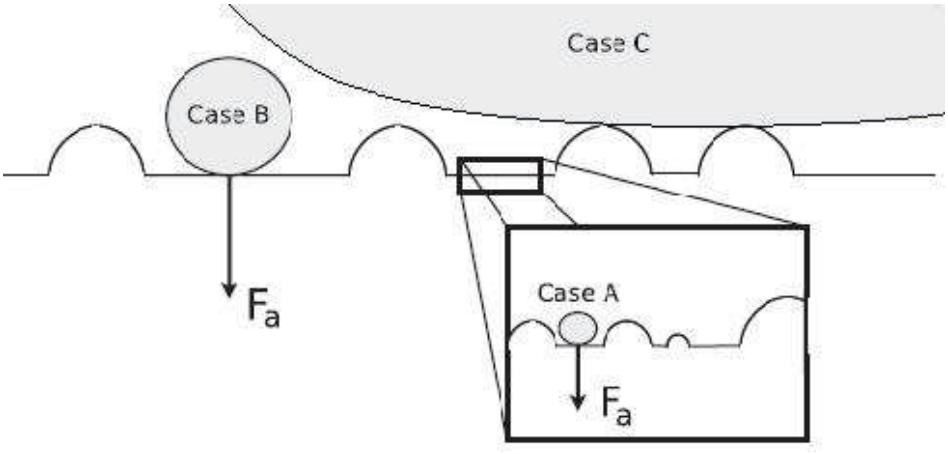

Figure 2.19 - Adhesion model in 3 cases with different particle sizes (Guingo & Minier, 2008)

iii, Case C: large particles

A large particle will be in contact with several large-scale asperities and the number of contact points is estimated as a Poisson distribution with mean $2r/L_{large}$ where L_{large} is the mean distance between two large-scale asperities. Then the total adhesive force is given by:

$$F_a = \sum_{i=1}^{I} P_i(\rho_{fine}\pi r_c^2)\frac{H_c L_i(r_{fine})}{6H_0^2}, \quad \text{where } I = P(2r / L_{large}) \qquad [2.45]$$

In all three cases the aerodynamic drag force is taken as 1.7 times the Stokes drag (see Eq.[2.9]). The model was used to simulate the experiments of Ibrahim *et al*. (2003) and it reproduces the main features of their results, as can be seen in Figure 2.20 (dot: alumina particles r = 36μm, square: alumina particles r = 16μm).

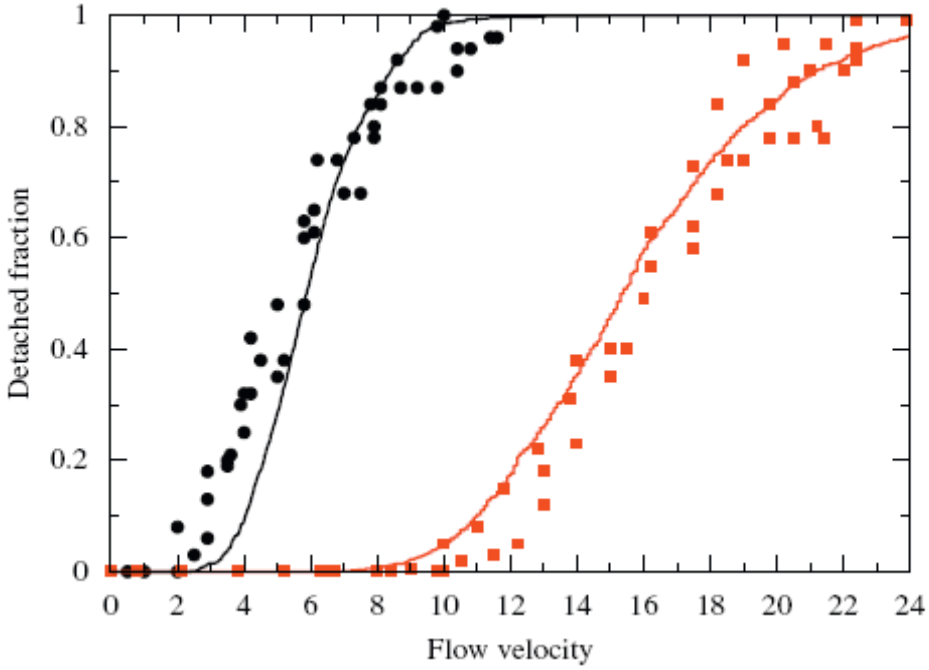

Figure 2.20 - Comparison of model results to experimental data (Guingo & Minier, 2008)

The model was also used to simulate Hall's experiment (Reeks & Hall, 2001) with 10μm graphite particle resuspension, as shown in Figure 2.21. Based on these comparison, Guingo and Minier concluded that the surface roughness and Hamaker constant, which are input variables for their model, do represent physical quantities or material properties and have strong intrinsic physical meaning which are important aspects of particle resuspension.

However, such models are very useful in the precise way they can handle the complexity of the particle-surface interaction and the aerodynamic forces. They can be very useful in providing the input data to the simple analytical models like the R'n'R that are discussed in this thesis. They could also comprise an important source of validation. Furthermore, it is perhaps worth noting that the R'n'R model deals with the detachment of a particle from a surface and not the subsequent particle motion in the turbulent boundary layer.

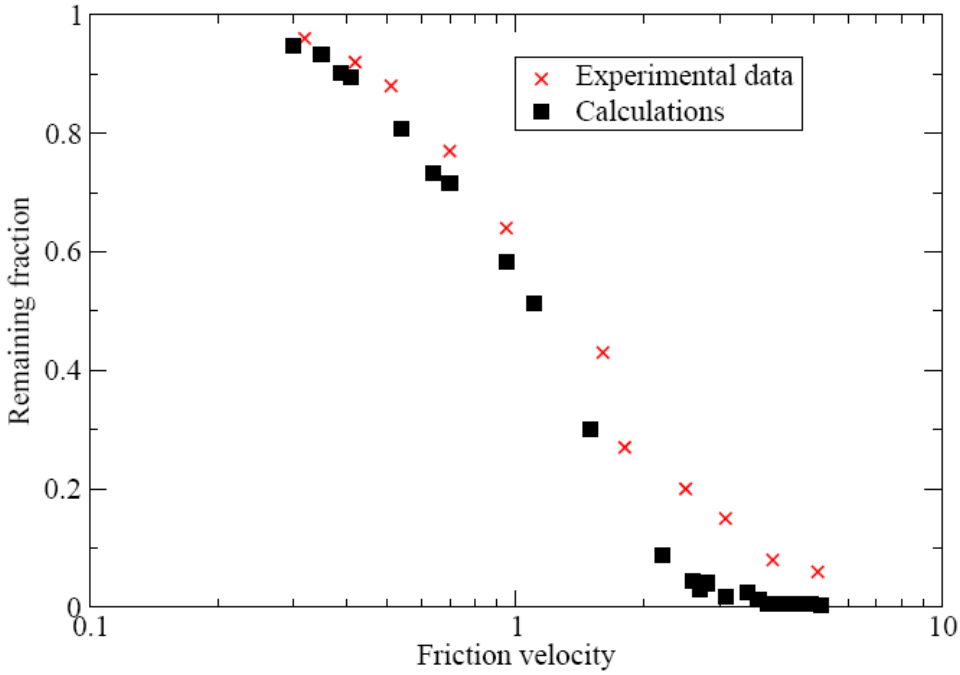

Figure 2.21 - Results of G&M model and Hall's experiment (Guingo & Minier, 2008)

2.3.2 Models Based on Energy Accumulation

Force-balance approaches imply that particles are resuspended instantaneously from a surface when the aerodynamic forces exceed the resistance forces (adhesion, etc.). However, Sehmel (1980) showed from experimental measurements that particle resuspension from a surface is not instantaneous but increases with time. According to Corn and Stein (1965), the removal of nominally identical small particles from a smooth surface in high-velocity air also depends on the time of exposure. Based on the observation that small particles can be resuspended, even when the adhesive force exceeds the aerodynamic force, Reeks, Reed and Hall (1988) (hereafter RRH) proposed a new model, based on the idea that the adhesion of the particle to the substrate can be represented as a particle in a potential well, with a potential that decreases as the particle moves away from the surface. The action of the unsteady turbulent flow on the particle then causes it to vibrate – to oscillate within the well – until it acquires enough vibrational energy to escape from the well, and becomes resuspended. They defined a resuspension rate constant p, for a long-term resuspension of the form

$$p = \omega_0 \exp\left(-\frac{Q}{2\langle PE \rangle} \right) \qquad [2.46]$$

where ω_0 is the typical natural frequency of the system, Q is the height of the surface adhesive potential well and $\langle PE \rangle$ is average potential energy of a particle in a well. Later, Reeks and Hall (2001) developed this model to include aerodynamic drag, applied using a quasi-static analysis of the particle at the top of the potential well; thus has become known as the Rock'n'Roll model. These two models will now be discussed in detail.

2.3.2.1 RRH Model

The initial model developed by Reeks *et al.* (1988) describes a close analogy of particle motion in turbulent flow with the behaviour of molecules desorption in the surface, and the escape of Brownian particles from a potential well. They represented a potential well between particle and substrate formed from a surface adhesive force, a repulsive elastic force and a mean aerodynamic lift force.

Figure 2.22 shows the potential energy varying with displacement normal to the surface. Point A is the stable equilibrium position that adhesive force balances with the repulsive elastic force and the mean lift force; and point B is the unstable equilibrium position in which the adhesive force balances with the mean lift force. At position y_B, particle will leave the potential well (or resuspend) from the surface when it accumulates enough energy from the turbulence to escape over the potential barrier at B, which has height of Q. The particle motion in the well is approximated by a lightly damped harmonic oscillator driven by fluctuating lift force $f_L(t)$, as in Eq.[2.47].

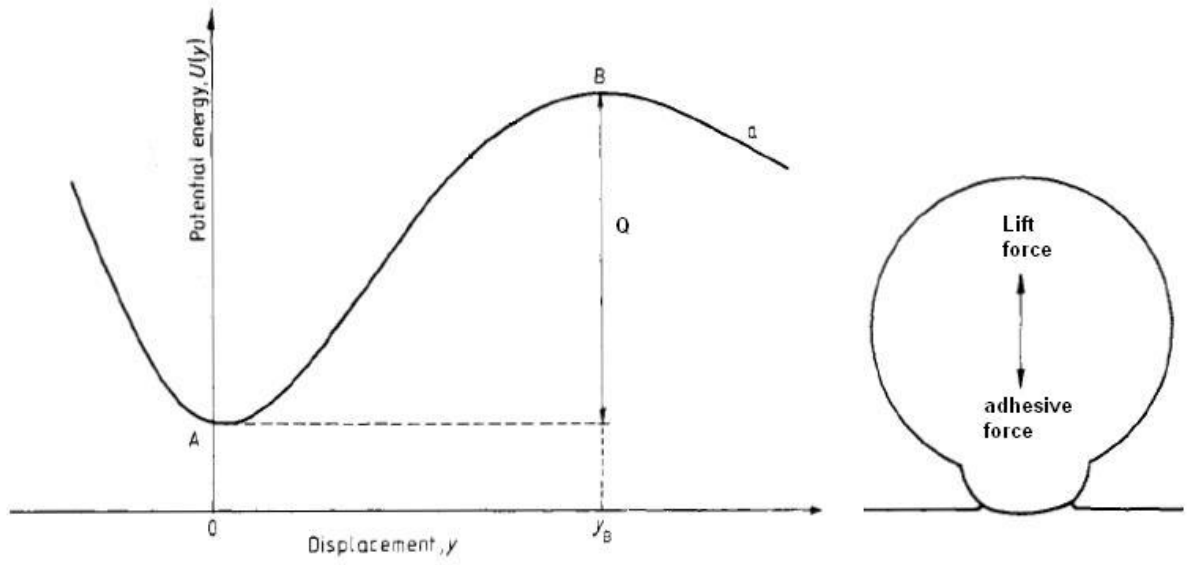

Figure 2.22 - Surface potential well and particle motion (Reeks *et al.*, 1988)

$$\ddot{y} + \beta\dot{y} + \omega^2 y = m^{-1} f_L(t) \qquad [2.47]$$

where y is the displacement normal to the surface, β is the damping constant, ω is the natural frequency of the particle in the potential well and m is the particle mass. Based on the general solutions of the equation above, they derived the mean square displacement $\langle y^2 \rangle$ and velocity $\langle v^2 \rangle$ in a harmonic potential in order to calculate the accumulation of vibrational energy.

$$\left\langle y^2 \right\rangle = \frac{\left\langle f_L^{\,2} \right\rangle}{m^2\omega^4}(1+\eta)$$
$$\left\langle v^2 \right\rangle = \frac{\left\langle f_L^{\,2} \right\rangle}{m^2\omega^2}\left(\eta + \frac{\left\langle \dot{f}_L^{\,2} \right\rangle}{\left\langle f_L^{\,2} \right\rangle \omega^2}\right) \qquad [2.48]$$

where $\langle f_L^{\,2} \rangle$ is mean square fluctuating lift force, η is a resonance contribution factor which depends on the energy spectrum of the fluctuating lift force around resonance, the natural frequency of the particle and the damping constant

$$\eta = \frac{\pi}{2\beta}\omega^2 \hat{E}_L(\omega) \qquad [2.49]$$

η will be zero if there is no resonance energy transfer.

i Energy spectrum of the fluctuating lift force

The normalized energy spectrum of the fluctuating lift force ($\hat{E}_L(\omega)$) is obtained from the dimensionless energy spectrum ($E^+(\omega^+)$), which in the RRH model is a simplified form of Schewe's (1983) spectrum, as given by Eq.[2.51].

$$\hat{E}_L(\omega) = \frac{v_f}{u_\tau^{\,2}} E^+(\omega^+) \qquad \omega^+ = \frac{v_f}{u_\tau^{\,2}}\omega \qquad [2.50]$$

$$E^+(\omega^+) = \begin{cases} 1.4286 & \omega^+ < 0.4 \\ 0.1684(\omega^+)^{-7/3} & \omega^+ \geq 0.4 \end{cases} \quad [2.51]$$

where u_τ is the wall friction velocity and v_f is the fluid kinematic viscosity.

ii Natural frequency of the particle

The stiffness of the system is derived by using the JKR model (Johnson *et al.*, 1971), and then the particle natural frequency is derived as

$$\omega = \sqrt{\frac{\varepsilon}{m}} \qquad \varepsilon = \frac{9}{2} K^{2/3} \left(P_1 r_a' r\right)^{1/3} \left(\frac{P_1 + P_0}{5P_1 + P_0}\right) \quad [2.52]$$

where ε is the stiffness of the system, K is the composite Young's modulus Eq.[2.43], r_a' is the normalized asperity radius, P_0 is the force acting on the particle and P_1 is the apparent Hertzian force.

$$P_0 = -\langle F_L \rangle + mg \quad P_1 = P_0 + 2f_a \left(1 + \sqrt{\frac{P_0}{f_a} + 1}\right) \quad [2.53]$$

The adhesive force in the RRH model is generated by scaling up the adhesive force for a smooth surface (F_a) using a random normalized asperity radius r_a', drawn from a log-normal distribution with geometric mean $\bar{r}_a'$ (also referred as adhesion reduction factor) and geometric standard deviation (also referred as adhesive spread factor) σ_a'. In RRH model, $\bar{r}_a'$ and σ_a' are assumed to be 0.1 and 4, respectively. The values used here represent the surface characteristics as determined from measurements made by Reed (1986, unpublished).

$$\varphi(r_a') = \frac{1}{\sqrt{2\pi}} \frac{1}{r_a'} \frac{1}{\ln \sigma_a'} \exp\left(-\frac{\left[\ln(r_a'/\bar{r}_a')\right]^2}{2(\ln \sigma_a')^2}\right) \quad [2.54]$$

Then the adhesive force is given by

$$f_a = F_a r_a' = \frac{3}{2} \pi \gamma r r_a' \quad [2.55]$$

where F_a is the adhesive force on the smooth surface, as given by Johnson *et al.* (1971). It is noted that other adhesive models were considered in Reeks *et al.* (1985) which gave similar results on the resuspension rate constant.

iii Damping constant

The vibrational energy of a particle in contact with a surface can be dissipated by fluid damping and mechanical damping, and then the total damping of particle motion in the normal direction is assumed to be the sum of these two.

$$\beta = \beta_f + \beta_m = \frac{6\pi r^2 \mu_f}{m} \sqrt{\frac{\omega}{2\nu_f}} + \frac{2.4}{\pi} \frac{m\omega^4 \sqrt{\rho_s}}{E_2^{3/2}} \quad [2.56]$$

where β_f is the fluid damping constant, as given by Batchelor (1967), β_m is the mechanical damping constant, obtained by balancing net energy lost from the surface with the energy transferred to the

particle in oscillation (Miller & Pursey, 1954), ρ_s is the substrate density and E_2 is the Young's modulus of the substrate.

In the RRH model the particle velocity and the particle displacement are assumed to be drawn from independent Gaussian distributions, with joint probability density function *W(v,y)*.

$$W(v,y) = \frac{1}{2\pi\sqrt{\langle v^2\rangle\langle y^2\rangle}} \exp\left(-\frac{v^2}{\langle v^2\rangle}\right)\exp\left(-\frac{y^2}{\langle y^2\rangle}\right) \qquad [2.57]$$

The resuspension rate constant *p* is then derived as the net current of particles at the removal point B (Figure 2.22) over the number of particles on the surface.

$$p = \frac{\int_0^\infty vW(v,y_B)dv}{\int_{-\infty}^{\infty}\int_{-\infty}^{y_B} W(v,y)dydv} \qquad [2.58]$$

where $\int_{-\infty}^{\infty}\int_{-\infty}^{y_B} W(v,y)dydv \approx \int_{-\infty}^{\infty}\int_{-\infty}^{\infty} W(v,y)dydv = 1$

At the detachment point B, the adhesive force (f_a) balances the lift force F_L (which is the sum of mean and fluctuating lift forces), so Eq.[2.47] becomes

$$m\omega^2 y_B = f_a - \langle F_L\rangle \qquad [2.59]$$

Hall (1988) measured the mean lift forces on particles in a turbulent boundary layer. This gives an expression (Eq.[2.18]) which is valid over the range ($1.8 < ru_\tau/v_f < 70$).

$$\langle F_L\rangle = 20.9\rho_f v_f^{\,2}\left(\frac{ru_\tau}{v_f}\right)^{2.31}$$

Substitute Eq.[2.48], Eq.[2.57] and Eq.[2.59] into Eq.[2.58], the resuspension rate constant in a harmonic potential is given by

$$p = \frac{\omega}{2\pi}\sqrt{\frac{\langle \dot{f}_L^{\,2}\rangle / \langle f_L^{\,2}\rangle\omega^2 + \eta}{1+\eta}} \exp\left(-\frac{1}{2}\frac{\left(f_a - \langle F_L\rangle\right)^2}{\langle f_L^{\,2}\rangle(1+\eta)}\right) \qquad [2.60]$$

where $\langle \dot{f}_L^{\,2}\rangle$ and the root mean square (rms) fluctuating lift force are assumed to be given by

$$\langle \dot{f}_L^{\,2}\rangle \approx \int_0^\infty \omega^2 \hat{E}_L(\omega)\langle f_L^{\,2}\rangle d\omega \qquad \sqrt{\langle f_L^{\,2}\rangle} \approx \langle F_L\rangle \qquad [2.61]$$

The maximum value of *p* in the RRH model is limited to the bursting frequency of turbulent motion in a turbulent boundary layer, which according to Blackwelder and Haritonidis (1983), is given by

$$\sqrt{\frac{\langle \dot{f}_L^{\,2}\rangle}{\langle f_L^{\,2}\rangle}} \approx 0.0207\left(\frac{u_\tau^{\,2}}{v_f}\right) \qquad [2.62]$$

General form of resuspension rate constant

For a general potential well, the average potential energy <*PE*> is defined as $\frac{1}{2}m\omega^2\left\langle y^2\right\rangle$ and the height of potential well *Q* is given by $k\left(f_a-\left\langle F_L\right\rangle\right)^2\Big/\varepsilon$. Then by substituting <*PE*> and *Q* into Eq.[2.46], the general resuspension rate constant is given by

$$p=\frac{\omega}{2\pi}\sqrt{\frac{\left\langle \dot{f}_L^{\,2}\right\rangle\Big/\left\langle f_L^{\,2}\right\rangle\omega^2+\eta}{1+\eta}}\exp\left(-k\frac{\left(f_a-\left\langle F_L\right\rangle\right)^2}{\left\langle f_L^{\,2}\right\rangle(1+\eta)}\right) \qquad [2.63]$$

where *k* is a numerical constant dependent upon the shape of the potential, which equals ½ for a harmonic potential and 1 for the JKR potential model (Johnson *et al.*, 1971). In the RRH model, k = 1 is used.

The particle fraction remaining is given by the integration of the remaining fraction in each identical adhesive condition; the adhesive condition depends on the normalized asperity radius varying from 0 to ∞.

$$f_R(t)=\int_0^\infty \exp\left[-\left(p(r_a')\right)t\right]\varphi(r_a')dr_a' \qquad [2.64]$$

Then the resuspension rate is derived as

$$\Lambda(t)=-\dot{f}_R(t)=\int_0^\infty p(r_a')\exp\left[-\left(p(r_a')\right)\,t\right]\varphi(r_a')dr_a' \qquad [2.65]$$

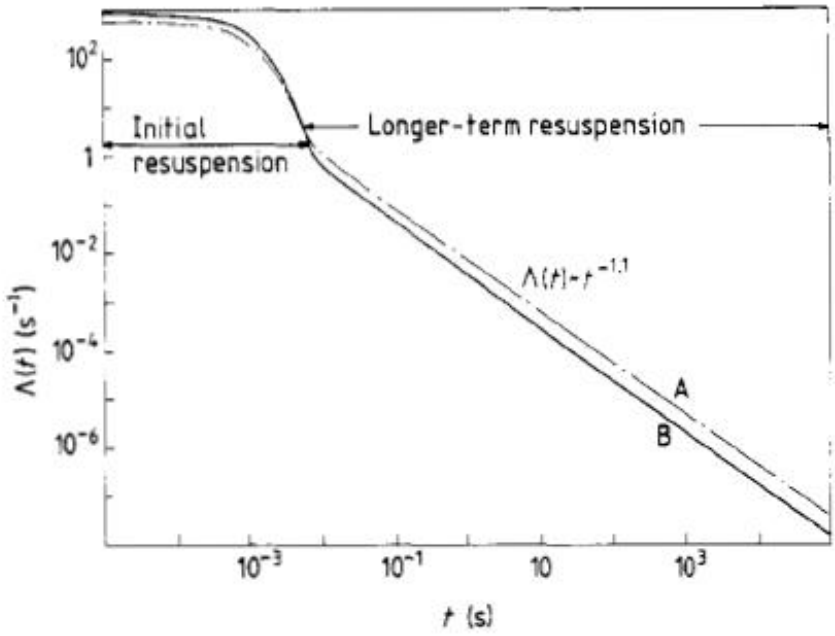

Figure 2.23 - Resuspension rate vs. time (Reeks *et al.*, 1988)

The modelling results in Figure 2.23 show that the resuspension of particles (radius around 25-50μm) from a rough surface can be divided into two regimes: the initial resuspension in which many

particles are resuspended within a very short time; and the long-term resuspension where its rate is proportional to approximately $t^{-1.1}$. This relationship is observed for wide variations of particle diameter, flow conditions and surface roughnesses and this behaviour of reverse time relationship has also been confirmed by other models and experiments (Wen & Kasper 1989, Jurcik & Wang 1991).

Improvements of RRH model

Vainshtein *et al.* (1997) observed resuspension due to rolling and they concluded that the drag force is a more effective agent than lift for the transfer of turbulent energy from the flow to a particle on a surface. The Vainshtein *et al.* model uses the potential-well approach and considers the particle-wall effect as though the particle is connected to the wall by a spring. They defined a tangential pull-off force which pulls the particle off against the spring. Compared with the RRH model, the ratio of the height of the potential well to the average potential energy in Eq.[2.46] ($Q/2\langle PE\rangle$) is rewritten as the ratio of the pull-off force to turbulent drag force. The particle resuspension rate constant is then given as

$$p = \frac{u_\tau^{\,2}}{300 v_f} \exp\left[-\left(\frac{\gamma^{4/3}}{r^{4/3} \kappa^{1/3} u_\tau^{\,2} \rho_f} \right)^{4/3} \right] \qquad [2.66]$$

where u_τ is the wall friction velocity, v_f is the fluid kinematic viscosity, ρ_f is the fluid density, γ is the surface energy, κ is the elastic constant (used as the composite Young's modulus K in Eq.[2.43]) and r is the particle radius. In their model, the particle fraction remaining and resuspension rate are calculated same as in Eq.[2.64] and Eq.[2.65], respectively.

Komen (2007) commented on Vainshtein *et al.* model that the largest uncertainties in the model are from the adhesion modelling; the adhesion moment overestimates the magnitude of the moment necessary to rotate the particle and the restoring force from adhesion is over predicted due to a constant spring stiffness where the maximum equilibrium value is used.

Subsequently, Reeks and Hall modified the RRH model, Reeks and Hall (2001), to account for the influence of drag that can provoke rolling: this leads us to the well-known Rock'n'Roll model.

2.3.2.2 Rock'n'Roll Model

In addition to the lift and adhesive forces, the drag force is also considered in the model. Thus, the particle will be oscillating about a pivot point P rather than oscillating vertically in a potential well, as shown in Figure 2.24. In this case, the particle contacts with two asperities.

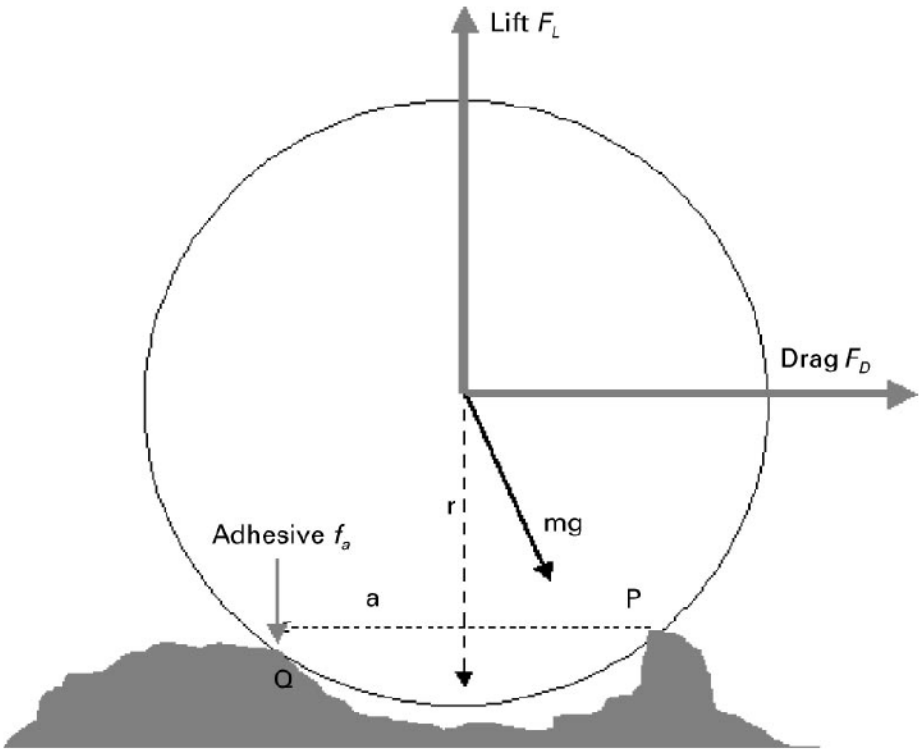

Figure 2.24 - Particle surface geometry for Rock'n'Roll model (Reeks & Hall, 2001)

When the vibrational energy is being accumulated, the particle will break the contact point Q and start oscillating on the pivot point P before it leaves the surface. Therefore, the equation of motion will take into account moment of inertia and couple about point P. a is the distance between two asperities. The geometric factor (r/a) which refers to the ratio of the particle radius to the distance between asperities is suggested to be close to 100 according to Hall's experiment (Reeks and Hall, 2001).

Eq.[2.47] then becomes:

$$\ddot{\theta} + \beta_\theta \dot{\theta} + \omega_\theta^2 \theta = I^{-1}\Gamma'(t) \qquad [2.67]$$

where θ is the angle of small oscillation about P, I is the particle moment of inertia ($5/7\ mr^2$) and Γ' is the fluctuating component of the couple. It is assumed that the drag $m\beta$ caused by small oscillation θ is the same for a sphere particle of radius r oscillating in position with velocity $r\dot{\theta}$; so the damping constant β_θ is derived by equalling the moment of this force about P with $I\beta_\theta\dot{\theta}$. The displacement (deformation) of the particle about P is given by $a\theta$ so that the restoring couple is given by $m\omega^2a^2\theta$. The relationship between the natural frequency ω_θ (for vertical and horizontal

oscillations) and the natural frequency ω (for vertical oscillations) is obtained by balancing the restoring couple with $I\omega_\theta{}^2\theta$.

$$B_\theta = \frac{5}{7}B \quad \omega_\theta = \sqrt{\frac{5a^2}{7r^2}}\omega \qquad [2.68]$$

The couple acting at point P can be expressed in terms of the relevant forces, Eq.[2.63] is replaced by:

$$p = \frac{\omega_\theta}{2\pi}\sqrt{\frac{\left\langle \dot{f}^2 \right\rangle / \left\langle f^2 \right\rangle \omega_\theta{}^2 + \eta}{1+\eta}}\exp\left(-k\frac{\left(f_a + \frac{1}{2}mg_n - \frac{r}{a}mg_t - \langle F \rangle \right)^2}{\left\langle f^2 \right\rangle (1+\eta)} \right) \qquad [2.69]$$

g_n and g_t are the gravitational components of acceleration acting normally and tangentially to the wall surface. F is resultant aerodynamic force (obtained from the moment) acting on P which is given by drag and lift forces and f is its fluctuating component. As for the RRH model, the mean lift force is given by Eq.[2.18] and the mean drag force is equal to 1.7 times the Stokes drag (Eq.[2.9]).

$$F = \frac{1}{2}F_L + \frac{r}{a}F_D \quad \left\langle F_D \right\rangle = 32\rho_f \nu_f{}^2 \left(\frac{ru_\tau}{\nu_f} \right)^2 \qquad [2.70]$$

The experiments by Hall (1998) measured the energy spectrum of the lift force (Eq.[2.62]); the R'n'R model have renewed the energy spectrum by including the effect of the drag force and the effective zero mean fluctuating force, f. The ratio of rms to the mean aerodynamic force is 0.2 obtained by Hall's measurements, and the ratio of the rms derivative to the rms force is derived from Hall's measurements of the energy spectrum of the lift force (where the lift force here is assumed to be the same as the fluctuating aerodynamic force).

$$\sqrt{\frac{\left\langle \dot{f}^2 \right\rangle}{\left\langle f^2 \right\rangle}} = 0.0413\left(\frac{u_\tau{}^2}{\nu_f} \right) \quad \sqrt{\left\langle f^2 \right\rangle} \approx 0.2\langle F \rangle \qquad [2.71]$$

The universal energy spectrum for the fluctuating lift force ($E^+(\omega^+)$) used in the R'n'R model is a modified version of the one used in the RRH model, where following Hall (1994)

$$E^+(\omega^+) = \begin{cases} 58.06 & \omega^+ \le 0.0054 \\ 0.0812(\omega^+)^{-1.26} & 0.0054 < \omega^+ < 0.104 \\ 0.0000173(\omega^+)^{-5} & \omega^+ \ge 0.104 \end{cases} \qquad [2.72]$$

Quasi-static case

If the motion of particles is driven by turbulent aerodynamic forces and there is no resonant energy transfer, the particle motion can be described as a force balance between aerodynamic forces and

the adhesive force; this is often referred to as the 'Quasi-static' case. Then, for a particle in equilibrium at the detachment point

$$\langle F \rangle + f = f_a \qquad [2.73]$$

If a relationship (ψ) between f and particle displacement and velocity exist,

$$y(t) = \psi(f) \quad v(t) = \dot{f}\psi'(f) \qquad [2.74]$$

Substituting Eq.[2.74] into Eq.[2.58], the resuspension rate constant for the quasi-static case is given by

$$p = \int_0^\infty \dot{f}\, P(f_a - \langle F \rangle, \dot{f})d\dot{f} \Big/ \int_{-\infty}^{\infty}\int_{-\infty}^{f_a - \langle F \rangle} P(f_a - \langle F \rangle, \dot{f})df d\dot{f} \qquad [2.75]$$

where $p(f, \dot{f})$ is the distribution of fluctuating aerodynamic force and its derivative, which is assumed as a joint Gaussian distribution with zero correlation between f and $\dot{f}$.

Then the resuspension rate constant is obtained

$$p = \frac{1}{2\pi}\sqrt{\frac{\langle \dot{f}^2 \rangle}{\langle f^2 \rangle}} \exp\left(-\frac{\left(f_a - \langle F \rangle\right)^2}{2\langle f^2 \rangle}\right) \Big/ \frac{1}{2}\left[1 + \mathrm{erf}\left(\frac{f_a - \langle F \rangle}{\sqrt{2\langle f^2 \rangle}}\right)\right] \qquad [2.76]$$

where erf is the error function.

More details about Quasi-static case will be described in Chapter 4 (p97).

The particle fraction remaining $f_R(t)$ and the resuspension rate $\Lambda(t)$ are then defined by using the same forms as Eq.[2.64] and Eq.[2.65], respectively

$$\begin{aligned} f_R(t) &= \int_0^\infty \exp\left[-\left(p(r_a')\right)t\right]\varphi(r_a')dr_a' \\ \Lambda(t) &= -\dot{f}_R(t) = \int_0^\infty p(r_a')\exp\left[-\left(p(r_a')\right)t\right]\varphi(r_a')dr_a' \end{aligned} \qquad [2.77]$$

where $\varphi(r_a')$ is assumed as log-normal distribution according to Eq.[2.54].

Reeks and Hall reported 20 resuspension experiments that used both alumina and graphite particles (more details about the experiments are described in Chapter 4.1.4, p129). The Material properties required to calculate particle resuspension for both the RRH and the R'n'R models are listed below.

Material	Graphite	Alumina
Interfacial surface energy, Jm^{-2}	0.15	0.56
Substrate density (steel), Kg m^{-3}	7830	7830
Substrate Young's modulus, Pa	2.1×10^{11}	2.1×10^{11}
Particle Young's modulus, Pa	2.0×10^{10}	3.5×10^{11}
Substrate Poissons ratio	0.29	0.29
Particle Poissons ratio	0.3	0.3
Particle density, Kg m^{-3}	2300	1600

Table 2.2 - Material properties in Hall's experiment (Reeks and Hall, 2001)

The parameters for adhesive force log-normal distribution in the RRH and the R'n'R models are produced based on Reed and Rochowiak (1988).

RRH lift force model			Rock'n roll model		
Data set	Adhesive spread σ_a'	Adhesion reduction $\bar{r}_a'$	Adhesive spread σ_a'	Adhesion reduction $\bar{r}_a'$	Geometric factor r/a
10 μm alumina	2.55	**0.027**	10.4	**0.027**	100
20 μm alumina	2.55	**0.392**	10.4	**0.018**	100
Graphite	489	**0.645**	19	**0.645**	100

Table 2.3 - Parameters of adhesive force distribution (Reeks and Hall, 2001)

The results for 10μm alumina (in diameter) and graphite particle are shown in Figure 2.25 and Figure 2.26, respectively. It can be clearly seen from the figures that the Rock'n'Roll model gives much better agreement with experimental values of the resuspension than the original RRH model, the agreement being quite good considering the large uncertainty in the adhesive force measurement. Furthermore, the comparison between the Rock'n'Roll model results with and without resonant energy transfer shows only a slight difference. This means that the resonant energy transfer only makes a very small contribution to resuspension and the quasi-static version (without resonant energy transfer) can be used for certain conditions.

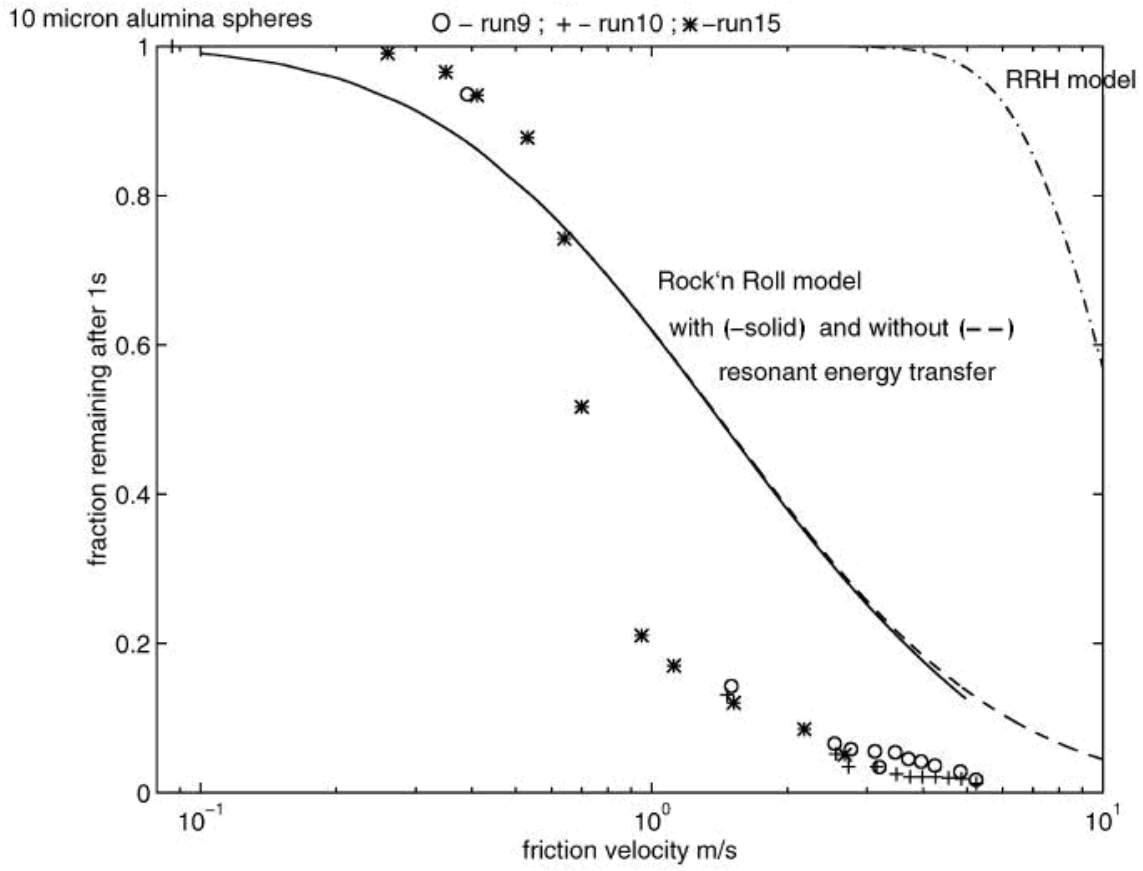

Figure 2.25 - Comparison of alumina particle fraction remaining after 1s (Reeks & Hall, 2001)

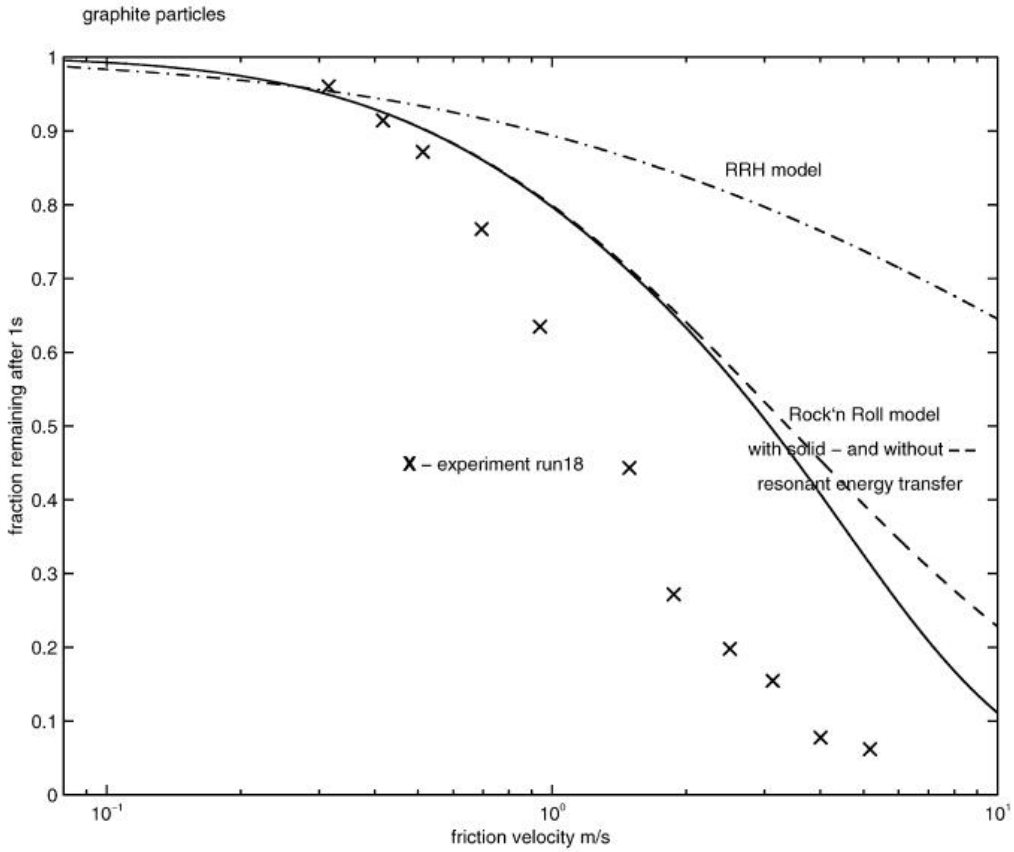

Figure 2.26 - Comparison of graphite particle fraction remaining after 1s (Reeks & Hall, 2001)

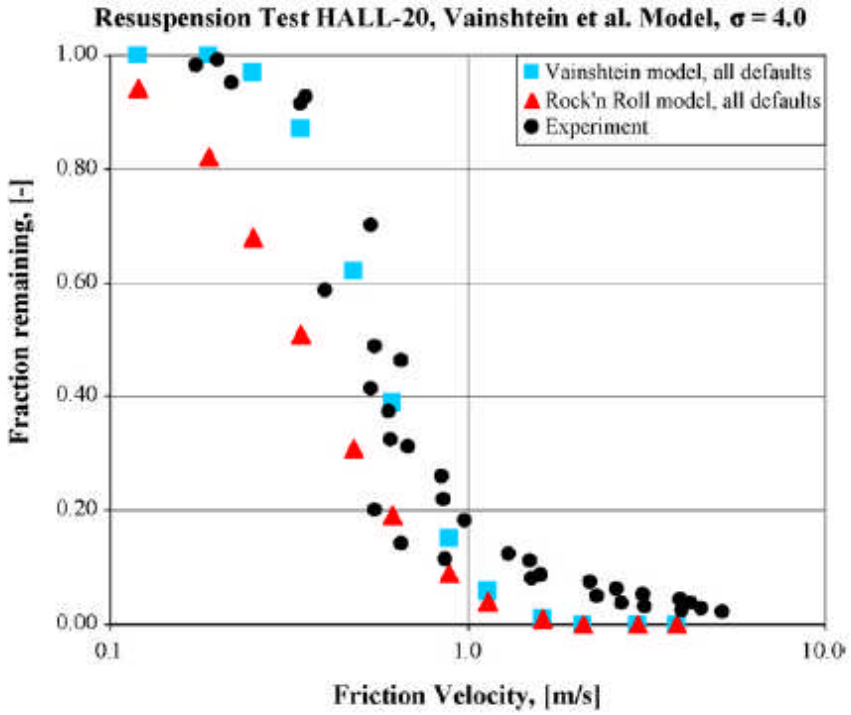

Figure 2.27 - Remaining fraction for R'n'R and Vainshtein (Stempniewicz *et al.*, 2008)

Stempniewicz *et al*. (2008) compared the results of the Rock'n'Roll model (Reeks and Hall, 2001) and Vainshtein model (1997) with the experiments of Reeks and Hall and STORM (Details on STORM is provided in Chapter 2.2.2, p29), and concluded that the Vainshtein model gives better agreement with the experiment results whereas the Rock'n'Roll model somewhat overestimates the resuspension at low value of the friction velocity. Figure 2.27 shows the comparison of the Rock'n'Roll prediction and Vainshtein predictions with the experimental data, for an adhesive spread factor of 4. They also concluded that the adhesive force and its distribution for dust particle deposited on a rough surface are very important in successful resuspension predictions.

Biasi *et al*. (2001) took the Rock'n'Roll model for resuspension with an empirical log-normal distribution of adhesive force to reproduce the resuspension data of a number of experiments. Some adhesion-force parameters were tuned to fit the data of the most highly-characterised experiments, i.e., those of Hall (Reeks & Hall, 2001) and Braaten (1994). Then, using an enlarged dataset including STORM and ORNL ART resuspension results, they obtained a global correlation for geometric mean adhesive force and geometric spread as a function of particle geometric mean radius (in microns)

$$\bar{r}_a' = 0.016 - 0.0023 r^{0.545}$$
$$\sigma_a' = 1.8 + 0.136 r^{1.4} \qquad [2.78]$$

The correlation is shown in Figure 2.28.

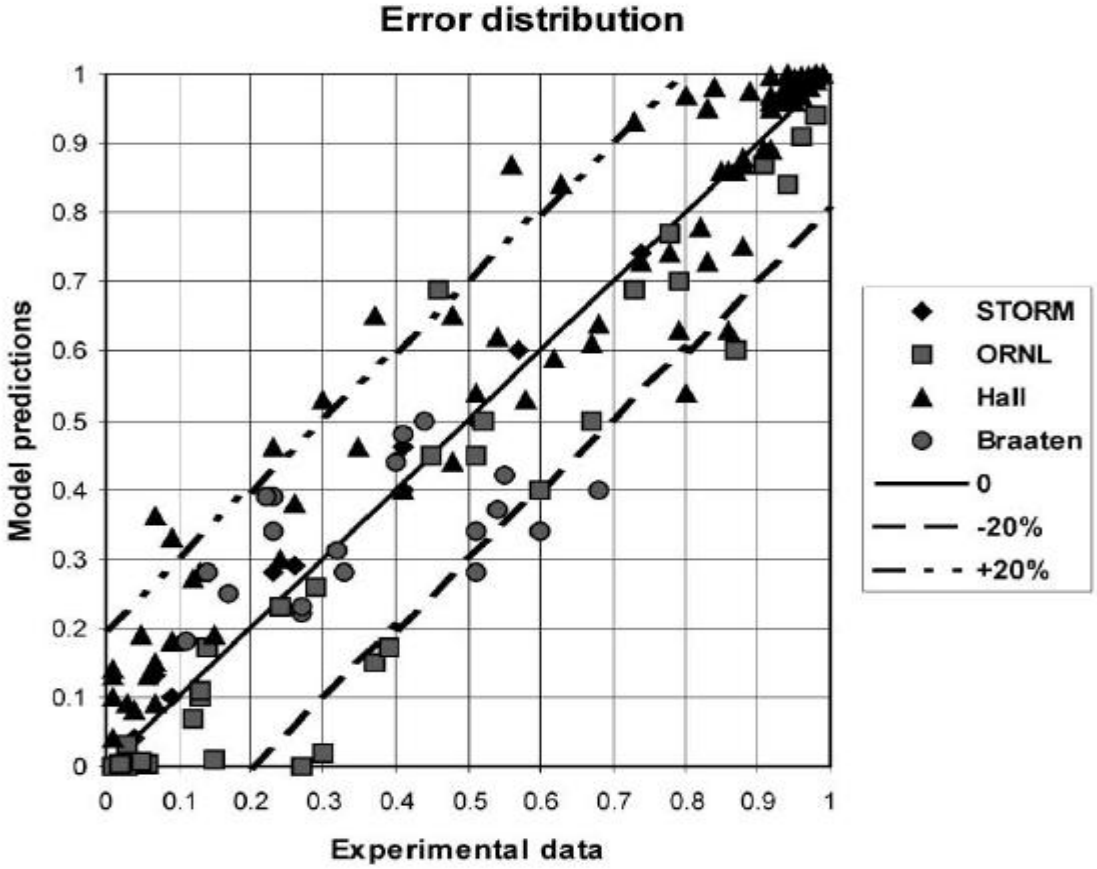

Figure 2.28 - Error distribution of Biasi's model predictions (Biasi *et al.*, 2001)

They also concluded that the measurements of adhesive force (Boehme *et al.*, 1962) show that the distribution of adhesive forces is close to a log-normal distribution, but that the validity of assuming a Gaussian distribution for the drag force might be questionable (i.e. there is no physical basis justifying the particular form of the Gaussian distribution). They also pointed out that, in reality, the geometric ratio of particle radius to average separation of asperities, r/a, appearing in the R'n'R model, rather than being a constant, has a spread as with the actual adhesive force.

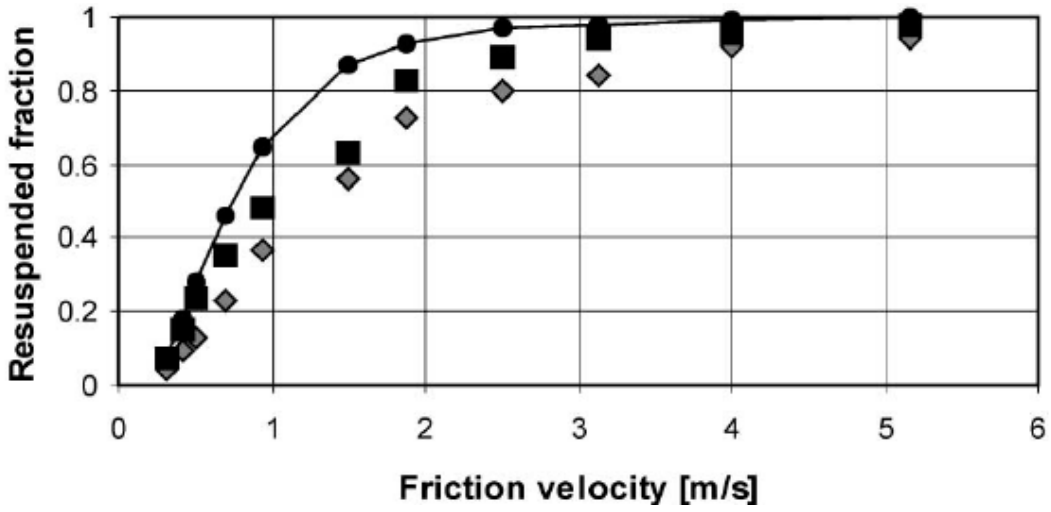

Figure 2.29 - Biasi's result compare with Reeks and Hall's experiment (Biasi *et al.*, 2001)

2.3.2.3 Simplified RRH Model

Based on the work by Davis and Hall's report (1988), Reeks (2008) developed a simplified model with the same statistical distribution of adhesive force as that used in RRH model. The adhesive force is assumed to scale on the adhesive force for a particle sitting on a perfectly smooth surface, which is proportional to the radius of the particle. The aerodynamic removal force is assumed to scale on the dynamic head associated with the flow, $\rho_f V^2$. Then

$$F = k\rho_f U^2 \qquad [2.79]$$

where F is the aerodynamic removal force, k is a factor that would depend on particle size, ρ_f is the fluid density and U is the mean fluid velocity at the centre of the particle.

The fraction resuspended is given by

$$F_R = \int_0^F P(f_a) df_a \qquad [2.80]$$

where $P(f_a)$ is the distribution of adhesive forces f_a scaled on the adhesive force for perfect contact. The crucial part of the evaluation of this integral is to assume on the basis of experiments that the adhesive forces have a log-normal distribution distributed. D&H show that over the region where the resuspension fraction is not saturated (neither close to zero nor 1), F_R is very close to proportional to $\ln(\rho_f V^2)$. Reeks (2008) mentioned that the broader the distribution of adhesive forces the closer

this becomes to an exact proportionality. For instance if the adhesive force was distributed uniformly on a logarithmic scale, this result would be exact, i.e.

$$F_R = \frac{A}{\sigma'_a} \ln \rho_f U^2 \qquad [2.81]$$

where σ'_a is the logarithmic spread of the adhesive force and A is a constant.

In the viscous sublayer, the fluid mean velocity U can be written as ru_τ^2/v_f, v_f is the fluid kinematic viscosity, then Eq.[2.81] becomes

$$F_R = \frac{A}{\sigma'_a} \ln \rho_f \left(\frac{r u_\tau^2}{v_f} \right)^2 \qquad [2.82]$$

2.3.3 Models for Resuspension from a Multilayer Deposit

In most nuclear accidents, particles will first be deposited on the walls, forming multilayer deposits, before being resuspended. But the models reviewed as far all consider the resuspension of an isolated particle from a clean surface. In reality, the surface particles will be in contact with other particles and they form agglomerates or clusters, and it is possible that particles will be resuspended in 'clumps' rather than individually. In the multilayer deposit, bulk density (related parameter, porosity) has been used to characterize the structure (i.e. how dense the deposit structure is) (Schmidt & Löffler, 1991). Coordination number (which is the average number of contacts of a particle) is an important parameter to the structure of agglomerates (Weber and Friedlander, 1997). Furthermore, the aerodynamic contribution should be taken into account through the shielding effect by existence of other particles in the deposits. The aerodynamic drag force acting on each constituent particle should be definitely smaller than that without other particles. Iimura *et al*. (2009) concluded that the morphology of deposits much affects the resuspension of particles and the sterically bulky deposit undergoes the stronger aerodynamic force and is easy to be resuspended and consequently a smaller number of particles remain attached to the surface.

The first multilayer model was probably that of Paw U (1982) which was initially an extension of the model of Cleaver and Yates (1973). In this model, the multilayer deposit ensures a continuous supply of particles for resuspension, so the resuspension fraction becomes

$$f_c(t) = \frac{1}{270} \cdot \frac{u_\tau^2 t}{100 v_f} \qquad [2.83]$$

where $100v_f/u_\tau^2$ is the average time between turbulent bursts in Cleaver and Yates (1976), v_f is the fluid kinematic viscosity and u_τ is the wall friction velocity. Paw U concluded that the model required further development to include saltation, and the physics of the atmospheric surface boundary layer and rebound/net-deposition phenomena. One can observe that it is a rough model since the resuspension fraction is determined as a resuspension probability constant (1/270) multiplied by the total number of bursts.

Fromentin (1989) set up a two-step experiment PARESS (PArticle RESuspension Study) in which the first step was deposition of different aerosols and the second step was resuspension. Experiments were performed with a range of mean flow velocities, between 5 and 20m/s. Throughout the experiments, the long-term resuspension flux (time > 2s) decreased with time of exposure to the flow and could be modelled by an expression of the form where *A* and *B* are empirical coefficients.

$$\Lambda = A \cdot t^{-B} \qquad [2.84]$$

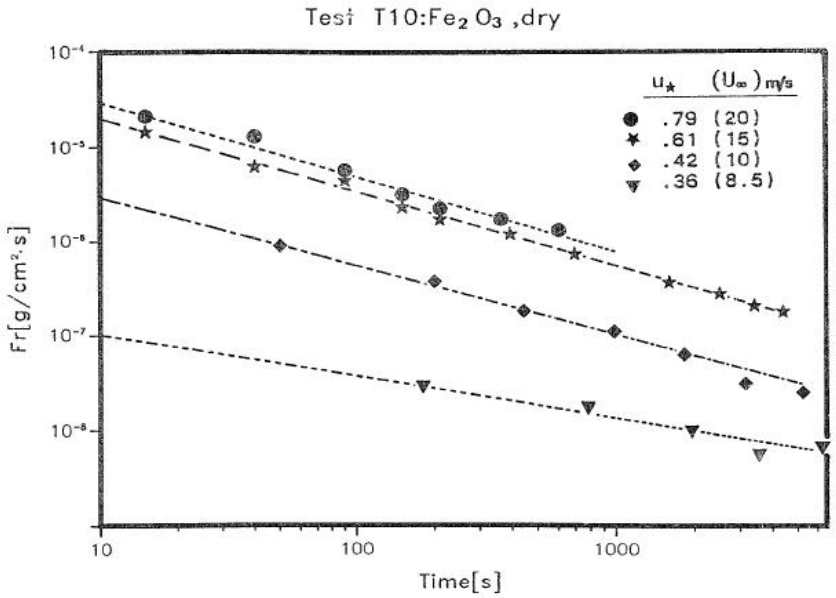

Figure 2.30 - Resuspension flux vs. time of Fromentin's model (Fromentin, 1989)

Figure 2.30 above shows the resuspension flux of deposited particles (AMMD ~ 2 μm) as a function of time. Fromentin showed that the constants *A* and *B* are proportional to the wall friction velocity u_τ. Therefore, the resuspension flux could be written as a function of time and wall friction velocity.

$$\Lambda = 0.025 \cdot (u_\tau - 0.29)^3 \cdot t^{-1.2\sqrt{u_\tau}} \qquad [2.85]$$

which is valid for 2s < t < 10000s, and 0.3m/s < u_τ < 1m/s.

Heames *et al.* (1992) presented a resuspension model (used in the US NRC code VICTORIA) that is based on a power law curve fit to the experimental data obtained by Wright *et al.* (1992) from the ORNL Aerosol Resuspension Test (ART). This fit is of the same type used in correlating the PARESS resuspension data (Fromentin, 1989) and the resuspension flux (which is assumed only to be calculated in turbulent flow, no resuspension in laminar flow) is obtained as:

$$\Lambda = 0.05 \cdot u_\tau^{\,2} \cdot t^{-1.25} \qquad [2.86]$$

In this model it is assumed that:

- all particles have the same properties of adhesion to the substrate;
- once particles are deposited they are taken to be immediately well mixed with previously deposited particles;
- resuspended particles have the same size as when they deposited;
- the exposure time in Eq.[2.86] is defined as the difference between current time and the point at when flow first becomes turbulent in the current cell.

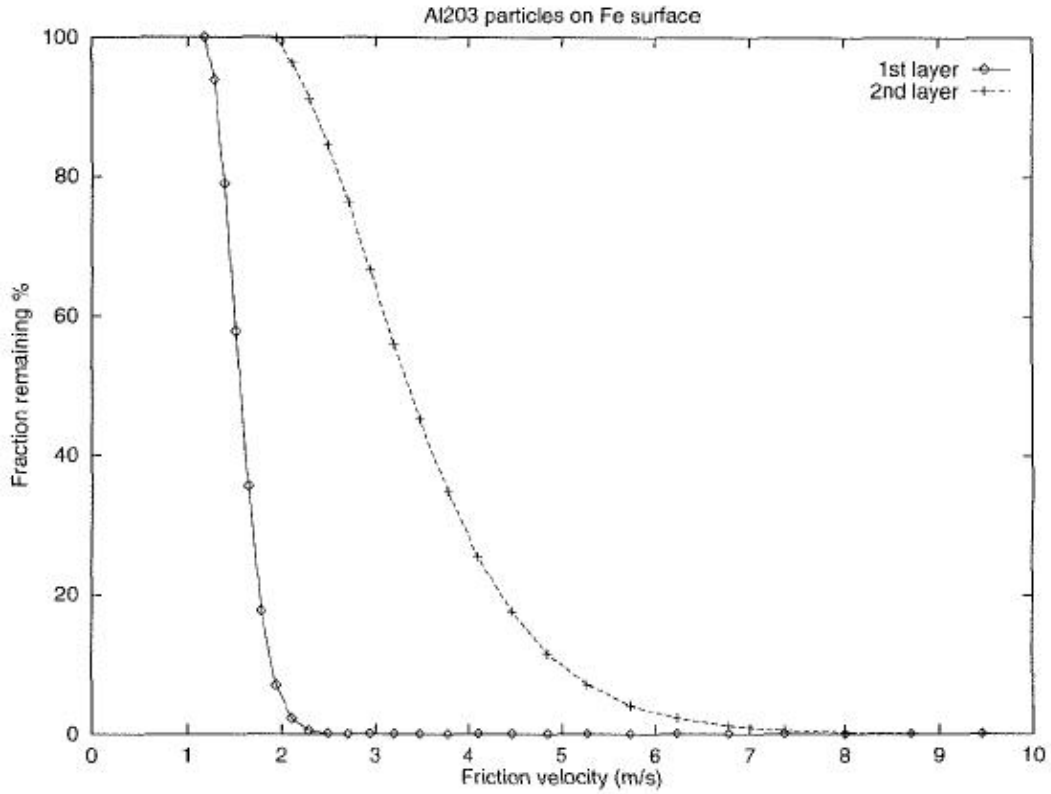

Figure 2.31 - Two-layer 10 μm Al_2O_3 particle fraction remaining (Lazaridis & Drossinos, 1998)

Lazaridis and Drossinos (1998) derived an expression for the total particle resuspension rate from a multilayer deposit in terms of the fixed resuspension rate from each layer, calculated using the RRH model. An interaction potential is considered between each layer and particle-particle interactions in the same layer are neglected (i.e. no particle interaction in the streamwise axial direction). The formulae for interaction energy between a particle and the surface or between particles are developed and used to evaluate the natural frequency of vibration which replaces the term Eq.[2.52] in the RRH model. In order to obtain an analytical solution for the particle fraction remaining on the surface as a function of time, the deposit was limited to two layers.

Friess and Yadigaroglu (2001) provide a generic model which uses a recursion relation which uses the resuspension rate of the first layer (i = 1) to calculate the resuspension rate of the layers below ($i \geq 2$). Detailed information on Friess and Yadigaroglu (2001) is presented in Chapter 5.1 (p156). The particle resuspension rate of the current layer, i, based on the previous layers is derived as,

$$\Lambda_i(t) = \int_0^t \Lambda_1(t-t')\Lambda_{i-1}(t')dt' \qquad i \geq 2 \qquad [2.87]$$

The total resuspension rate for L layers deposit is given by

$$\Lambda_L(t) = \Lambda_1(t) + \sum_{i=2}^{L} \int_0^t \Lambda_1(t-t')\Lambda_{i-1}(t')dt' = \Lambda_1(t) + \int_0^t \Lambda_1(t-t')\Lambda_{L-1}(t')dt' \qquad L \geq 2 \qquad [2.88]$$

They compared their model with that of Lazaridis and Drossinos (1998) and found that the exposure time required to resuspend half of the deposit predicted by their generic model (i = 150, typical value of STORM test) is 2.4 times longer than that computed by L&D's model. Friess and Yadigaroglu (2001) also modified the model of Fromentin (1989) by including the dimensionless variables

$$\Lambda^{+}_{i}(t^{+}) = b_f^{-1}\Lambda_i(t) \qquad t^{+} = b_f t\,, \quad b_f = 0.012\,\frac{u_\tau^{\,2}}{\nu_f} \qquad [2.89]$$

where b_f is the burst frequency as given by Rashidi and Banerjee (1990).

Figure 2.32 shows the dimensionless resuspension flux vs. dimensionless time for the various thickness deposits (L = 1, 2, 3…, 10, 20, 30, 40, infinity). It appears that the resuspension flux becomes a nonzero value at infinite time. Friess and Yadigaroglu (2001) mentioned that the fact that the resuspension flux is predicted to always become zero after an infinite time might seem paradoxical: One might expect that eroding an infinitely thick deposit by means of a fluid of constant velocity eventually leads to a stationary state with a nonzero value $\Lambda_\infty(\infty)$ of the resuspension flux.

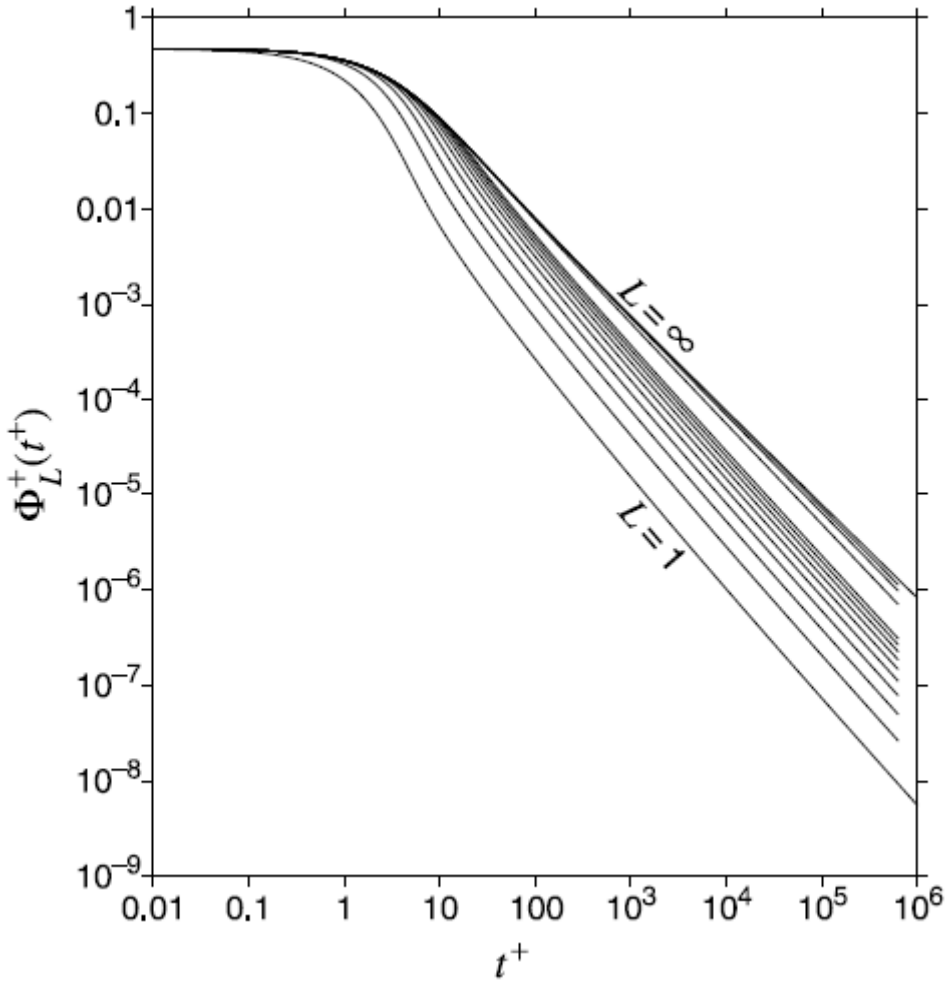

Figure 2.32 - Dimensionless resuspension rate vs. time (Friess & Yadigaroglu, 2001)

Friess and Yadigaroglu (2001) also extended the RRH isolated-particle model (Reeks *et al.*, 1988) to the multilayer case, based on a simplified assumption that a particle sitting on top of the multilayer deposit has the same resuspension rate constant p (Eq.[2.60]) as an isolated particle sitting on a clean surface. This is analogous to the assumption made in the Lazaridis and Drossinos model (1998). Figure 2.33 shows that the long-term behaviour of resuspension rate follows the 1/t law and is independent of the initial deposit thickness (Application on Reeks, Reed and Hall (1988) model).

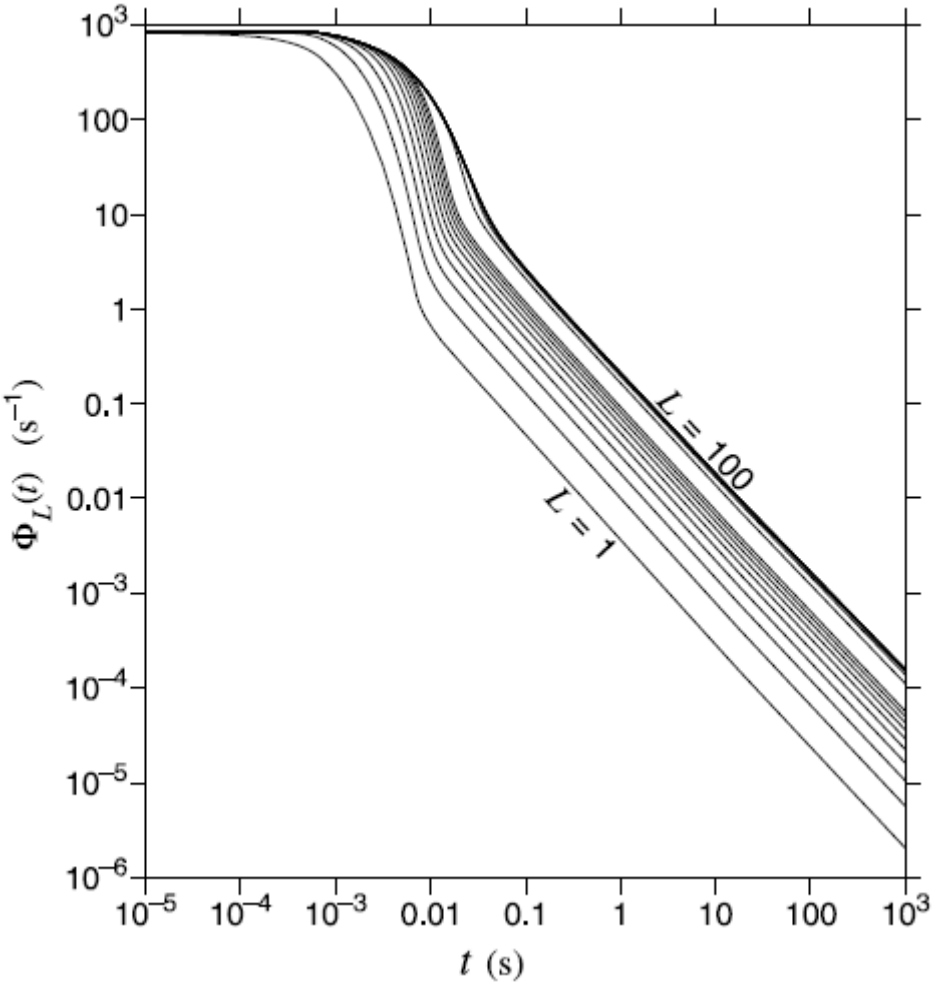

Figure 2.33 - Resuspension rate vs.time using RRH model (Friess & Yadigaroglu, 2001)

The main conclusion of Friess and Yadigaroglu (2001) is that major discrepancies between theory and experiment are to be expected if a monolayer model is used for a wide range of initial deposit thicknesses. The monolayer models also over predict the resuspension mass and the short term resuspension flux. For long-term flux, the results of a monolayer model are acceptable. This trend was also observed by Alloul-Marmor (2002) for resuspension of piles of alumina dust with diameter between a few microns and 100 μm. The experimental data (Alloul-Marmor, 2002) were compared with the results of the model developed by Biasi et al. (2001); this showed that the model overestimated the resuspension fraction, and it was not possible to improve the model predictions for the whole data set by modifying the adhesive force correlations (Eq.[2.78]) used in the model.

The data from the experiments were used to derive a new correlation for the resuspension fraction, of the form:

$$f_c(t) \propto (d_{50} \cdot u_\tau / v_f)^{5.7}$$

where d_{50} is the mass-median diameter of the particles in the deposit.

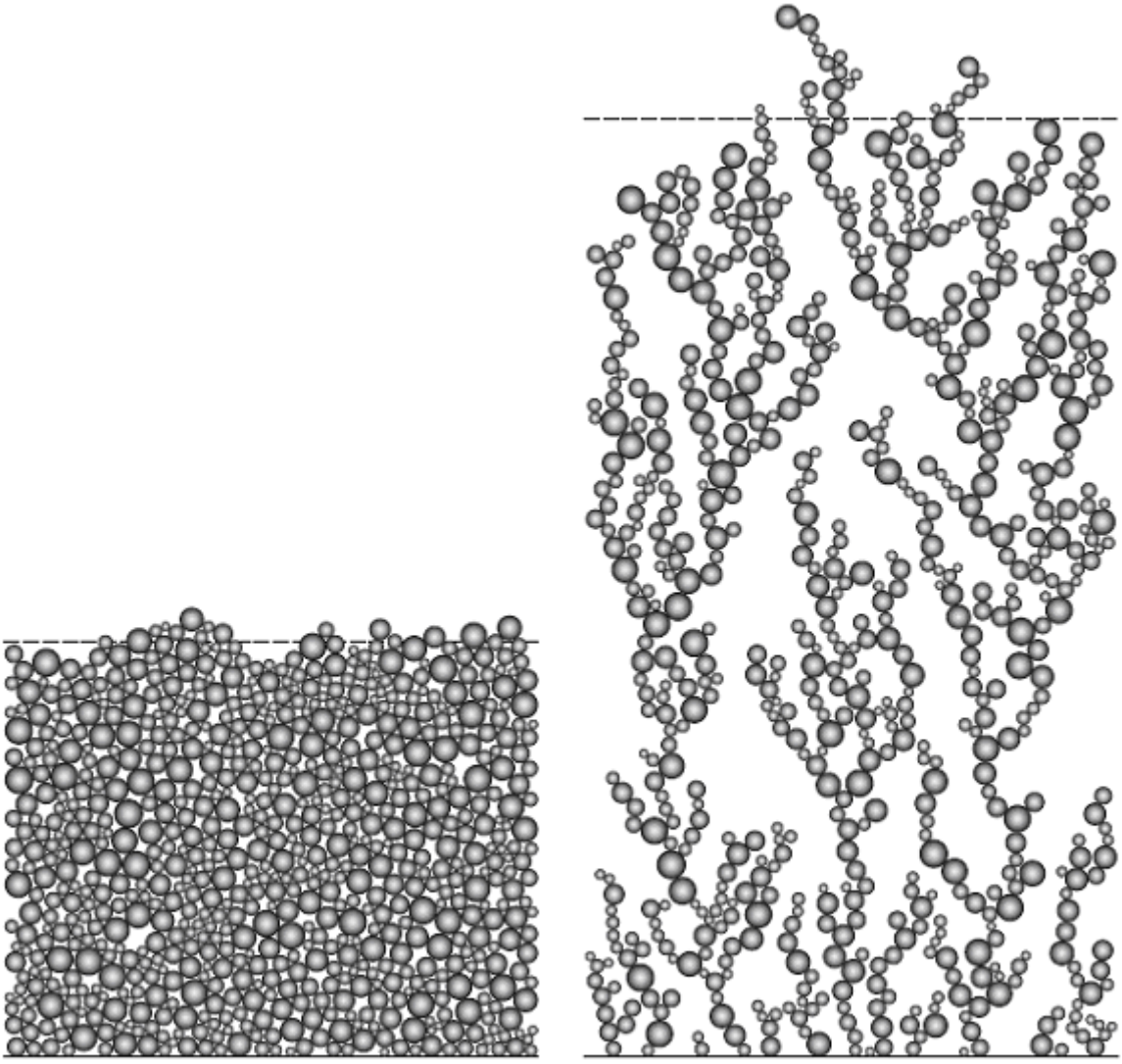

Figure 2.34 - Two-dimensional particle deposits structure (Friess & Yadigaroglu, 2002)

In order to investigate the influence of the deposit structure on particle resuspension, Friess and Yadigaroglu (2002) developed a new simulation, in which individual particles were first deposited on a wall, to build up a multilayer deposit. Each particle is deposited with a 'sticking probability' (s) which is used to determine, randomly, whether a particle will stick to another deposited particle or slide over it. This sticking probability directly determines the porosity, ς of the bed that is formed, as can be seen in Figure 2.34, which shows two particle beds, formed with two different values of s. When the sticking probability is very low (s = 0, Figure 2.34a) the bed is closely packed and the

porosity tends to its minimum value; as the sticking probability increases the bed tends to grow in bifurcating chains of particles, like trees (Figure 2.34b), and the porosity increases.

Every cluster is associated with a resuspension probability per unit time, p_c, which is based on a balance between adhesion forces and the forces exerted by the turbulent bursts (which the distribution of burst forces exerted on a cluster is assumed to be Gaussian). It is similar to the model that originally proposed by Fromentin (1989) and later refined by Friess and Yadigaroglu (2001). The resuspension mass flux is then derived as:

$$\varphi_r(t) = -\frac{d}{dt}m(t) = \frac{\pi}{6}\rho_p D_m p_c \frac{d}{dt}\int_0^t e^{-p_c t'}\sum_{i=0}^{L_n-1}\frac{(p_c t')^i}{i!}dt' \qquad [2.90]$$

where $m(t)$ is the remaining mass per unit wall surface area as a function of time, D_m is the mass mean diameter of deposited particles, and L_n is the quantity layer number, defined as the number of particles intersected on average by a line normal to the wall (Friess and Yadigaroglu, 1998). The dimensionless resuspension flux obtained is similar to Eq.[2.89].

$$\varphi_r{}^+(t^+) = \frac{6}{\pi}\frac{\varphi_r(t)}{b_f \rho_p D_m} \qquad t^+ = b_f t\,, \quad b_f = 0.012\frac{u_\tau^{\,2}}{\nu_f} \qquad [2.91]$$

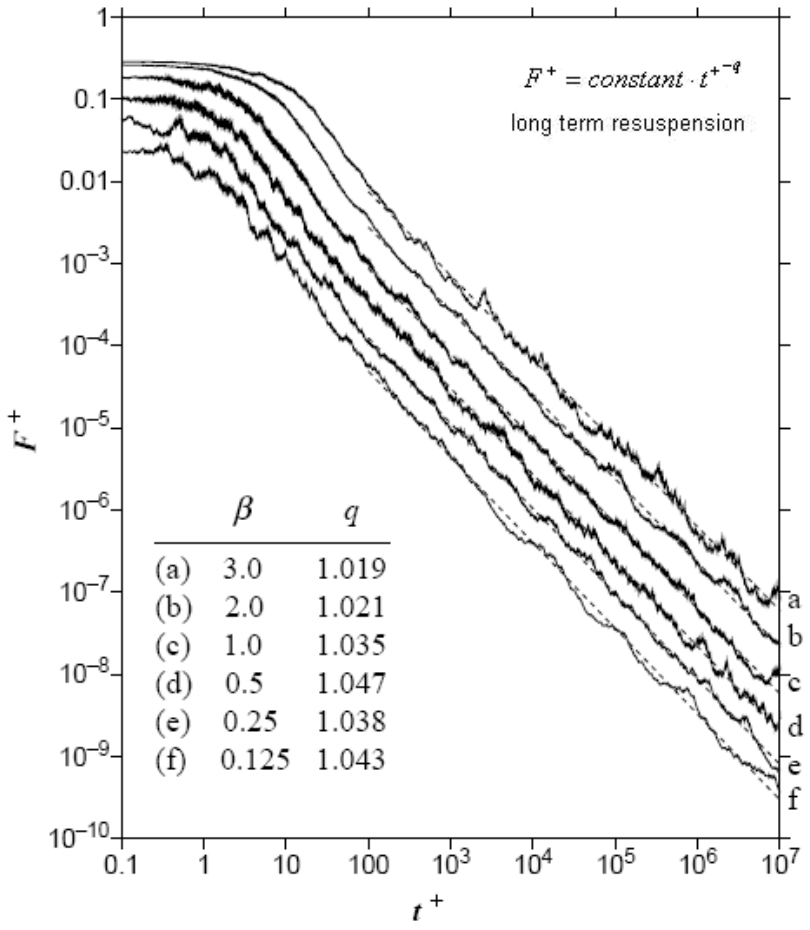

Figure 2.35 - Dimensionless resuspension flux (Friess & Yadigaroglu, 2002)

Friess and Yadigaroglu (2002) showed that the model predictions confirm the 1/t law for long-term resuspension (shown in Figure 2.35, B is the relative burst strength which is the ratio of the average burst force on a particle to this particle's adhesion force on a flat base) and conclude that the values of exponent q = 0.8 (see equation in Figure 2.35) from the PARESS experiments are still theoretically unexplained. They also analyze the sensitivity of the model to bed porosity, using the data from STORM experiment. The characteristic shape of model responses can be seen to depend strongly on the bed porosity. The model results also indicated a hypothesis that the porosity of the deposits in the PARESS experiment (Fromentin, 1989) was high compared to the STORM deposits.

Ziskind (2006) notes that this model is restricted to one-foot clusters, while a two-point contact has been widely accepted in monolayer resuspension modelling (Ziskind *et al*. 2000, Reeks and Hall 2001). Also the magnitude of adhesive force is calculated going back to Zimon (1982).

2.3.4 Conclusions on Resuspension Models

Models for the resuspension of particles from a wall are based either on balance of aerodynamic and adhesive force, or on the accumulation of kinetic and potential energy by the particles. Three different approaches have been developed for modelling the balance between adhesive and aerodynamic forces:

- a statistical approach which simulates the stochastic nature of particle resuspension and normally calculates the fraction of particle resuspended without concerning the time effect; turbulent burst is considered to be generated by following some probability distribution;
- a kinetic approach which is analyzed in a manner similar to the approach applied in chemical kinetics and normally generates the resuspension rate; and
- a Lagrangian approach which simulates the particles' trajectories while they are moving in turbulent flow.

These are all based on one basic rule: that the particles would resuspend from the surface when the aerodynamic forces acting on them exceed the adhesive forces. However, this force-balance approach takes no account of the timescales over which particles are resuspended (Reeks *et al.*, 1988) or in other words, all particles of the same size will either resuspend instantaneously or stay on the surface regardless of time where, in fact, experimental measurements indicate that particle removal takes place over a period of time (Sehmel, 1980).

Leighton and Acrivos (1985) showed in their paper that the mean and fluctuating lift force are much smaller than the experimental adhesive force (Wen *et al.*, 1989) when particles are small. It can also be seen from the formula of the mean aerodynamic moment which takes account of the drag effect (Laufer 1954, O'Neill 1968) and adhesive moment (Wang, 1990) that for small particles, the latter is larger. However, Sehmel (1971) showed that even particles as small as 2 μm can be resuspended in turbulent pipe flow. Unlike the force-balance model, the models based on energy accumulation allow for particles to resuspend from a surface as long as they accumulate enough potential energy from the surrounding turbulent flow over a period of time, even in the cases when surface forces may be very strong (especially for small particles).

Multilayer resuspension has seldom been studied in the last decade. The most recent model is presented by Friess and Yadigaroglu (2002) which puts forward a central hypothesis: that the structure of the deposit which is characterised by the bed porosity becomes an important parameter in multilayer resuspension modelling. Particles form clusters during the deposition process and the resuspendable clusters are associated with a variable called resuspension probability per unit time which is obtained from a balance between adhesive forces (which are considered as a function of particle diameter) and forces caused by turbulent bursts.

To sum up, in order to obtain a successful resuspension model, a good simulation of adhesive force distribution for particles deposited on the surface and statistics of turbulent fluctuating forces are necessarily needed.

Chapter 3
Modification of the
Force Balance Model

It is a bad plan that admits of no modification.

- Publilius Syrus

In this Chapter we present and discuss the results of a modification to the traditional force /moment balance resuspension models by introducing a statistical distribution of aerodynamic removal forces (moments). As a particular example we focus our attention on the recently published NRG resuspension models (Komen, 2007) which are based on the aerodynamic/ adhesion system of forces and moments contained in the Vainhstein model for a spherical particle in smooth contact with a surface. We begin with a brief description of the Vainshtein (1997) model. This is followed by a description of the NRG3 (force balance) and NRG4 (moment balance) models and how they incorporate the Vainhstein model for particle adhesive / aerodynamic removal forces and moments. For the reason explained, modifications to allow for the influence of distribution of aerodynamic removal moments are applied only to the NRG4 model whose predictions are subsequently compared for the system of moments based on the Vainhstein model with those based on that used in the R'n'R model

3.1 Vainshtein Model

In the Vainshtein model (Vainshtein *et al.*, 1997), the adhesion moment is defined in terms of the adhesive force F_a of a particle sitting on a smooth surface ($F_a = 1.5\pi\gamma r$) and the equilibrium radius r_e (contact radius) when the adhesion attraction balanced with elastic tension. The equilibrium radius is defined if only the adhesive force is dominant (Wang, 1990), as

$$r_e = \left(6\pi\gamma r^2 / \kappa\right)^{1/3} \qquad [3.1]$$

where γ is surface energy per unit contact area, r is the particle radius and κ is the elastic constant.

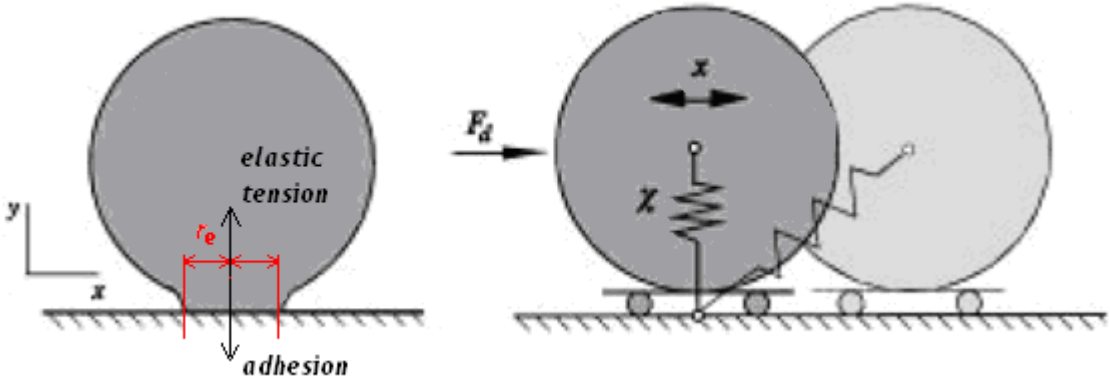

Figure 3.1 - Vainshtein nonlinear particle oscillation model (Vainshtein *et al.*, 1997)

This can be modelled using a spring to represent the attractive force, as shown in Figure 3.1. In principle, the spring stiffness (ε) should be a function of the particle displacement, decreasing from a maximum value at the equilibrium point to zero at the separation point. However, in order to simplify the problem, and to compare with the RRH model (Reeks *et al.*, 1988) it is assumed to take a constant value, obtained from the JKR adhesion model, and given by

$$\varepsilon = \frac{9}{10}\left(6\pi\gamma\right)^{1/3}\kappa^{2/3}r^{2/3} \qquad [3.2]$$

Then the maximum spring extension S_B, corresponding to detachment of the particle from the surface at point B (Figure 3.2) is given by

$$S_B = 1.96\frac{\gamma^{2/3}r^{1/3}}{\kappa^{2/3}} \qquad [3.3]$$

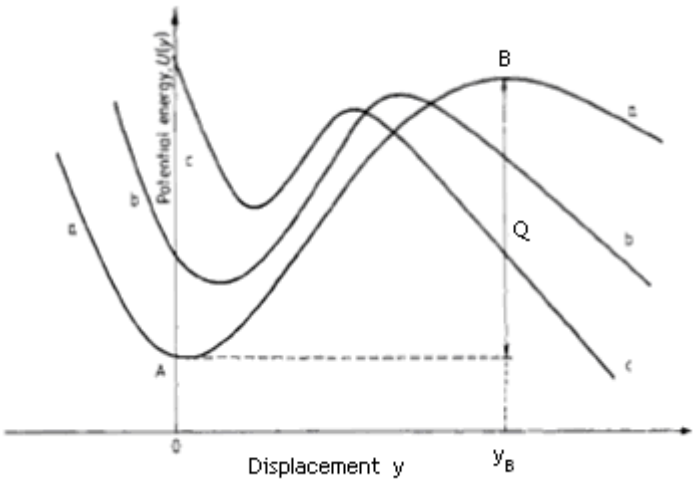

Figure 3.2 - Potential well diagram (Reeks *et al.*, 1988)

The equation of particle motion around the detachment point and the condition of small oscillations is given as follow

$$m\ddot{x} + \frac{\varepsilon}{2r^2}x^3 = F_D \qquad [3.4]$$

where m is the particle mass and x is the horizontal displacement. It is noted the damping term in caused by the transmission of elastic waves in the solid substrate is negligible at low frequencies.

The drag moment is proportional to the drag force which is defined as 1.7 times than the Stokes drag as assumed in the Rock'n'Roll model (Reeks & Hall, 2001).

$$M_D = 1.399 \cdot F_D r \qquad F_D = 1.7 \cdot 6\pi\rho_f u_\tau^{\,2} r^2 \tag{3.5}$$

where ρ_f is the fluid density and u_τ is the wall friction velocity.

The first inertial term in Eq.[3.4] is also negligible at low frequencies, so Eq.[3.4] can be simplified to

$$\frac{\varepsilon}{2r^2} x^3 = F_D \tag{3.6}$$

It is assumed that the maximum spring extension during oscillation does not exceed S_B. Therefore the maximum x-direction displacement x_B is determined approximately by

$$x_B = \sqrt{S_B^{\,2} - r^2} \approx \sqrt{2rS_B} = 1.98 \frac{\gamma^{1/3} r^{2/3}}{\kappa^{1/3}} \tag{3.7}$$

At the maximum spring extension ($x = x_B$) the driving force from the aerodynamic drag balances the tangential pull-off force, which can therefore be written, from Eq.[3.2] and Eq.[3.7], as

$$F_{a\tau} = \frac{\varepsilon}{2r^2} x_B^{\,3} = 9.3 \frac{\gamma^{4/3} r^{2/3}}{\kappa^{1/3}} \tag{3.8}$$

It has been demonstrated by Vainshtein *et al.* (1997) that the pull-off forces are smaller than the drag force, then according to the RRH model (Reeks *et al.*, 1988), the height of the potential well Q can be expressed in terms of the pull-off force by integration of $F_{a\tau}$ from zero to the maximum displacement x_B, and the potential energy <PE> can be expressed in terms of the drag force. The typical natural frequency in Vainshtein model is taken to be the same as in the RRH model.

$$\omega_0 = 0.0033 \left(\frac{u_\tau^{\,2}}{\nu_f} \right) \tag{3.9}$$

where ν_f is the fluid kinematic viscosity.

As a result, the resuspension rate constant is defined as

$$p = \omega_0 \exp\left[-\left(\frac{F_{a\tau}}{F_D} \right)^{4/3} \right] = 0.0033 \frac{u_\tau^{\,2}}{\nu_f} \exp\left[-\left(\frac{\gamma^{4/3}}{r^{4/3} \kappa^{1/3} u_\tau^{\,2} \rho_f} \right)^{4/3} \right] \tag{3.10}$$

Therefore, the fraction of particles remaining on the surface at time t is derived using the same formula as in the RRH model.

$$f_R(t) = \int_0^\infty \exp\left[-\left(p(r_a') \right) t \right] \varphi(r_a') dr_a' \tag{3.11}$$

where r_a' is the normalized asperity radius defined as the ratio of the asperity radius r_a to the particle radius r, i.e. r_a/r. The pull-off force (i.e. adhesive force) should be calculated using the

asperity radius r_a rather than the particle radius r since the adhesive force is smaller than that for a smooth surface. $\varphi(r_a')$ is the adhesive force distribution which is assumed to have a log-normal distribution with geometric mean $\overline{r}_a'$ and geometric standard deviation (adhesive spread factor) σ_a', shown in Eq.[3.18].

Komen (2007) developed two simple quasi-static resuspension models, in which the formula of the used for the adhesive moment is similar to that used in the Vainshtein model for particle adhesion to a surface. In the next section we will focus on his NRG models (named after Nuclear Research and consultancy Group, in the Netherlands).

3.2 NRG Models

The Nuclear Research and consultancy Group (NRG) recently developed two quasi-static resuspension models (Komen, 2007). The first model NRG3 is based on a quasi-static balance of the drag force and the tangential pull-off force similar to that used in the Vainshtein model. The pull-off force is computed using the asperity radius r_a, rather than the particle radius, and is given by

$$F_{a\tau} = 9.3\frac{\gamma^{4/3}\left(rr_a'\right)^{2/3}}{\kappa^{1/3}} \qquad [3.12]$$

In a similar way as in the Vainshtein model, the NRG3 model assumes that this adhesive reduction r_a' is equivalent to the ratio of the asperity radius and the particle radius.

There is a step function δ given in the NRG3 model which equals 1 when the pull-off forces ($F_{a\tau}$) exceed the drag forces (F_D). It is described as the fraction of particles (either 0 or 1) with radius r remaining on the surface asperities with normalized asperity radius r_a', in other word, if the drag force dominates ($F_D > F_{a\tau}$) all particles are resuspended from the surface.

$$\delta = \begin{cases} 0 & F_D > F_{a\tau} \\ 1 & F_D \le F_{a\tau} \end{cases} \qquad [3.13]$$

However, if the moment balance is used instead of the force balance, considering the adhesive moment from the Vainshtein model,

$$M_a = F_a r_e = 12.5\frac{\gamma^{4/3}\left(rr_a'\right)^{5/3}}{\kappa^{1/3}} \qquad [3.14]$$

the normalized asperity radius r_a' will be increased to the power of 5/3 whereas it is 2/3 in the force balance case. Since it has been demonstrated that the considered force and moment balance are equivalent, it can be concluded that the models are not fully consistent for rough surfaces. Therefore, the following pragmatic approach is considered by NRG when constructing the NRG4 particle resuspension model. This resuspension model is based on a balance of moments. In the NRG4 resuspension model, the adhesive reduction r_a' due to surface roughness is defined as the ratio of the adhesive moment on rough surface to the adhesive moment on smooth surface, see Eq.[3.16].

In the NRG4 model, the step function is determined by the relative magnitudes of the adhesion moment (M_a) and the drag moment (M_D).

$$\delta = \begin{cases} 0 & M_D > M_a \\ 1 & M_D \le M_a \end{cases} \qquad [3.15]$$

The drag moment takes the same form as that in the Vainshtein model, see Eq.[3.5]. Komen (2007) concluded that the adhesive moment of JKR adhesion model on rough surface is theoretically more correct than that in the Vainshtein model. Therefore, the adhesive moment of JKR adhesion is applied in the NRG4 model.

$$M_a = \frac{2}{3} F_a r_e r_a' = \frac{2}{3}\left(\frac{3}{2}\pi\gamma r\right)\left(6\pi\gamma r^2/\kappa\right)^{1/3} r_a' = 8.361\frac{\gamma^{4/3} r^{5/3}}{\kappa^{1/3}} r_a' \qquad [3.16]$$

Assuming that the distribution of adhesive reduction is similar to that for the Vainshtein and the Rock'n'Roll models, the particle fraction remaining on the surface is then computed as

$$f_R = \int_0^\infty \delta\varphi(r_a')dr_a' \qquad [3.17]$$

The log-normal distribution of the adhesive asperities radii in Vainshtein model is given by

$$\varphi(r_a') = \frac{1}{\sqrt{2\pi}}\frac{1}{r_a'}\frac{1}{\ln\sigma_a'}\exp\left(-\frac{\left[\ln(r_a'/\overline{r_a'})\right]^2}{2(\ln\sigma_a')^2}\right) \qquad [3.18]$$

with geometric mean $\overline{r_a'}$ (reduction factor) and geometric standard deviation (adhesive spread factor) σ_a'.

The three models – Vainshtein, NRG3 and NRG4 – have been used to compute resuspension as a function of wall friction velocity for the same conditions (Hall's experiment, Reeks & Hall, 2001) – alumina particles with three different values of diameters, $\overline{r_a'}$ = 0.027 and σ_a' = 10.4 (values obtained from Reeks & Hall, 2001 and Biasi *et al.*, 2001). The results of these calculations are plotted in Figure 3.3, Figure 3.4 and Figure 3.5. Komen concluded from the graphs that the NRG4 model predictions are in reasonable agreement with the experimental data, whereas the Vainshtein and NRG3 models yield an under prediction of the amount of resuspended particles for the selected surface roughness parameters. Therefore, the modification in next section will be based on the NRG4 model.

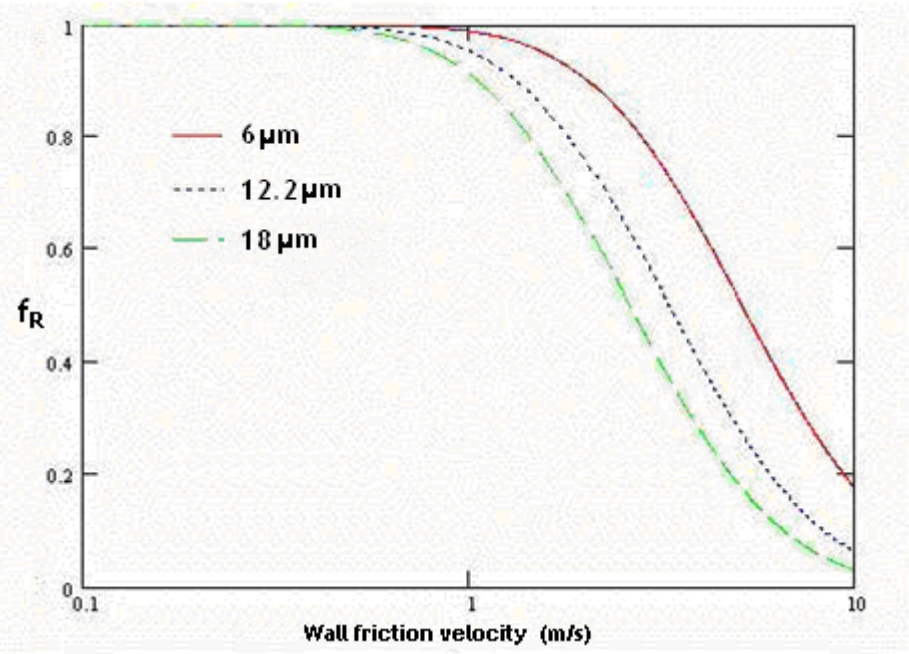

Figure 3.3 - Particle fraction remaining after 1s by the Vainshtein model (Komen, 2007)

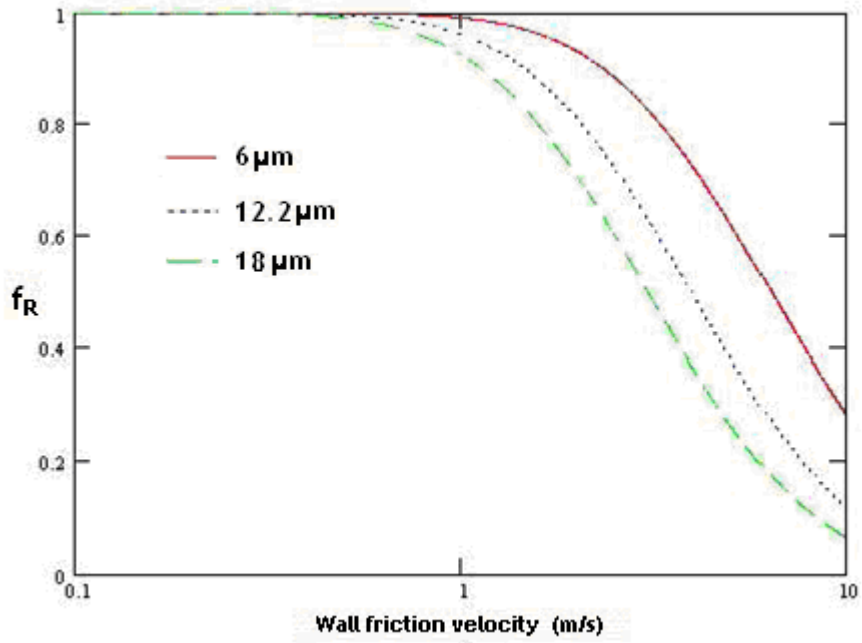

Figure 3.4 - Particle fraction remaining after 1s by the NRG3 model (Komen, 2007)

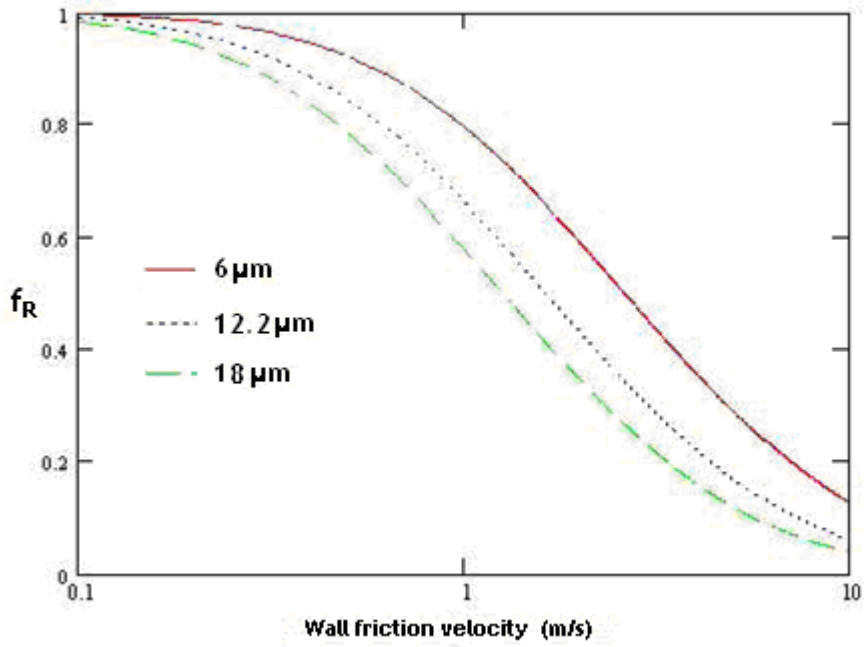

Figure 3.5 - Particle fraction remaining after 1s by the NRG4 model (Komen, 2007)

It is noted that the NRG4 model is simply based on the error function. Consider that the resuspension will occur (none left on the surface) when the drag moment exceeds the adhesive moment, for any value of friction velocity (u_τ) and particle radius resuspension will occur if

$$M_D > M_a \Rightarrow r_a' < r_{ab}' = 5.362 \frac{\rho_f}{y^{4/3}} \kappa^{1/3} r^{4/3} u_\tau^{\,2} \qquad [3.19]$$

where r_{ab}' is the normalized asperity radius when the drag moment balanced with the adhesive moment. So the step function δ becomes

$$\delta = \begin{cases} 0 & r_a' < r_{ab}' \\ 1 & r_a' \geq r_{ab}' \end{cases} \qquad [3.20]$$

Therefore, the fraction remaining on the surface is derived as

$$f_R = \int_{r_{ab}'}^{\infty} \frac{1}{\sqrt{2\pi}} \frac{1}{r_a'} \frac{1}{\ln \sigma_a'} \exp\left(-\frac{\left[\ln(r_a'/\overline{r}_a')\right]^2}{2(\ln \sigma_a')^2} \right) dr_a' \qquad [3.21]$$

Now introduce the new variable θ, let

$$\theta = \frac{\ln(r_a'/\overline{r}_a')}{\sqrt{2}\ln \sigma_a'} \quad \text{and} \quad \theta_b = \frac{\ln(r_{ab}'/\overline{r}_a')}{\sqrt{2}\ln \sigma_a'}$$

So the fraction remaining can be obtained as

$$\begin{aligned} f_R &= \int_{\theta_b}^{\infty} \frac{1}{\sqrt{\pi}} \exp\left(-\theta^2\right) d\theta = \frac{1}{2} \int_{\theta_b}^{\infty} \frac{2}{\sqrt{\pi}} \exp\left(-\theta^2\right) d\theta \\ &= \frac{1}{2}\left[1 - erf(\theta_b)\right] \end{aligned} \qquad [3.22]$$

where $\theta_b = \dfrac{\ln\left[5.362 \dfrac{\rho_f}{\gamma^{4/3} \overline{r}_a'} \kappa^{1/3} r^{4/3} u_\tau^{\,2} \right]}{\sqrt{2}\ln \sigma_a'}$.

In order to calculate the adhesive force or moment for a rough surface, in the Vainshtein and Rock'n'Roll models, the asperity radius is assumed physically much smaller than the particle radius, i.e. $r_a' \ll 1$. If $r_a' = 1$, it is considered that the particle is sitting on a smooth surface. However, the log-normal distribution generates a non-zero (although vanishing) probability for all positive values of the asperity radius so its part of the distribution inevitably consists of asperities for which $r_a' > 1$. Indeed, with the values for the geometric mean $\overline{r}_a'$ and adhesive spread factor σ_a' used in the Vainshtein and Rock'n'Roll models, a significant fraction of the asperity distribution lies outside the range $0 < r_a' < 1$. For this larger values of r_a', the particle adhesion is much closer to that for a particle on a smooth surface, so Komen (2007) modified the adhesion asperity distribution to take account of this; he introduced a truncated distribution $\varphi_t(r_a')$, with a log-normal form in the range $0 < r_a' \leq 1$, and zero outside this range.

$$\begin{aligned} 0 < r_a' \leq 1: \quad & \varphi_t(r_a') = \frac{\varphi(r_a')}{\int_0^1 \varphi(r_a') dr_a'} \\ r_a' > 1: \quad & \varphi_t(r_a') = 0 \end{aligned} \qquad [3.23]$$

It is noted that regarding of the truncated distribution, the lower limit of the integration in Eq.[3.21] becomes

$$r'_{ab} = \min\left\{5.362\frac{\rho_f}{y^{4/3}}\kappa^{1/3}r^{4/3}u_\tau^{\,2},\ 1\right\}$$

So the maximum value of θ_b for the integration occurs when $r_{ab}' = 1$,

$$\theta_{b-\max} = -\frac{1}{\sqrt{2}}\frac{\ln \bar{r}'_a}{\ln \sigma'_a} \qquad [3.24]$$

However, Komen (2007) showed that the use of a truncated log-normal distribution did not result in any significant change in resuspension fraction.

3.3 Modification of the NRG4 Model

The NRG4 model assumes that resuspension will occur when the aerodynamic moment exceeds the adhesive moment. The aerodynamic moment is obtained from the mean drag and does not include the effects of fluctuating drag or any contribution from the lift force (although the lift will not have much effect on resuspension, compared with the influence of the drag force). In reality, however, the aerodynamic drag will fluctuate, and the aerodynamic moment ought to be calculated from this fluctuating force. In this section, therefore, the NRG4 model is firstly modified to include a fluctuating aerodynamic moment (within the frame work of a quasi-static analysis) and then the aerodynamic resultant force (F) and adhesive force (f_a), as developed in the R'n'R model (Reeks & Hall, 2001) is incorporated. In both cases, the adhesive forces are assumed given by a log-normal distribution (Eq.[3.18]), and the influence of these modifications for a range of particle sizes (r) and adhesive spread factor (σ_a') is compared.

3.3.1 Part I

It is assumed that the aerodynamic moment has a Gaussian distribution, with mean $\langle M_D \rangle$ and root mean square m_D.

$$G(M) = \frac{1}{\sqrt{2\pi}\, m_D} \exp\left[-\left(\frac{M - \langle M_D \rangle}{\sqrt{2}\, m_D} \right)^2 \right] \qquad [3.25]$$

where $\langle M_D \rangle$ is given by from Eq.[3.5] and m_D is assumed to be equal to $0.2\langle M_D \rangle$, as given in the R'n'R model. Later, the influence of the ratio $\langle M_D \rangle / m_D$ on particle resuspension is investigated.

Then the fraction of particles that remains on the surface is given by

$$f_R = \int_0^\infty \int_{-\infty}^{\infty} G(M) \delta \varphi(r_a') dM dr_a' \qquad [3.26]$$

where $\delta = 0$ if $M > M_a$ and $\delta = 1$ if $M \le M_a$, and the adhesive moment is computed from Eq.[3.16].

Substituting Eq.[3.25] into Eq.[3.26],

$$f_R = \int_0^\infty \int_{-\infty}^{\infty} G(M) \delta dM \, \varphi(r_a') dr_a'$$

$$= \int_0^\infty \int_{-\infty}^{\infty} \frac{1}{\sqrt{2\pi}\, m_D} \exp\left[-\left(\frac{M - \langle M_D \rangle}{\sqrt{2}\, m_D} \right)^2 \right] \delta dM \, \varphi(r_a') dr_a' \qquad \delta = \begin{cases} 0 & M > M_a \\ 1 & M \le M_a \end{cases}$$

The aerodynamic moment distribution can be written in normalized form: $A = \dfrac{M - \langle M_D \rangle}{\sqrt{2}\, m_D}$, and

which $dA = \dfrac{1}{\sqrt{2} m_D} dM$

and $G(A) = \frac{1}{\sqrt{\pi}} \exp(-A^2) dA$

Therefore,

$$f_R = \int_0^{\infty} \int_{-\infty}^{\infty} \frac{1}{\sqrt{\pi}} \exp(-A^2) \delta \, dA \, \varphi(r_a') dr_a'$$

Since *G(A)* is symmetric along 0, then

$$f_R = \int_0^{\infty} 2 \int_0^{\infty} \frac{1}{\sqrt{\pi}} \exp(-A^2) \delta dA \, \varphi(r_a') dr_a'$$

The step function δ define the domain of integration, so the upper limit for the integration is given by

$A_0 = \frac{M_a - \langle M_D \rangle}{\sqrt{2}\, m_D}$ from which

$$f_R = \int_0^{\infty} 2 \int_0^{A_0} \frac{1}{\sqrt{\pi}} \exp(-A^2) dA \, \varphi(r_a') dr_a'$$

Finally, the fraction of particle remaining on the surface (f_R) is given by

$$f_R = \int_0^{\infty} erf\left(\frac{M_a - \langle M_D \rangle}{\sqrt{2} m_D} \right) \varphi(r_a') dr_a' \qquad [3.27]$$

where M_a depends on r_a', as given by Eq.[3.16]. The numerical method of calculating Eq.[3.27] is shown in Appendix 2 (p202). The resuspension fraction shown later in all figures is defined as ($1-f_R$).

The normalized asperity radius (r_a') is assumed to have a log-normal distribution, as given by Eq.[3.18]; to examine the influence of the fluctuating drag force we have performed simulations with a mean value (also called 'reduction') $\overline{r_a'}$ = 0.01 and three different spread factors σ_a'. For one of these the Biasi's correlation (Biasi *et al.*, 2001), which based on resuspension experiments (Reek & Hall, 2001), is used.

$$\sigma_a' = 1.8 + 0.136(r \times 10^6)^{1.4} \qquad [3.28]$$

Biasi's correlation values for 2µm, 10µm and 20µm particles (diameter) are given below

	2µm	10µm	20µm
σ_a'	1.936	3.094	5.216

The results are plotted in Figure 3.6, Figure 3.7 and Figure 3.8. The models will be noted as NRG4 and NRG4 modified.

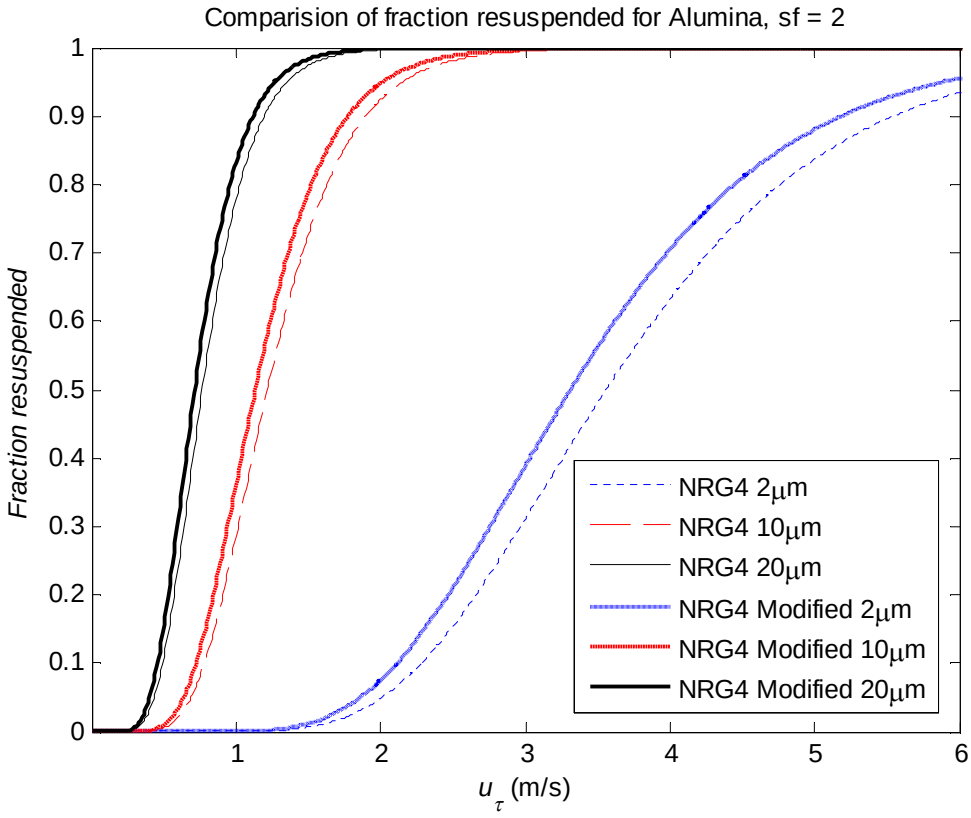

Figure 3.6 - Comparison of NRG4 and modified NRG4 with spread factor = 2

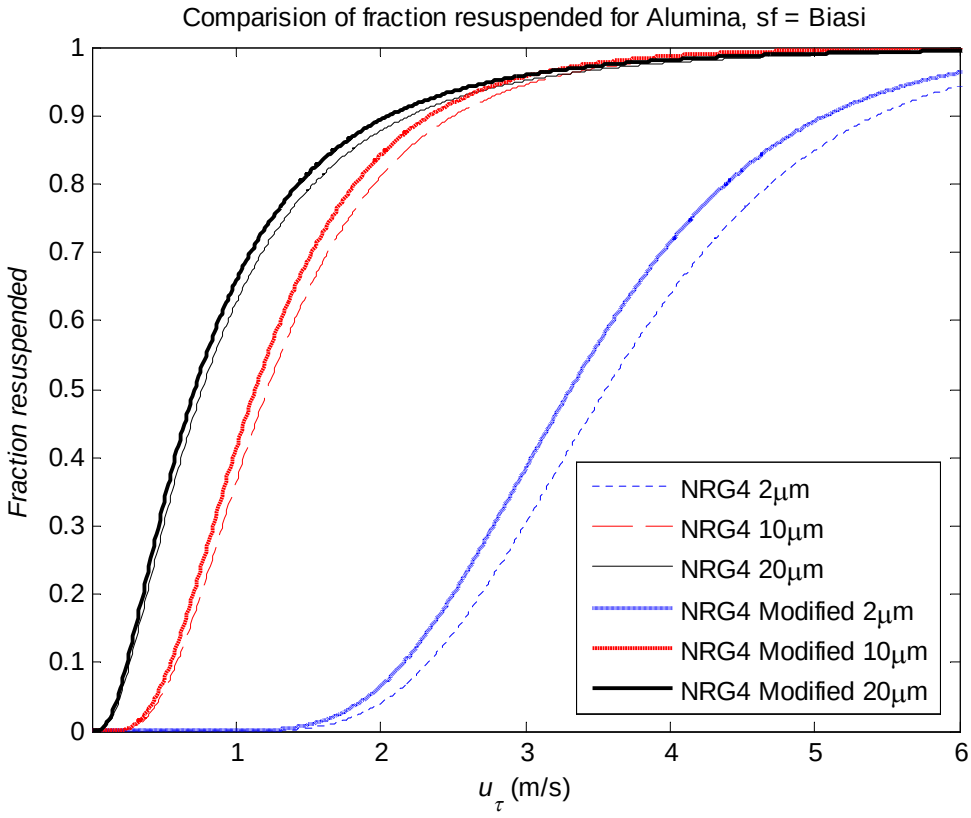

Figure 3.7 - Comparison of NRG4 and modified NRG4 with spread factor = Biasi

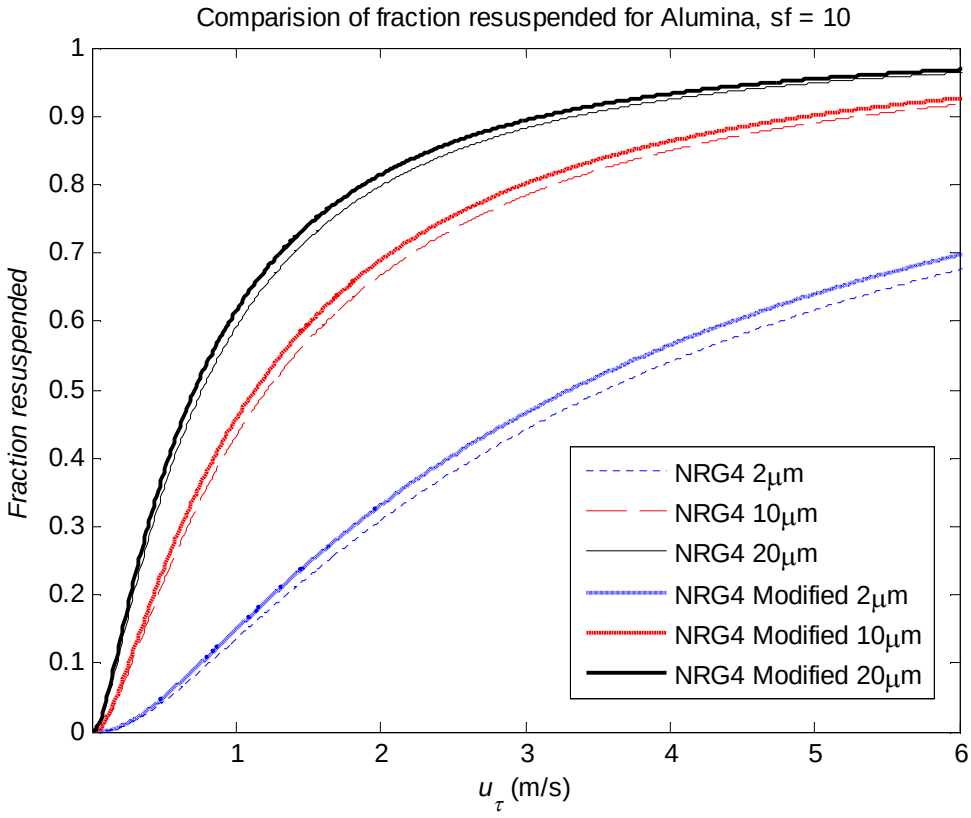

Figure 3.8 - Comparison of NRG4 and modified NRG4 with spread factor = 10

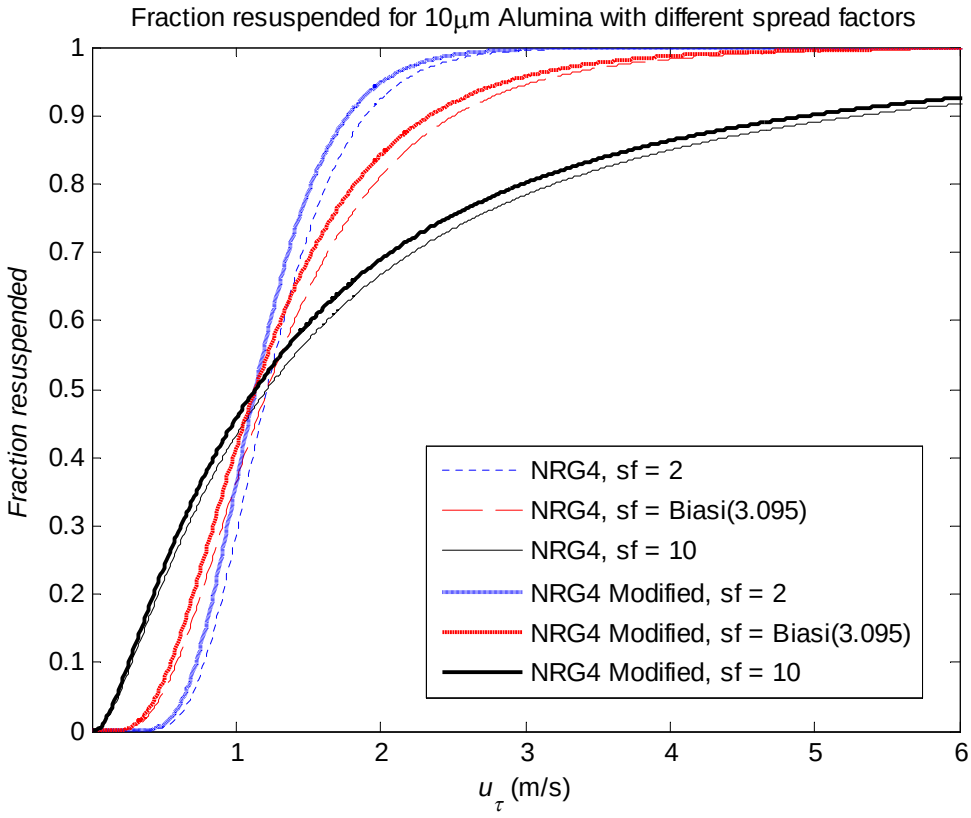

Figure 3.9 - Comparison of NRG4 and modified NRG4 for 10μm particle

A comparison of these figures shows that in all cases the inclusion of the fluctuating drag increases the fraction resuspended, as might be expected. This effect is most evident for the smallest particles (particularly 2μm) and for the lowest spread factors – in fact there is very little difference between the value computed by Biasi's correlation (for 10μm particles) and the assumed value of 2.

The influence of the spread factor on the resuspension fraction is illustrated in Figure 3.9 for 10μm alumina particles, and 3 values of spread factors. All three curves intersect at the point where the resuspension fraction is equal to 0.5, and this is therefore independent of the spread factor. Consider Eq.[3.22], the resuspension remaining by the NRG4 model can be rewritten as

$$f_R = \int_{\theta_b}^{\infty} \frac{1}{\sqrt{\pi}} \exp\left(-\theta^2\right) d\theta = \frac{1}{2} \int_{\theta_b}^{\infty} \frac{2}{\sqrt{\pi}} \exp\left(-\theta^2\right) d\theta$$

$$= \frac{1}{2}\left[1 - erf(\theta_b)\right]$$

where $\theta_b = \dfrac{\ln\left[5.362 \dfrac{\rho_f}{\gamma^{4/3} \overline{r}_a'} \kappa^{1/3} r^{4/3} u_\tau^{\,2}\right]}{\sqrt{2} \ln \sigma_a'}$.

Now when $f_R = 0.5$, $\theta_b = 0$, then the friction velocity to resuspend 50% of the particles is derived as

$$u_{\tau 50} = \sqrt{\frac{1}{5.362} \frac{\gamma^{4/3}}{\rho_f \kappa^{1/3}} \frac{\overline{r}_a'}{r^{4/3}}} \qquad [3.29]$$

from which the friction velocity necessary to resuspend 50% of the particles is computed

$$u_{\tau 50} = 1.215\ m \cdot s^{-1}$$

It is important to emphasize that this is independent of the spread factor, since this also explains the influence of the spread factor for resuspension fraction less than or greater than 50%.

For friction velocities less than $u_{\tau 50}$, increasing the spread factor increases the fraction resuspended, whereas for friction velocities greater than $u_{\tau 50}$ an increase in spread factor leads to a drop in the fraction resuspended. The spread factor affects the fraction resuspended because it determines the lower limit of integration for the particle size distribution.

$$\theta_b = \frac{\ln(r_{ab}'/\overline{r}_a')}{\sqrt{2} \ln \sigma_a'}$$

The limiting value of the normalized asperity radius r_{ab}' is determined by the balance of adhesive and aerodynamic moments and depends on u_τ and particle radius, but not on the spread factor (Eq.[3.19]). The geometric mean normalized asperity radius $\overline{r}_a'$ does not vary in these calculations, so increasing the spread factor σ_a' leads to a decrease on the integration limit θ_b. At first sight it might be thought that decreasing the lower limit of integration should inevitably lead to an increase in the integral of fraction remaining (f_R), and hence a reduction in the fraction resuspended ($1-f_R$). But for $u_\tau < u_{\tau 50}$, resuspension fraction is < 0.5 and the lower limit of integration is negative (because $r_{ab}' < \overline{r}_a'$). So decreasing the value of θ_b moves it closer to zero, and hence decreases the integral.

Of course, once $r_{ab}' > \overline{r}_a'$ ($u_\tau > u_{\tau 50}$) then the lower limit becomes positive, and increasing σ_a' does indeed result in an increase in f_R (decrease in fraction resuspended).

Physically, this can be explained by the way the log-normal distribution changes with the spread factor. The median value of the log-normal distribution used in these simulations occurs at $r_a' = \overline{r}_a'$ and the modal value (the peak) occurs at $\overline{r}_a' \Big/ \exp\left[\left(\ln \sigma_a'\right)^2\right]$. Note that the median is independent of the spread factor, but the mode – the peak – decreases as σ_a' increases (it shifts towards $r_a' = 0$, and the peak value of the frequency distribution decreases). Now for $u_\tau < u_{\tau 50}$, $r_{ab}' < \overline{r}_a'$, and only asperities with normalized radii between zero and r_{ab}' contribute to resuspension ($1-f_R$), so as σ_a' increases, the peak in the distribution shifts towards $r_a' = 0$ and the proportion of asperities in the region $0 < r_a' < r_{ab}'$ increases, so the resuspension fraction increases. See diagram below

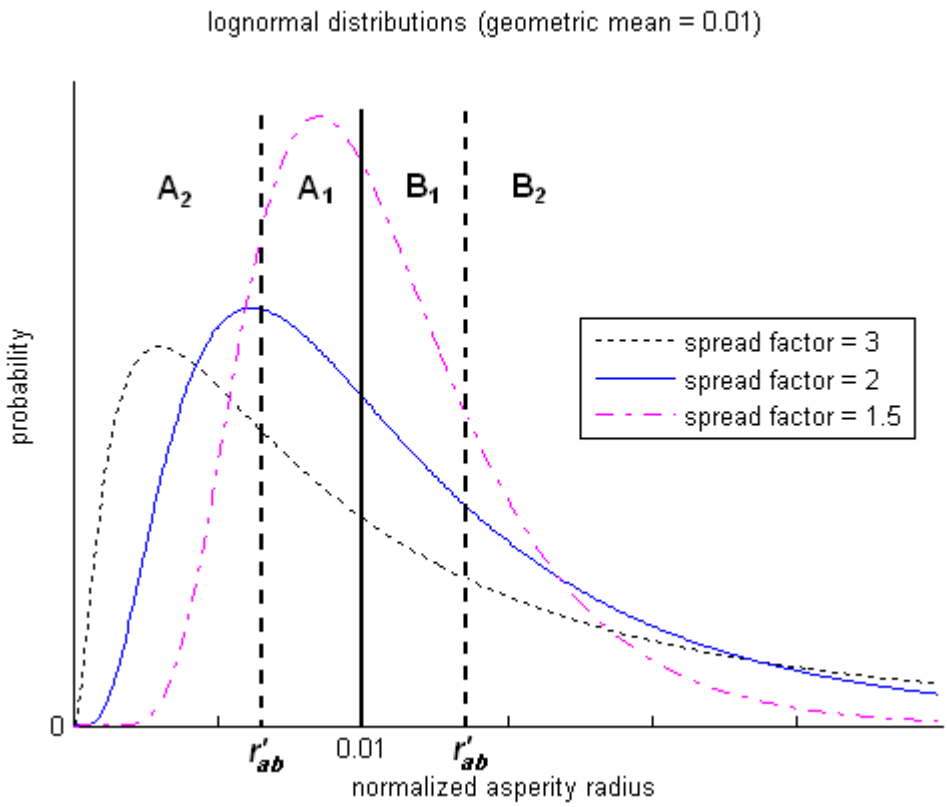

Figure 3.10 - Log-normal distributions with different spread factors

- $A_1 + A_2 = 0.5$ as σ_a' increases A_1 decreases, so A_2 must increase.
- $B_1 + B_2 = 0.5$ as σ_a' increases B_1 decreases, so B_2 must increase.

More information and discussion is shown in Appendix 1 (p200).

If the limiting asperity radius is greater than $\overline{r}_a'$ then as σ_a' increases the proportion of asperities in the tail of the distribution increases, and the proportion of asperities with radii less than r_{ab}' decreases, so increasing the spread factor decreases the fraction resuspended.

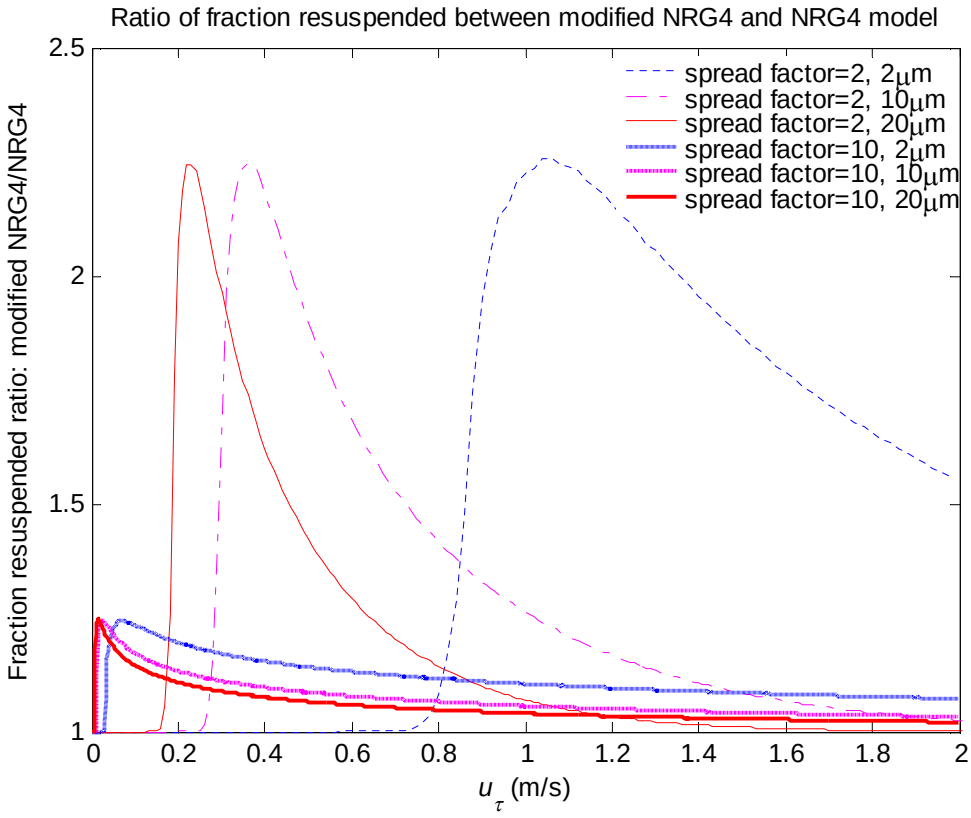

Figure 3.11 - Resuspension ratio of the modified NRG4 to NRG4 model for different spread factors

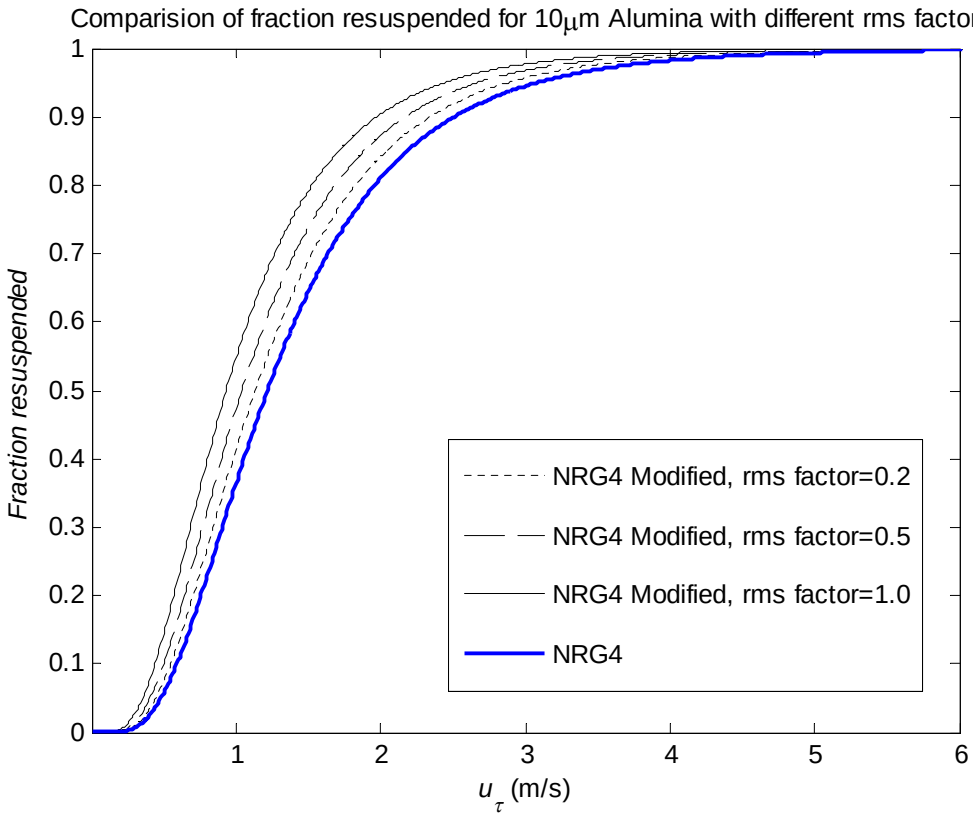

Figure 3.12 - Comparison of NRG4 and modified NRG4 with different rms factor

In order to identify more clearly the influence of the fluctuating drag moment, the ratio of the fraction resuspended in the modified NRG model to the fraction resuspended in the NRG4 model is plotted, for 2μm, 10μm and 20μm particles, and for two spread factors – 2 and 10. The results are shown in Figure 3.11. The fluctuating drag has the biggest effect at low friction velocities and low spread factors. The ratio of the three resuspended fractions seems independent of the particle size.

The influence of the rms coefficient (0.2 in the modified NRG model) of the fluctuating force is illustrated in Figure 3.12 and Figure 3.13; the fraction of particles resuspended increases as the rms factor of the fluctuating moment increases, as might be expected, and the effect is greatest at the low value of u_τ (shown in Figure 3.13). It should be noted that the largest value of the rms coefficient (which corresponds to m_D = <M_D>) is much larger than anything likely to be encountered in practice.

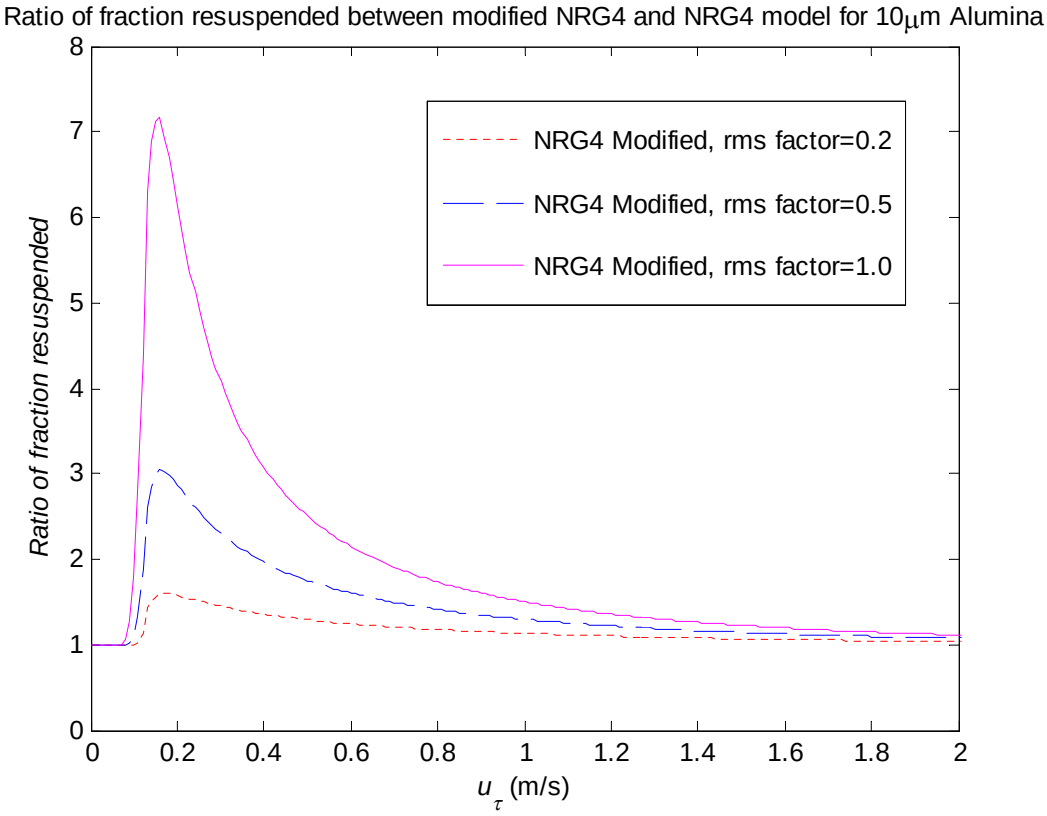

Figure 3.13 - Resuspension ratio of the modified NRG4 to NRG4 model for different rms factors

These are the parameters used in Part I,

$\rho_f = 1.181\ kg \cdot m^{-3}, \quad y = 0.56\ J \cdot m^{-2}, \quad \overline{r_a'} = 0.01$

$\kappa = 1.915 \times 10^{11} Pa$

3.3.2 Part II

This section describes a new model which based on the NRG4 model but with a new moment system that as used in R'n'R model (Reeks & Hall, 2001), which is referred as NRG4-RNR model. Then the model is modified by including the fluctuating aerodynamic forces, which is referred as modified NRG4-RNR model. Reeks and Hall's (2001) method of deriving mean aerodynamic resultant force is applied.

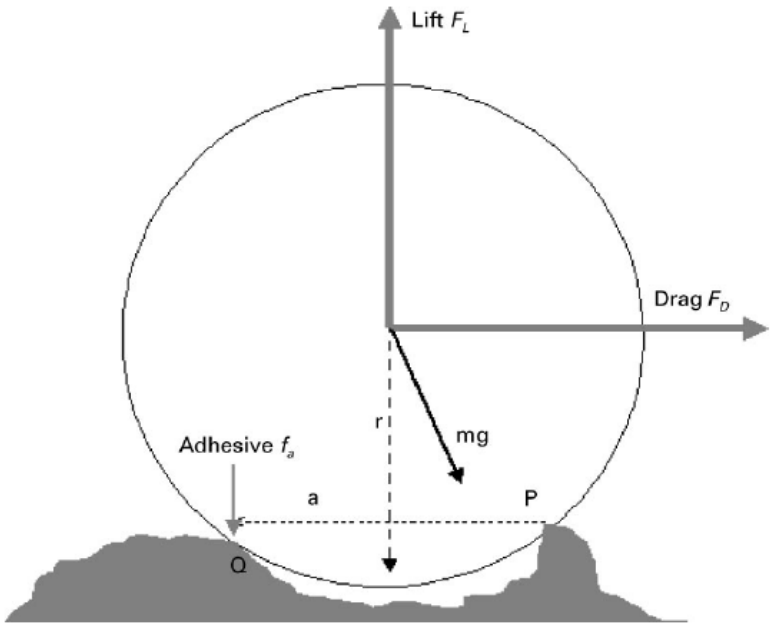

Figure 3.14 - Rock'n'Roll model geometry (Reeks & Hall, 2001)

The basic configuration is shown in Figure 3.14; a spherical particle, radius r, is supported on two asperities, with contact points O and P separated by a distance a. The drag and lift forces, F_D and F_L, act through the centre of the particle, and the adhesive force F_A acts vertically downwards at O.

The couple of the system about P is that given by

$$\Gamma = \frac{a}{2}F_L + \sqrt{r^2 - \left(\frac{a}{2}\right)^2}F_D \qquad [3.30]$$

Assuming that $r/a \gg 1$, the resultant aerodynamic force F is derived as

$$F = \frac{\Gamma}{a} = \frac{1}{2}F_L + \sqrt{\left(\frac{r}{a}\right)^2 - \frac{1}{4}}F_D \approx \frac{1}{2}F_L + \frac{r}{a}F_D \qquad [3.31]$$

The ratio r/a is thought to be typically of the order of 100 (Reeks & Hall, 2001). Then it is assumed that the resultant aerodynamic force F is fluctuating, and can be modelled by a Gaussian distribution with the mean $\langle F \rangle$ and the rms fluctuating component f.

$$G(F) = \frac{1}{\sqrt{2\pi}\,f}\exp\left[-\left(\frac{F - \langle F \rangle}{\sqrt{2}\,f}\right)^2\right] \qquad [3.32]$$

The mean aerodynamic force is derived based on Eq.[3.30]. The fluctuating component is defined as a rms coefficient times the mean, the rms coefficient is 0.2 as suggested by Reeks and Hall (2001).

$$\langle F \rangle = \frac{1}{2}\langle F_L \rangle + \frac{r}{a}\langle F_D \rangle \qquad f = 0.2\langle F \rangle \tag{3.33}$$

The effect of modifying the rms factor will be investigated later. Following Reeks and Hall (2001), the mean drag and lift force are defined as

$$\langle F_D \rangle = 32\rho_f \nu_f^{\,2}\left(\frac{r u_\tau}{\nu_f}\right)^2 \qquad \langle F_L \rangle = 20.9\rho_f \nu_f^{\,2}\left(\frac{r u_\tau}{\nu_f}\right)^{2.31} \tag{3.34}$$

The drag force is based on the principle of Stokes drag on a small particle, radius r, immersed in the viscous sub-layer.

The adhesion moment is derived following Figure 3.14 and the adhesive force f_a is simply defined based on scaling on the adhesive force for the smooth contact surface F_a in the JKR model, as below

$$M_a = f_a a = F_a r_a' a = \frac{3}{2}\pi\gamma r r_a' a \tag{3.35}$$

Then the particle fraction remaining of the surface, according to NRG model, is obtained as

$$f_R = \int_0^\infty \int_{-\infty}^{\infty} G(F)\delta dF\ \varphi(r_a')dr_a' \tag{3.36}$$

The derivation is similar as that derives Eq.[3.27], then

$$f_R = \int_0^\infty erf\left(\frac{f_a - \langle F \rangle}{\sqrt{2}f}\right)\varphi(r_a')dr_a' \tag{3.37}$$

As in Part I, the mean normalized asperity radius is set equal to 0.01 and the resuspension fraction is computed as a function of u_τ for different spread factors.

Figure 3.15, Figure 3.16 and Figure 3.17 show the resuspension fraction as a function of friction velocity for three different particle diameters (2μm, 10μm and 20μm) and different adhesive spread factors (2, Biasi and 10). In all cases, curves are plotted for the NRG4-RNR model and for the modified NRG4-RNR model. The results are similar in form to those obtained with the NRG4 model (Figure 3.6, Figure 3.7 and Figure 3.8) although the actual fraction resuspended is sensitive to the lift-off model. This is discussed in detail later. The curves all show that including the influence of fluctuations in the lift-off force results in an increase in the fraction resuspended, and this increase is most noticeable for the smallest particle diameter (2μm); even in that case, the increase in resuspension fraction over most of the curve is of the order of 10%. This is evident from the graph in Figure 3.19 of the ratio of resuspended fractions for the two conditions. At very low friction velocities the ratio reaches a maximum of about 2.2 – very similar to that obtained in the earlier simulation (Figure 3.11) – but the actual fraction resuspended at such a low friction velocity is so small that this amplification is not really practically significant.

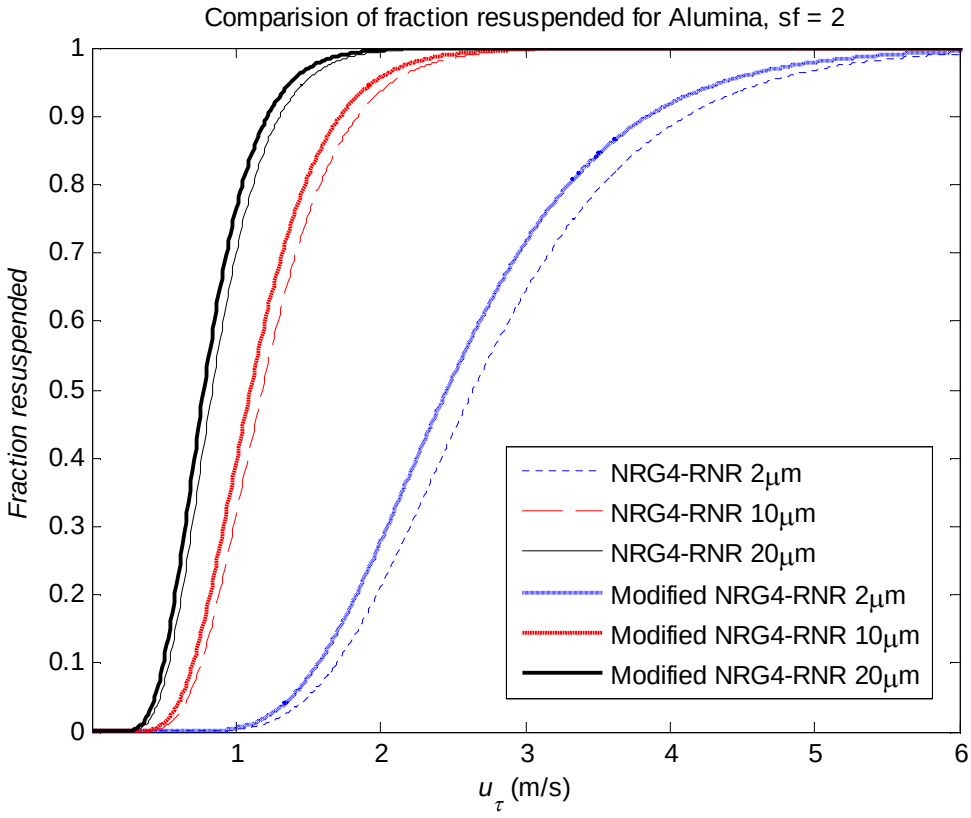

Figure 3.15 - Comparison of NRG4-RNR and modified NRG4-RNR with spread factor = 2

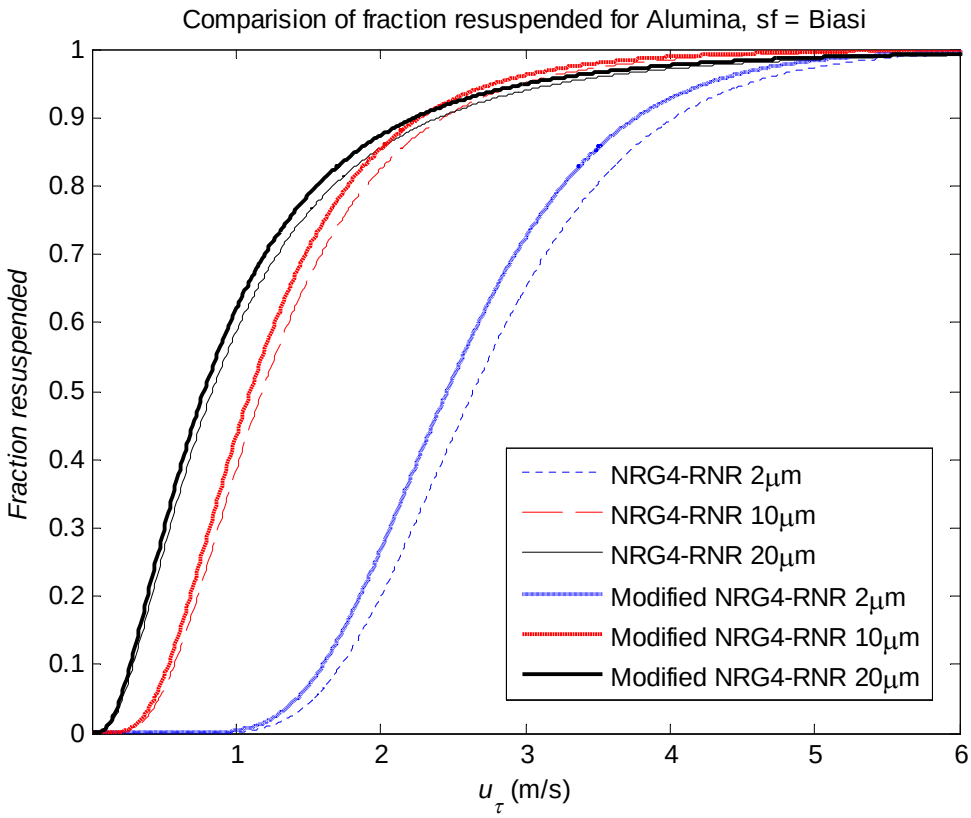

Figure 3.16 - Comparison of NRG4-RNR and modified NRG4-RNR with spread factor = Biasi

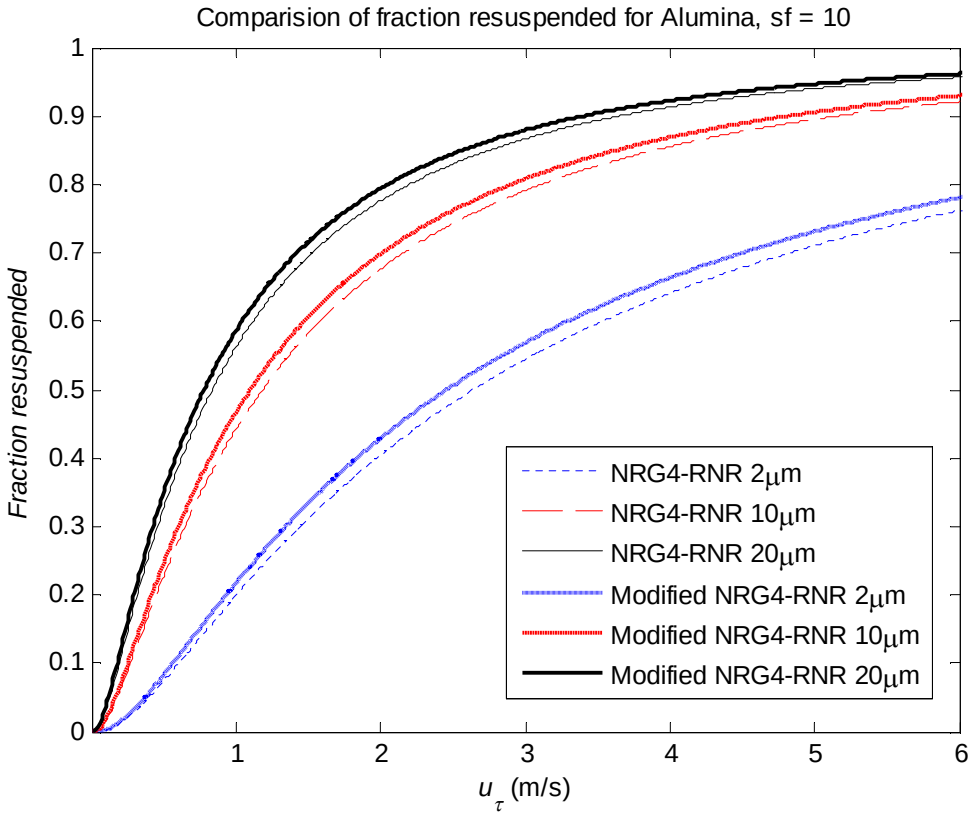

Figure 3.17 - Comparison of NRG4-RNR and modified NRG4-RNR with spread factor = 10

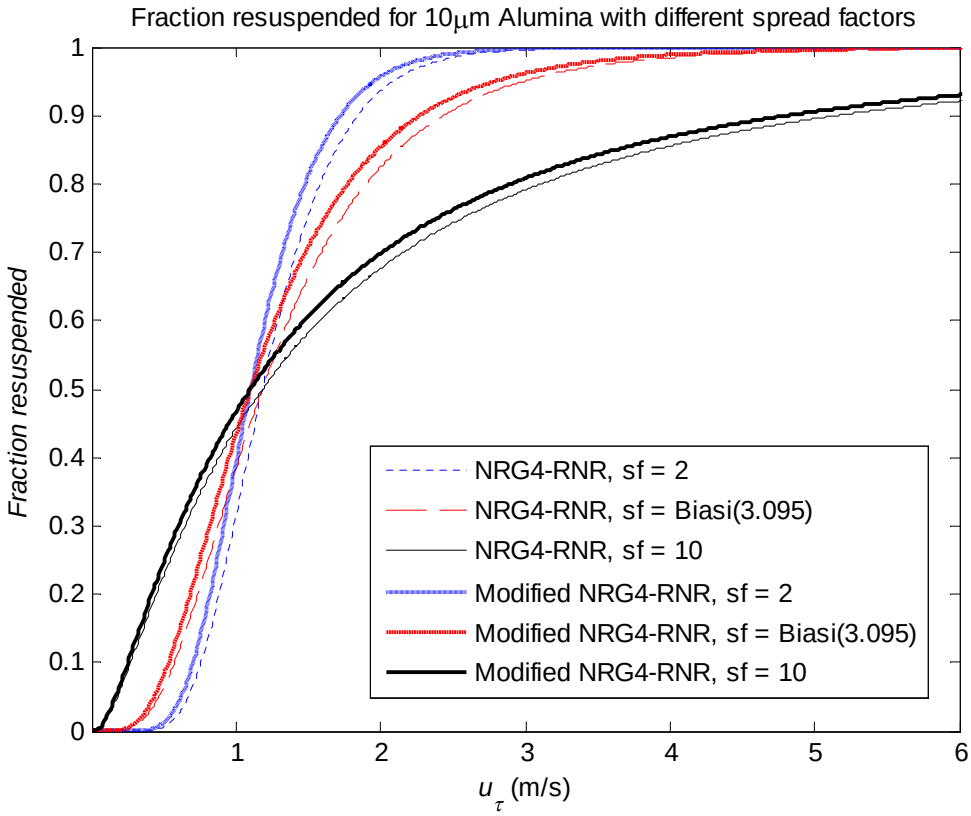

Figure 3.18 - Comparison of NRG4-RNR and modified NRG4-RNR for 10μm particle

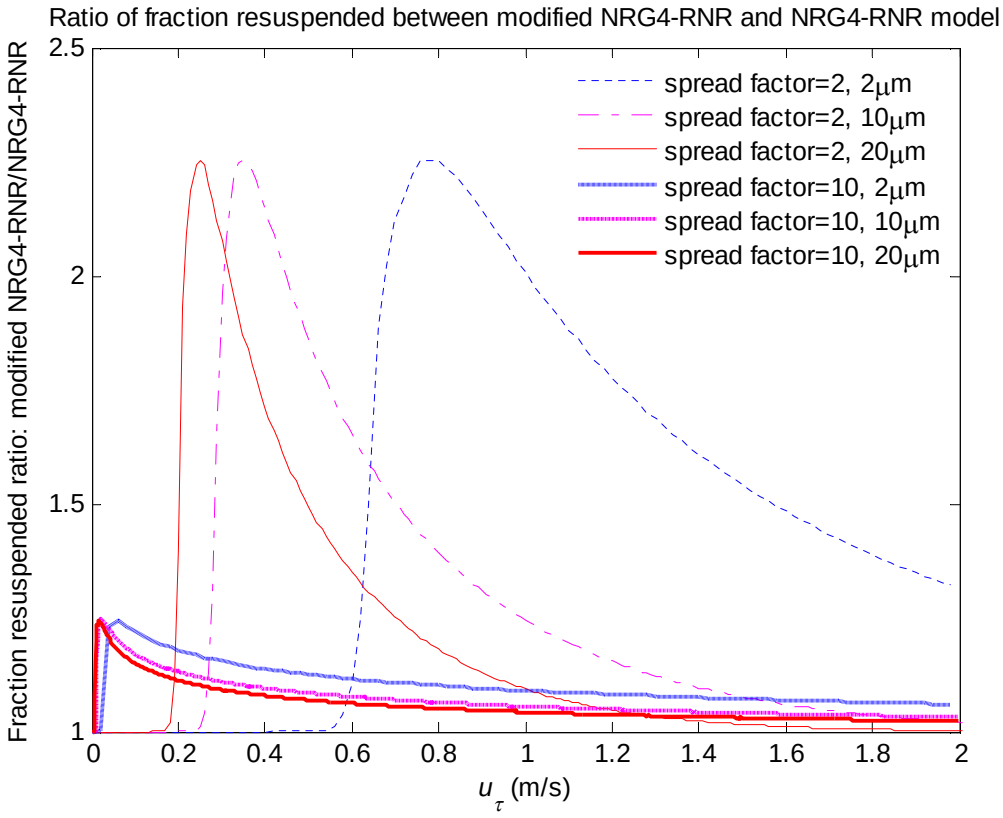

Figure 3.19 - Ratio of resuspension fraction between the modified NRG4-RNR and NRG4-RNR model

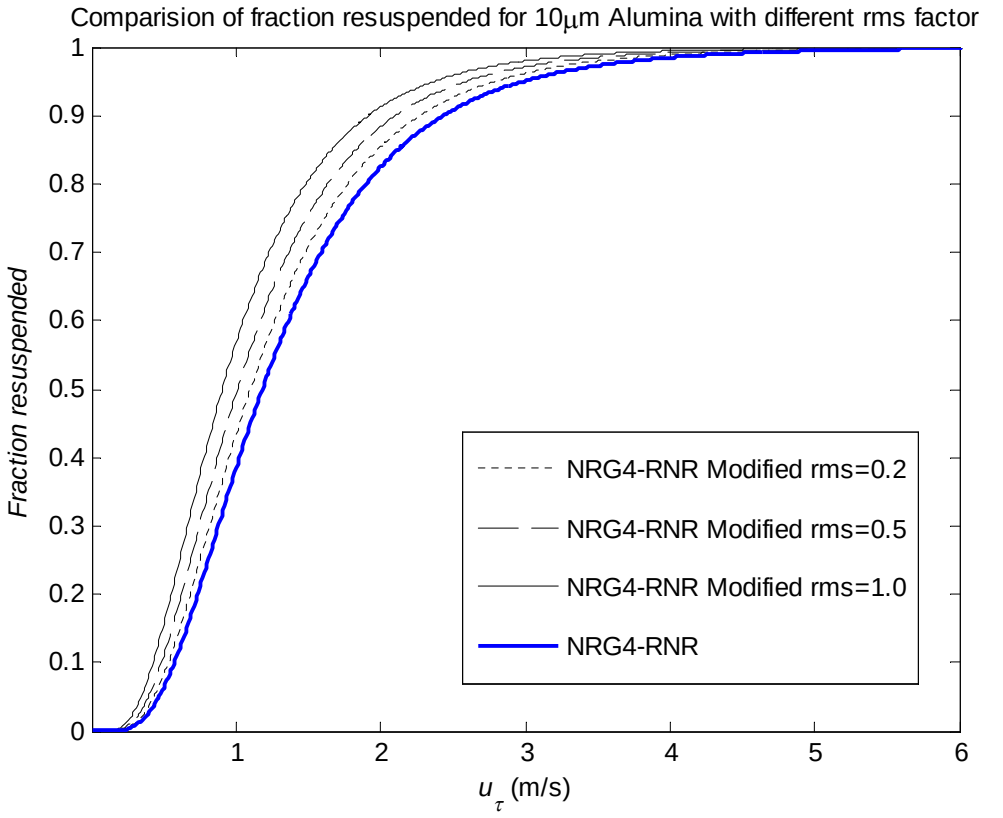

Figure 3.20 - Comparison of NRG4-RNR and modified NRG4-RNR with different rms factor

The influence of the level of fluctuation in the aerodynamic force has been investigated by simulating one case (particle diameter = 10μm; spread factor = Biasi) for several different values of the rms coefficients, and the results are shown in Figure 3.20. This shows that the additional resuspension caused by fluctuations in the aerodynamic force is really rather small when the rms coefficient = 0.2, and only seems to become significant for the rms coefficient > 0.5. This corresponds to a very high lead of fluctuation – much higher than would be encountered in practice. The effect of rms coefficient on particle resuspension is further studied in next the Chapter.

The four models NRG4, NRG4 modified, NRG4-RNR and NRG4-RNR modified have been compared for spread factors of 2 and 10, and the results are plotted in Figure 3.21 and Figure 3.22. These show that the resuspension fraction for large particles (diameter 20μm) is fairly insensitive to the choice of model, but that the resuspension fraction of small particles is much more sensitive to the resuspension model. But for both values of spread factor the choice of lift off model (NRG4-RNR) has much more influence than the inclusion (or not) of a fluctuating lift-off force.

It is noted that as particle size increases the tendency between the models using NRG4 moment system (NRG4, NRG4 modified) and the models using R'n'R moment system (NRG4-RNR, NRG4-RNR modified) is reversed. The reason of this is from the difference between the moment systems of these models. In order to study this, now consider the different moment systems in the NRG4 and NRG4-RNR models

$$M_a = 8.361\frac{\gamma^{4/3}r^{5/3}}{\kappa^{1/3}}r'_a, \quad M_D = 1.399\cdot 1.7\cdot 6\pi\rho_f u_\tau^{\,2} r^3 \qquad \text{NRG4 System}$$

$$M_a = \frac{3}{2}\pi\gamma r r'_a a, \quad \Gamma = \frac{a}{2}\langle F_L\rangle + r\langle F_D\rangle \qquad \text{R'n'R System}$$

When aerodynamic moment balances with the adhesive moment, the normalized asperity radii in balanced state for both systems are derived as

$$r'_{a-RnR} = \langle F\rangle \Big/ \frac{3}{2}\pi\gamma r, \quad r'_{a-NRG} = M_D \Big/ 8.361\frac{\gamma^{4/3}r^{5/3}}{\kappa^{1/3}} \qquad [3.38]$$

Then according to Eq.[3.22], the fractions remaining on the surface for both the NRG4-RNR and NRG4 models are derived as

$$f_{R-RNR} = \frac{1}{2}\left[1-erf(\theta_b)\right], \quad \theta_b = \frac{\ln\left[r'_{a-RnR}/\overline{r}'_a\right]}{\sqrt{2}\ln\sigma'_a}$$

$$f_{R-NRG} = \frac{1}{2}\left[1-erf(\theta_b)\right], \quad \theta_b = \frac{\ln\left[r'_{a-NRG}/\overline{r}'_a\right]}{\sqrt{2}\ln\sigma'_a}$$

The ratio of the fraction remaining between the NRG4-RNR and NRG4 model is plotted in Figure 3.23. The figure show that ratio = 1 as particle size is around 6μm. As particle size is greater than 6μm, the model with R'n'R moment system (NRG4-RNR) starts resulting more particles remaining on the surface.

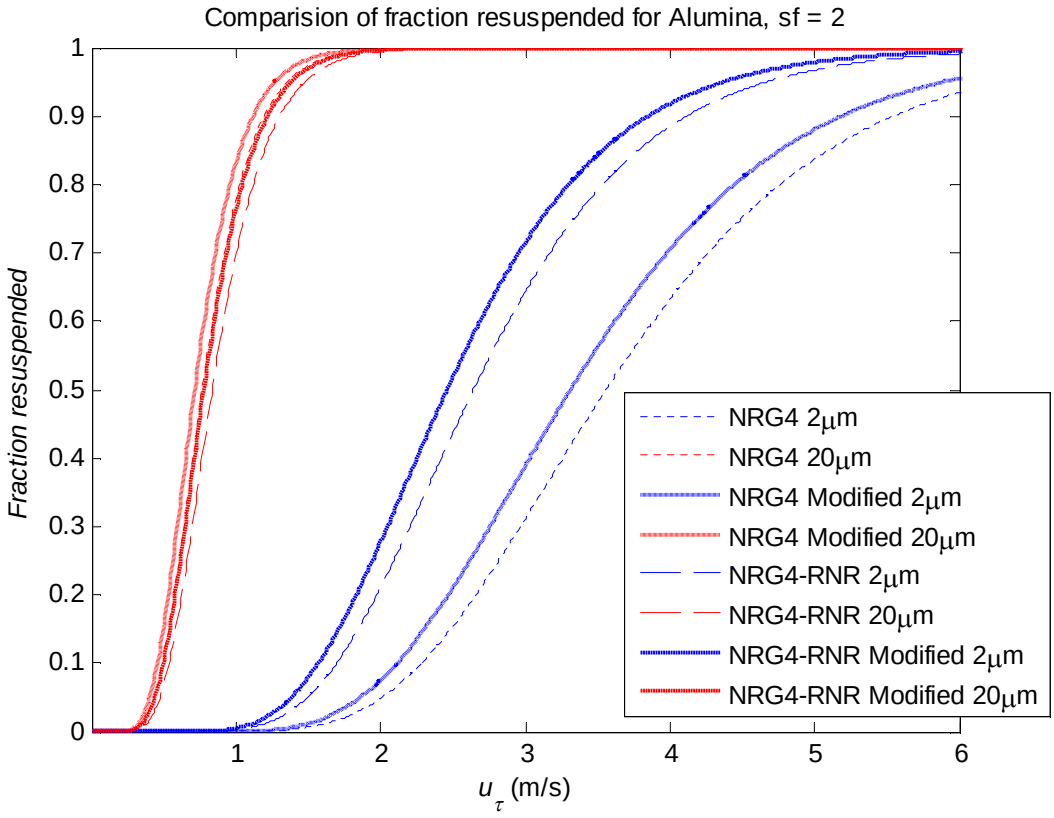

Figure 3.21 - Comparison of NRG4 and NRG4-RNR models with spread factor = 2

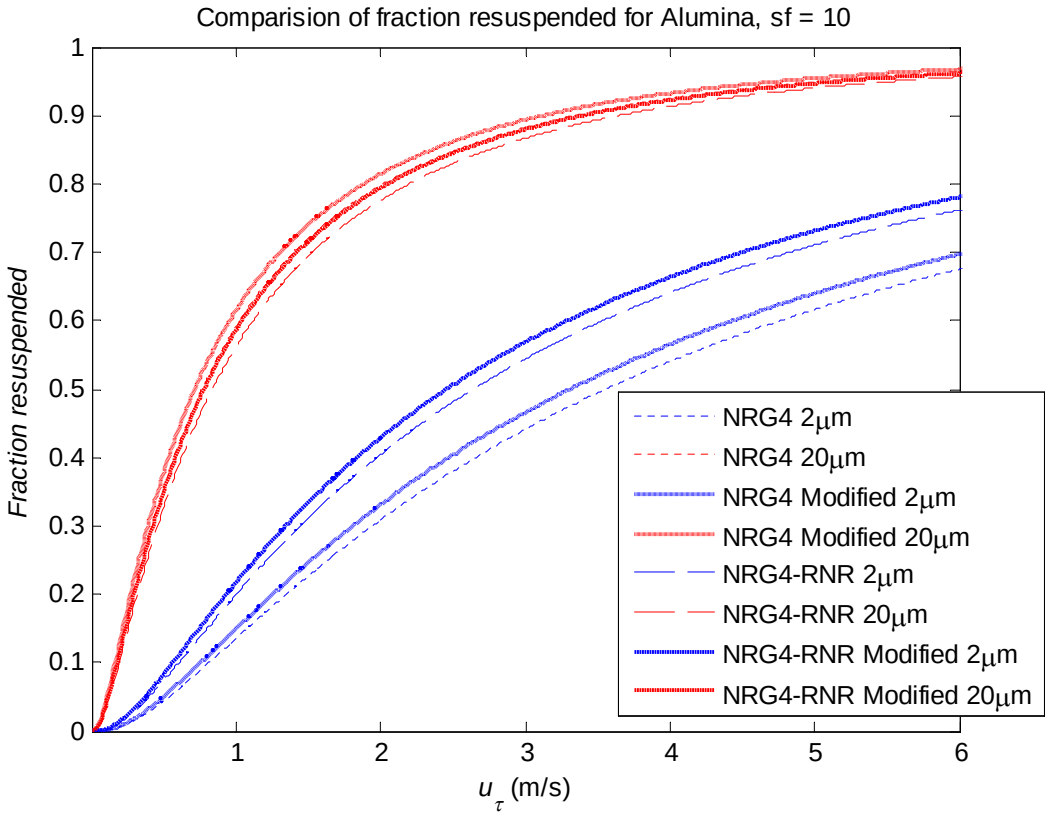

Figure 3.22 - Comparison of NRG4 and NRG4-RNR models with spread factor = 10

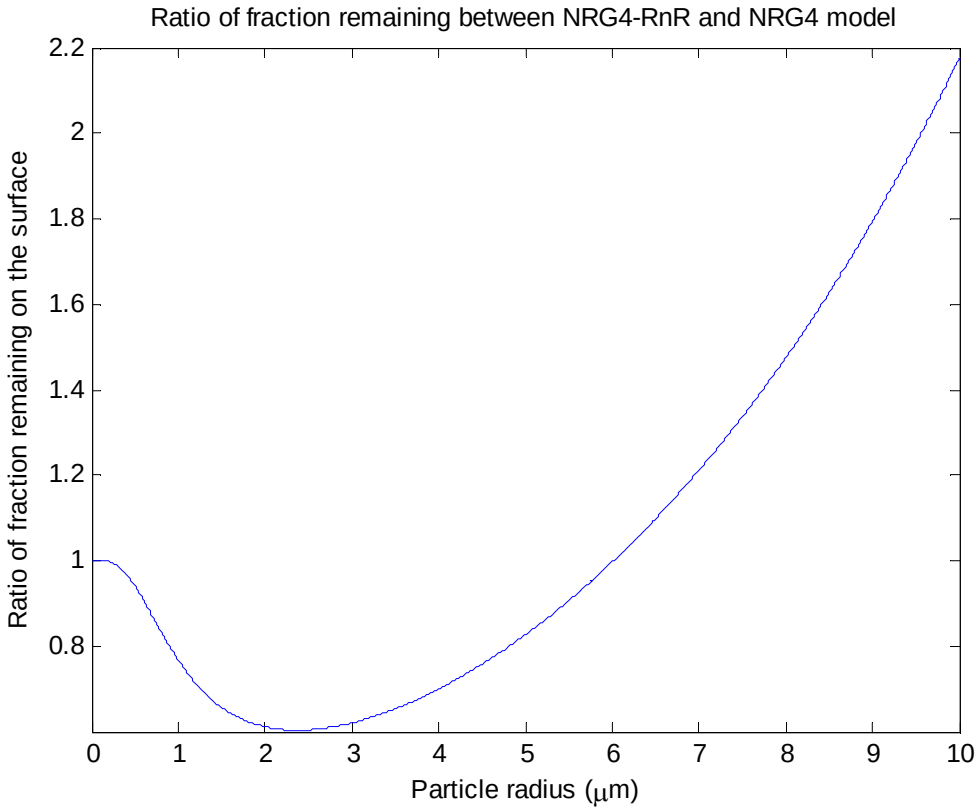

Figure 3.23 - Comparison of the moment system between R'n'R and NRG4 model

These are the parameters used in Part II,

$\rho_f = 1.181\, kg \cdot m^{-3}, \quad \gamma = 0.56\, J \cdot m^{-2}, \quad \overline{r}_a' = 0.01$

$v_f = 1.539 \times 10^{-5} m^2 \cdot s^{-1}$

3.4 Conclusion and Discussion

In this chapter, the Vainshtein's model and NRG models have been reviewed and compared via their predictions for the resuspension fraction. The effect of various possible improvements to the NRG4 model has been investigated, and quantified for a range of practical conditions. The different effects that have been studied include

- the form of the aerodynamic removal force and the force (or moment) balance at particle removal from a surface
- the influence of the fluctuating aerodynamic removal force

In all case the asperity radius is assumed to have a log-normal distribution.

Inclusion of the influence of fluctuating removal forces has little influence on the resuspension fraction for large particles (diameter ~ 20μm), and is independent of the spread factor. Smaller particles (diameter ~ 2μm), however, are much more sensitive to this inclusion and it has more influence than the fluctuations in the aerodynamic drag force. Increasing the spread factor decreases the resuspension fraction, for strong flows and increases the resuspension fraction for low flows; this is at least partly due to the assumption of a log-normal distribution for the normalized asperity radius.

Chapter 4
Modification on the Rock'n'Roll Model

The sciences do not try to explain, they hardly even try to interpret, they mainly make models. By a model is meant a mathematical construct which, with the addition of certain verbal interpretations, describes observed phenomena. The justification of such a mathematical construct is solely and precisely that it is expected to work.

- John Von Neumann

In this Chapter, the modification of the Rock'n'Roll (R'n'R) model will be presented and the impact this has upon the resuspension predictions examined and discussed. We begin by giving a brief description of the original R'n'R model as described in Reeks and Hall (2001). We then follow that with a description of the aerodynamics removal forces and how their statistics was obtained from LES and DNS measurements of turbulent velocities in a fully developed boundary layer. We show how these statistics are incorporated into a new improved R'n'R model and in particular the effect they have on the model predictions for resuspension compared to the original model.

The R'n'R model presented by Reeks and Hall (2001) is an energy accumulation resuspension model. In which particles on a surface are considered to be resuspended when they have accumulated enough kinetic energy to be detached from the surface. This energy accumulation can take place at the natural frequency of the particle-surface deformation (resonant energy transfer) or at the forcing frequency of the fluctuating aerodynamic force acting on the particles at the surface referred to as the quasi static case. In particular, this means that the particle motion is approximated by a force balance (or moment balance if the couples of the system are considered) between aerodynamic force and adhesive force. The quasi-static case is widely used in practice instead of the case considered in the original R'n'R model where both resonant energy and quasi static cases are included e.g. as in the nuclear severe accident analysis code, i.e. SOPHAEROS (Cousin *et al.*, 2008) and AERORESUSLOG (Guentay *et al.*, 2005); this neglect of resonant energy transfer is not only due to a reduction of computational time, but also the similar results between quasi-static case and original R'n'R model as can be seen in Figure 4.1.

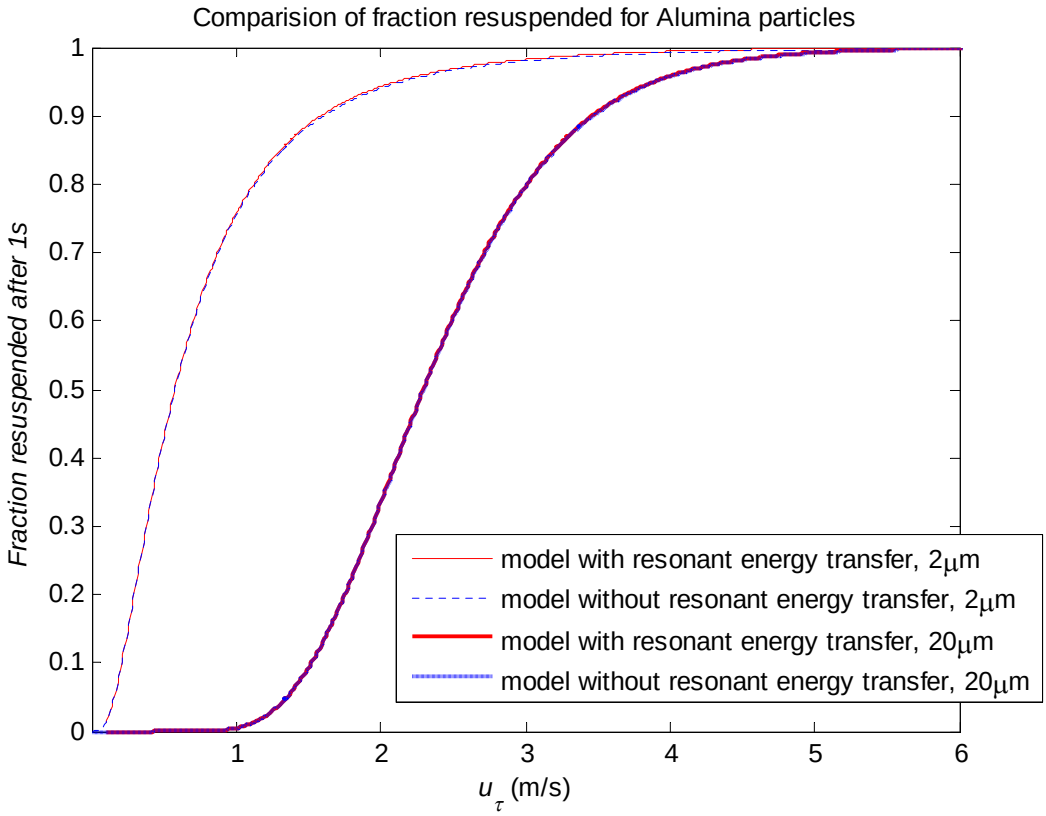

Figure 4.1 - Comparison of Quasi-static case and R'n'R model

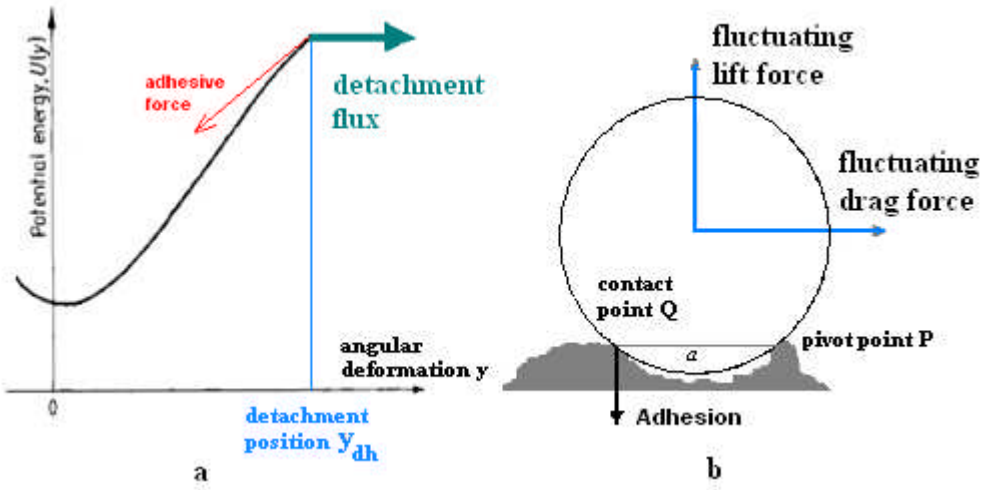

Figure 4.2 - Potential well and particle couple system

Recalling the R'n'R quasi-static model, the geometry of the particle-surface contact in the revised model (as also in the original) is shown in Figure 4.2b in which the distribution of asperity contacts is reduced to a two-dimensional model of two-point asperity contact. Thus rather than the centre of the particle oscillating vertically as in the original Reeks Reed and Hall (1988) (RRH) model, it will oscillate about the pivot P until contact with the other asperity at Q is broken. When this happens it is assumed that the lift force is either sufficient to break the contact at P and the particle

resuspends or it rolls until the adhesion at single-point contact is sufficiently low for the particle to resuspend. In either situation the rate of resuspension is controlled by the rate at which contacts are initially broken. The formula for the resuspension rate has the same form as in the original RRH model except that couples are taken account of by replacing vertical lift forces by equivalent forces based on their moments. That is referring to Figure 4.2b, the equivalent force F is derived from the net couple (Γ) of the system above so that

$$\Gamma = \frac{a}{2}F_L + rF_D \quad \Rightarrow \quad F = \frac{1}{2}F_L + \frac{r}{a}F_D \qquad [4.1]$$

where a is the typical distance between asperities, r the particle radius, F_L the lift force and F_D the drag force. The geometric factor (r/a) which refers to the ratio of the particle radius to the distance between asperities is suggested to be close to 100 according to Hall's experiment (Reeks and Hall, 2001). We recall that for the quasi-static case in the R'n'R model, at the detachment point (i.e. point y_{dh} in Figure 4.2a, referring to the angular displacement of the asperity contact at Q about P as in Figure 4.2b), the aerodynamic force acting on the particle (which includes the mean $\langle F \rangle$ and fluctuating parts $f(t)$) is considered to balance the restoring force at each instant of time (hence the term quasi –static). So

$$\langle F \rangle + f(t) + F_{AR}(y) = 0 \qquad [4.2]$$

where $F_{AR}(y)$ is the adhesive restoring force as a function of the angular deformation (y) of the particle. At the point of detachment (y_{dh}) the adhesive force is denoted by $f_a = -F_{AR}(y_{dh})$, so that from Eq.[4.2], the fluctuating component of the equivalent aerodynamic force at the detachment point (f_{dh}) can be written as

$$f_{dh} = f_a - \langle F \rangle \qquad [4.3]$$

Based on their measurements the mean drag and lift force for a spherical particle of radius r is given by Reeks and Hall (2001) (Eq.[2.70] and Eq.[2.18]) as

$$\langle F_D \rangle = 32\rho_f \nu_f^2 \left(\frac{ru_\tau}{\nu_f}\right)^2 \qquad \langle F_L \rangle = 20.9\rho_f \nu_f^2 \left(\frac{ru_\tau}{\nu_f}\right)^{2.31} \qquad [4.4]$$

where ρ_f is the fluid density, ν_f is the fluid kinematic viscosity, u_τ is the wall friction velocity. The adhesive force is considered as a scaled reduction of the adhesive force on a smooth surface based on the JKR model (Johnson, Kendal and Roberts, 1971) (Eq.[2.55]). Thus

$$f_a = \frac{3}{2}\pi\gamma r r_a' \qquad [4.5]$$

where γ is the surface energy and r_a' the normalized asperity radius r_a/r where r_a is the asperity radius. r_a' is assumed to have a log-normal distribution $\varphi(r_a')$ with geometric mean $\overline{r_a'}$ (also called reduction factor) and geometric standard deviation σ_a' (also called spread factor). Physically, these two parameters define the roughness of the surface. $\overline{r_a'}$ defines how adhesive force reduces from smooth surface and σ_a' describes how narrow the distribution is.

$$\varphi(r_a') = \frac{1}{\sqrt{2\pi}}\frac{1}{r_a'}\frac{1}{\ln\sigma_a'}\exp\left(-\frac{\left[\ln(r_a'/\overline{r_a'})\right]^2}{2(\ln\sigma_a')^2}\right) \qquad [4.6]$$

Biasi *et al*. (2001) took the Rock'n'Roll model for resuspension and added an empirical log-normal distribution of adhesive forces to reproduce the resuspension data of a number of experiments. Some adhesion-force parameters were tuned to fit the data of the most highly-characterised experiments, i.e., those of Hall (Reeks & Hall, 2001) and Braaten (1994). Then, for an enlarged dataset including STORM and ORNL ART resuspension results, the best global correlation for geometric mean adhesive force and geometric spread as a function of particle geometric mean radius (in microns) was obtained, namely

$$\begin{aligned} \overline{r}_a' &= 0.016 - 0.0023 r^{0.545} \\ \sigma_a' &= 1.8 + 0.136 r^{1.4} \end{aligned} \qquad [4.7]$$

The resuspension rate constant *p*, according to Reeks *et al*. (1988), is defined as the number of particles per second detached over the number of particles attached on the surface.

$$p = \int_0^\infty v\, P(y_{dh}, v)\, dv \Bigg/ \int_{-\infty}^{\infty} \int_{-\infty}^{y_{dh}} P(y, v)\, dy\, dv \qquad [4.8]$$

The numerator can also be described as the particle detachment flux (density flux) out of the potential well (Figure 4.2a). The denominator is the number of particles in the well.

Referring to Eq.[4.2] for the quasi-static case, we note that the angular deformation or displacement y can be written as an implicit function of the fluctuating aerodynamic force (f), i.e.

$$y(t) = \psi(f) \quad \textit{and so} \quad \dot{y}(t) = \dot{f}\psi'(f) \qquad [4.9]$$

where $\psi'(f)$ is the first derivative of $\psi(f)$ with respect to f.
then

$$p = \int_0^\infty \dot{f}\, P(f_{dh}, \dot{f})\, d\dot{f} \Bigg/ \int_{-\infty}^{\infty} \int_{-\infty}^{f_{dh}} P(f, \dot{f})\, df\, d\dot{f} \qquad [4.10]$$

where the joint distribution P of fluctuating aerodynamic force (f) and its derivative ($\dot{f}$) is assumed to be a joint normal distribution with zero correlation between the force and its derivative. Thus

$$P(f, \dot{f}) = \left[2\pi \sqrt{\left\langle f^2 \right\rangle \left\langle \dot{f}^2 \right\rangle} \right]^{-1} \exp\left(-\frac{f^2}{2\left\langle f^2 \right\rangle} \right) \exp\left(-\frac{\dot{f}^2}{2\left\langle \dot{f}^2 \right\rangle} \right) \qquad [4.11]$$

where $\sqrt{\left\langle f^2 \right\rangle}$ is the root mean square of fluctuating force and assumed as the rms coefficient f_{rms} multiplied by the average aerodynamic force $\left\langle F \right\rangle$ (In R'n'R model, f_{rms} is 0.2).

Substituting Eq.[4.11] into Eq.[4.10], the resuspension rate constant is then given by

$$p = \frac{1}{2\pi} \sqrt{\frac{\left\langle \dot{f}^2 \right\rangle}{\left\langle f^2 \right\rangle}} \exp\left(-\frac{{f_{dh}}^2}{2\left\langle f^2 \right\rangle} \right) \Bigg/ \frac{1}{2} \left[1 + erf\left(\frac{f_{dh}}{\sqrt{2\left\langle f^2 \right\rangle}} \right) \right] \qquad [4.12]$$

where $\sqrt{\frac{\langle \dot{f}^2 \rangle}{\langle f^2 \rangle}} = \omega^+ \left(\frac{u_\tau^{\,2}}{\nu_f} \right)$ [4.13]

ω^+ is the value of $\sqrt{\langle \dot{f}^2 \rangle / \langle f^2 \rangle}$ in wall units and represents the typical frequency of particle motion in the surface adhesive potential well. In the R'n'R model ω^+ is 0.0413. It is noted that the maximum value of resuspension rate constant is given by

$$p = \frac{1}{2\pi} \sqrt{\frac{\langle \dot{f}^2 \rangle}{\langle f^2 \rangle}} \qquad [4.14]$$

Therefore when $f_{dh} \Big/ \sqrt{\langle f^2 \rangle} \leq 0.75$, the resuspension rate constant reaches its maximum value.

The particle fraction remaining $f_R(t)$ and resuspension rate $\Lambda(t)$ at time t are defined as

$$\begin{aligned} f_R(t) &= \int_0^\infty \exp\left[-\left(p(r_a') \right) t \right] \varphi(r_a') dr_a' \\ \Lambda(t) &= -\dot{f}_R(t) = \int_0^\infty p(r_a') \exp\left[-\left(p(r_a') \right) t \right] \varphi(r_a') dr_a' \end{aligned} \qquad [4.15]$$

In next sections, the modification of the R'n'R model quasi-static case will be presented and discussed which includes the modification of the fluctuating aerodynamic force.

4.1 Fluctuating Aerodynamic Force

In this section, we describe how LES and DNS have been used to obtain the distributions of fluctuating aerodynamic force and its time derivative. We then show how the Rock 'n' Roll model is modified by these new distributions and the impact this has on the resuspension predictions.

4.1.1 Large Eddy Simulation

The Smagorinsky dynamic sub-grid scale model (Germano *et al.*, 1991) is applied in Large Eddy Simulation (LES). The domain for LES approach is described below in Figure 4.3. The periodic boundary condition is applied in the streamwise and spanwise directions and the computational grid is in essence following the flow down stream. The top and bottom surface are the wall. Table 4.2 in next section also showed the parameters applied in the simulation.

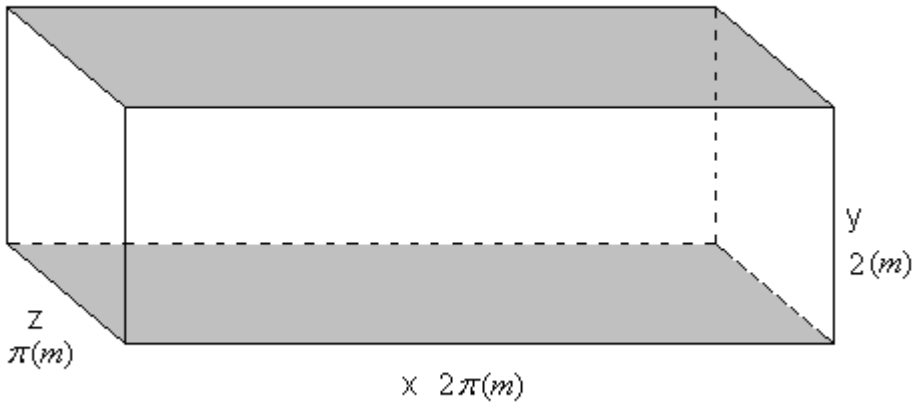

Figure 4.3 - Domain of LES calculation

In order to maintain a time dependent flow, an external force must be applied to the flow. In the case of the channel, a negative streamwise pressure gradient is used to sustain the flow which is calculated as

$$\frac{dp}{dx} = -\frac{u_\tau^2 \rho_f}{h} = -1.0\,Pa \cdot m^{-1} \qquad [4.16]$$

where ρ_f is the fluid density and h is the characteristic height which is 1 in this simulation. The shear Reynolds number Re_τ applied in the simulation is

$$Re_\tau = \frac{u_\tau \rho_f h}{\mu_f} = 182.87 \qquad [4.17]$$

where μ_f is fluid viscosity.

The time interval Δt is 0.0015s and there are 60116 time steps calculated. The fluid parameters are listed below:

$$\rho_f = 1.000\,kg\cdot m^{-3}, \quad \mu_f = 0.0055555\,kg\cdot m^{-1}\cdot s^{-1}$$

$$U_C = 18.0\,m\cdot s^{-1} \quad , \quad \tau_w = 1.0132\,Pa \quad , \quad u_\tau = \sqrt{\tau_w/\rho_f} = 1.0159\,m\cdot s^{-1}$$

where U_c is characteristic flow velocity and τ_w is the shear stress at the wall.

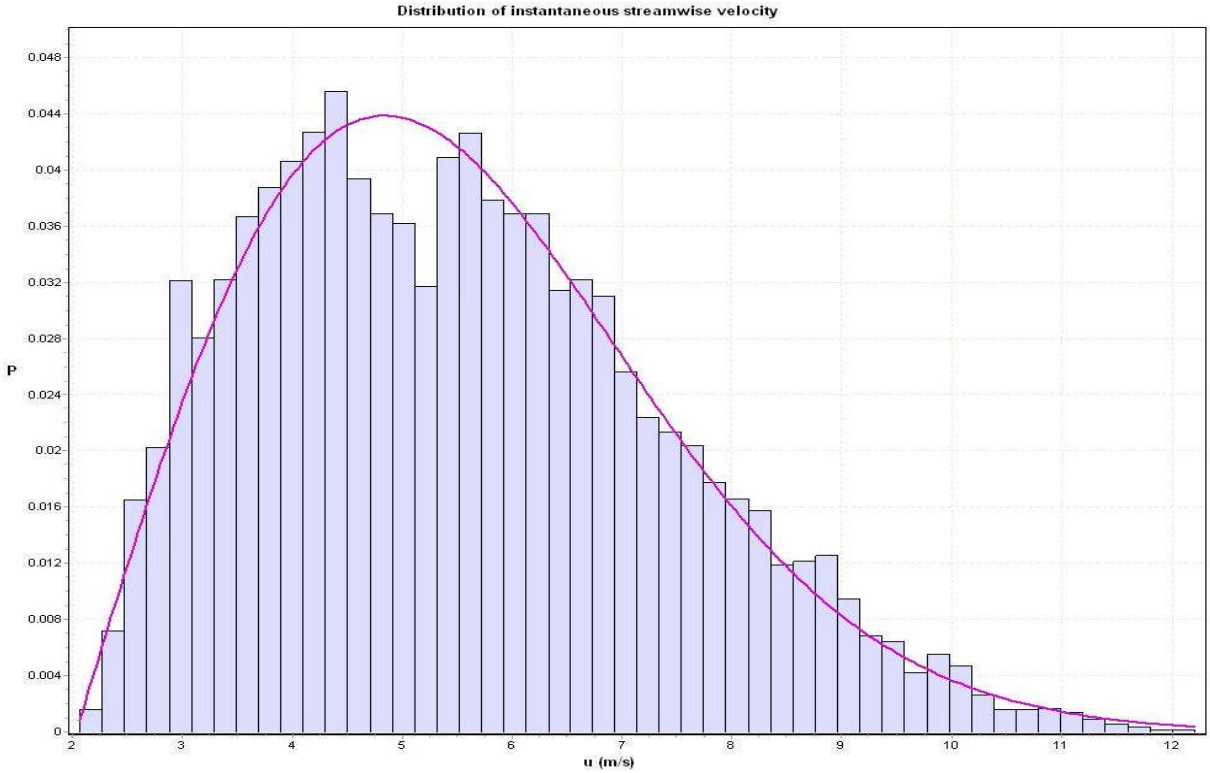

Figure 4.4 - Histogram and fitted distribution of instantaneous streamwise velocity ($y^+ = 6$)

The fluid instantaneous streamwise velocity u was obtained for different y^+ ($y^+ = 1$, $y^+ = 2$ and $y^+ = 6$) away from the wall at each time step. The histogram of the streamwise velocities ($y^+ = 6$) is obtained as shown in Figure 4.4. Assuming the local fluid velocity is similar to the particle velocity, the instantaneous drag forces acting on the particle is then calculated from the velocities by O'Neill's (1968) method which derived a simple drag force solution of the Stokes flow equation via Fourier – Bessel transforms for the sphere particle sitting on the wall in viscous sublayer.

$$F_D = 1.7\cdot 6\pi\mu_f r\,u = 10.2\pi\frac{r^+\mu_f{}^2\rho_f}{u_\tau}u \qquad [4.18]$$

where r^+ is the dimensionless particle radius which considered as y^+ away from the wall. Since in R'n'R model the drag force contribute the main part to the aerodynamic force (the drag force is multiplied by a factor of 100 (r/a = 100) and the lift force is reduced to half, following Eq.[4.1]), at the moment it is assumed that the lift force is neglected. Then the aerodynamic equivalent force is obtained according to Eq.[4.1].

$$F = \frac{r}{a} F_D = 100 \cdot F_D \qquad [4.19]$$

The aerodynamic equivalent force contains two parts: the mean and the fluctuating component. The fluctuating aerodynamic equivalent force is obtained by subtracting the mean part (arithmetic mean calculated from the data) from the instantaneous aerodynamic force.

$$f = F - \langle F \rangle \qquad [4.20]$$

The derivative of the fluctuating aerodynamic force $\dot{f}$ is calculated by the first order method,

$$\dot{f}_i = \frac{f_{i+1} - f_i}{\Delta t} \qquad [4.21]$$

In order to regenerate the new joint distribution for P (Eq.[4.11]), f and $\dot{f}$ will be normalized first by their rms values. Let z_1 and z_2 be the normalized fluctuating force and derivative, then

$$z_1 = \frac{f}{\sqrt{\langle f^2 \rangle}}, \quad z_2 = \frac{\dot{f}}{\sqrt{\langle \dot{f}^2 \rangle}} \qquad [4.22]$$

Then the histograms of z_1 and z_2 are obtained and the results indicate that the distribution of fluctuating aerodynamic resultant force fits to a Rayleigh distribution (Figure 4.5 (y^+ = 6), Figure 4.6 (y^+ = 2) and Figure 4.7 (y^+ = 1)) and the distribution of the derivative of the fluctuating aerodynamic resultant force fits to a Johnson SU distribution (Figure 4.8 (y^+ = 6), Figure 4.9 (y^+ = 2) and Figure 4.10 (y^+ = 1)). It is noted that there are two important reasons for choosing a Rayleigh distribution for the distribution of fluctuating aerodynamic resultant force: 1) best fit in the wings. 2) only two parameters are required.

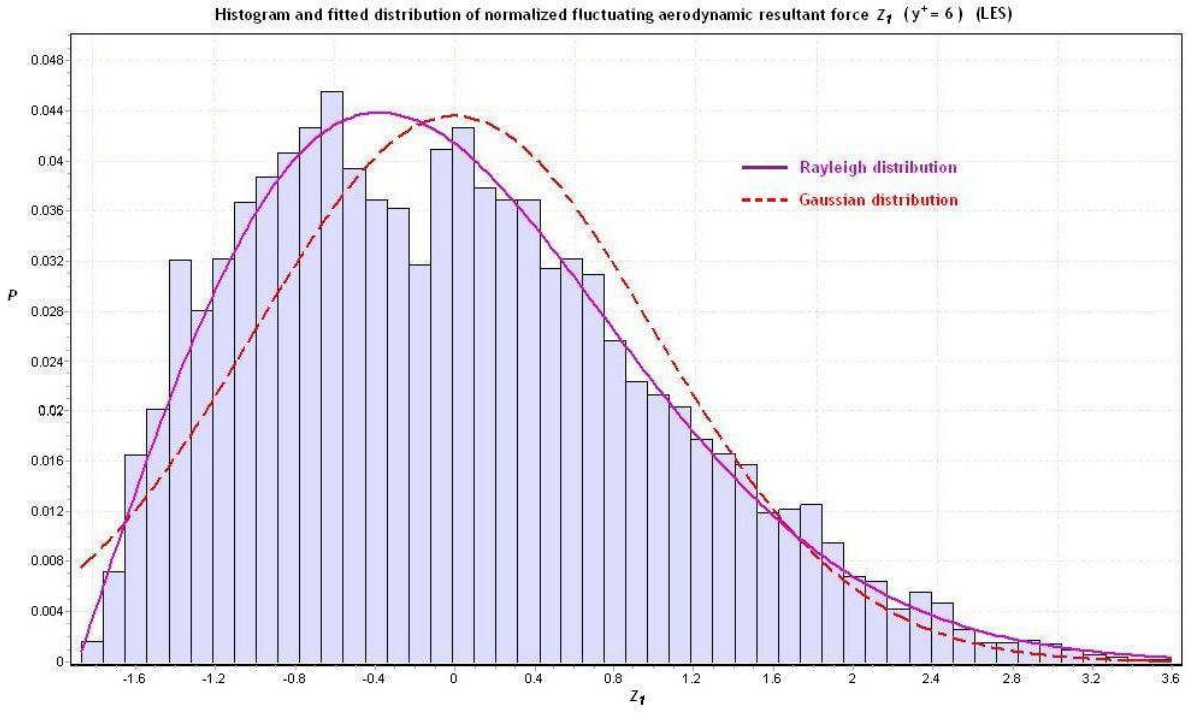

Figure 4.5 - Histogram and fitted distribution of fluctuating resultant force from LES data (y^+=6)

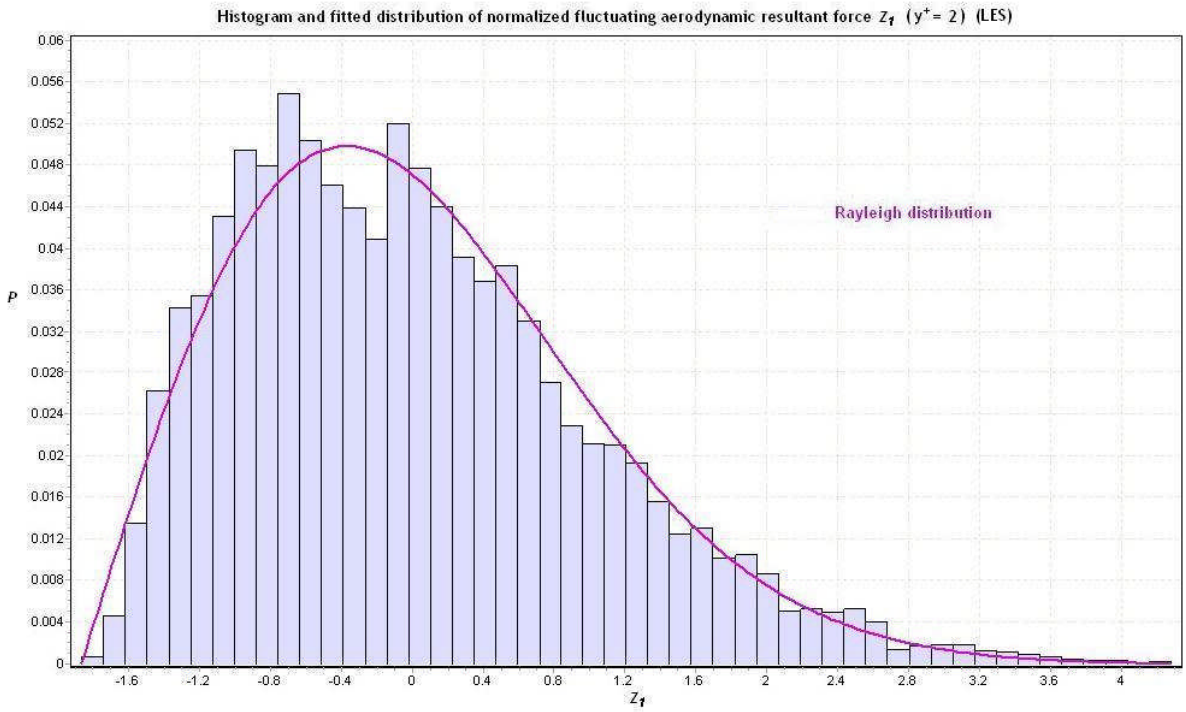

Figure 4.6 - Histogram and fitted distribution of fluctuating resultant force from LES data (y^+=2)

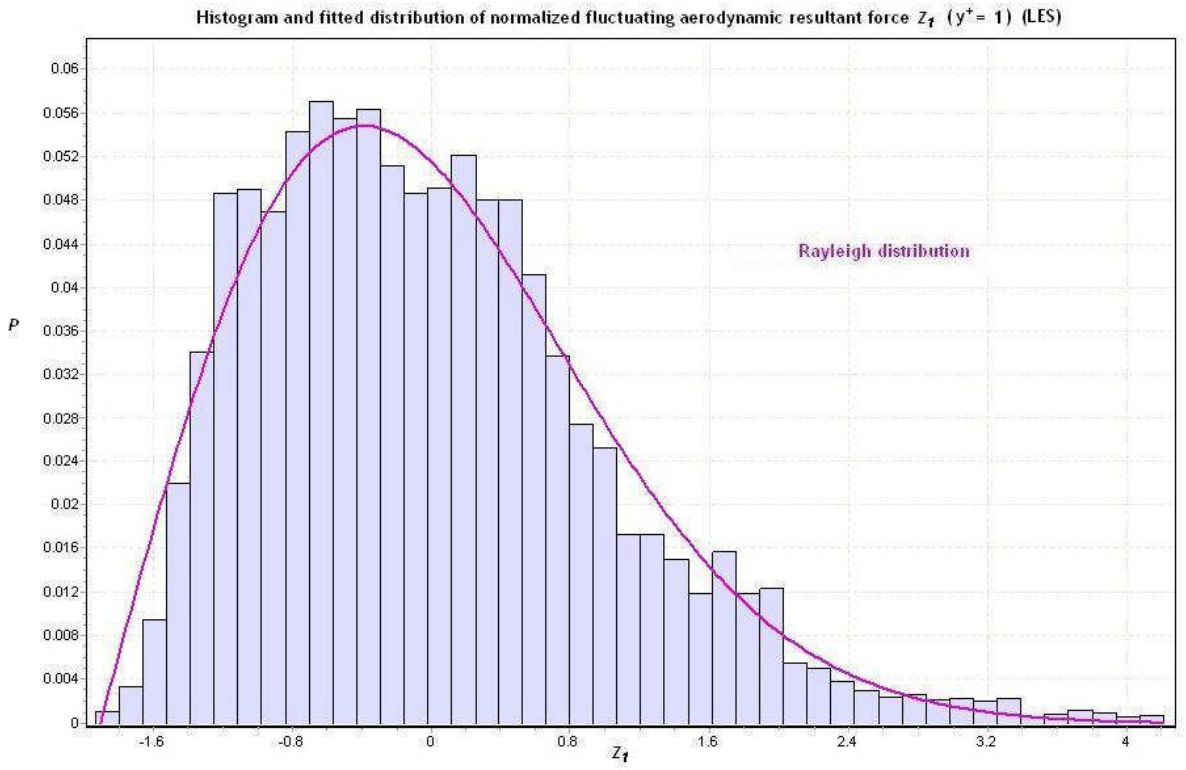

Figure 4.7 - Histogram and fitted distribution of fluctuating resultant force from LES data (y^+=1)

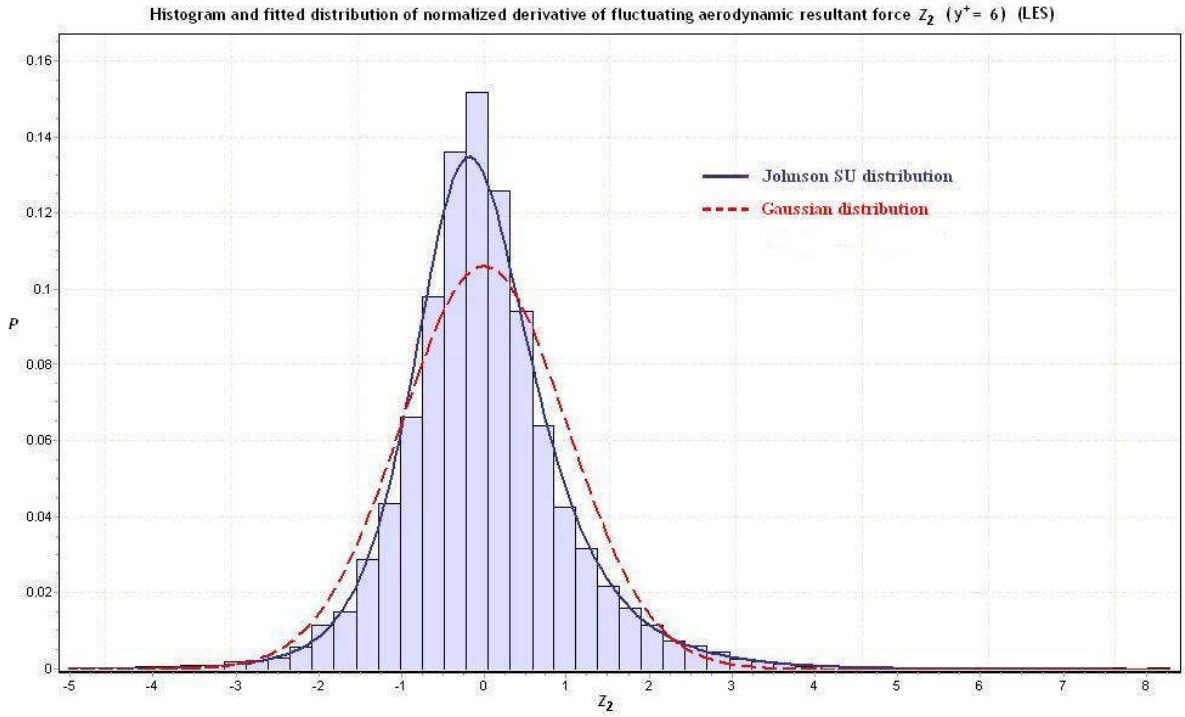

Figure 4.8 - Histogram and fitted distribution of derivative of fluctuating force from LES data (y^+=6)

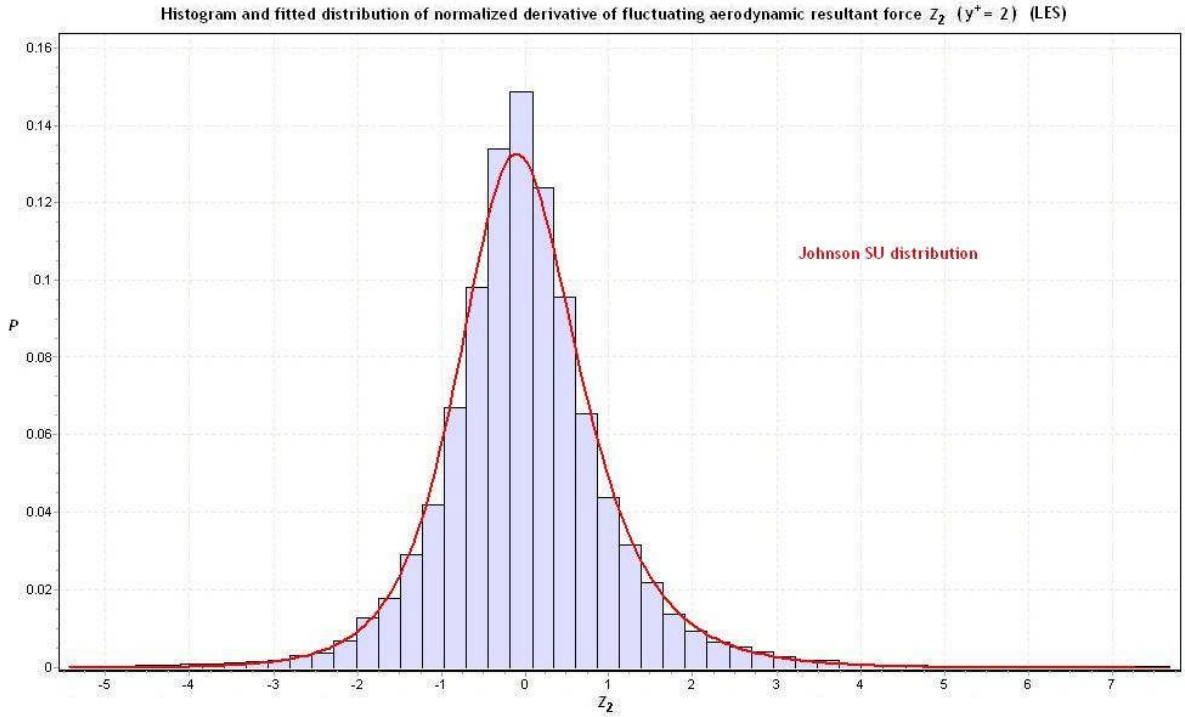

Figure 4.9 - Histogram and fitted distribution of derivative of fluctuating force from LES data (y^+=2)

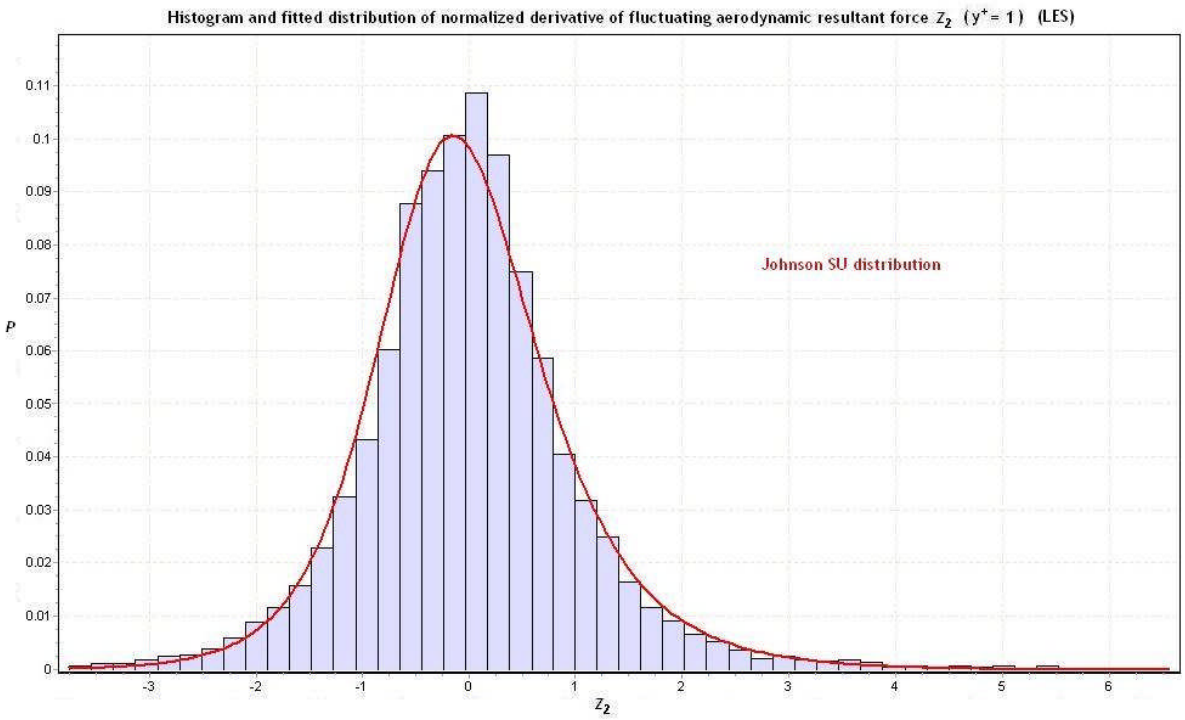

Figure 4.10 - Histogram and fitted distribution of derivative of fluctuating force from LES data (y^+=1)

According to the histogram plot (Figure 4.5) of fluctuating resultant force at y^+ = 6, one can observe that the Rayleigh distribution is highly skewed compared to Gaussian distribution. However for the histogram plot (Figure 4.8) of the derivative at y^+ = 6, the skewness of Johnson SU distribution is similar to Gaussian distribution; the difference occurs in the wings. More discussion about the histogram and fitted distribution will be provided in Section 4.1.2 (p109).

Recall that in the quasi-static case of R'n'R model, it is assumed that distribution of fluctuating aerodynamic force and its derivative (Eq.[4.11]) are statistically independent. From the LES data generated above, the distribution of fluctuating resultant force (Rayleigh distribution) and its derivative (Johnson SU distribution) can then replace the normal distribution assumption.

Then the new normalized joint distribution can be obtained by

$$P(z_1, z_2) = \frac{z_1 + A_1}{{A_2}^2} \exp\left(-\frac{1}{2}\left(\frac{z_1 + A_1}{A_2} \right)^2 \right) \cdot \frac{B_1}{B_2 \sqrt{2\pi}\sqrt{z^2+1}} \exp\left(-\frac{1}{2}\left(B_3 + B_1 \ln\left(z + \sqrt{z^2+1} \right) \right)^2 \right) \qquad [4.23]$$

where A_1, A_2, B_1, B_2, B_3 and B_4, are all constants depending on the fluid condition, $z = \frac{z_2 - B_4}{B_2}$. The former part of Eq.[4.23] which contains constants A_i is the Rayleigh distribution and the latter which contains B_i constants is the Johnson SU distribution.

As the differential $P(z_1, z_2)dz_1dz_2$ equals to $P(f, \dot{f})dfd\dot{f}$ and Eq.[4.22] also gives

$$df = \sqrt{\langle f^2 \rangle} dz_1,\ d\dot{f} = \sqrt{\langle \dot{f}^2 \rangle} dz_2 \qquad [4.24]$$

then the relationship between the normalized joint distribution and original one is obtained,

$$P(f, \dot{f}) = \frac{P(z_1, z_2)}{\sqrt{\langle f^2 \rangle}\sqrt{\langle \dot{f}^2 \rangle}} \qquad [4.25]$$

Substitute Eq.[4.22], Eq.[4.24] and Eq.[4.25] to Eq.[4.10] (derivation is shown in Appendix 3, p203), the modified resuspension rate constant is obtained,

$$p = B_{\dot{f}} \sqrt{\frac{\langle \dot{f}^2 \rangle}{\langle f^2 \rangle}} \frac{z_{dh} + A_1}{A_2^{\,2}} \exp\left(-\frac{1}{2}\left(\frac{z_{dh} + A_1}{A_2} \right)^2 \right) \Bigg/ 1 - \exp\left(-\frac{1}{2}\left(\frac{z_{dh} + A_1}{A_2} \right)^2 \right) \qquad [4.26]$$

where $z_{dh} = f_{dh} \Big/ \sqrt{\langle f^2 \rangle}$, f_{dh} is the fluctuating resultant force at detachment point (Eq.[4.3]). The term $\sqrt{\langle f^2 \rangle}$ is calculated as the rms coefficient f_{rms} multiplied by the mean of aerodynamic resultant force. f_{rms} equals 0.2 in R'n'R model whereas here it is calculated from the simulation data.

$$\sqrt{\langle f^2 \rangle} = f_{rms} \langle F \rangle \qquad [4.27]$$

In R'n'R model, the maximum value of p is limited to the bursting frequency of turbulent motion in a turbulent boundary layer (ω), the ratio of the rms value of the force derivative to the rms value of the fluctuating resultant force is given as

$$\omega = \sqrt{\frac{\langle \dot{f}^2 \rangle}{\langle f^2 \rangle}} = \omega^+ \left(\frac{u_\tau^{\,2}}{\nu_f} \right) \qquad [4.28]$$

where ω^+ which is called the typical forcing frequency equals to 0.0413 in R'n'R model based on Hall's experiment. Here it is calculated from the simulation data. ω^+ is ω in wall unit.

Table 4.1 shows the values of all the parameters appear in the equations based on LES data (for y^+ = 1, 2 and 6).

	$B_{\dot{f}}$	A_1	A_2	ω^+	f_{rms}
y^+ = 1	0.370063	1.90124	1.511536	0.100202	0.355
y^+ = 2	0.365629	1.86330	1.495317	0.08484	0.356
y^+ = 6	0.366081	1.88837	1.510938	0.08553	0.335

Table 4.1 - Parameters used in modified R'n'R model calculated from LES data

4.1.2 Direct Numerical Simulation

A spectral projection method for incompressible flow simulation based on an orthogonal decomposition of the velocity into two solenoidal fields (Buffat *et al.*, 2011) is applied for Direct Numerical Simulation. The approximation is based on Fourier expansions in the streamwise (x) and spanwise (z) directions and an orthogonal expansion of Chebyshev polynomials (proposed by Moser *et al.*, 1983) in the wall normal (y) direction in order to satisfy the wall boundary conditions. The boundary conditions are no-slip on the wall and periodic in the streamwise and spanwise directions. The domain is shown in Figure 4.11.

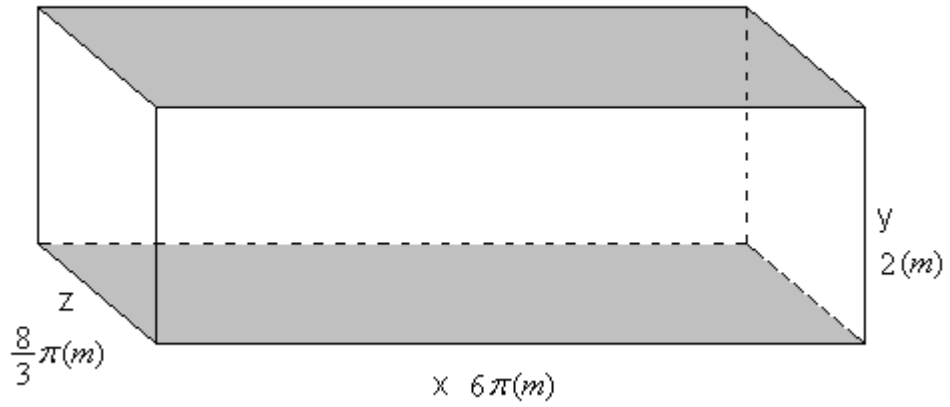

Figure 4.11 - Domain of DNS calculation

Consider an incompressible, Newtonian fluid moving between two fixed, parallel plates distant from 2*h* apart (*h* is 1). The volume force is introduced in order to simulate flows that are not naturally periodic in the streamwise direction, while keeping the benefits of Fourier expansions in this direction.

	x	*y*	*z*	*h*	*grid*	Re_τ	*Δt*	*steps*
LES	2π	2	π	1	72 x 72 x 72	183	0.0015s	60116
DNS	6π	2	8/3 π	1	384 x 193 x 384	180	0.0034s	63738

Table 4.2 - Simulation parameters in LES and DNS

Table 4.2 showed the simulation parameters compared to LES and the other parameters in DNS are listed below,

$$\rho_f = 1.000\, kg \cdot m^{-3}, \quad \mu_f = 0.00030506\, kg \cdot m^{-1} \cdot s^{-1}, \quad u_\tau = 0.054945\, m \cdot s^{-1}$$

The flow instantaneous velocities are recorded in each time step and the recording positions are y^+ = 0.1, y^+ = 0.6, y^+ = 1.9 and y^+ = 6, respectively, away from the wall. The same approach of calculating fluctuating force (Eq.[4.18], Eq.[4.19] and Eq.[4.20]) and its derivative (Eq.[4.21]) as in

LES case is applied and they also are normalized by their rms values (Eq.[4.22]). The distributions of the normalized fluctuating resultant force and its derivative for each y^+ are shown below.

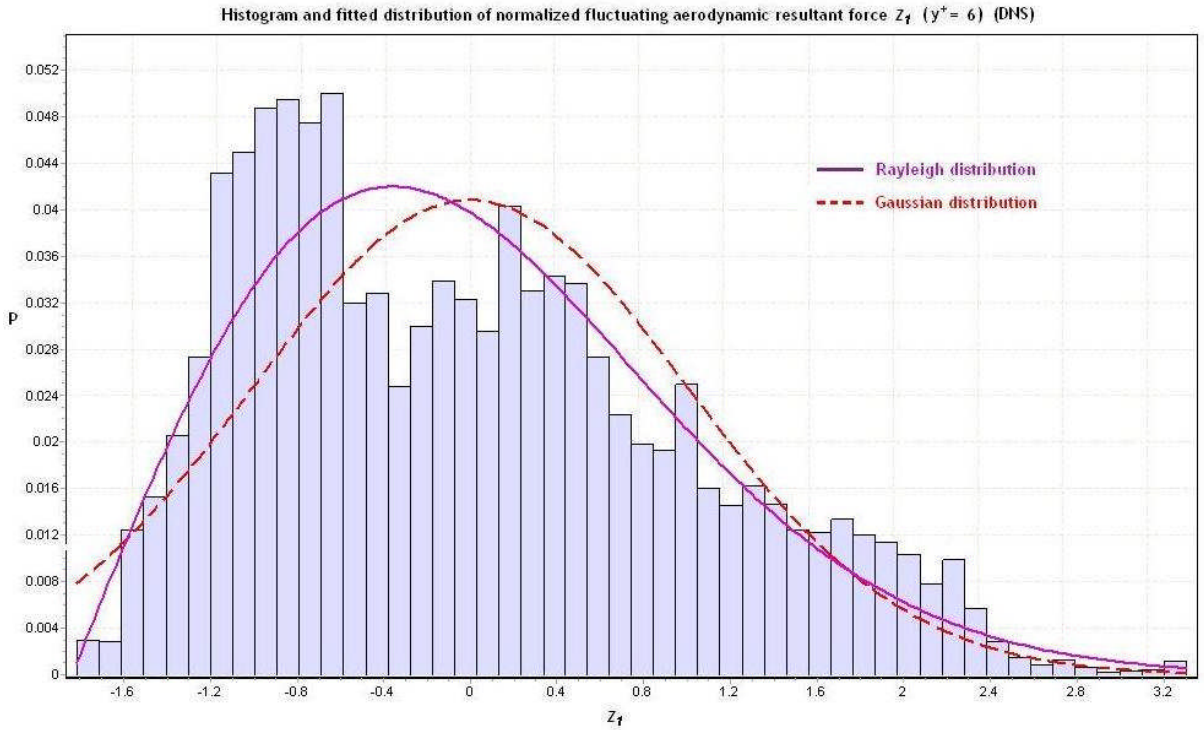

Figure 4.12 - Histogram and fitted distribution of fluctuating resultant force from DNS data (y^+=6)

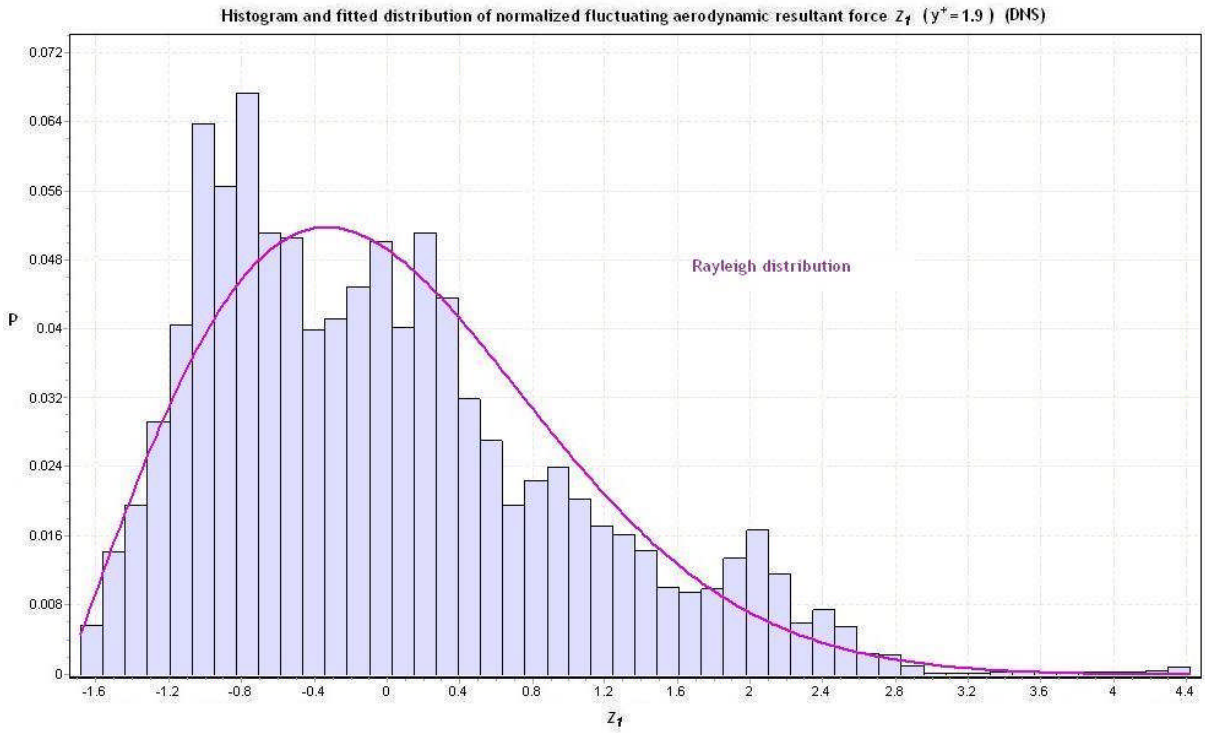

Figure 4.13 - Histogram and fitted distribution of fluctuating resultant force from DNS data (y^+=1.9)

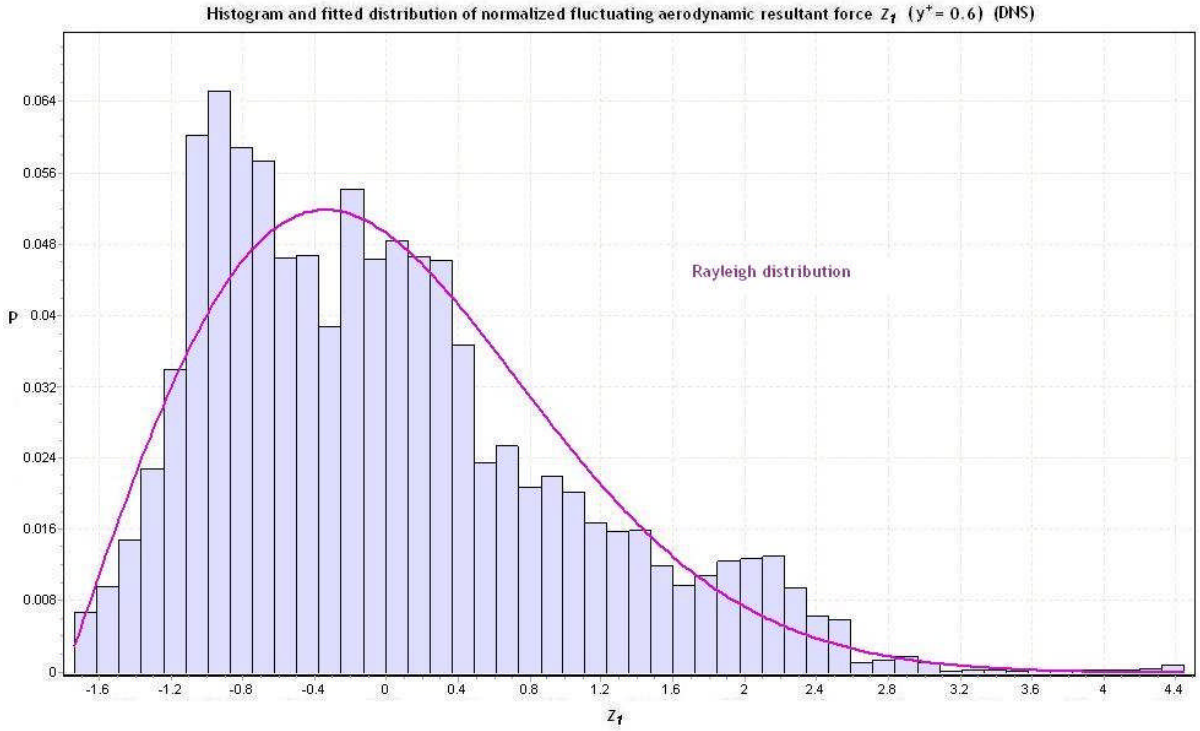

Figure 4.14 - Histogram and fitted distribution of fluctuating resultant force from DNS data (y^+=0.6)

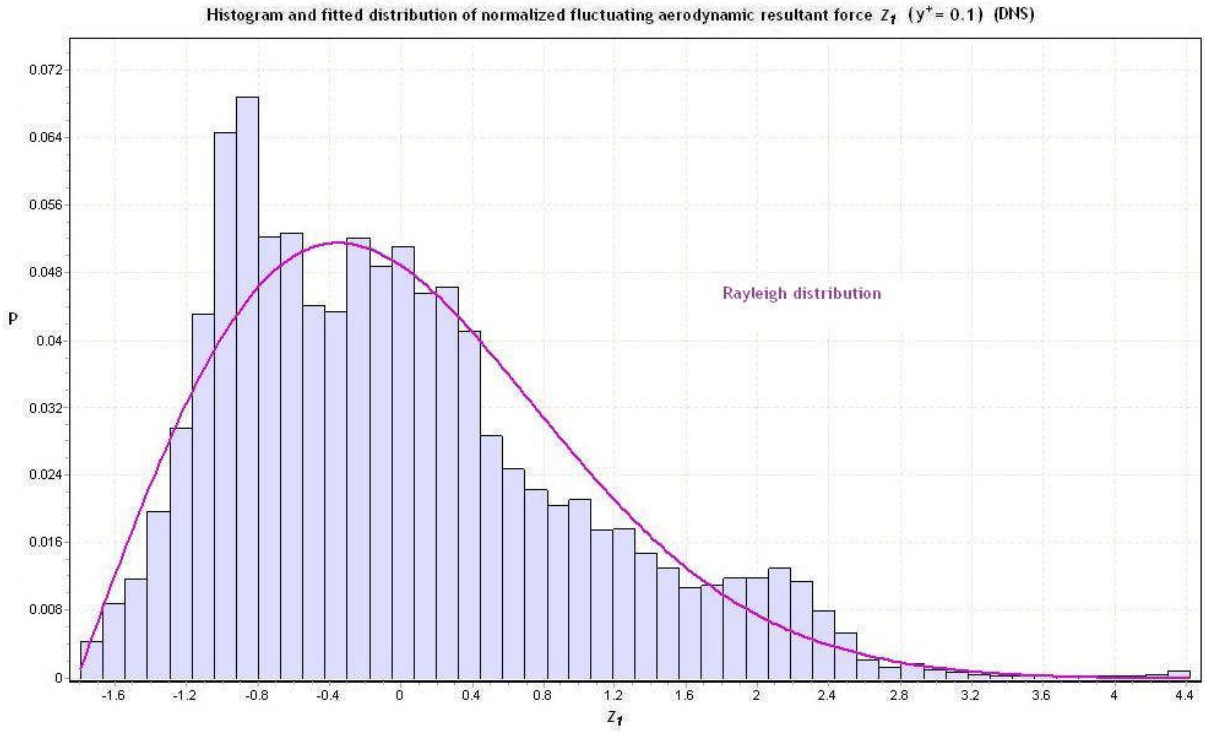

Figure 4.15 - Histogram and fitted distribution of fluctuating resultant force from DNS data (y^+=0.1)

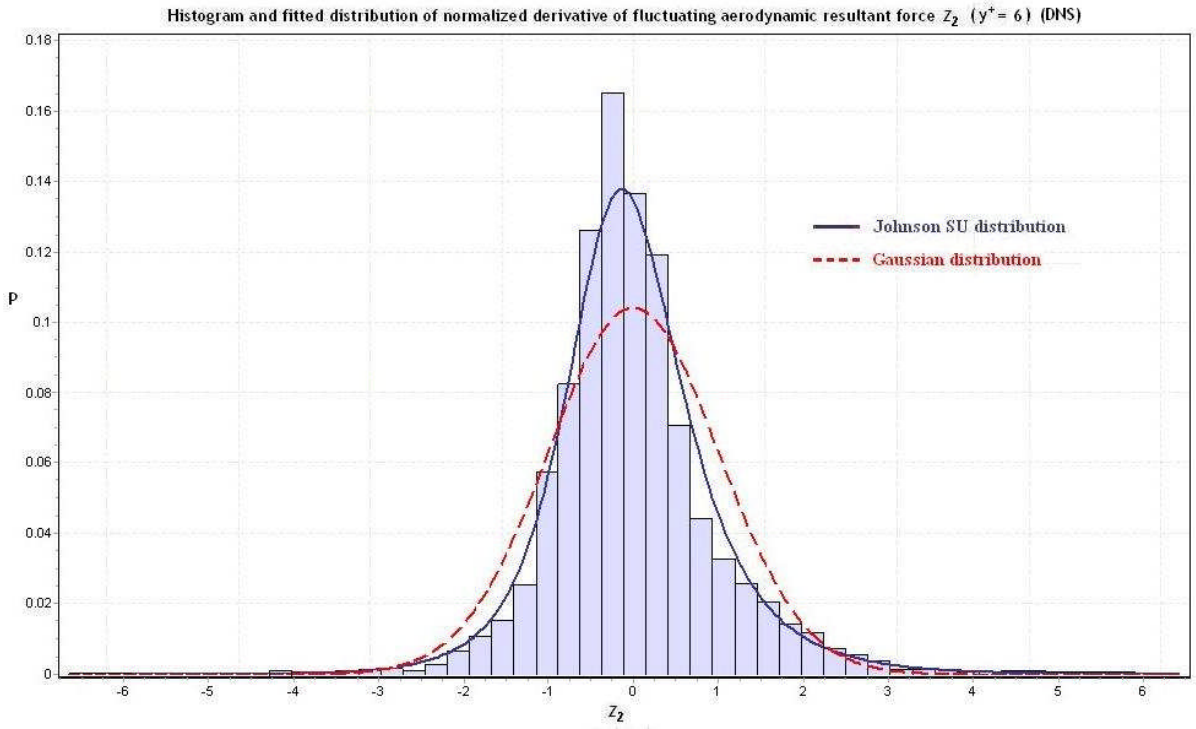

Figure 4.16 - Histogram and fitted distribution of derivative of fluctuating force from DNS data (y^+=6)

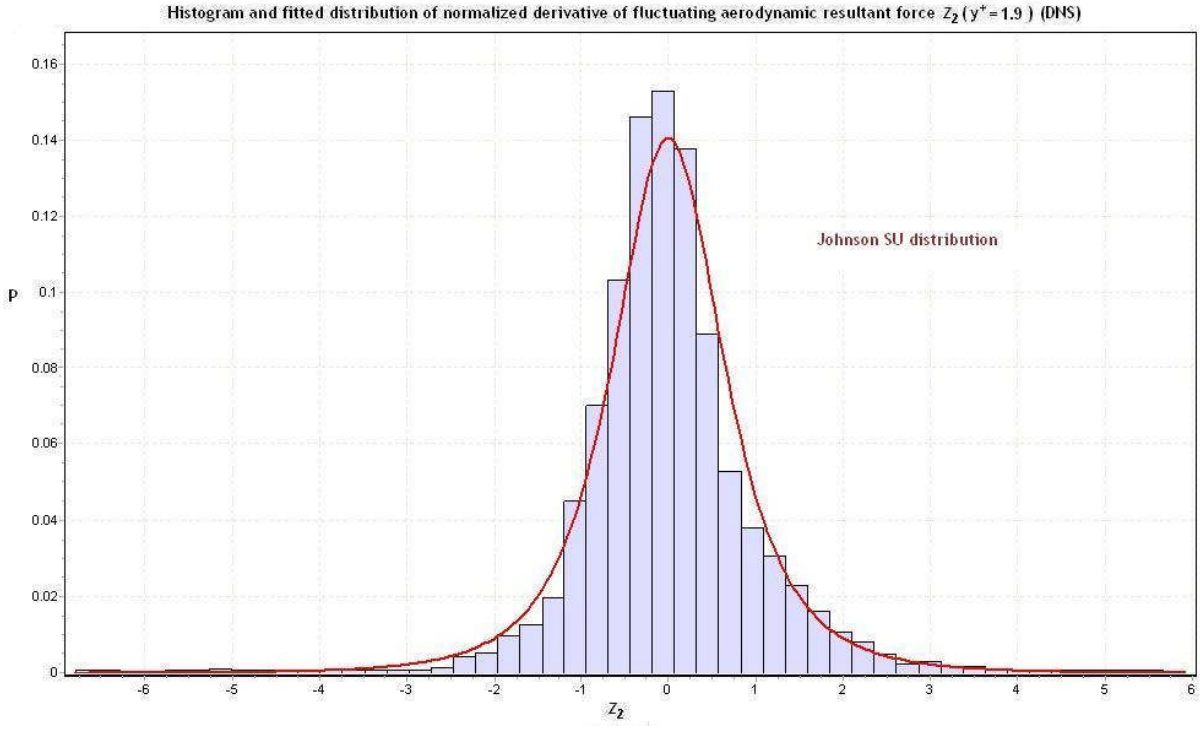

Figure 4.17 - Histogram and fitted distribution of derivative of fluctuating force from DNS data (y^+=1.9)

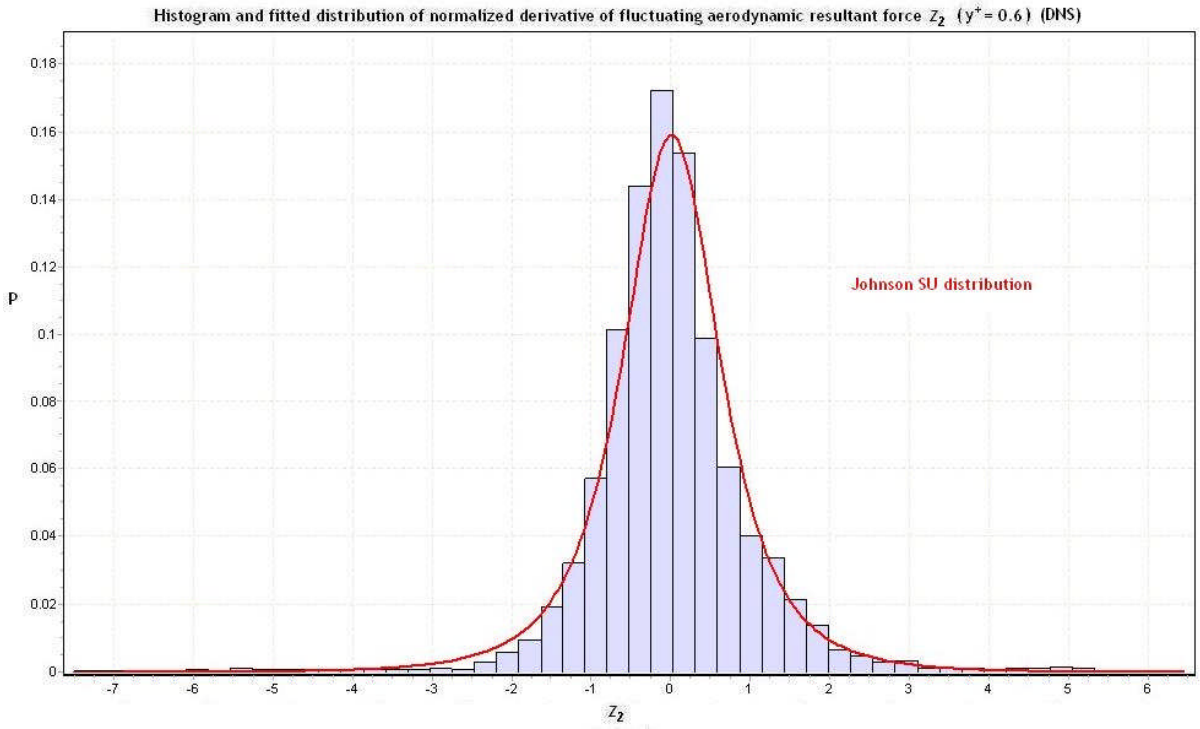

Figure 4.18 - Histogram and fitted distribution of derivative of fluctuating force from DNS data (y^+=0.6)

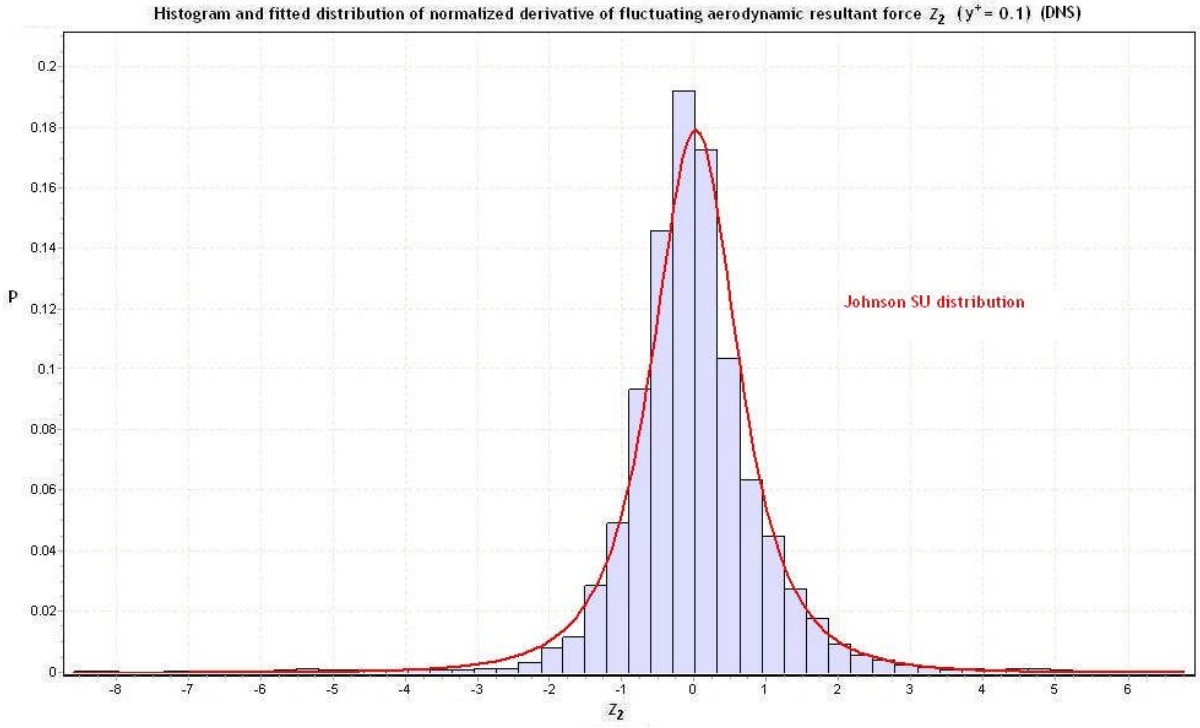

Figure 4.19 - Histogram and fitted distribution of derivative of fluctuating force from DNS data (y^+=0.1)

The results indicated that the distribution of fluctuating aerodynamic resultant force also fits to a Rayleigh distribution and the distribution of the derivative of the fluctuating aerodynamic resultant force fits to a Johnson SU distribution which is consistent with LES results.

Then with the same calculation of LES approach, the resuspension rate constant is obtained as

$$p = B_{\dot{f}} \sqrt{\frac{\langle \dot{f}^2 \rangle}{\langle f^2 \rangle}} \frac{z_{dh} + A_1}{{A_2}^2} \exp\left(-\frac{1}{2} \left(\frac{z_{dh} + A_1}{A_2} \right)^2 \right) \Bigg/ 1 - \exp\left(-\frac{1}{2} \left(\frac{z_{dh} + A_1}{A_2} \right)^2 \right) \qquad [4.29]$$

with the same assumption on the rms coefficient f_{rms} and the typical forcing frequency ω^+.

$$\sqrt{\langle f^2 \rangle} = f_{rms} \langle F \rangle \quad , \qquad \sqrt{\frac{\langle \dot{f}^2 \rangle}{\langle f^2 \rangle}} = \omega^+ \left(\frac{{u_\tau}^2}{\nu_f} \right)$$

The table below shows the values of all the parameters in LES and DNS.

LES	$B_{\dot{f}}$	A_1	A_2	ω^+	f_{rms}
$y^+ = 1$	0.370063	1.90124	1.511536	0.100202	0.355
$y^+ = 2$	0.365629	1.86330	1.495317	0.08484	0.356
$y^+ = 6$	0.366081	1.88837	1.510938	0.08553	0.335
DNS	$B_{\dot{f}}$	A_1	A_2	ω^+	f_{rms}
$y^+ = 0.1$	0.343658	1.812562	1.463790	0.164189	0.366
$y^+ = 0.6$	0.346911	1.784751	1.446609	0.152035	0.366
$y^+ = 1.9$	0.351181	1.759902	1.431301	0.131261	0.365
$y^+ = 6$	0.358568	1.836052	1.478360	0.127143	0.346

Table 4.3 - Parameters used in modified R'n'R model calculated by LES and DNS data

From the table above one can observe from both LES and DNS results that in the viscous sublayer ($y^+ < 6$), the statistics of fluctuating resultant force and its derivative (normalized on their rms values) are almost independent of y^+ (parameters $B_{\dot{f}}$, A_1 and A_2 are very close). Also the value of the rms coefficient f_{rms} (namely $\sqrt{\langle f^2 \rangle} / \langle F \rangle$) is almost independent of y^+ and with approximately the same values for both the LES and DNS measurements. However, the typical 'burst' frequency ω^+ varies with y^+ and there is noticeable difference between the values obtained from the LES and DNS data. The importance of the parameters $B_{\dot{f}}$, A_1 and A_2 that define the non-Gaussian distributions as distinct from a Gaussian distribution and the two parameters (f_{rms} and ω^+) on resuspension will be investigated in the subsequent analysis and figures given below.

4.1.3 Results and Analysis

In this section, we compare the predictions of the modified R'n'R model based on the LES and DNS data with those of the original R'n'R model. This is done in 3 stages because the difference depends on 3 distinguishable effects. First the difference between the Gaussian and non-Gaussian models is compared where the difference lies in the role of Gaussian versus non-Gaussian distributions of the fluctuating aerodynamic force and its time derivative (both with the same mean and rms). In particular the dependence of the resuspension rate constants on the adhesive force is dependent upon a Gaussian distribution in the Gaussian models and in the non-Gaussian model it is dependent on a Rayleigh distribution. Then we consider the sensitivity of the predictions of the modified model to the LES and DNS results (y^+ = 6) based on the measured parameters in Table 4.3. Finally we compare predictions of the original Gaussian R'n'R model with those of the modified non-Gaussian R'n'R model based on the DNS results (y^+ = 0.1) in Table 4.3 where the difference also depends upon the different values of ω^+ and the values of f_{rms} (the ratio of the rms of the aerodynamic removal force to it is mean value). In this case we shall compare predictions with the experimental results in the Hall experiment (Reeks and Hall, 2001).

4.1.3.1 Gaussian vs. Non-Gaussian Distribution (DNS)

In this section we will compare the predictions using a non-Gaussian model for the resuspension rate constant p_{nG} based on Eq.[4.29] with those obtained using a Gaussian model. The values of the constants in Eq.[4.29] are those given in Table 4.3. For the Gaussian model the resuspension rate constant p_G is given by

$$p_G\left(z_{dh}\right) = \tfrac{1}{2\pi}\omega \exp\left(-\tfrac{1}{2} {z_{dh}}^2\right)$$

where $\omega = \sqrt{\left\langle \dot{f}^2 \right\rangle / \left\langle f^2 \right\rangle}$ and $z_{dh} = \left(f_a - \left\langle F \right\rangle\right) / \sqrt{\left\langle f^2 \right\rangle}$. For future reference we shall also use the normalized adhesive force $z_a = f_a / \sqrt{\left\langle f^2 \right\rangle}$ so that $z_{dh} = z_a - {f_{rms}}^{-1}$, because unlike z_{dh}, a log normal distribution of asperity radii corresponds to a Lognormal distribution of z_a with the same geometric spread (shown later).

In comparing the non-Gaussian and Gaussian models we shall naturally use the same value of $\omega = \sqrt{\left\langle \dot{f}^2 \right\rangle / \left\langle f^2 \right\rangle}$ and f_{rms}. In fact we shall plot the results so that the differences are independent of the value of ω reflecting only the difference between a Gaussian and non-Gaussian distribution of fluctuating aerodynamic forces with the same standard deviation. (To be more precise a Gaussian with a Rayleigh distribution) Later on we will compare the predictions based on the original R'n'R model with those based on the non-Gaussian resuspension rate (which we refer to as the modified R'n'R model), but in these cases the values of ω are different.

To begin with we compare the values for the resuspension rate constant for the Gaussian and non-Gaussian models when the adhesive force balances the mean aerodynamic force i.e. f_{dh} or $z_{dh} = 0$. For the Gaussian model this value corresponds to the maximum value of the resuspension rate constant. For a Gaussian model (as in the original R'n'R model),

$$p_G(0) = \tfrac{1}{2\pi}\omega = 0.15915\omega$$

This is also the maximum value and applies for $z_{dh} < 0.75$.

We recall that using Hall's measurements for the original R'n'R model $p_G(0) = 0.00658u_\tau^2 / v_f$. In the case of the non-Gaussian model,

$$p_{nG}(0) = B_f \left(\frac{A_1}{A_2{}^2}\right)\exp\left(-\frac{1}{2}\left(\frac{A_1}{A_2}\right)^2\right)\left(1-\exp\left(-\frac{1}{2}\left(\frac{A_1}{A_2}\right)^2\right)\right)^{-1}\omega$$

which using the values for A_1, A_2, B_f of $y^+ = 0.1$ given in Table 4.3 gives

$$p_{nG}(0) = 0.25223\omega$$

We note from Figure 4.20 that $p_{nG}(z_{dh}) > p_G(z_{dh})$ for $z_{dh} < 0.5$ because the maximum value of the resuspension rate constant in the Gaussian model is set at $p_G(0)$ as in the original model. Note the negative skewness of the distribution of aerodynamic forces means there are more particles on the surface which experience forces < the mean removal force $\langle F \rangle$. However as shown in Figure 4.20 as z_{dh} increases beyond 0.5, the difference between Gaussian and non-Gaussian decreases until at $z_{dh} \approx 2.1$ they are both the same. Beyond this value, the non-Gaussian rate constant exceeds the Gaussian value. Particularly striking is the large difference between the two predictions for values of the resuspension rate constant for $z_{dh} \gg 1$ which although $\ll p_{nG}(0), p_G(0)$, reflects the significant difference between the two distributions for aerodynamic removal forces in the wings of the distribution (corresponding to the highly intermittent bursting and sweeping events of fluid motion near the wall). Note that when z_{dh} is large the adhesive force on the particle is larger than the mean aerodynamic resultant force (in other words, in the situation particles are very difficult to be removed). Therefore, in this situation, the non-Gaussian distribution results significantly more resuspension than the original Gaussian case.

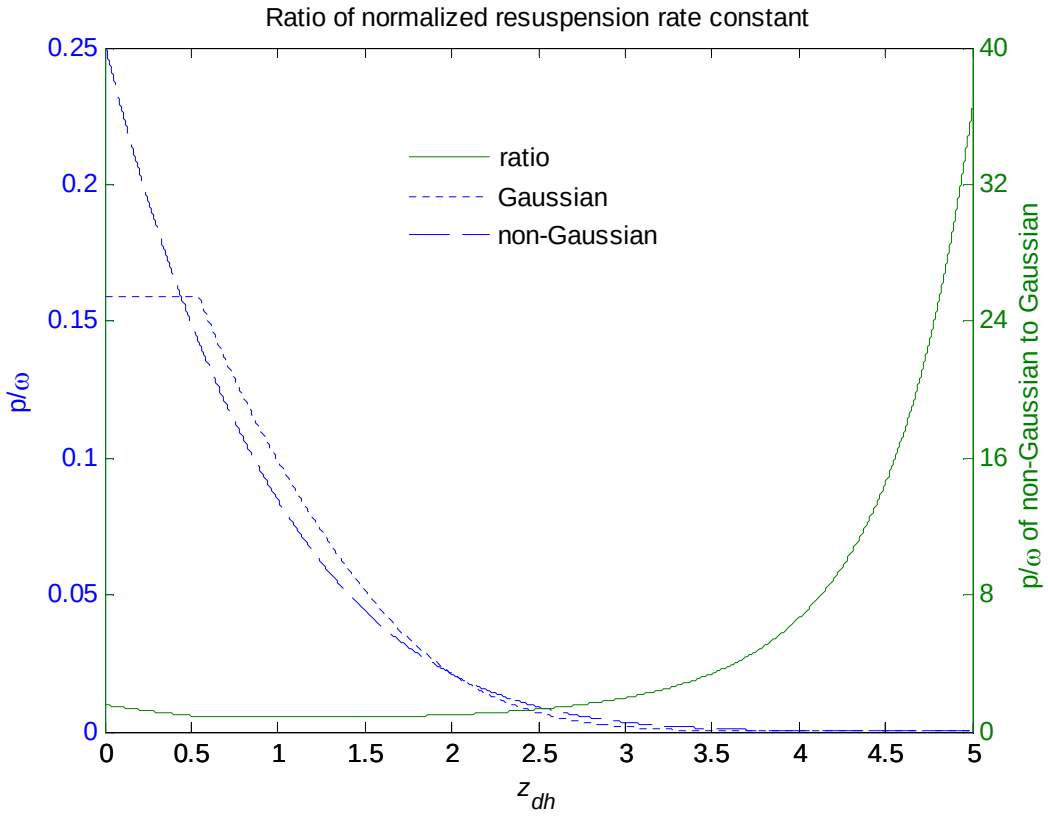

Figure 4.20 - Normalized resuspension rate constant between non-Gaussian and Gaussian

The LES/DNS measurements are only reliable out to $z_{dh} \approx 4$, but even so from Figure 4.20, the ratio of $p_{nG} / p_G \approx 10$. The form of the distribution for values of $z_{dh} > 4$ would seem to indicate the difference between the two predictions increases significantly.

Noted that the normalized fluctuating resultant force at the detachment point (z_{dh}), as shown before, is

$$z_{dh} = \frac{f_a - \langle F \rangle}{\sqrt{\langle f^2 \rangle}} = \frac{F_a r_a' - \langle F \rangle}{f_{rms} \langle F \rangle} \qquad [4.30]$$

Then the normalized adhesive force (or the ratio of adhesion to the rms of aerodynamic force) is derived as

$$z_a = z_{dh} + \frac{1}{f_{rms}} = \frac{F_a r_a'}{f_{rms} \langle F \rangle} \qquad [4.31]$$

where r_a' is the normalized asperity radius which is from a log-normal distribution $\varphi(\overline{r_a'}, \sigma_a')$. Then z_a also forms a log-normal distribution. The mean is defined as

$$\overline{z}_a = \frac{F_a \overline{r_a'}}{f_{rms} \langle F \rangle} = \frac{3/2 \pi \gamma r}{f_{rms} \langle F \rangle} \overline{r_a'} \qquad [4.32]$$

The spread is defined as $\sqrt{\left[\ln(z_a) - \langle \ln(z_a) \rangle\right]^2}$ and is identical with σ'_a which is derived as $\sqrt{\left[\ln(r'_a) - \langle \ln(r'_a) \rangle\right]^2}$.

Then the log-normal distribution $\varphi(\bar{r}'_a, \sigma'_a)$ is replaced by $\varphi(\bar{z}_a, \sigma'_a)$.

The resuspension rate constant p is, according to Eq.[4.26], a function of z_{dh}. Then the particle fraction remaining on the surface and the resuspension rate are given by

$$f_R(t) = \int_0^\infty \exp\left[-p(z_{dh})t\right]\varphi(z_a)dz_a$$
$$\Lambda(t) = -\dot{f}_R(t) = \int_0^\infty p(z_{dh})\exp\left[-p(z_{dh})t\right]\varphi(z_a)dz_a \qquad [4.33]$$

It is noted that ω is the typical forcing frequency of the particle in the potential well, defined as

$$\omega = \sqrt{\frac{\langle \dot{f}^2 \rangle}{\langle f^2 \rangle}} = \omega^+ \left(\frac{u_\tau^{\,2}}{\nu_f}\right) \qquad [4.34]$$

Then the resuspension rate (Λ), resuspension rate constant (p) and the time (t) are normalized based on the typical forcing frequency.

$$\hat{\Lambda} = \Lambda/\omega, \quad \hat{p} = p/\omega, \quad \hat{t} = \omega t \qquad [4.35]$$

The normalized resuspension rate is then derived as

$$\hat{\Lambda}(t) = \int_0^\infty \hat{p}(z_{dh})\exp\left[-\hat{p}(z_{dh})\hat{t}\right]\varphi(z_a)dz_a \qquad [4.36]$$

It is interesting to see how this significant difference in the values of the rate constants for the two models for large values of the adhesive force is reduced when in practice we have a broad spread of adhesive forces. To show this we effectively plot the ratio of the initial resuspension rate as a function of geometric mean of the normalized adhesive force, z_a for various values of the spread (Figure 4.21) and then the same ratio as a function of the spread for a large value of the geometric mean (Figure 4.22). Note that a log-normal distribution of normalized asperity radii will have the same spread as a log normal distribution of normalized adhesive forces (as shown before). For a very narrow spread ~ 1.01 we would expect to reproduce the ratio of resuspension rate constant shown in Figure 4.20. However as the spread increases so the relative importance and contribution form the resuspension rates from the higher values of the normalized adhesive force z_a is markedly less, even when the geometric mean of z_a ~ 8 (note that for comparison with Figure 4.20 a value of z_a = 8, z_{dh} ~ 5.27 for a value of $1/f_{rms}$ ~ 2.73). In fact for a spread of 2 (nominally smooth surfaces), the ratio is less for large values of the geometric mean of the normalized adhesive force compared to its value for zero geometric mean of z_a.

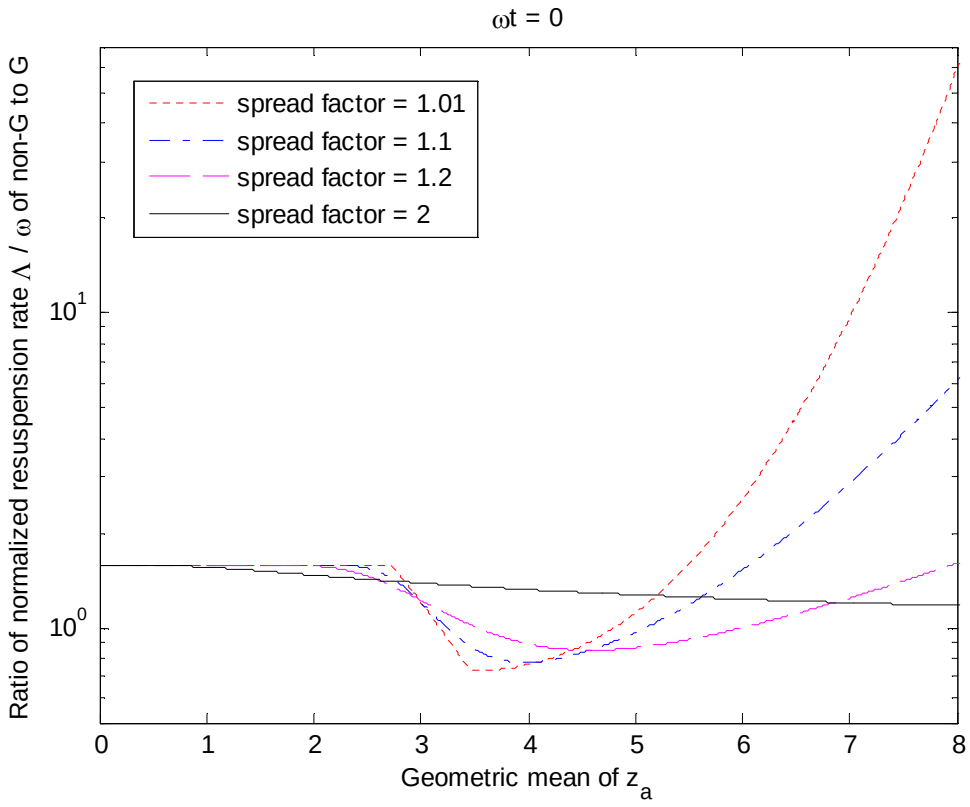

Figure 4.21 - Ratio of normalized resuspension rate of non-Gaussian to Gaussian vs. Geometric mean of z_a (ratio of adhesive force f_a/ rms of fluctuating aerodynamics force $\sqrt{\langle f^2 \rangle}$

Figure 4.22 shows the sensitivity of the ratio of normalized resuspension rates to changes in the spread for a large of the geometric mean of z_a = 8. Note the ratio drops to unity for a spread as narrow as 1.2 and actually drops below unity but flattens out to a value ~ 1.5 as the spread increases. All this reflects the regions where the ratio of the rate constants is less than 1 for values of z_a between 2.73 (when mean aerodynamic forces $\approx$ adhesive force) and 5 and $z_a > 5$ when the ratio > 1 and the relative contributions these regions of the curve of the resuspension rate constant make to the overall net resuspension rate. Of course resuspension is not an instantaneous process and we know that the resuspension rates will vary significantly in the short term for $0 < \omega t < 10$ to $\omega t \gg 1$ in the long-term.

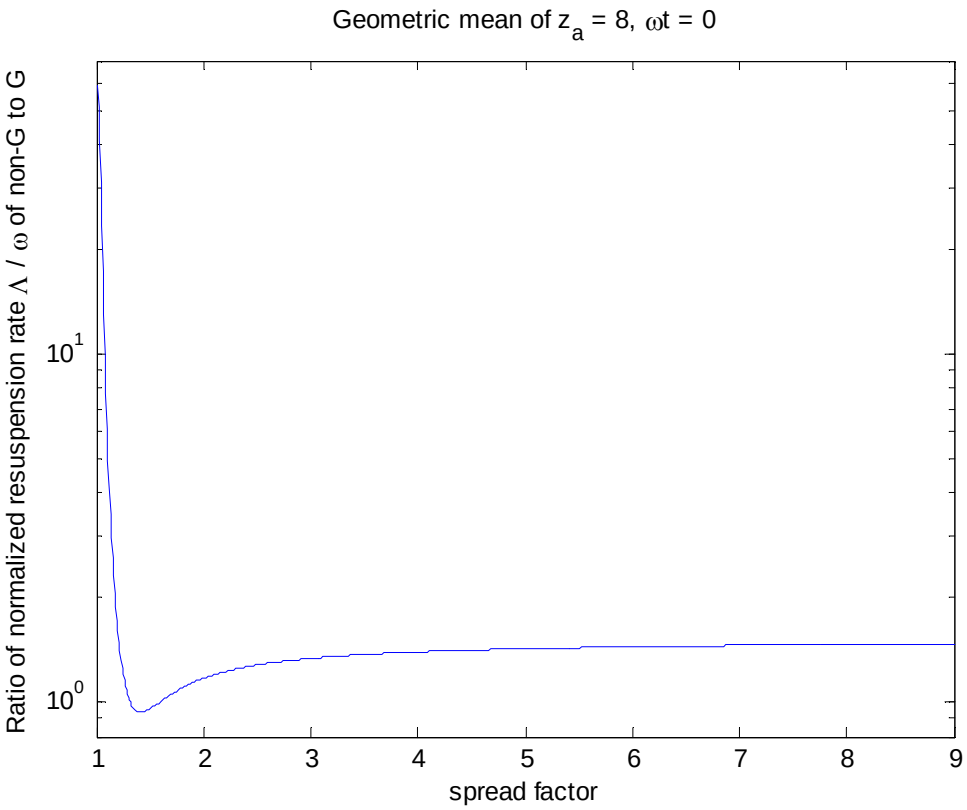

Figure 4.22 - Ratio of normalized resuspension rate of non-Gaussian to Gaussian vs. spread

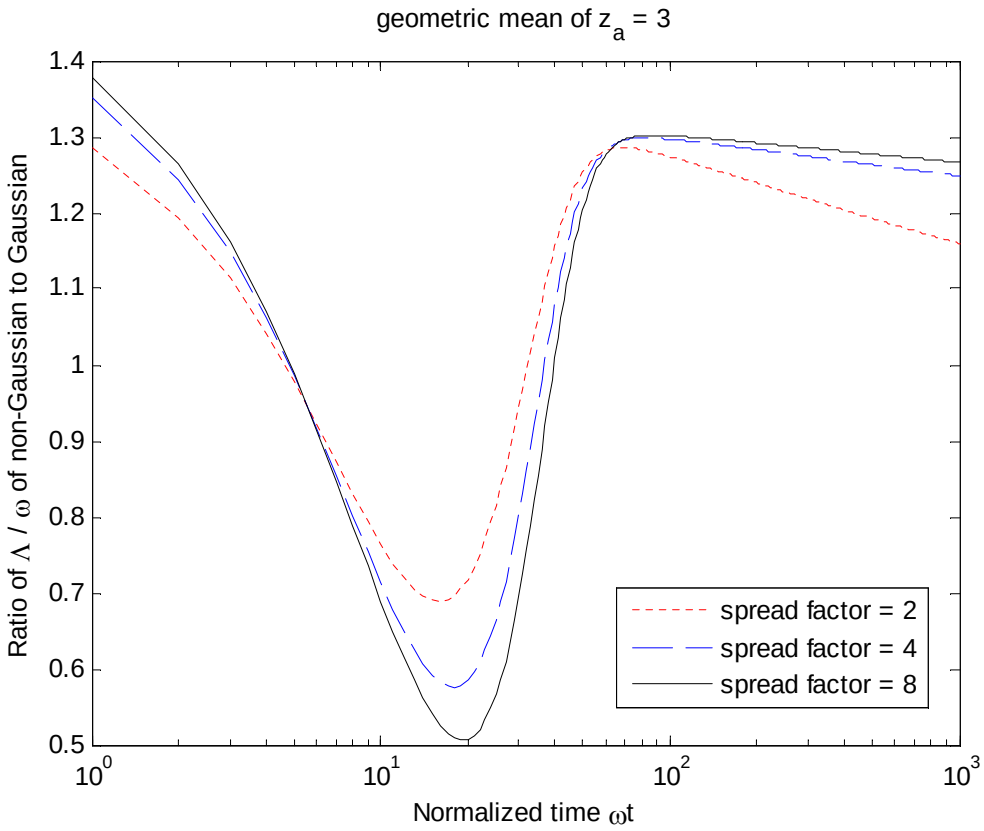

Figure 4.23 - Ratio of normalized resuspension rate of non-Gaussian to Gaussian vs. ωt (z_a = 3)

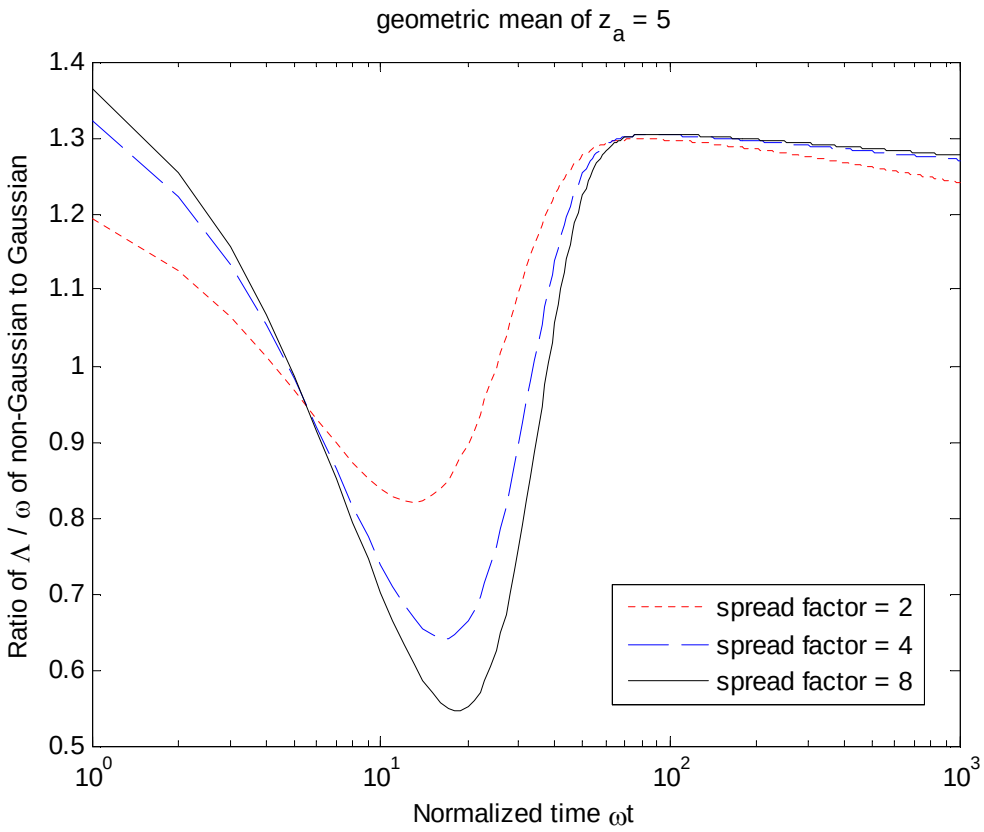

Figure 4.24 - Ratio of normalized resuspension rate of non-Gaussian to Gaussian vs. ωt (z_a = 5)

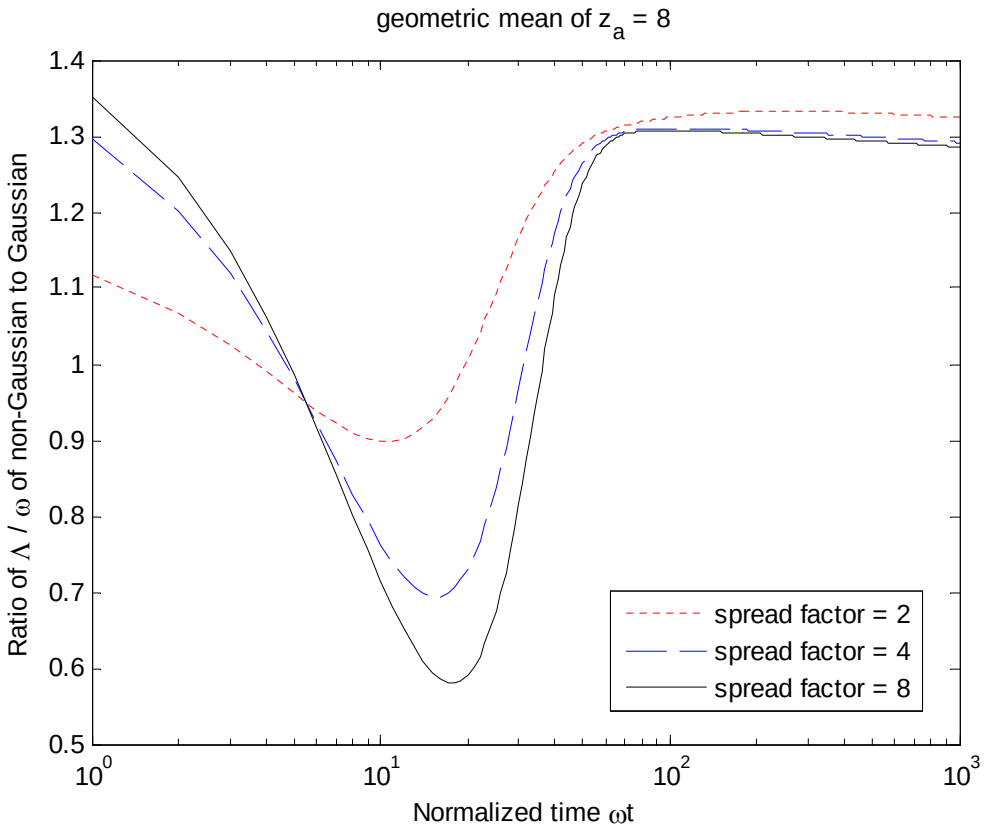

Figure 4.25 - Ratio of normalized resuspension rate of non-Gaussian to Gaussian vs. ωt (z_a = 8)

Figure 4.23 - Figure 4.25 show the ratio of non-Gaussian to Gaussian normalized resuspension rates as a function of time for a range of spread factors (typical of smooth to rough surfaces) and values of the geometric mean of the normalized adhesive forces z_a when the geometric mean ≈ mean aerodynamic force (z_a ~ 3) to when it is significantly greater than mean aerodynamic force (but still within the range of the experimental results for z_{dh}). In all cases the resuspension rates and times are suitably normalized on ω. The figures show that for a spread from 2 to 8, the ratio starts off > 1 (as in Figure 4.21) and decreases reaching close to unity at values of ωt ~ 5, and reaching a minimum value for value of ωt ~ 20 but whose precise value increases with the spread. The actual minimum value is less the greater the spread. In the region of 5 < ωt < 40, the ratio is less than 1 and for ωt > 40 the ratio is greater than 1 and rising to a maximum value ~ 1.3 at ωt ~ 60. Beyond this value of ωt, the ratio flattens out to a constant value larger than 1 which depends on the spread factors and geometric means of z_a. It shows that for the long-term, the resuspension rate of the non-Gaussian model is always larger than the Gaussian case at a fix ratio value. In Figure 4.26 we show the actual values of the resuspension rates for the Gaussian and non-Gaussian models which indicating the transition from short to long-term resuspension occurring at ωt ~ 20.

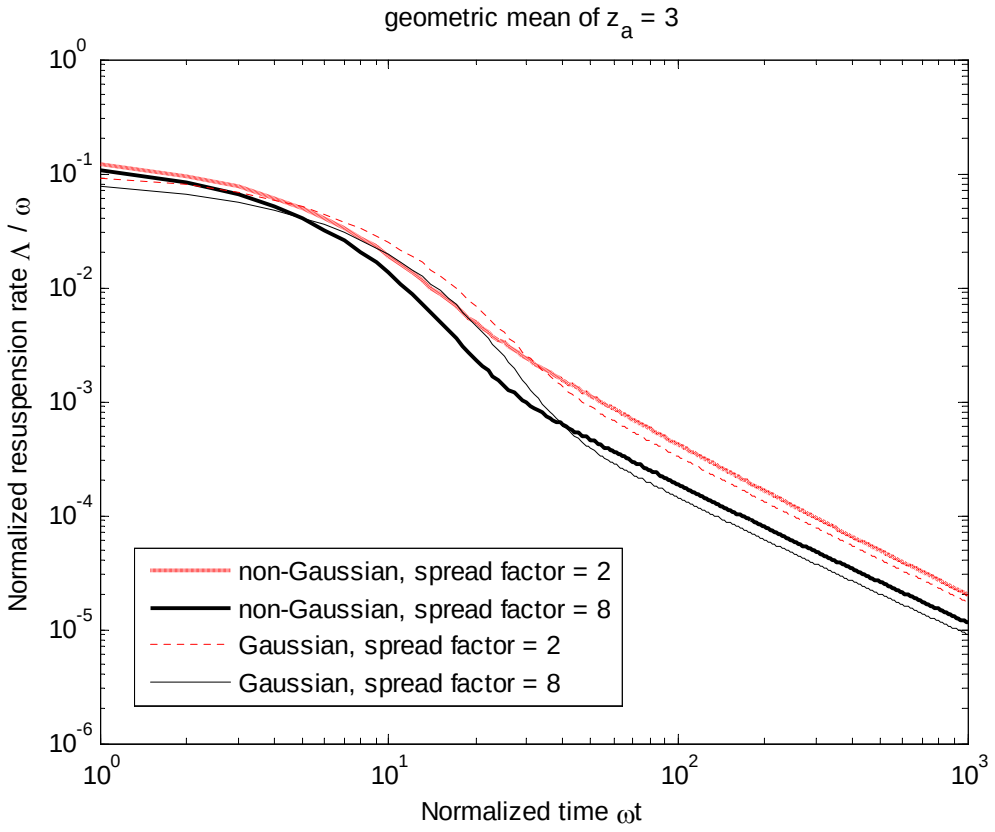

Figure 4.26 - Normalized resuspension rate of non-Gaussian and Gaussian model vs. ωt (z_a = 3)

4.1.3.2 Comparison of DNS and LES for Resuspension Predictions

In this section we show the sensitivity of the resuspension rate and fraction resuspended to the values of the parameters in Table 4.3 based on the LES and DNS data. The main difference is reflected in the difference in values for ω^+ values of frms being very similar in either case for the values of y^+ that were measured. The typical forcing frequency due to the turbulence, ω whether in real time or wall units ω^+ is a scaling parameter for the resuspension rates so we can use Figure 4.26 to obtain the value of the resuspension rates for any value of ω^+ at any real time (recognising that the values of the normalized resuspension rates in Figure 4.26 at any give value of ωt don't refer to the same values in real time if the value of ω or ω+ are different. The resuspension rates for LES or DNS can be obtained directly from Figure 4.26 by compressing or expanding the horizontal and vertical scales appropriately. Thus if the real time is t we have the formula

$$\frac{\Lambda_{DNS}(t)}{\Lambda_{LES}(t)} = \frac{\omega_{DNS}\widehat{\Lambda}(\omega_{DNS}t)}{\omega_{LES}\widehat{\Lambda}(\omega_{LES}t)}$$

where subscripts DNS and LES refer to the DNS and LES measurements. So whether this radio is > or < 1 depends on the ratio of ω_{DNS} / ω_{LES} and the ratio of the normalized resuspension rates in Figure 4.26 measured at different values of the normalized time.

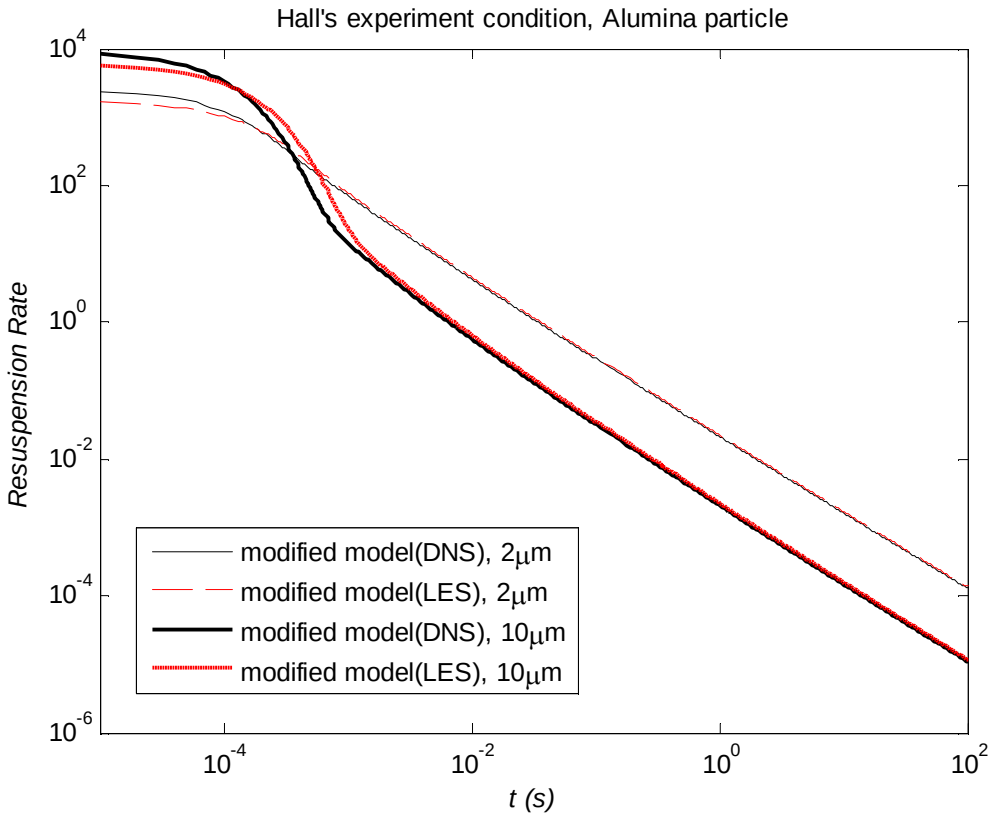

Figure 4.27 - Comparison of resuspension rate between LES and DNS, Biasi's correlation is applied for the adhesive reduction and spread

DNS values are not universally > LES values and vice versa. The features are illustrated in Figure 4.27 using the specified flow and particle adhesions properties measured in Hall's experiment and two different particles (2μm and 10μm in diameter).

Hall's experiment condition:

$\rho_f = 1.181\, kg \cdot m^{-3}, \quad y = 0.56\, J \cdot m^{-2}$, $v_f = 1.539 \times 10^{-5} m^2 \cdot s^{-1}, \quad u_\tau = 2.19\, m \cdot s^{-1}$

Biasi's correlation (Eq.[4.7]):
2μm (diameter): m (reduction) = 0.0137 and sf (spread factor) = 1.936;
10μm (diameter): m = 0.0105 and sf = 3.095.

Note that resuspension rate based on the DNS data is not consistently larger than that for the LES measurements even though $\omega_{DNS} > \omega_{LES}$ (subscripts DNS and LES refer to the DNS and LES measurements).

Long-term resuspension rate

We recall that the long-term resuspension rate follows a power law decay of the form (Reeks *et al.*, 1988),

$$\Lambda(t) = \xi_1 t^{-\xi_2} \qquad [4.37]$$

where ξ_1 and ξ_2 are constants and ξ_2 is close to 1.

Here we have computed using both the DNS and LES data the power law exponent ξ_2 and the constant ξ_1 as functions of the friction velocity for the 10 micron (diameter) alumina particles using a reduction in adhesion 0.0105 and a spread in adhesion of 3.095 based on Biasi's correlation (Eq.[4.7]). Hall's experimental flow conditions are used to calculate the results.

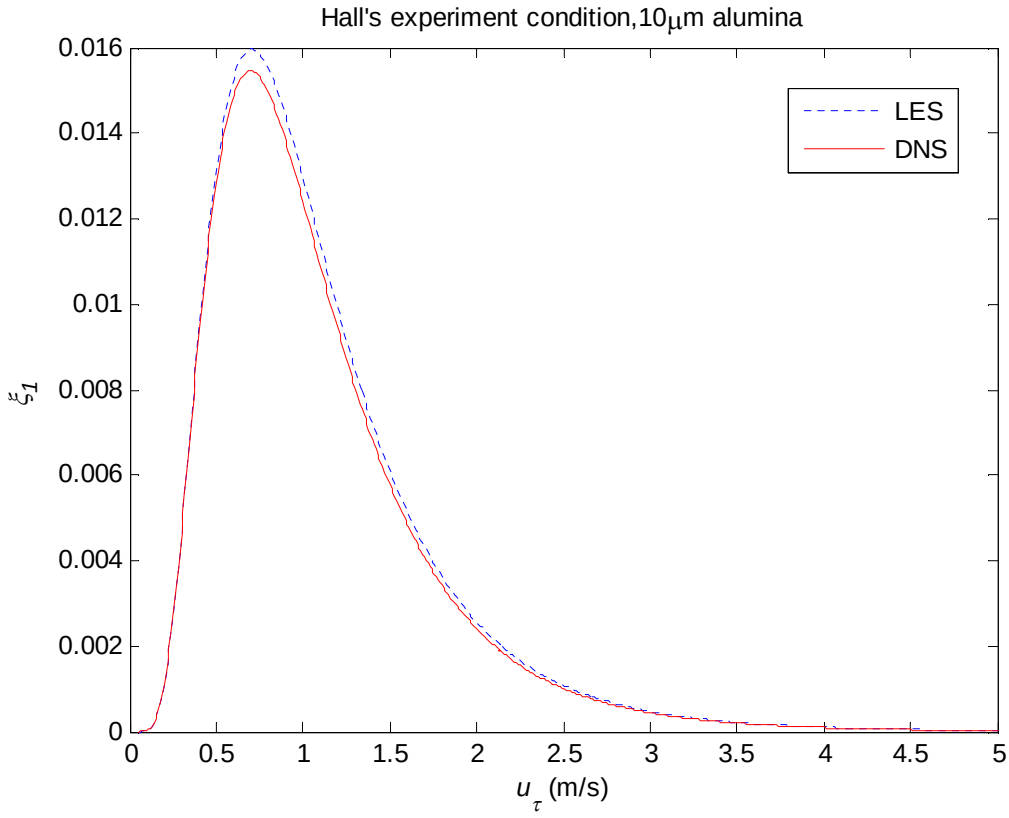

Figure 4.28 - Comparison of long-term resuspension rate constant 1 between LES and DNS, Biasi's correlation for adhesion is applied

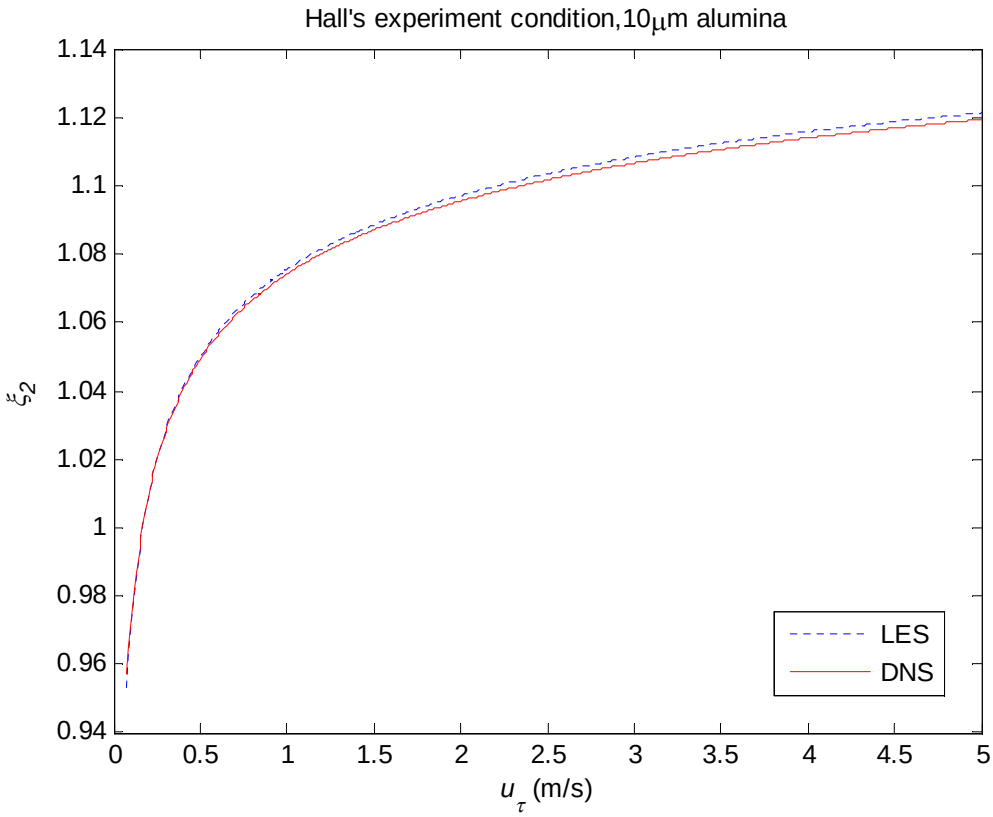

Figure 4.29 - Comparison of long-term resuspension rate constant 2 between LES and DNS, Biasi's correlation for adhesion is applied

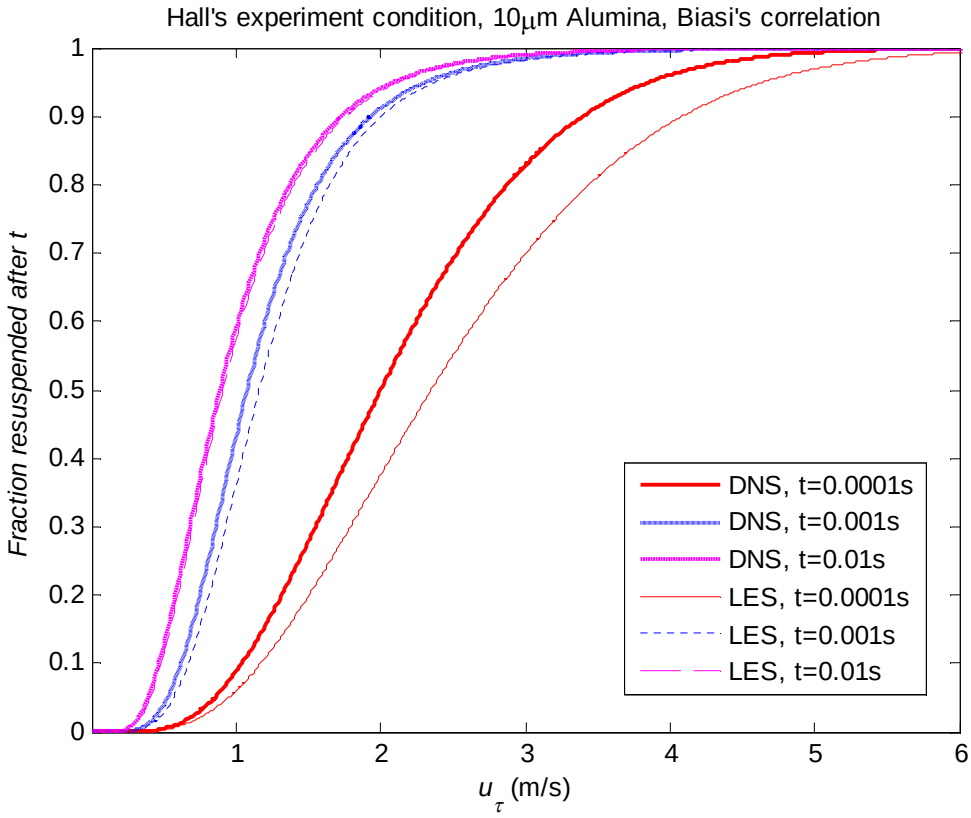

Figure 4.30 - Comparison of fraction resuspended for exposure time step between LES and DNS

Figure 4.28 shows the relationships between ξ_2 and friction velocity based on the DNS and LES measurements. Both the LES and DNS data give values of ξ_2 ~ 1 as expected but the LES values are slightly > DNS value indicating a slightly > decay in time. Note that the exponent approaches unity for a friction velocity approaching zero. Figure 4.29 shows how ξ_1 varies with friction velocity based on the DNS and LES data indicating that the two curves are remarkably close to one another despite the significant difference in the corresponding values of ω^+. We note that the constant ξ_1 approaches zero as the friction velocity tends to zero i.e. zero resuspension rate. At the other extreme as the friction velocity approaches infinity, ξ_1 also approaches zero. In this case the fraction of particles removed initially in the short term resuspension phase approaches unity, so that the fraction available for long term resuspension approaches zero and hence the long term resuspension rate reflected in the value of ξ_1 approaches zero. There is clearly a maximum value somewhere in between.

In Figure 4.30, we examine the influence of the difference in values of ω^+ (See Table 4.3) on the fraction resuspended as a function of time. We employ the same flow conditions using the same flow and adhesion properties as in Hall's experiment. The most significant difference occurs when resuspension times t ~ 0.0001 or $\omega^+ t^+$ <~ 1 (where $t^+ = t u_\tau^{\,2} / v_f$). The value of $1/\omega^+$ in this case is

7.8652 based on the DNS data (y^+ = 6). The DNS data gives more resuspension rate for $\omega^+ t^+ <\sim 1$ than the LES data because the measured value of ω^+ is greater.

For the case of t = 1s, there is very little difference between the LES and DES predictions because for this value all the short term resuspension has occurred (what is left is the fraction that resuspends over a much longer timescale). Figure 4.31 shows that the modified model based on DNS gives results very close to LES case for both 2μm and 10μm particles.

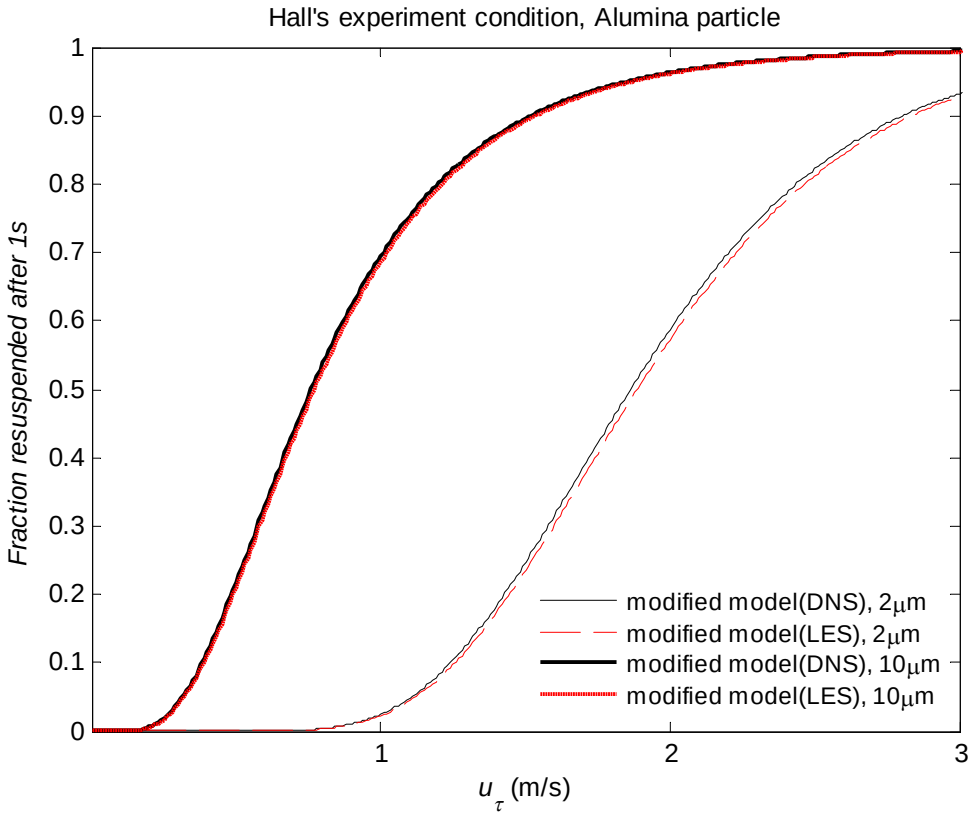

Figure 4.31 - Comparison of resuspension fraction after 1s between LES and DNS

Furthermore, the effect of spread factor for different sizes particles is presented in Figure 4.32. Values for the fraction resuspended after 1s based on DNS and LES data are very close, except there is a noticeable difference (ratio up to 1.3) when the friction velocity is small. It is also shown that when the spread factor is small, in other words, the adhesive distribution is very narrow the ratio between two models decreased which indicated that the non-Gaussian DNS model removes particles much easier than in the small friction velocity region on a very rough surface. The forms of the curves and the maximum reflect the fact that the predictions based on DNS and LES data both tend towards zero when the friction velocity tends to zero, and tends to unity when the friction velocity is very large. Most of the resuspension that occurs in the time of 1s is largely short term resuspension. For small friction velocities this is very small and is dominated by the value of ω^+ where there is a significant difference between the values based on DNS and LES data (the ratio of DNS / LES frequencies ~1.5 for y^+ = 6).

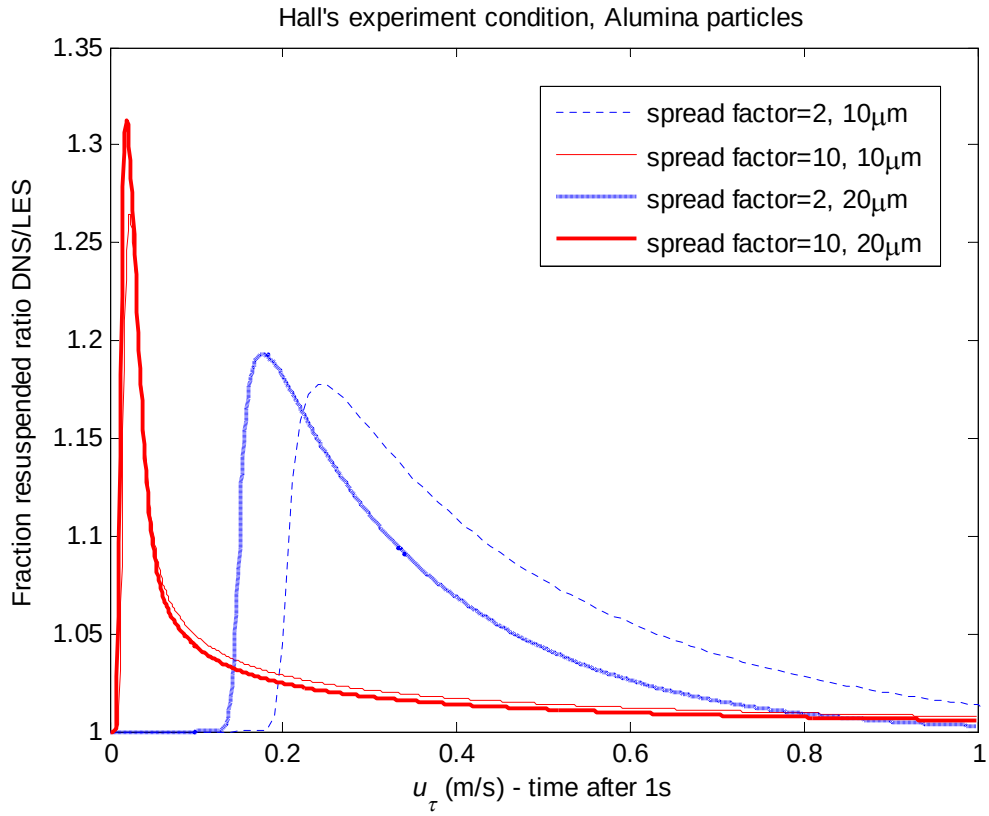

Figure 4.32 - Comparison of resuspension fraction ratio for DNS and LES approaches

In summary, the modified models by LES and DNS approach give similar results. The major difference between the two approaches reflects the difference in the values of the typical forcing frequency ω^+ (for $y^+ = 6$, ω^+ is 0.08553 for LES case and 0.127143 for DNS case). This is probably the reason that DNS approach considers the small eddies in the simulations. From now on, we will use the DNS approach ($y^+ = 0.1$) as the modified R'n'R model, because where the data obtained is much closer to the wall.

4.1.4 Comparison of Original and Modified R'n'R model

There are several points that need to be clarified before we make a comparison of the predictions made by the two models.

- O'Neill's formula (Eq.[4.18]) is used to calculate the resultant fluctuating aerodynamic force from the fluctuating streamwise velocity.
- The correlations (Eq.[4.38]) between the distribution of fluctuating force and its derivative are not significant and are therefore neglected in the modified model.
- The parameters from DNS ($y^+ = 0.1$) are used in the modified model because the value of y^+ is much closer to the value of the typical particle radius r^+ (in wall units). Although it is shown in Table 4.3 that the typical forcing frequency ω^+ varies with y^+, at the moment the typical forcing frequency ω^+ value is a fixed value chosen from the case $y^+ = 0.1$ due to the fact that there are not enough simulation data to produce the relationship between ω^+ and y^+. It will be recommended in future work.
- Biasi's correlation (Eq.[4.7]) is applied in both the modified and original models to calculate the reduction and spread in adhesion as a function of particle size. It is the up-to-date adhesion correlation and is also based on Hall's experimental data.

As a useful preliminary we recall that in Hall's experiment (Reeks & Hall, 2001) there were three types of particles (10μm alumina, 20μm alumina and 10μm graphite) used in the experiment. Hall measured both the adhesive force and resuspension of those particles. The measurement of adhesion forces for a mono layer of these three particle types distributed uniformly over a polished type 316 stainless-steel surface were carried out using an MSE Superspeed 75 centrifuge. In all three cases, measurements of the fraction removed were made for forces applied both normal and tangential to the substrate upon which the particles were deposited in dry conditions. It was reported that the centrifuge had to spin 10 times faster to dislodge a proportion of particles normally than by removing the same proportion tangentially. As the applied force is proportional to the square of the spin speed this implies that the net value of $r/a = 100$ (particle radius over the distance between neighbouring asperities).

For the resuspension phase, the air flow, provided by a Griffin blower, passed through a series of ducts into a plenum chamber to damp out any flow fluctuations. The air passed through an absolute filter to ensure that no particulate was present in the air stream. To establish fully developed flow, the air then passed through a 5 m long 0.2 m x 0.02 m rectangular duct in which the test section was situated 3.5 m downstream along the duct. At the end of the duct a sample of the air passed through a counter which had the facility to record the particle concentration as a function of time in four size intervals. Prior to each resuspension run, the particles used were sub-divided using a spinning riffler to ensure that the size distributions of particles used in the various runs were as similar as possible. The test section was polished with diamond paste, and then degreased using a 5% solution of Decon 90 in distilled water. The particles were deposited on the surface by

transporting them by compressed air through two impinging jets which broke up any agglomerates. The suspension was then injected into still air and allowed to settle on the test surface and on the centrifuge cells for adhesion measurements. Samples of the particles deposited both upstream and downstream of the test section were taken for subsequent size analysis using an IBAS image analyzer. The test section was then placed in the air rig. A photograph of the particles was then taken when the air rig was started and the velocity increased in steps with photographs taken of the test surface at each step. After the run the photographs taken were compared and the fraction remaining on the surface at each stage was determined by observing which particles had left the surface.

There were 20 resuspension runs for both graphite and alumina particles performed in Hall's experiment. Here the experimental data of Run – 9, 10, 15 (for 10μm alumina, in diameter) and Run – 7, 8, 20 (for 20μm alumina particles) will be used to compare with the modified and original model results.

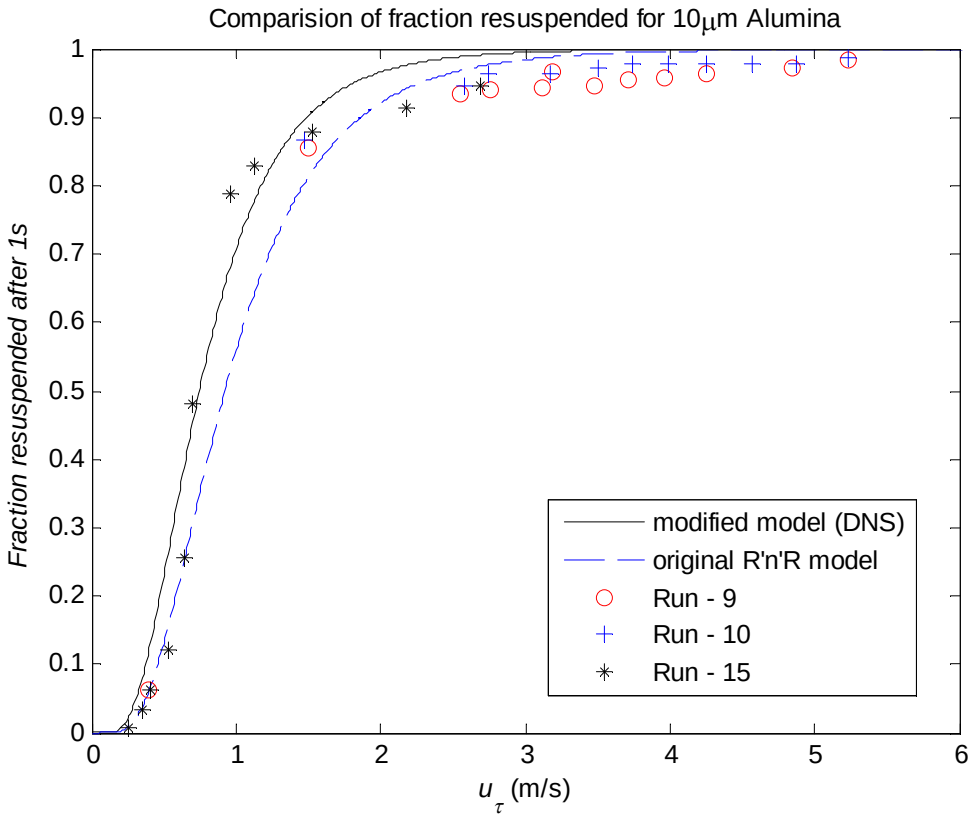

Figure 4.33 - Comparison of resuspension fraction to Hall's experiment (10μm)

Note the calculation of the fraction responds after 1 s is a nominal time, just so long as the time is sufficient for the resuspension rates at the end of the exposure time are very small (and in the long term resuspension range).

Figure 4.33 also shows the comparison of resuspension fraction calculated from the modified and original R'n'R model with the experimental data for 10μm alumina particles. It can be observed that the modified model gave closer results to the experimental data in the region which the friction velocity is from around 0.5m/s to 1.5m/s. Although the modified model gave more resuspension than the experimental data when friction velocity was smaller than 0.5m/s and larger than 1.5m/s, the solid curve still had a closer trend to the experimental data than the original model did. This observation is also true for 20μm alumina particles as can be observed in Figure 4.34.

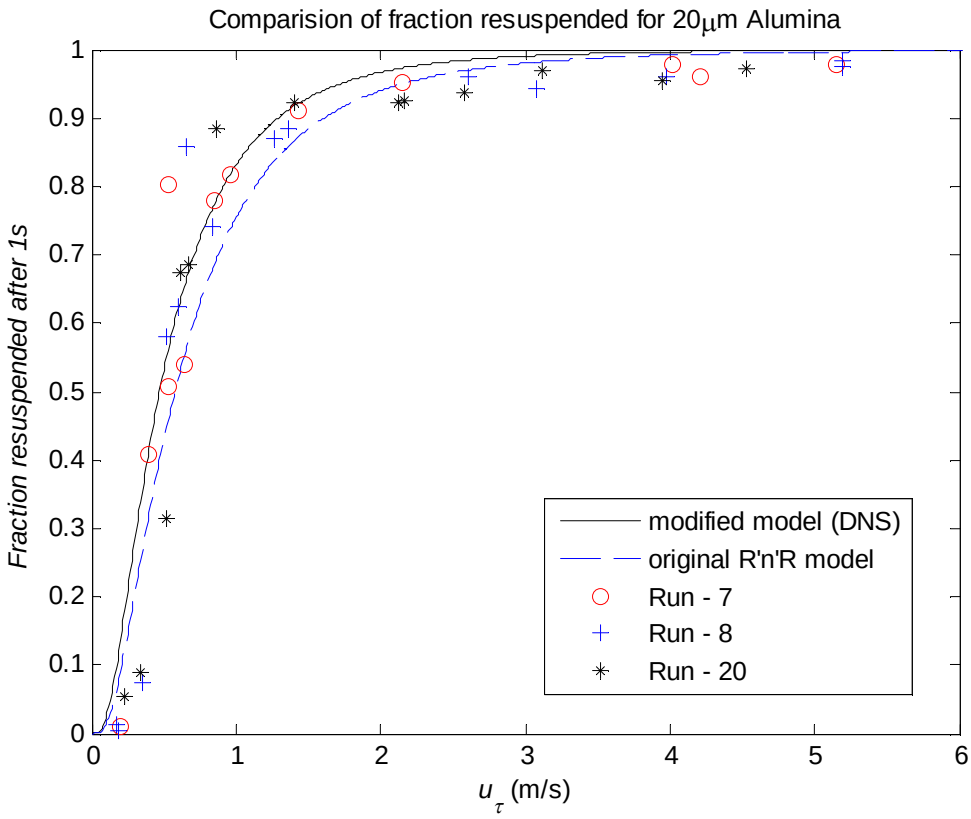

Figure 4.34 - Comparison of resuspension fraction to Hall's experiment (20μm)

To investigate the difference between the modified and original model predictions, the effect of two important parameters (the typical forcing frequency ω^+ and the rms coefficient f_{rms}) are studied here. A table is shown below for the difference of these two parameters.

	ω^+	f_{rms}
Modified (DNS)	0.164189	0.366
Original R'n'R	0.0413	0.2

We have calculated the fraction resuspended after 1s as a function of friction velocity and resuspension rate as a function of time for 10μm alumina particle using a reduction in adhesion 0.0105 and a spread in adhesion of 3.095 based on Biasi correlation (Eq.[4.7]). Hall's experimental

condition is used to calculate the results. In order to compare, we used the values of the two parameters which are from original R'n'R model in the modified model. The results are shown below.

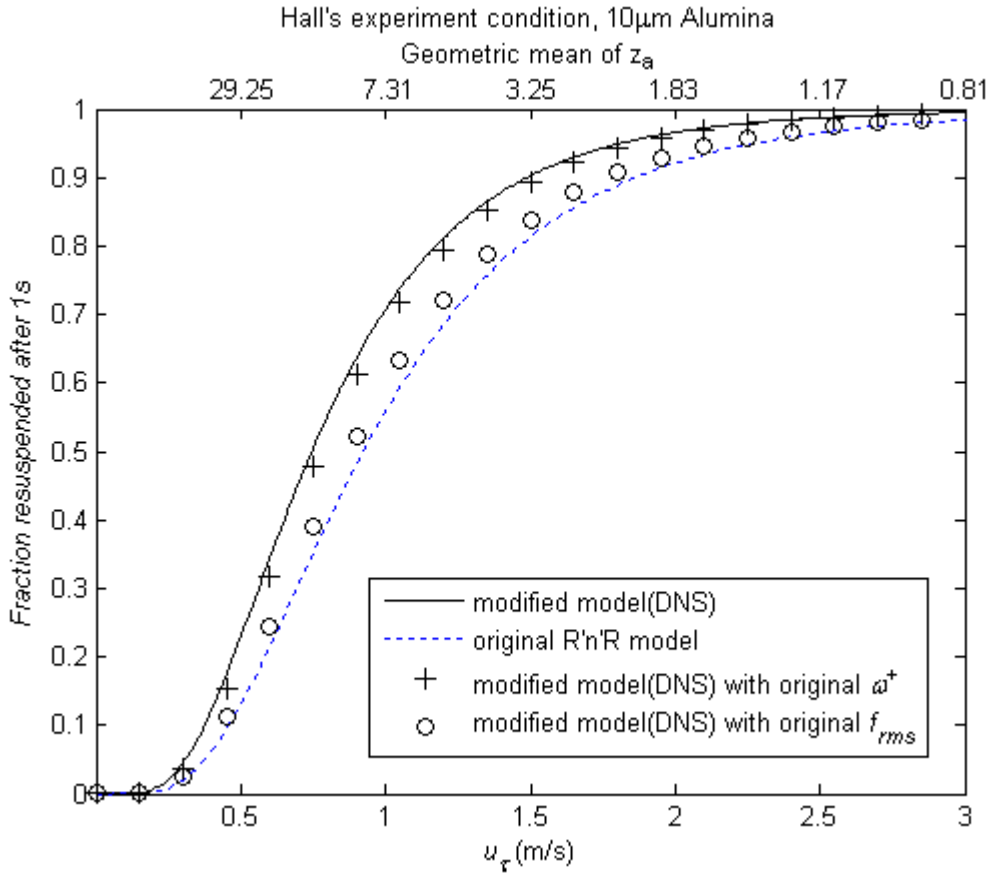

Figure 4.35 - Comparison of resuspension fraction after 1s between modified and original model

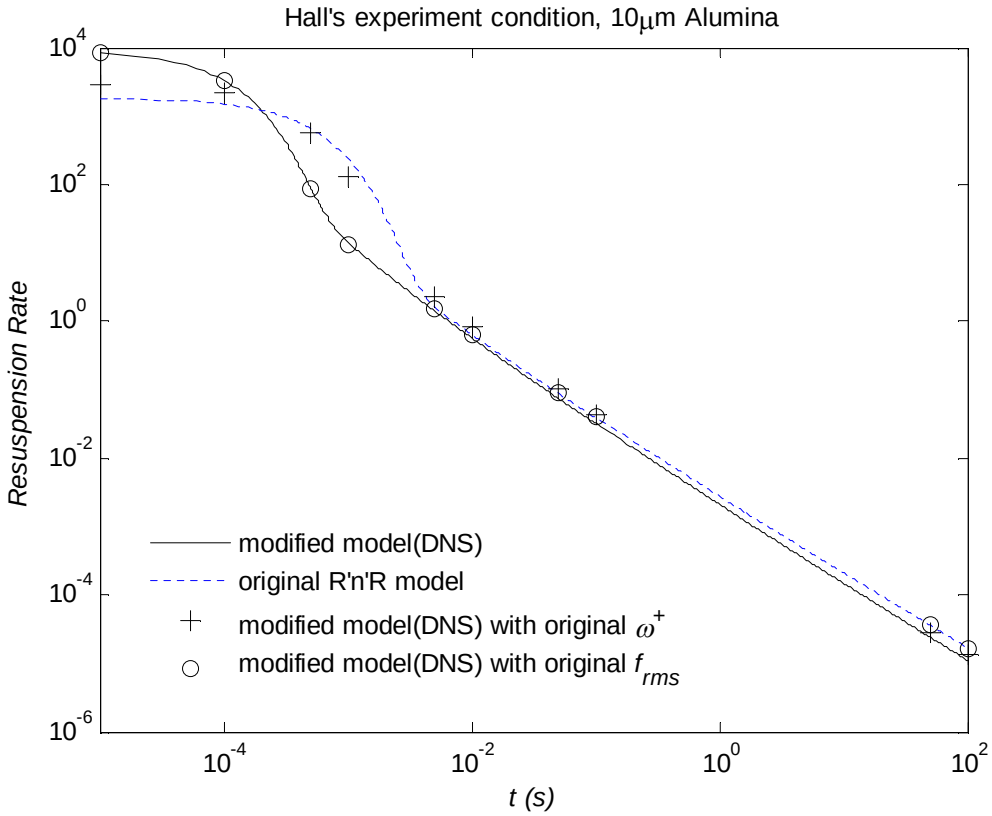

Figure 4.36 - Comparison of resuspension rate between modified and original model

Figure 4.35 and Figure 4.36 show the fraction resuspended and resuspension rate of modified and original model. There are two points noted here:

- The effect of the typical forcing frequency ω^+ on the resuspension fraction after 1s is not significant (consistent with our observations in the previous section). However, it affects dramatically the short term resuspension rate t < 0.0001 (or $\omega^+ t^+ <\sim 1$). From Figure 4.36, one can observe that as the original ω^+ is applied in the modified model (cross point) the initial rates reduce significantly as compared to the modified model results (straight line).

- The rms coefficient f_{rms} is the key parameter for long term resuspension fraction (not to be confused with long term resuspension rates, the long term resuspension fraction includes the integrated history from time zero and includes the short term resuspension rates). As one can observe from Figure 4.35, when the original rms coefficient f_{rms} (0.2) was used in the modified model (circle point) the result is much closer to the original model result (dotted line).

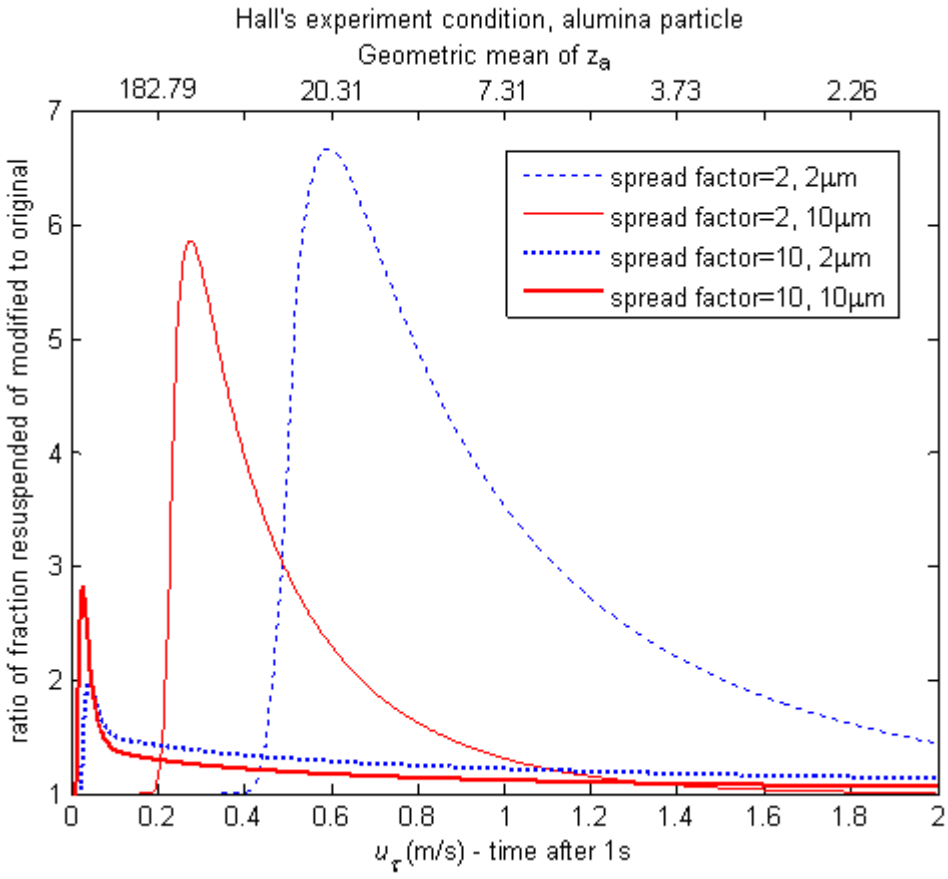

Figure 4.37 - Comparison of resuspension fraction ratio of modified (DNS) to original model

Furthermore, it is noted that the difference between the fraction resuspended of modified and original model could become significant when the friction velocity is small. As shown in Figure 4.37, the ratio increases to around 6 or 7 on a nominally smooth surfaces (spread = 2) when friction velocity is smaller than 1m/s.

Long-term Resuspension Rate

Recall the long-term resuspension rate

$$\Lambda(t) = \xi_1 t^{-\xi_2}$$

where ξ_1 and ξ_2 are constants and ξ_2 is close to 1. Here we have computed the power law exponent ξ_2 and the constant ξ_1 for both the modified model (DNS) and original model as functions of the friction velocity for the 10 micron (diameter) alumina particles using a reduction in adhesion 0.0105 based on Biasi correlation (Eq.[4.7]) and varies spread factors (Biasi 3.095, 5 and 8). Hall's experiment condition is applied in the calculation.

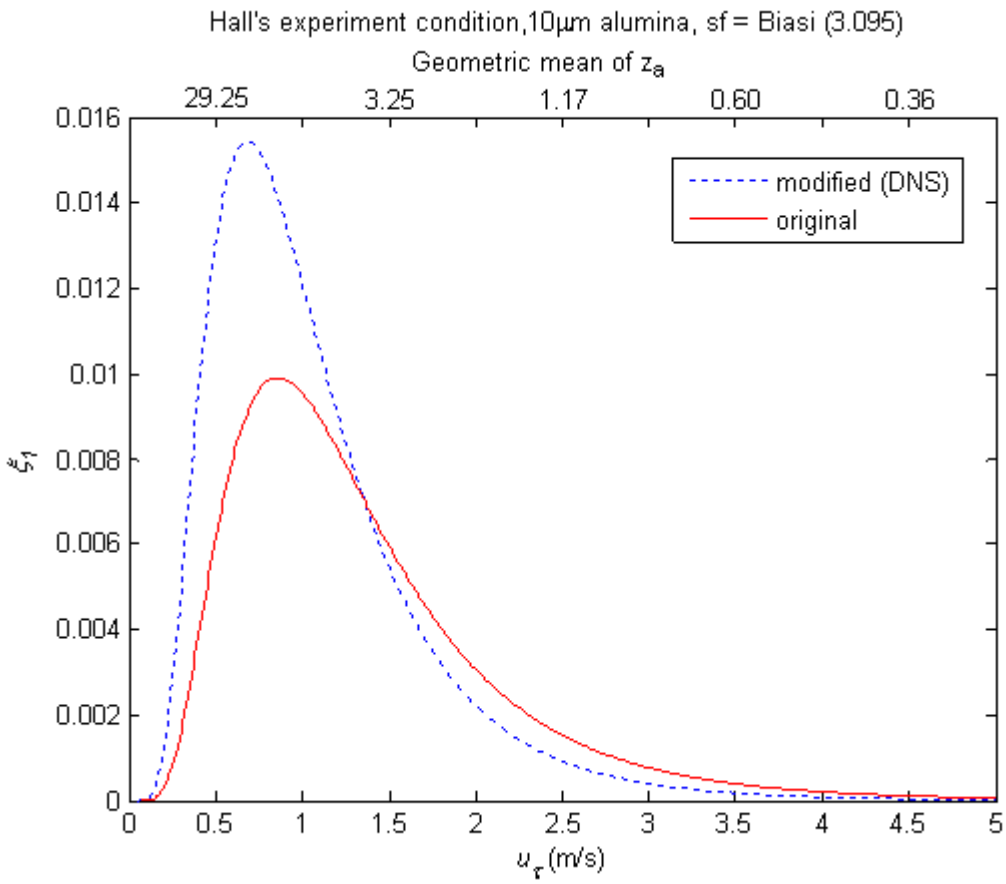

Figure 4.38 - Comparison of long-term resuspension rate constant 1 between modified and original

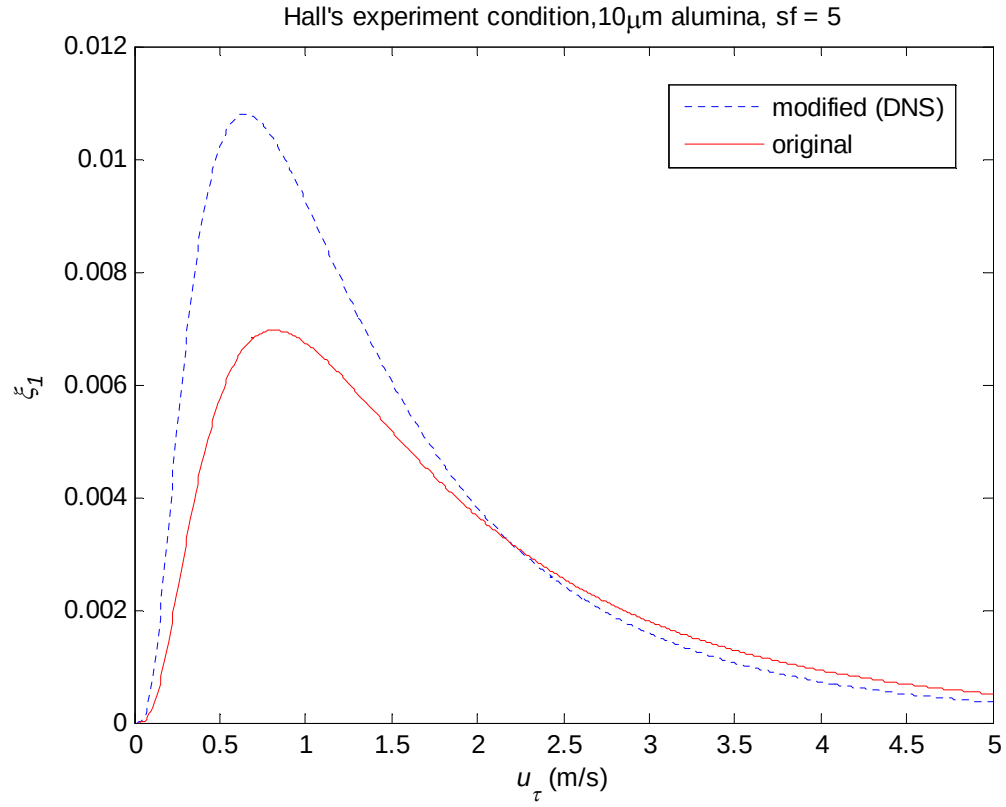

Figure 4.39 - Comparison of long-term resuspension rate constant 1 between modified and original

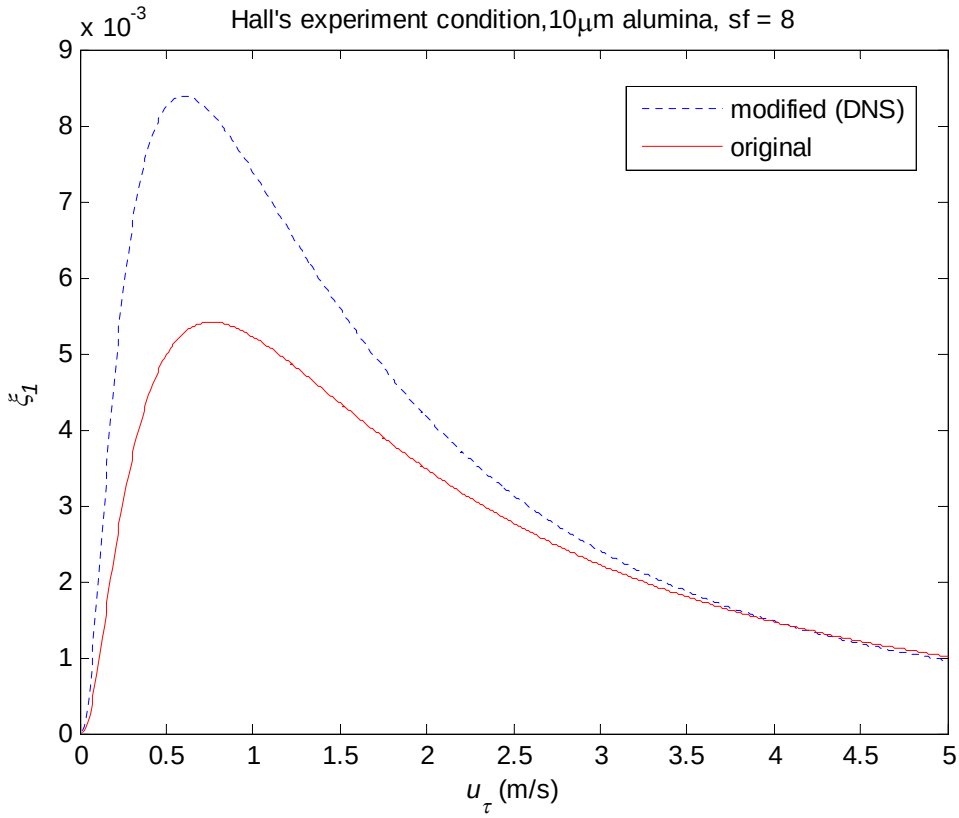

Figure 4.40 - Comparison of long-term resuspension rate constant 1 between modified and original

Figure 4.38 - Figure 4.40 shows how ξ_1 varies with the friction velocity for different spread factors. There is always a maximum value of ξ_1 in each graph. These features are also apparent in the earlier graphs where we compared the DNS and LES (see Figure 4.28) and the explanation is the same as that provided. We recall there was no discernable difference between the LES and DNS predictions where the values of f_{rms} were the same but the values of ω^+ significantly different. We can conclude that the difference between the modified and original model is due to the difference in values of f_{rms}. Figure 4.41 shows that the ratio of ξ_1 between the two models for different spread factor. One can observe that when for a spread factor < 3 (the lowest value taken), there is a remarkable difference between two models for small values of the friction velocity < 0.1 m/s).

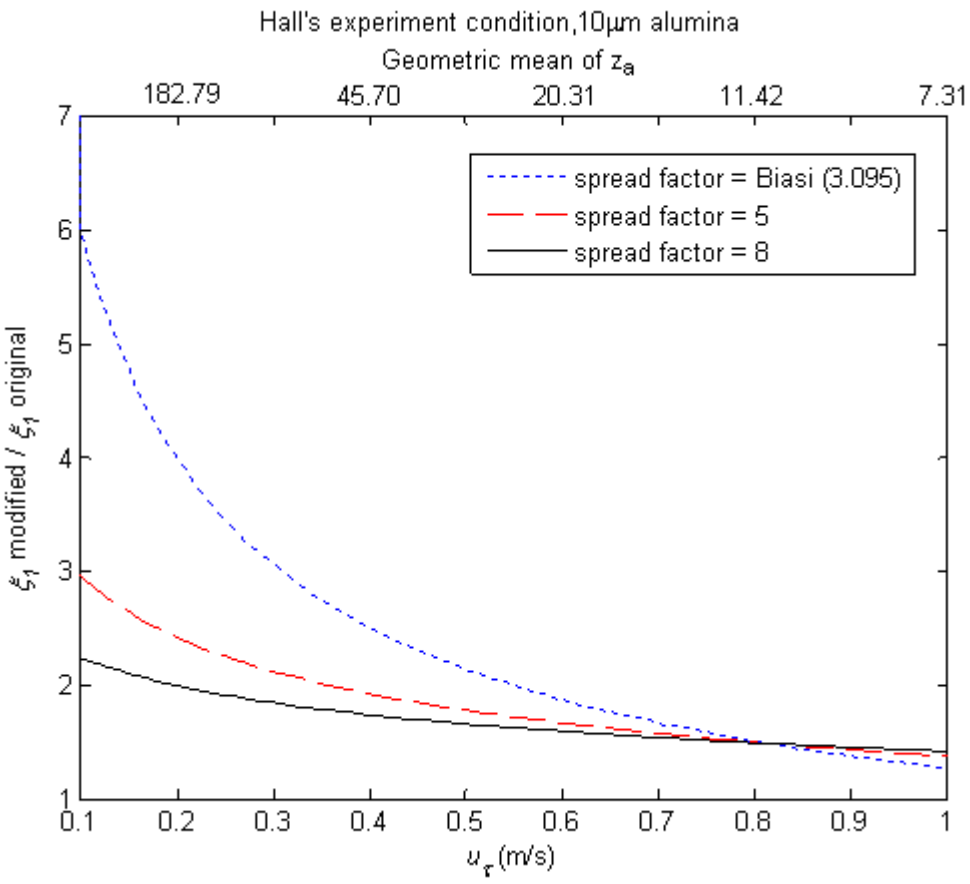

Figure 4.41 - Ratio of long-term resuspension rate constant 1 of modified to original

Figure 4.42 - Figure 4.44 described the relationship between ξ_2 and friction velocity for different spread factors. The values of ξ_2 are close to 1 for both modified and original model as expected. Also as the spread factor increases from 3.095 to 8, the difference between the two models predictions reduces as the value of ξ_2 reduces.

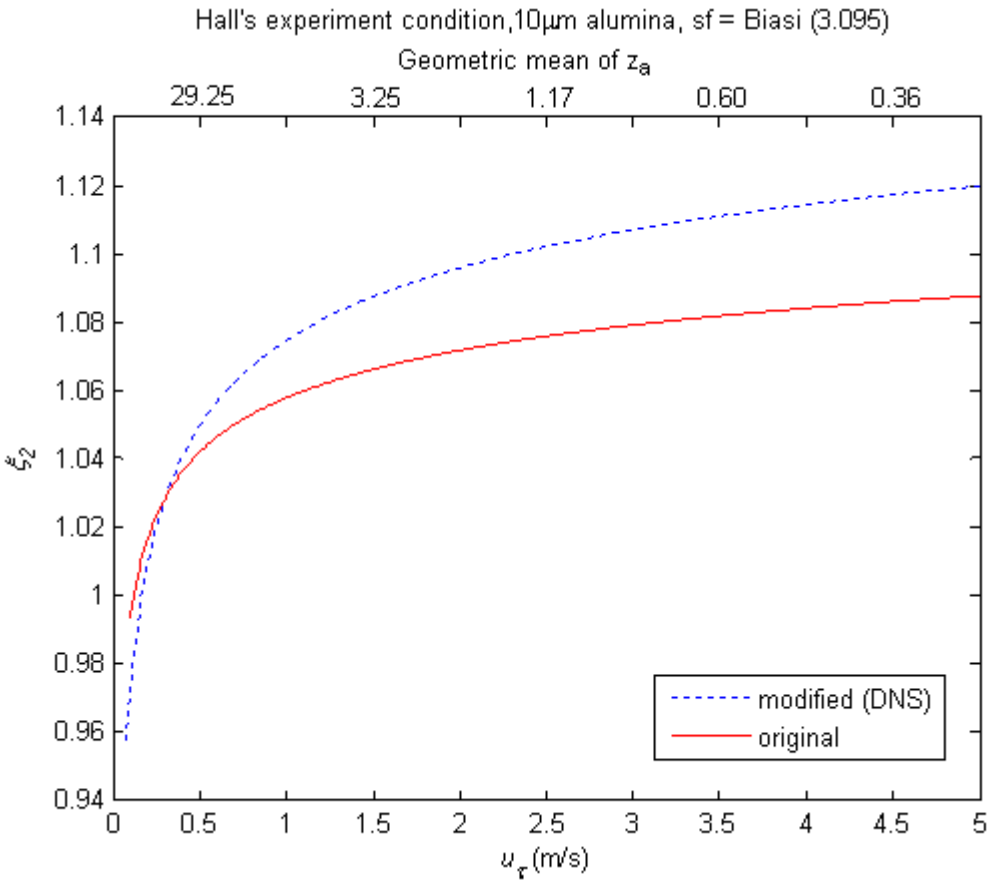

Figure 4.42 - Comparison of long-term resuspension rate constant 2 (spread factor = Biasi, 3.095)

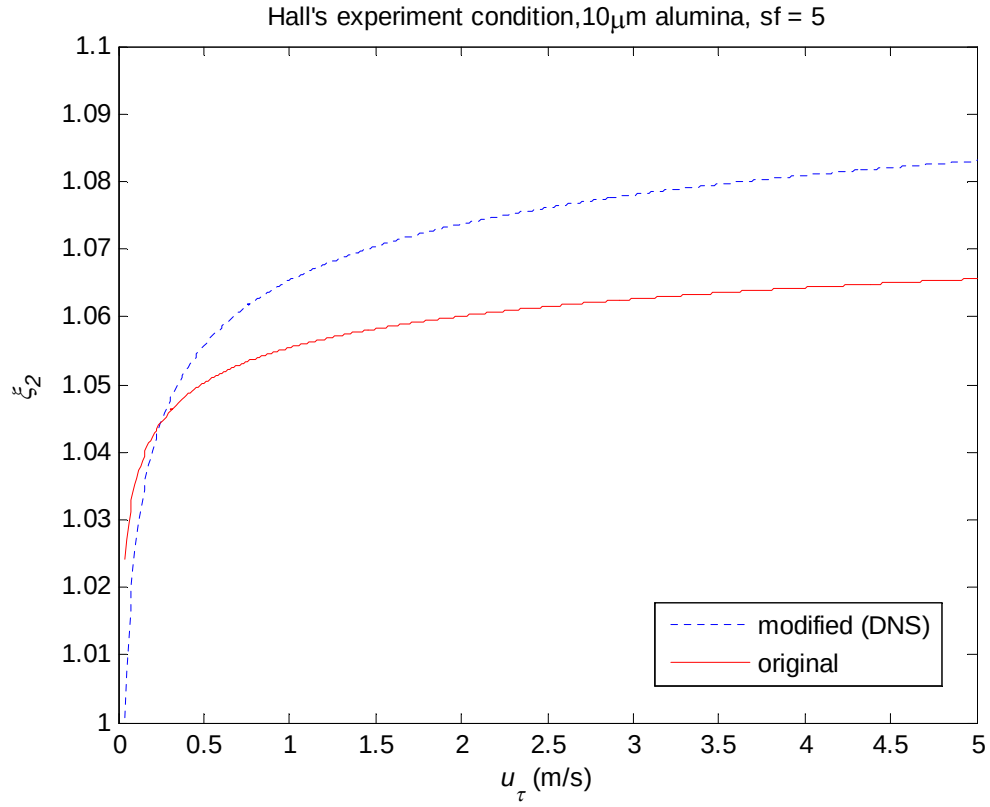

Figure 4.43 - Comparison of long-term resuspension rate constant 2 (spread factor = 5)

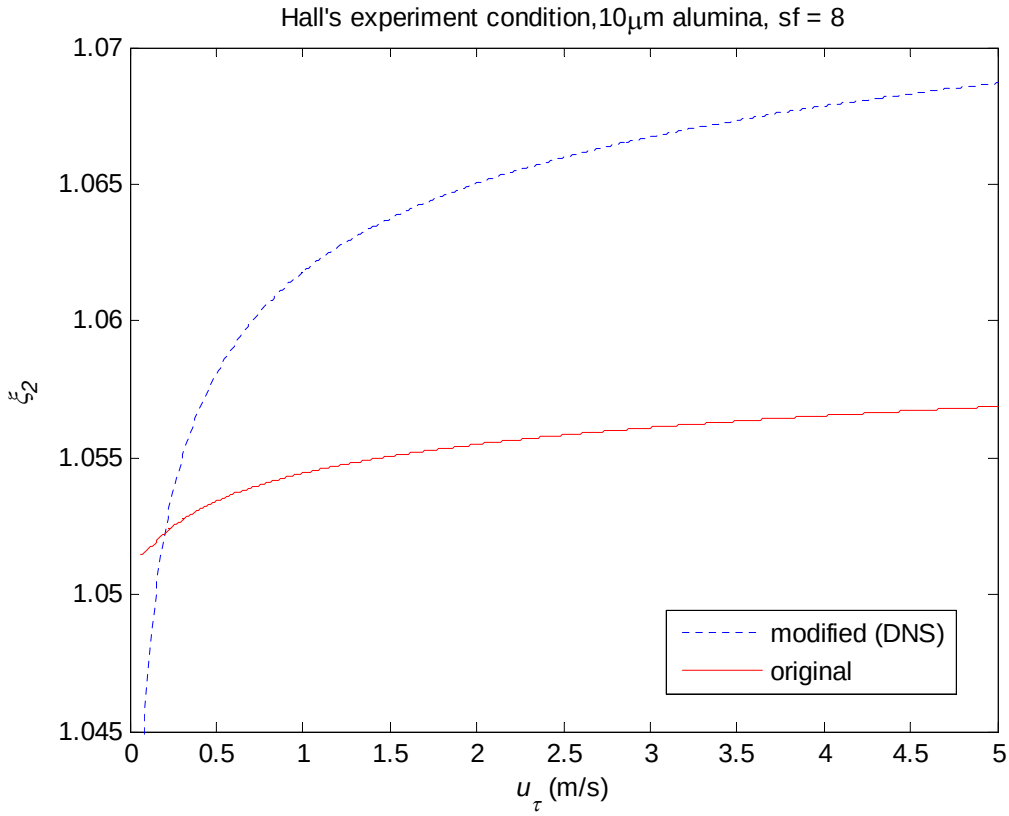

Figure 4.44 - Comparison of long-term resuspension rate constant 2 (spread factor = 8)

4.1.5 Literature Comparison on Streamwise Fluctuating Velocity

The fluctuating aerodynamic resultant force according to Eq.[4.18] is proportional to the streamwise fluctuating velocity. In this section in order to validate the Rayleigh distribution of fluctuating streamwise velocity, other similar measurements reported in the literature will be considered in terms of a comparison of distribution (histogram) and skewness. There are surprisingly few measurements of the distribution of the fluctuating velocities reported in the literature. Here our LES and DNS results are compared to the DNS data produced by Moser *et al.* (1999) for different shear Reynolds numbers (Figure 4.45). One can observe that although there is a dip in the small velocity region (near 0) in both the DNS and LES result, the histograms are very close in the wings and they are independent of the shear Reynolds numbers. The reason for the dip might be because of the lack of sufficient velocity data in that region (near 0) or more likely the nature of the flow. At the moment, the evidence is not enough to draw conclusions. However, those very small fluctuations will not affect the values of the resuspension we predict.

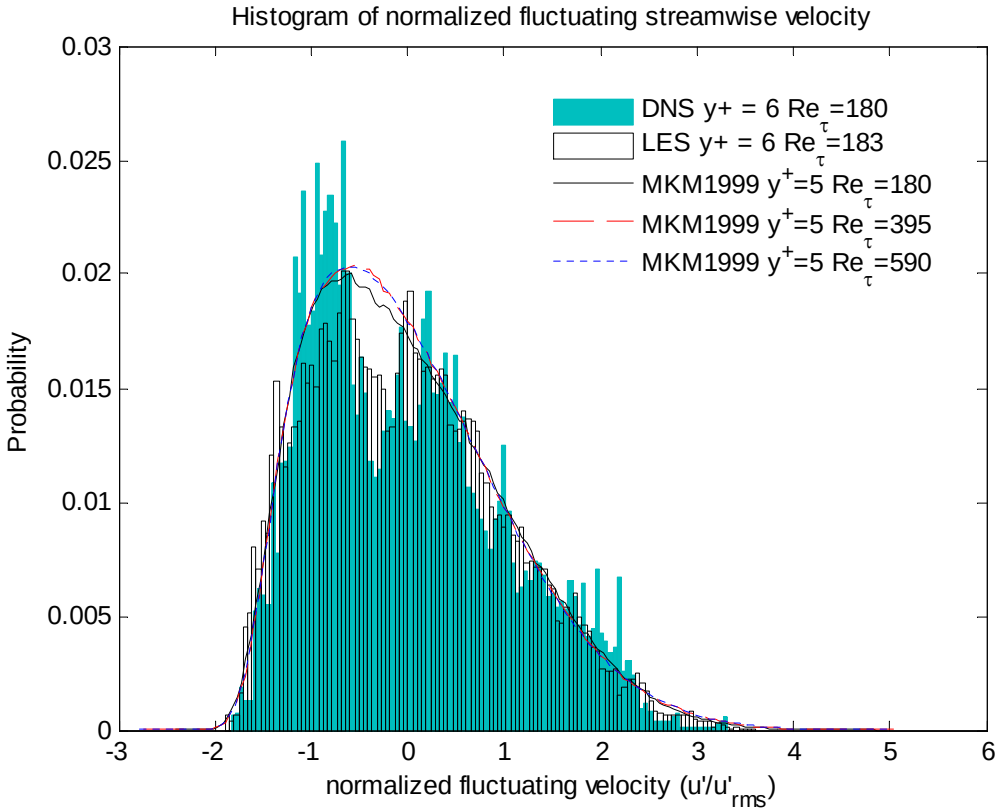

Figure 4.45 - Histogram of LES result compared to Moser *et al.* (1999) DNS results

The skewness and kurtosis of LES and DNS data will be compared to the experimental data with different Reynolds numbers because in reality the Reynolds number of the flow in the reactor system is quite high. The experimental data compared is from Eckelmann (1974) for *Re* = 4800, 7100 and Ueda & Hinze (1975) for *Re* = 11450, 35500.

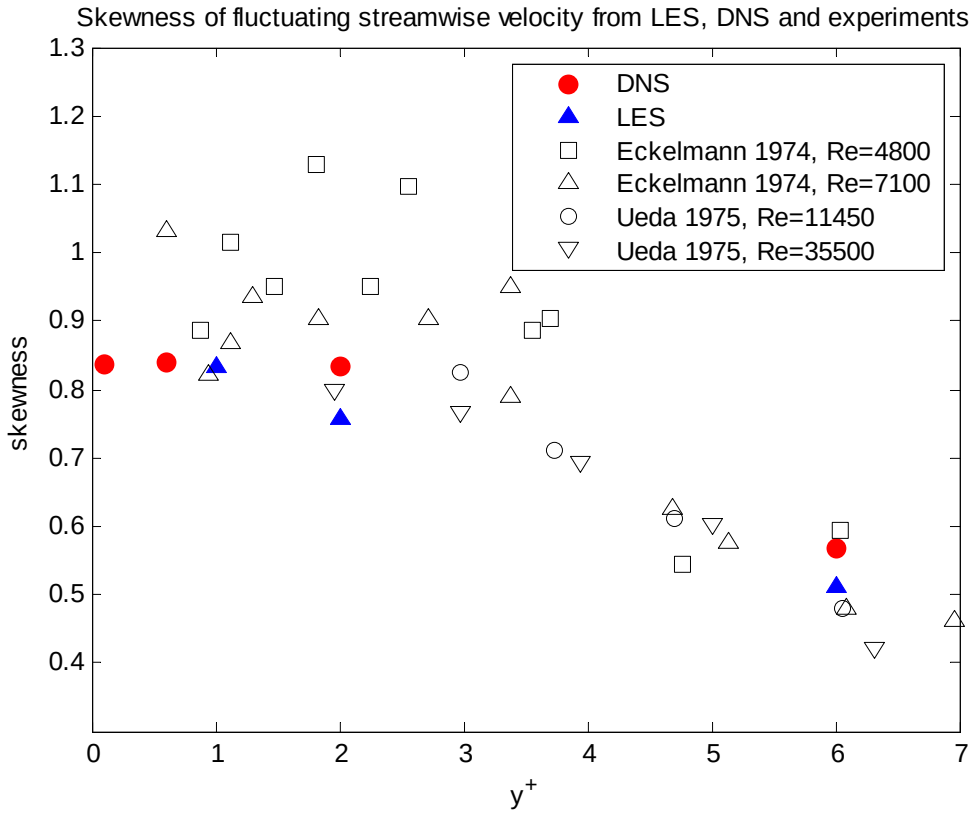

Figure 4.46 - Comparison of skewness of fluctuating streamwise velocity

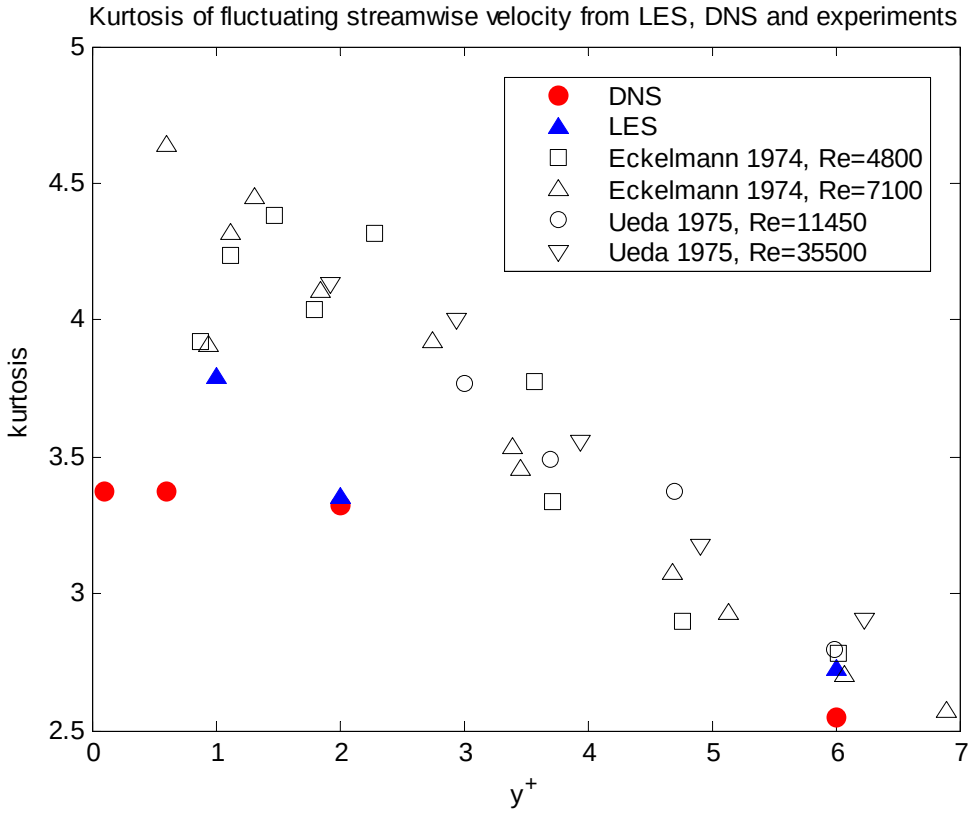

Figure 4.47 - Comparison of kurtosis of fluctuating streamwise velocity

Figure 4.46 shows the skewness comparison between the simulation results and the experimental data. It can be observed that the skewness of simulation results are very close to the experimental data in high Reynolds numbers (>7100) in the viscous sublayer.

Figure 4.47 shows the kurtosis comparison between the simulation results and the experimental data. Although the results of experiment with higher Reynolds number became closer to the simulation data, there is still a difference between them when y^+ was small. However, since the kurtosis only affects the peak of the distribution and in the histogram the highest peak occurs in the small fluctuating velocity region, the effect of the kurtosis is not so important compared to the skewness which the latter determines the value of the distribution in the wings.

The comparison indicates that the statistics of the fluctuating resultant force (i.e. proportional to fluctuating streamwise velocity) from the simulation results are consistent with the experimental data in high Reynolds numbers. Therefore, it is appropriate to use the simple Rayleigh distribution for the fluctuating resultant force.

4.1.6 Correlation between Fluctuating Force and Its Derivative

In the non-Gaussian model based on both LES and DNS statistics, the joint distribution of the fluctuating aerodynamic resultant force and its first derivative are assumed to be best fitted respectively by a Rayleigh distribution (for the fluctuating force *f(t)*) and a Johnson SU distribution (time derivative of the fluctuating force $\dot{f}(t)$) which are statistically independent. In this section, the effect of the possible correlation of *f(t)* and $\dot{f}(t)$ on resuspension is examined.

In this case, the joint distribution will be described by the probability distribution of the fluctuating force multiplied by the conditional probability distribution of $\dot{f}(t)$ given $f(t)$, i.e.

$$P(f,\dot{f}) = P_1(f)\cdot P_2(\dot{f} \mid f) \qquad [4.38]$$

However, it is not easy to calculate P_2. Therefore, the joint distribution will be calculated from the raw data of the fluctuating force and its derivative. Firstly, the forces and their derivatives in the data are normalized by their rms to give standard variables z_1 and z_2 respectively (Eq.[4.22]). Then the domain of z_1 and z_2 is divided into cells. The cell on the bottom left is named as (1, 1), the cell on the top right is marked as (N+1, N+1) and the one in the origin is marked as (N/2+1, N/2+1), as shown in Figure 4.48. In the raw data, for each time step there is a value of z_1 and z_2. If z_1 and z_2 appears in a cell, the counter in the cell is incremented by 1.

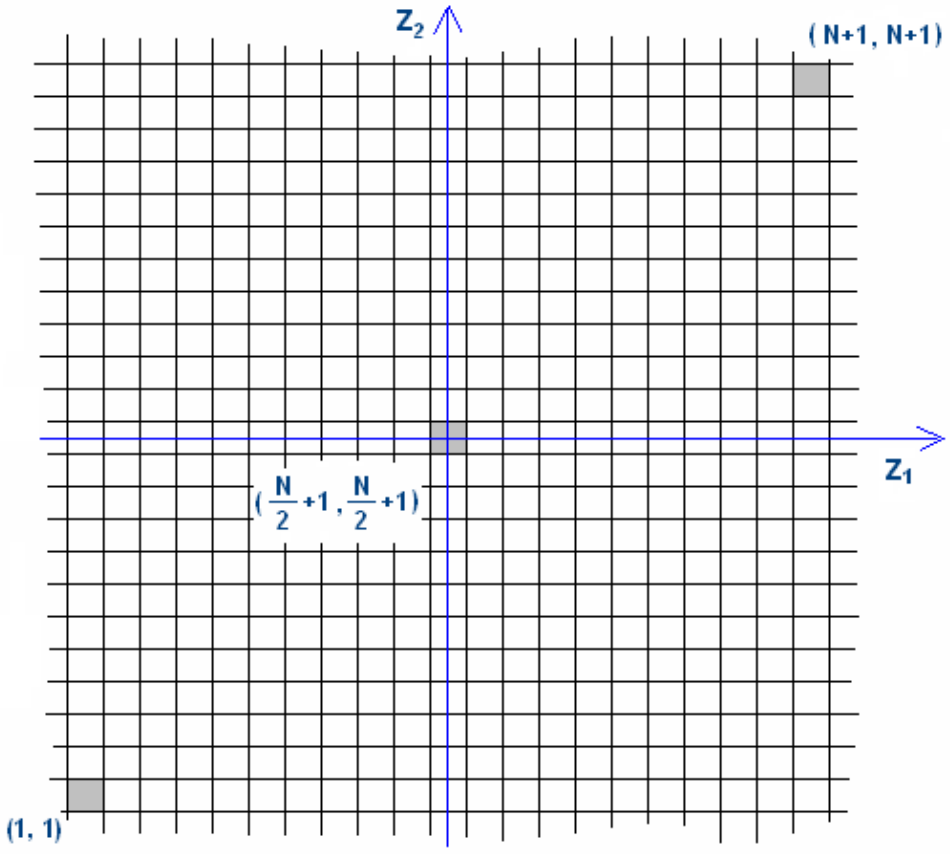

Figure 4.48 - Domain of PDF of fluctuating force and its derivative

Finally, the counter of each cell is divided by the total amount of the data. Therefore, the probability density function of the fluctuating force and its derivative are given as

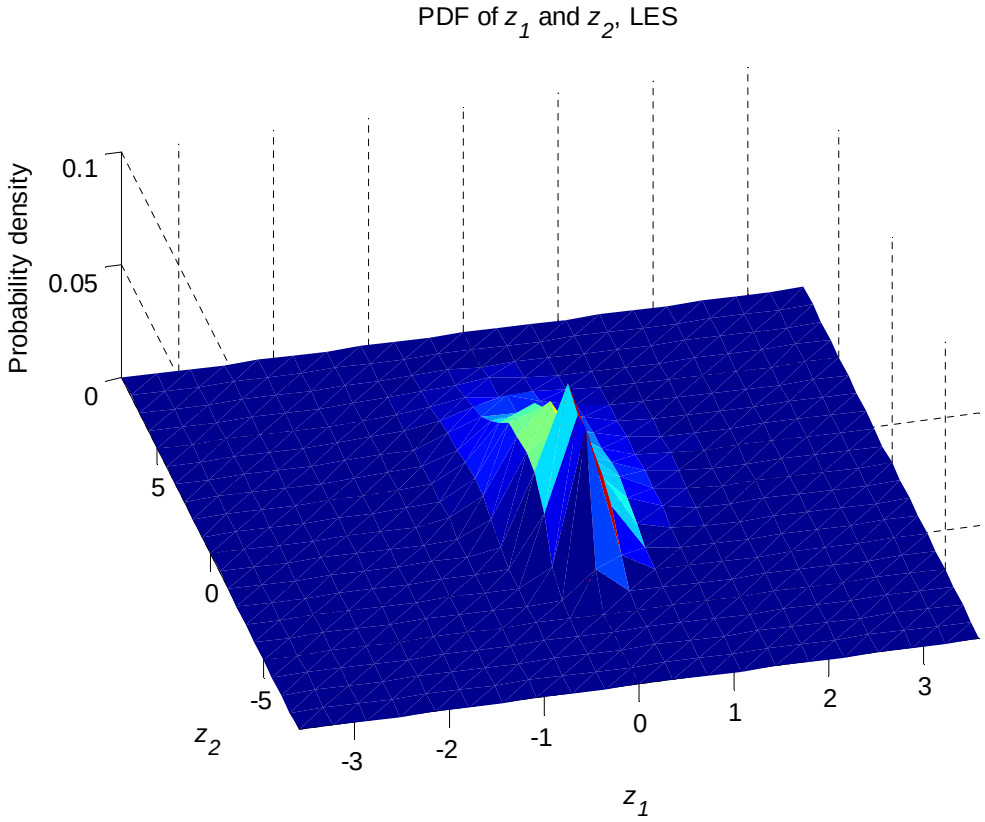

Figure 4.49 - PDF of normalized fluctuating force and its derivative (LES)

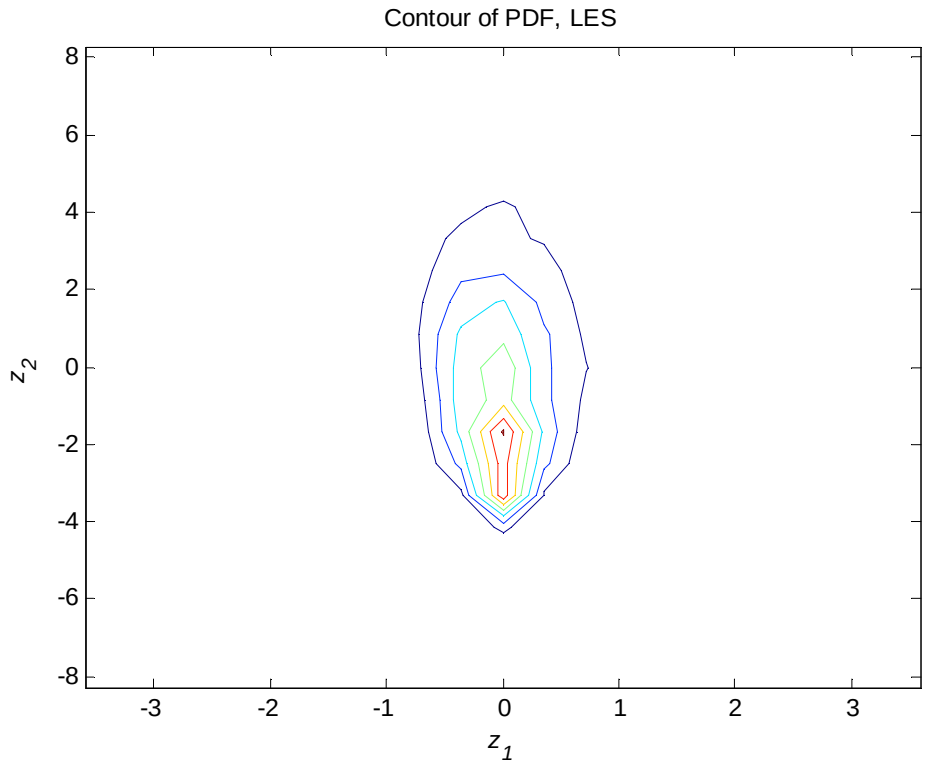

Figure 4.50 - Contour plot of PDF (LES)

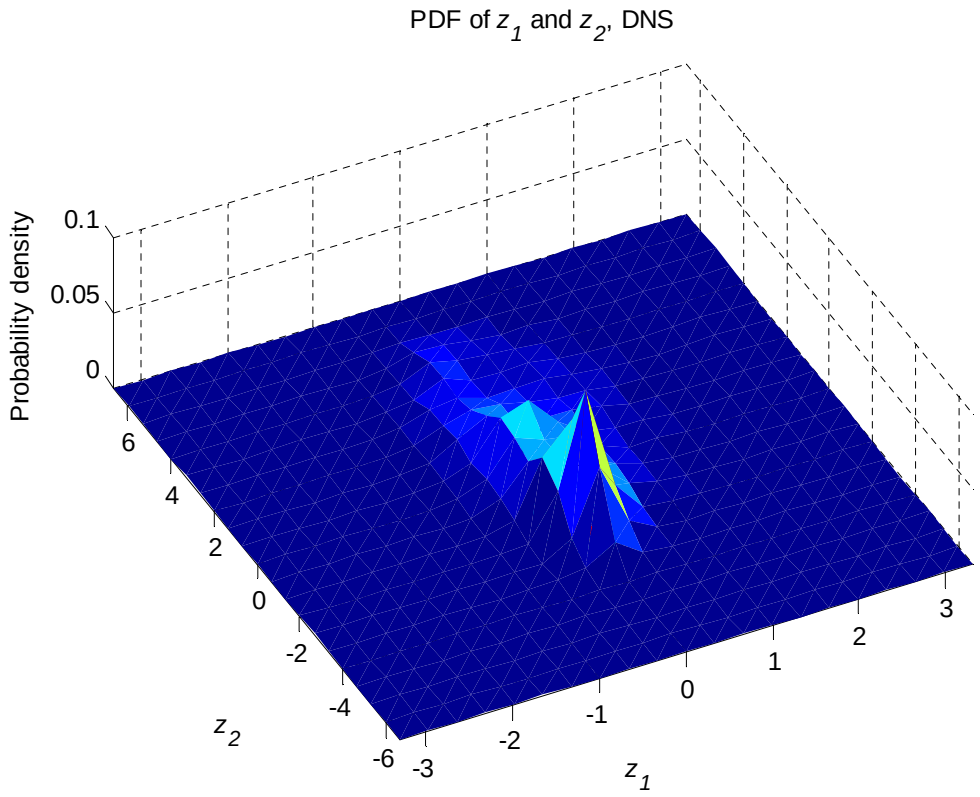

Figure 4.51 - PDF of normalized fluctuating force and its derivative (DNS)

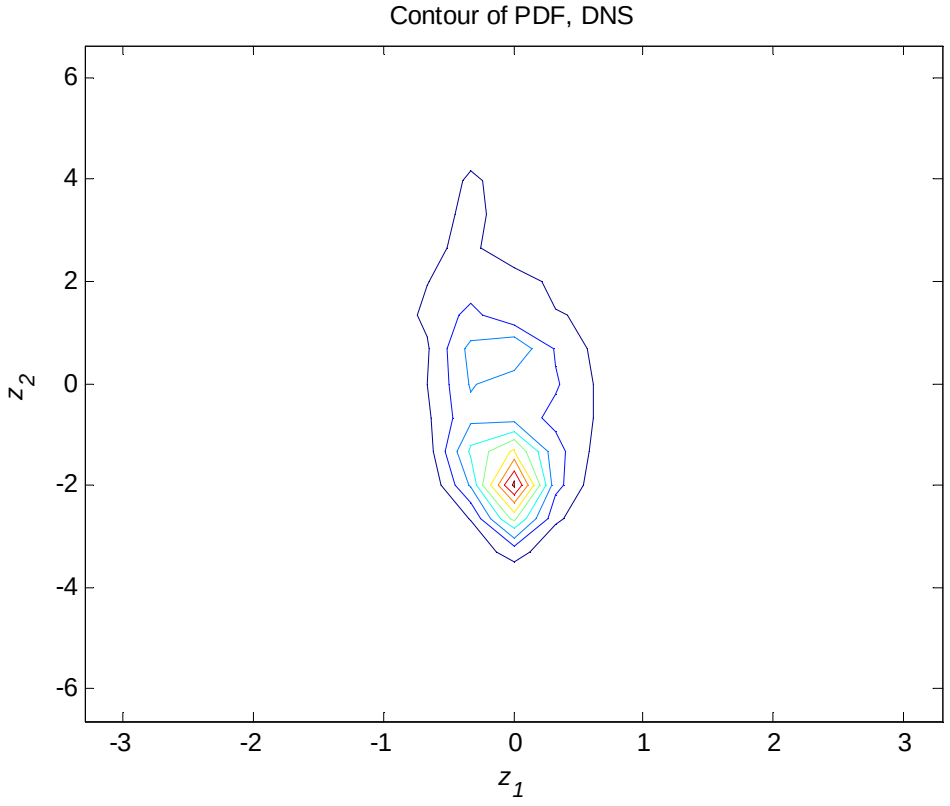

Figure 4.52 - Contour plot of PDF (DNS)

Figure 4.49 and Figure 4.50 shows the probability density function of the normalized fluctuating force and its derivative and the contour plot generated from LES data. Figure 4.51 and Figure 4.52 shows the PDF generated from DNS data. One can observe that the two sets of data generate similar results which the joint distribution is in an ellipse shape with the most likely probability density occurs in around (0, -2) in the domain. The correlation coefficient C_C is calculated as

$$C_C = \frac{\sum z_1 \cdot z_2}{N} \qquad [4.39]$$

with N is the amount of the data. The correlation coefficient equals -0.01267 for LES data, 0.00124 for DNS data.

In the calculation of the resuspension fraction based on this raw data distribution method, the fact is that as the cell number reduces the resuspension fraction result varies. Therefore, to define the proper cell number which should be used, the uncorrelated raw data distribution method is applied and the result is compared with the curve fitted model. The number of cells divided is recorded when the result from the uncorrelated raw data distribution method is very close to the result from the uncorrelated curve fitted method. Then this cell number will be used in calculating the resuspension fraction result for this correlated raw data distribution method. The results shown below are the comparison of the resuspension fraction between uncorrelated curve fitted model and correlated raw data distribution model for different size particles based on LES and DNS data.

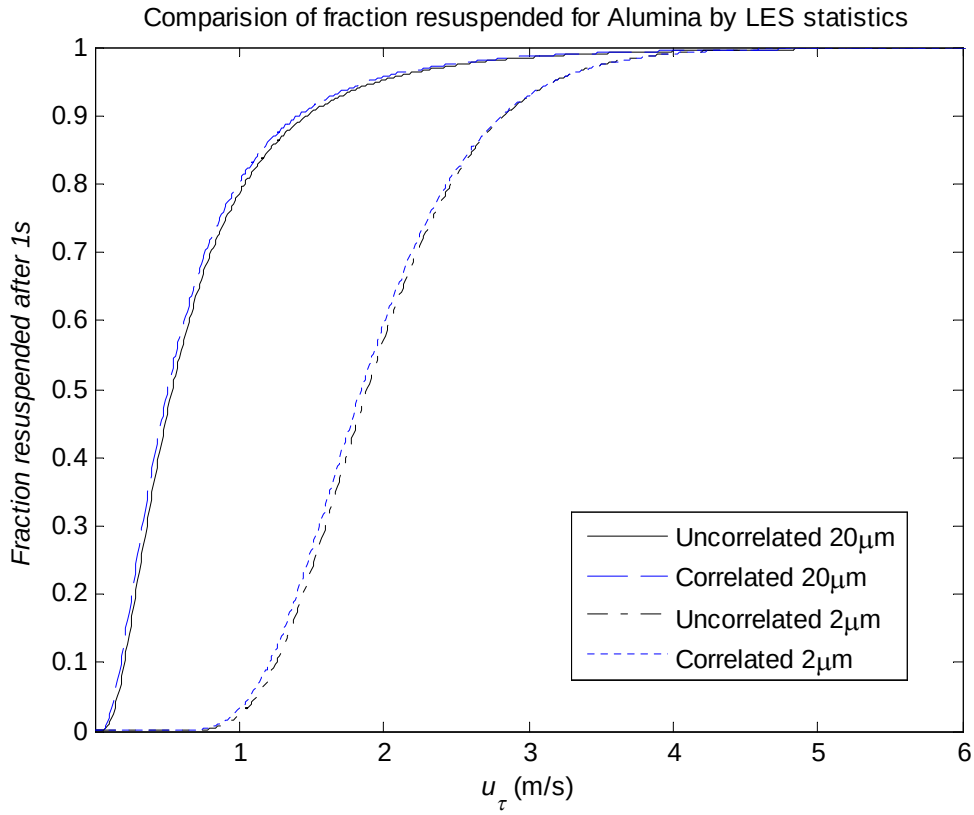

Figure 4.53 - Comparison of correlated and uncorrelated model, LES

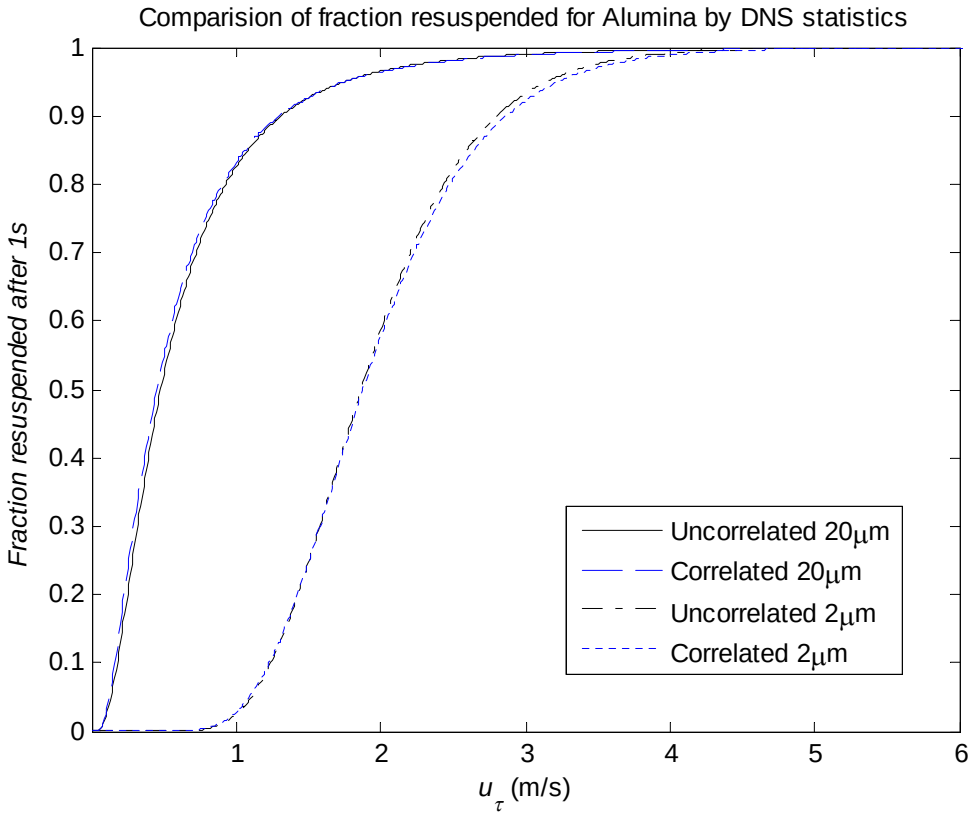

Figure 4.54 - Comparison of correlated and uncorrelated model, DNS

The results of the uncorrelated curve fitted model and the correlated raw data distribution model are very close to each other because the correlation coefficient in both LES and DNS approach is close to zero. Therefore, the correlation of fluctuating force and its derivative hardly affects the predicted resuspension and the uncorrelated curve fitted model can be used in the modified model instead of calculating from the raw data.

4.1.7 A comparison with model predictions based on Lee & Balachandar's measurements of the drag force

In the previous studies, the drag force acting on the particle was calculated using the modified Stokes drag formula given by O'Neill (1968) for the drag force of a spherical particle on or near a wall. Recently Lee & Balachandar (2010) have made extensive calculations of the aerodynamic forces acting on a small particle on or near a wall in a turbulent boundary layer generated by DNS. In what follows we shall use these results to calculate the corresponding drag forces generated in our DNS flow and compare the model predictions of the resuspension with those based on O'Neill's formula.

Application of O'Neill Formula

Assuming the local fluid velocity is similar to the particle velocity, the instantaneous drag force acting on a spherical particle is then calculated from the velocity by applying O'Neill's (1968) formula.

$$F = 1.7 \cdot 6\pi\mu_f r\, u$$

where r is the particle radius and represents the distance of the particle from the wall (i.e. corresponding to y^+). Then the fluctuating drag force f is defined by subtracting the mean $\langle F \rangle$ from F. (i.e. $F - \langle F \rangle$).

And then it is normalized by its rms

$$z_S = \frac{f}{\sqrt{\langle f^2 \rangle}} \qquad [4.40]$$

The first derivative of fluctuating force is calculated via $\dot{f} = \frac{f_{i+1} - f_i}{\Delta t}$, then normalized as

$$\dot{z}_S = \frac{\dot{f}}{\sqrt{\langle \dot{f}^2 \rangle}} \qquad [4.41]$$

where z_S is the normalized fluctuating drag force and $\dot{z}_S$ is its first derivative.

Application of Lee & Balachandar (2010) Analysis

Lee and Balachandar (2010) worked towards a superposition of drag and lift contributions on a sphere particle from shear, translation and rotation mechanisms that is applicable at modest Reynolds numbers. Here in this case, the particle is considered as sitting on the wall and the lift force is neglected. Therefore, the translation and rotation force are not considered. The drag force is then derived as:

$$F = C_D \cdot \frac{\pi}{2} \rho_f G |G| {L_w}^2 r^2 \qquad [4.42]$$

where C_D is the drag coefficient solely due to the local shear, G is the local shear rate L_w is the distance from the wall to the centre of the particle which the radius is r. The drag coefficient is

$$C_D = \frac{40.81}{Re_r}\left(1 + 0.104 Re_r^{0.753}\right) \quad [4.43]$$

where Re_r is the shear Reynolds number which is determined as

$$Re_r = \frac{2|G|L_W r}{v_f} \quad [4.44]$$

The distance from the wall to the centre of the particle can also be written as

$$L_W = \frac{v_f y^+}{u_\tau} \quad [4.45]$$

which is the same form for particle radius r.

From the DNS data, we obtained the instantaneous velocity gradient (dU/dy) for certain y^+ (e.g. y^+ = 0.1). Then the normalized drag force and its derivative are determined as the same in the first case by O'Neill's formula.

$$z_{LB} = \frac{f}{\sqrt{\langle f^2 \rangle}} \quad \dot{z}_{LB} = \frac{\dot{f}}{\sqrt{\langle \dot{f}^2 \rangle}} \quad [4.46]$$

The graphs below show that the distribution of normalized fluctuating resultant force in L&B method is also a Rayleigh. The first derivative of the fluctuating force also fits well to the Johnson SU distribution which the histogram is not shown below.

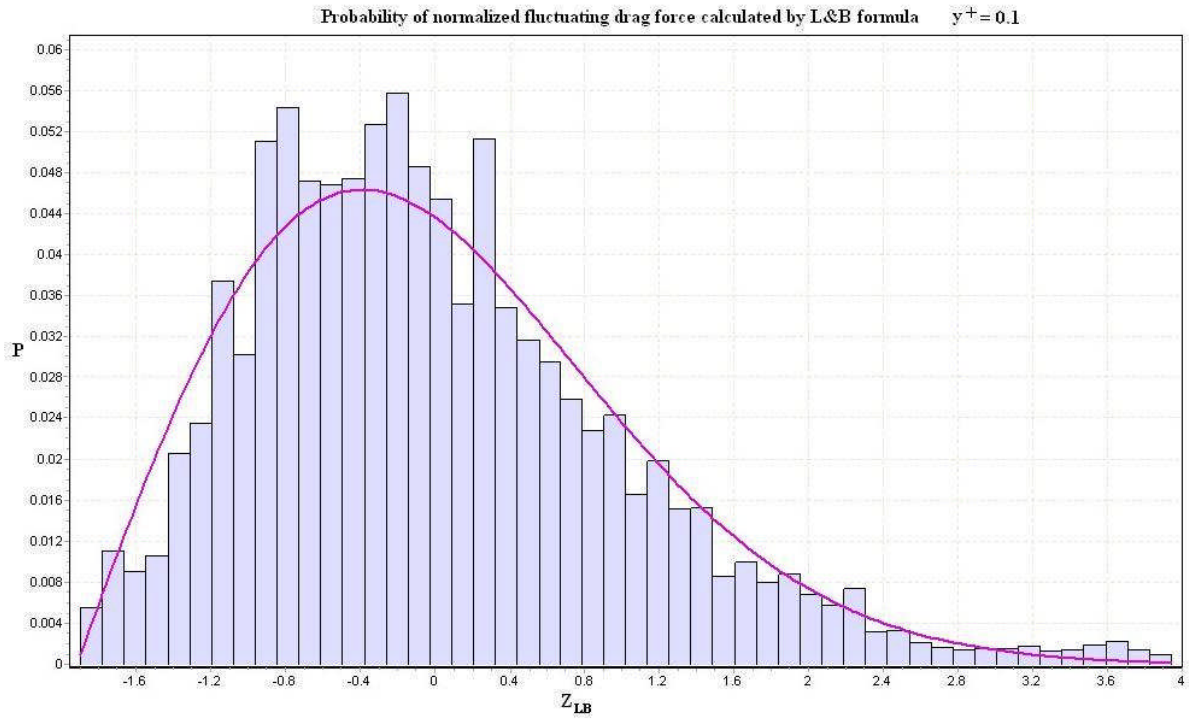

Figure 4.55 - Distribution of normalized fluctuating drag force calculated by L&B formula (y^+ =0.1)

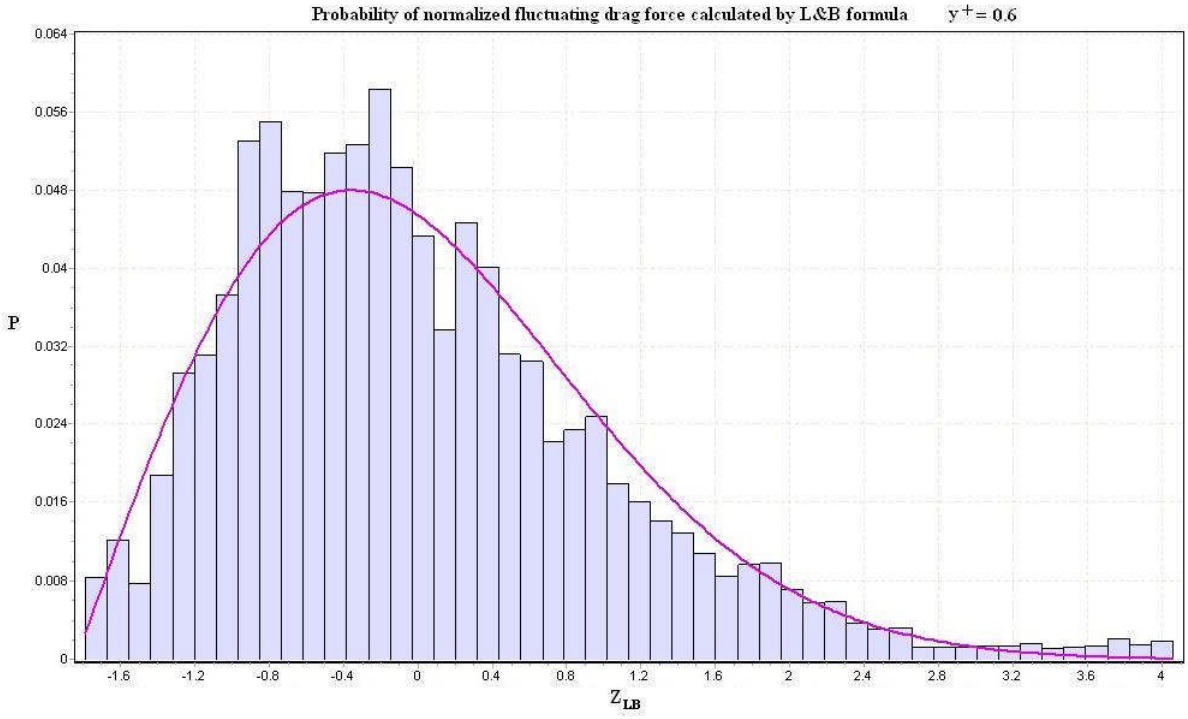

Figure 4.56 - Distribution of normalized fluctuating drag force calculated by L&B formula (y^+ =0.6)

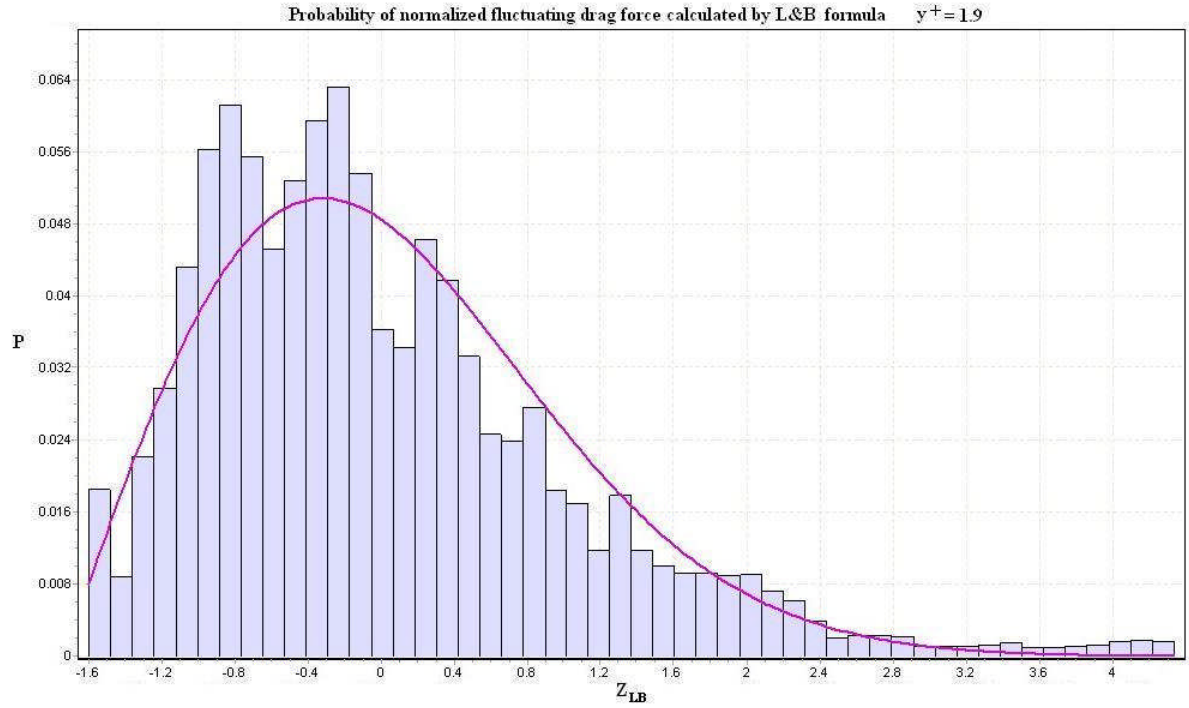

Figure 4.57 - Distribution of normalized fluctuating drag force calculated by L&B formula (y^+ =1.9)

The comparison of the best fit distributions of the normalized fluctuating force and its derivative obtained using O'Neill's and L&B's formulae for the drag forces are shown below. For different y^+ (0.1, 0.6 and 2), the application of O'Neill's formula gives distribution for both z_1 and z_2 which are higher in the range $-1 < z_1, z_2 < 1$ than the equivalent distributions based on the L&B (see Figure 4.58 and Figure 4.59).

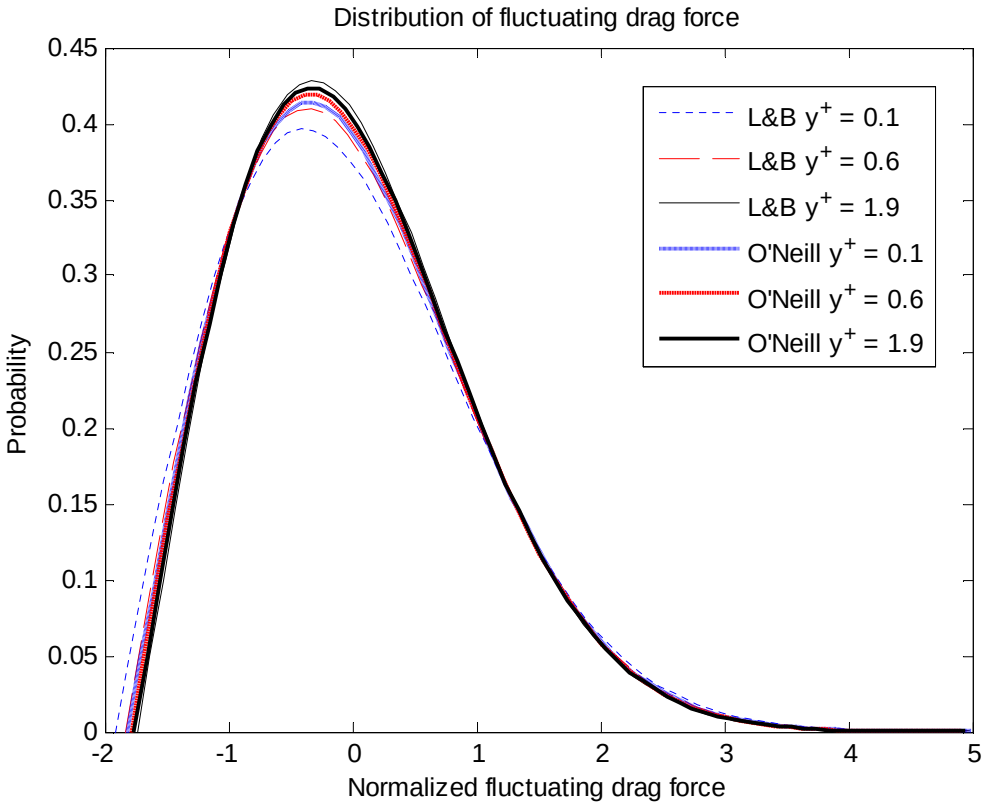

Figure 4.58 - Distribution of normalized fluctuating resultant force by two formulas

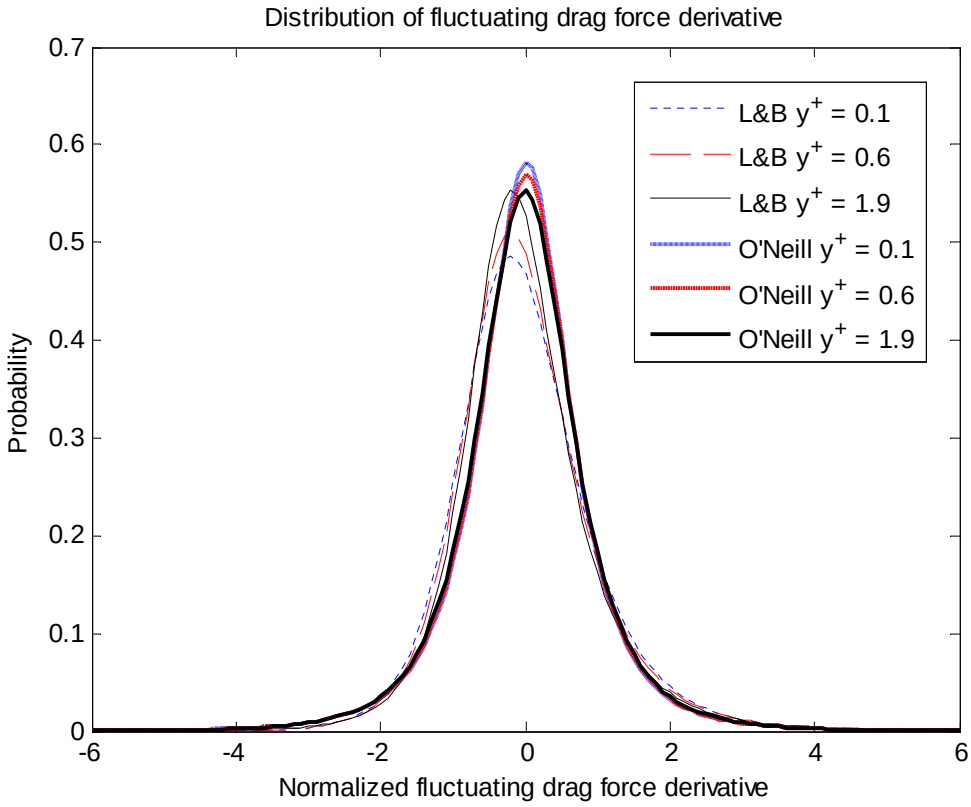

Figure 4.59 - Distribution of derivative of normalized fluctuating force by two formulas

Following the step Eq.[4.23] to Eq.[4.28], the parameters are listed below with the values based on O'Neill's and L&B formula for the drag force.

O'Neill formula	B_f	A_1	A_2	ω^+	f_{rms}
y^+ = 0.1	0.343658	1.812562	1.463790	0.164189	0.366
y^+ = 0.6	0.346911	1.784751	1.446609	0.152035	0.366
y^+ = 1.9	0.351181	1.759902	1.431301	0.131261	0.365
L&B formula	B_f	A_1	A_2	ω^+	f_{rms}
y^+ = 0.1	0.369894	1.917928	1.529456	0.137218	0.346
y^+ = 0.6	0.362101	1.836402	1.478577	0.127625	0.370
y^+ = 1.9	0.349816	1.731746	1.414021	0.129259	0.447

Table 4.4 - Comparison of parameters by two formulas of calculating fluctuating force

From the Table above, one can observe that the parameters calculated by these two formulas are on the whole significantly except the vale for frms for y^+ = 1.9. It is noted that unlike the application by O'Neill formula, the rms coefficient f_{rms} using the L&B formula increased with increasing y^+ and the effect of this has on long term resuspension fraction will be shown later.

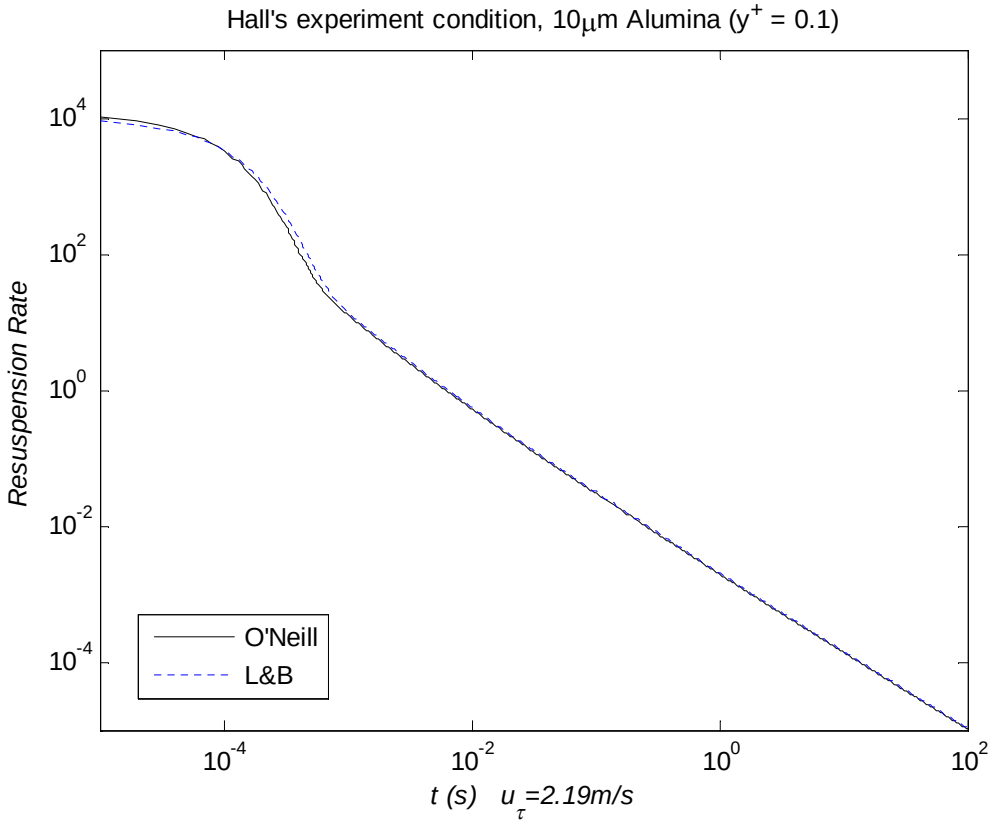

Figure 4.60 - Comparison of resuspension rate of two statistic generation formulas (y^+ = 0.1)

Figure 4.60 shows that the resuspension rate result calculated via the statistics based on O'Neill's formula are very close to the case using L&B formulae. There is a small difference between model predictions in the short term (< 0.001s) which is due to the difference of typical forcing frequency.

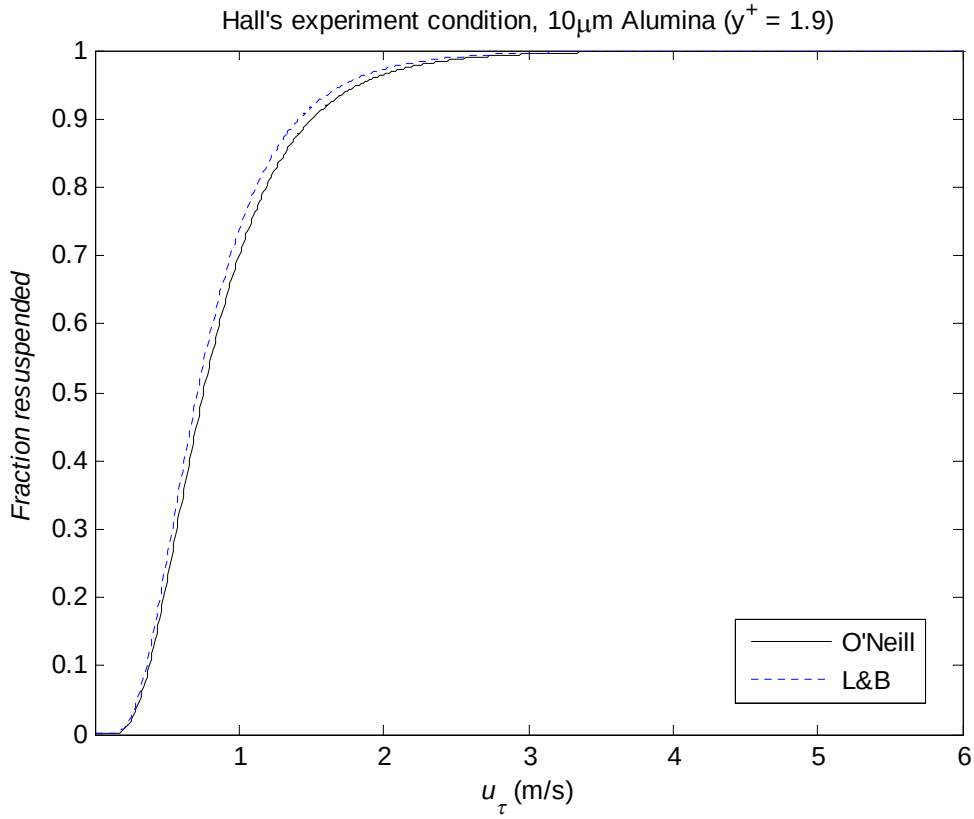

Figure 4.61 - Comparison of resuspension fraction of two statistic generation formulas (y^+ = 1.9)

Figure 4.61 shows that based on the DNS data for y^+ = 1.9 (where the difference is caused by the f_{rms} values), the difference of long term resuspension fraction (> 1s) based on the two formulas is under 5%.

The comparison indicates that predictions calculated from the L&B formula are quite close to the original model using O'Neill's formulae. Therefore on the grounds of the simplicity and application of O'Neill's formula, we will use this formula in our modified R'n'R model in subsequent analysis of resuspension from multilayer deposits.

4.2 Conclusion and Discussion

We have described how the statistics of the fluctuating aerodynamic resultant force f and its time derivative $\dot{f}$ (acting on a particle attached to a surface in a fully developed turbulent boundary layer) have been obtained from both LES and DNS. The distribution of both these variables normalized on their rms values is found to be approximately independent of y^+ in the viscous sublayer ($y^+ < 6$) and statistically independent of one another. The main difference between the 2 sets of data is in the values obtained for the typical forcing frequency $\omega = \sqrt{\langle \dot{f}^2 \rangle / \langle f^2 \rangle}$ applied to the particle-surface deformation (for $y^+ = 6$, ω^+ (the value of ω in wall units) is 0.085 for the LES case and 0.127 for the DNS case), the values of the ratio of the rms / mean of the aerodynamic drag force being very close to one another.

We have compared the differences between the predictions made by Gaussian and non-Gaussian models for resuspension where the difference lies in the role of Gaussian versus non-Gaussian distributions of f and $\dot{f}$ (with the same rms). It was noted that when the adhesive force/ rms aerodynamic force z_a is large (z_a ~ 8), the ratio of resuspension rate constant based on the non-Gaussian to that of the Gaussian model ~ 30 and reflects the much slower decay of the non-Gaussian Rayleigh distribution for the aerodynamic drag force in the tails of the distribution compared to that of the Gaussian distribution. However the broad range of adhesive forces in practice significantly reduces the influence of the tails of the distribution mainly because the contribution to the resuspension in this region of the adhesive force distribution is so small.

The difference between the modified models based on DNS and LES data and hence to the sensitivity of the measurements themselves has been examined. The difference in the resuspension predictions naturally reflects the difference in values of ω^+ which is a natural scaling parameter for the resuspension rate and for the real time t when it occurs. It means that DNS values of the resuspension rate are not universally > LES values as the ratio of the values of ω^+ might imply (See Figure 4.27 for the calculated resuspension rates using the particle adhesions properties measured in Hall's experiment and two different particles, 2μm and 10μm in diameter). However when considering the resuspended fraction for the case of t = 1s, there is very little difference between the LES and DES predictions because for this exposure time all the short term resuspension has occurred (what is left is the fraction that resuspends over a much longer timescale).

The main difference between the modified and original model is reflected in the different values of ω^+ and the ratio of the mean to the rms of the aerodynamic removal forces f_{rms} and the impact these differences have on the fraction resuspended and the resuspension rates. We took the experimental conditions in the Hall experiment as an example so we could compare predictions for

the fraction resuspended with experimental results. We found that the modified model gave closer results to the experimental data in the region where the friction velocity is from around 0.5m/s to 1.5m/s. Although the modified model gave more resuspension than the experimental data when friction velocity was smaller than 0.5m/s and larger than 1.5m/s, the results from modified model still had a closer trend to the experimental data than the original R'n'R model did. It was also noted that the difference between the fraction resuspended predicted by the modified and original models could become significant when the friction velocity is small. It was concluded that the typical forcing frequency ω^+ is the crucial parameter in short term resuspension rate and the rms coefficient f_{rms} is the key parameter for long-term resuspension fraction. The effect of the typical forcing frequency ω^+ on the resuspension fraction after 1s is not significant.

Finally, we have examined the implications for resuspension of using the recently published formula of Lee & Balachandar (2010) (L&B) for the drag force acting on a particle on a surface (based on their DNS measurements of drag forces on particles on or near a surface in a turbulent boundary layer). The comparison indicated that the resuspension predictions using the L&B formula were quite close to those of the original model which uses the O'Neill formula for the drag force except in the region $-1 < z_1, z_2 < 1$ where application of O'Neill's formula gives higher values. However, this has very little effect on the resuspension rate and resuspension fraction. Therefore on the grounds of simplicity and application of O'Neill's formula, we will use this formula in our modified R'n'R model in subsequent analysis of resuspension from multilayer deposits.

Chapter 5
Multilayer
Resuspension

Ordinary language is totally unsuited for expressing what physics really asserts, since the words of everyday life are not sufficiently abstract. Only mathematics and mathematical logic can say as little as the physicist means to say.

- Bertrand Russell

5.1 Multilayer Resuspension Models

Resuspension of multilayer deposits of radioactive particles is an important phenomenon in nuclear severe accidents. However, most of the models used to predict the amount of resuspended particulate are based on the resuspension of isolated particles as described in the previous chapters. There are only a few models which consider the multilayer case, namely Fromentin (1989), Lazaridis & Drossinos (1998) (referred to as LD) and Friess & Yadigaroglu (2001) (referred to as FY). In this Chapter, the modified R'n'R model will be adapted for application to multilayer deposits based on the FY multilayer approach. Furthermore, the coverage effect of layers on resuspension will be considered in this modified FY multilayer model in two ways: 1) introducing a coverage factor; 2) considering the influence of a distribution of particle size within each layer. Finally, the modified multilayer model resuspension predictions will be compared with the resuspension measurements in the STORM SR11 test (Castelo *et al.*, 1999) and the BISE experiment (Alloul-Marmor, 2002).

Fromentin's model is a semi-empirical model based on force-balance methods and the input parameters are limited to those in the PARESS experiment upon which the model is based. The LD model is restricted to a multilayer deposit in which the resuspension rate for each particle in the deposit is the same. In contrast the FY model (2001) takes account of the fact that the resuspension rate constant can vary according to the distribution of adhesive forces experienced by a particle in each layer. If we compare the two models in situations where the resuspension rate constant is the same for all particles, there is a difference in the way the fraction of particles exposed to the flow is calculated. If the layers are numbered 1, 2, 3...etc from the top layer exposed to the flow, then

the LD model takes this fraction in the *i*th layer to be the number of particles removed from the (*i*-1)th layer over the initial number of particles in the (*i*-1)th layer. Thus it assumes that whenever a particle is removed from the (*i*-1)th layer a particle in the *i*th layer is exposed and is immediately resuspended. Hence, the model is valid for large resuspension rates or equivalently, it gives the maximum multilayer resuspension rate (i.e., if a particle is exposed it resuspends). In these circumstances the FY model, on the other hand, takes the fraction of exposed particles in the *i*th layer to be the ratio of the number of particles in the (*i*-1)th layer to the number of particles in the *i*th layer at time *t*. Thus

$$\frac{dn_i}{dt} = -pn_i\left[1-\frac{n_{i-1}(t)}{n_{i-1}(0)}\right] \quad i \geq 2 \quad \text{LD model}$$

$$\frac{dn_i}{dt} = -pn_i\left[1-\frac{n_{i-1}(t)}{n_i(t)}\right] \quad i \geq 2 \quad \text{FY model}$$

where n_i is the number of particles in the *i*th layer at time *t* (i.e. the total number of particles in ith layer at time *t* being the sum of those particles exposed and unexposed to the flow) and *p* is the resuspension rate constant. Since every particle sits on top of a particle in the layer below, this ratio gives the exact number of exposed particles which the LD model does not provide.
The FY model is not only exact in this situation but as we stated above more generally applicable since the resuspension rate constant can vary from particle to particle in any given layer and from layer to layer. Since this is an important consideration in multilayer resuspension, the FY model is used as the basis for the multilayer modelling which will be presented in this chapter.

Let us now recall the essential features of the FY model (Friess & Yadigaroglu, 2001) which deals with the resuspension of a deposit composed of a regular array of identical spherical particles. FY (2001) first dealt with an infinitely thick deposit, defining a resuspension rate constant $p(\xi)$ for each particle exposed to the flow, where ξ is a statistical variable or number of variables upon which *p* depends (e.g. adhesion arising from the contact of a particle with other particles whose value controls the influence of the flow). The probability density function (pdf) for the occurrence of ξ is given by $n(\xi,t)$. It is supposed that every time a particle is removed (resuspended by the flow) another particle is uncovered and exposed to the flow but with a different ξ say ξ' with a probability distribution $\varphi(\xi')$ for uncovered particles. The particles are homogeneously distributed in the initial state with $n(\xi,0) = \varphi(\xi)$. The rate at which particles are exposed is given by

$$\Lambda(t) = \int_{\xi} p(\xi)n(\xi,t)d\xi \qquad [5.1]$$

and the fraction of those particles exposed per unit time with values between ξ, $\xi + d\xi$ will be

$$d\xi\varphi(\xi)\int_{\xi'} p(\xi')n(\xi',t)d\xi'$$

The equation for $n(\xi,t)$ is thus

$$\frac{\partial n(\xi,t)}{\partial t} = -p(\xi)n(\xi,t) + \varphi(\xi)\int_{\xi'} p(\xi')n(\xi',t)d\xi' \qquad [5.2]$$

Therefore, for an L-layer deposit, let $n_i(\xi,t)d\xi$ denote the probability of exposed particles between ξ, $\xi + d\xi$ in the ith layer at time t, the layers being numbered sequentially from the top layer (totally exposed to a flow) downward as $i = 1, 2, 3 \ldots L$. Then the set of ODEs (ordinary differential equations) is

$$\frac{\partial n_1(\xi,t)}{\partial t} = -p(\xi)n_1(\xi,t)$$

$$\frac{\partial n_i(\xi,t)}{\partial t} = -p(\xi)n_i(\xi,t) + \varphi(\xi)\int_{\xi'} p(\xi')n_{i-1}(\xi',t)d\xi' \quad (i \geq 2) \qquad [5.3]$$

The resuspension rate for ith layer is given by

$$\Lambda_i(t) = \int_{\xi} p(\xi)n_i(\xi,t)d\xi \qquad [5.4]$$

5.1.1 Modified Rock'n'Roll Model in Multilayer Case

The Modified Rock'n'Roll model (Chapter 4.1.4, p129) is a single particle kinetic model based on the Rock'n'Roll model (Reeks & Hall, 2001) with the resuspension rate constant $p(\xi_i)$ accounting for the non-Gaussian statistics of the fluctuating aerodynamic resultant force obtained from LES and DNS data.

The adhesive force of the isolated particle on the surface with two asperities is given by

$$f_a = \frac{3}{2}\pi\gamma r r'_a \qquad [5.5]$$

where γ is the adhesive surface energy (per unit area), r is the particle radius and r_a' is the normalized asperity radius which is the ratio of asperity radius (r_a) to particle radius and the distribution of r_a' is considered as log-normal ($\varphi(r_a')$) with geometric mean $\overline{r}'_a$ and geometric standard deviation σ_a' (adhesive spread) i.e.

$$\varphi(r'_a) = \frac{1}{\sqrt{2\pi}}\frac{1}{r'_a}\frac{1}{\ln\sigma'_a}\exp\left(-\frac{\left[\ln(r'_a/\overline{r}'_a)\right]^2}{2(\ln\sigma'_a)^2}\right)$$

Biasi *et al*. (2001) derived a correlation for these distribution parameters as a function of particle radius (in microns), namely

$$\begin{aligned}\sigma'_a &= 1.8 + 0.136r^{1.4}\\ \overline{r}'_a &= 0.016 - 0.0023r^{0.545}\end{aligned} \qquad [5.6]$$

We recall that in the FY multilayer model, this distribution of normalized asperity radii refers to the initial state of the pdf of exposed particles, $n(\xi,0)$, i.e.

$$n(r'_a, 0) = \varphi(r'_a) \qquad [5.7]$$

where the normalized asperity radius r_a' refers to the intrinsic statistical variable ξ.

The resuspension rate constant p in the modified R'n'R model (Eq.[4.29]) is a function of the normalized asperity radius for a fixed particle size. Hence, p is referred to as $p(r_a')$. Therefore, the set of ODEs for the pdf of exposed particles in a deposit composed of i = 1, 2, 3 … L layers at time t is given by

$$\begin{aligned}\frac{\partial n_1(r'_a,t)}{\partial t} &= -p(r'_a)n_1(r'_a,t)\\ \frac{\partial n_i(r'_a,t)}{\partial t} &= -p(r'_a)n_i(r'_a,t) + \varphi(r'_a)\int_0^\infty p(\tilde{r}'_a)n_{i-1}(\tilde{r}'_a,t)d\tilde{r}'_a \quad (i \geq 2)\end{aligned} \qquad [5.8]$$

The $\varphi(r_a')\int_0^\infty p(\tilde{r}_a')n_{i-1}(\tilde{r}_a',t)d\tilde{r}_a'$ part is thus a source term. It is considered as the extra source of particle exposure rate (exposing particles in a given layer by resuspending particles from the layer above).

The resuspension rate in the *i*th layer is given by

$$\Lambda_i(t) = \int_0^\infty p(r_a')n_i(r_a',t)dr_a' \qquad [5.9]$$

For $i = 1$, the first layer resuspension rate is given explicitly in the original R'n'R model appropriate for a monolayer (Eq.[4.15]) because there is no source term from the particles in the layer above, namely

$$\Lambda_1(t) = \int_0^\infty p(r_a')e^{-p(r_a')t}\varphi(r_a')dr_a' \qquad [5.10]$$

The initial value of exposed particles from the second layers downward $n_i(r_a',0) = 0$ ($i \geq 2$) which means all the particles in the layer below are covered by the particles from the layer above. Therefore, for the second layer and layers below ($i \geq 2$) using the initial condition for $n_i(r_a',t)$, gives

$$n_i(r_a',t) = \varphi(r_a')e^{-p(r_a')t}\int_0^t e^{p(r_a')t'}\int_0^\infty p(\tilde{r}_a')n_{i-1}(\tilde{r}_a',t')d\tilde{r}_a'dt' \quad (i \geq 2) \qquad [5.11]$$

$$i.e.\ \left[\frac{\partial n_i(r_a',t)}{\partial t} + p(r_a')n_i(r_a',t)\right] = \varphi(r_a')\int_0^\infty p(\tilde{r}_a')n_{i-1}(\tilde{r}_a',t)d\tilde{r}_a' \quad (i \geq 2)$$

$$\Rightarrow e^{p(r_a')t}\left[\frac{\partial n_i(r_a',t)}{\partial t} + p(r_a')n_i(r_a',t)\right] = e^{p(r_a')t}\varphi(r_a')\int_0^\infty p(\tilde{r}_a')n_{i-1}(\tilde{r}_a',t)d\tilde{r}_a'$$

$$\Rightarrow e^{p(r_a')t}n_i(r_a',t) = \int_0^t e^{p(r_a')t'}\varphi(r_a')\int_0^\infty p(\tilde{r}_a')n_{i-1}(\tilde{r}_a',t')d\tilde{r}_a'dt'$$

$$\Rightarrow n_i(r_a',t) = \varphi(r_a')e^{-p(r_a')t}\int_0^t e^{p(r_a')t'}\int_0^\infty p(\tilde{r}_a')n_{i-1}(\tilde{r}_a',t')d\tilde{r}_a'dt'$$

Substituting Eq.[5.11] in Eq.[5.9], the resuspension rate for the *i*th layer is given by

$$\Lambda_i(t) = \int_0^\infty p(r_a')\varphi(r_a')e^{-p(r_a')t}\left[\int_0^t e^{p(r_a')t'}\int_0^\infty p(\tilde{r}_a')n_{i-1}(\tilde{r}_a',t')d\tilde{r}_a'dt'\right]dr_a' \quad (i \geq 2) \qquad [5.12]$$

Initially it is assumed as in the FY model that the deposit is formed from identical spherical particles as shown in Figure 5.1.

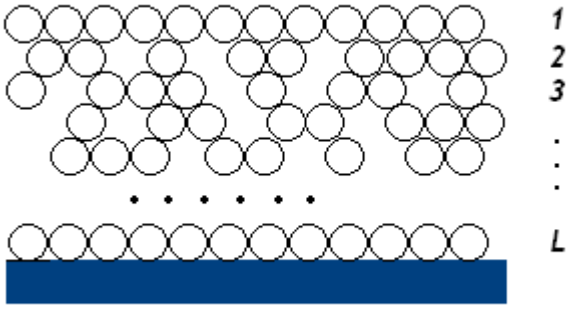

Figure 5.1 - Geometry of the multilayer system with same size particles

The micro roughness for all the particles is assumed to be the same so the same distribution of normalized asperity radius ($\varphi(r_a')$) is used for all the particles in the domain. In the calculation below, the parameters from the STORM SR11 experiment Phase 6 condition will be applied (more information is provided in next section). The parameters for Phase 6 are:

Average radius (μm)	Fluid density ($kg.m^{-3}$)	Fluid kinematic viscosity ($m^2.s^{-1}$)	Wall friction velocity ($m.s^{-1}$)	Surface energy ($J.m^{-2}$)	Reduction factor (Geometric mean)	Spread factor (Geometric standard deviation)
0.227	0.5730	5.2653×10^{-5}	6.249	0.5	0.015	1.817

where Biasi's correlation (Eq.[5.6]) is used for the adhesion distribution parameters.

Figure 5.2 shows the resuspension rate of particles in layer 1, 3, 5, 10 and 20. The resuspension rate of the first layer is identical to that of the isolated particle model. For the second and subsequent layers, the initial resuspension rate at t = 0 is zero. Starting from zero the resuspension rate rises to a maximum during which time most of the particles which are easily removed resuspend from a given layer (i.e. for these particles the mean effective aerodynamic force > adhesive force), the remainder being removed on a much longer period. The time to reach a maximum may therefore be regarded as a delay time for the particles in a given layer to be exposed by removing particles from all the layers above it. Note that the maximum resuspension rate decreases as the layer number increases. Also note that the resuspension rate of each layer beyond its maximum value, whilst being initially less than the layer above, eventually exceeds it so that the integrated amount (fraction resuspended) is the same (close to unity) for all layers in the long-term ($t \to \infty$) (Numerics were checked to make sure that this was the case).

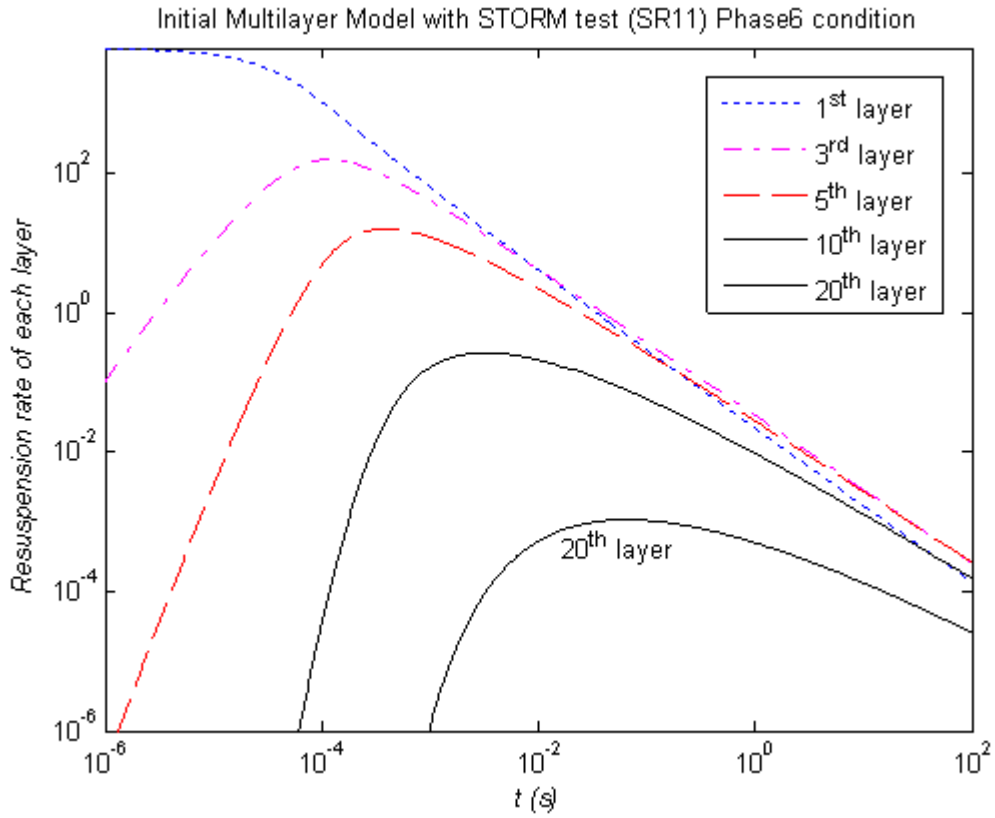

Figure 5.2 - Resuspension rate of each layer vs. time for the initial multilayer model (the FY model with rate constants based on the modified non-Gaussian R'n'R model)

The initial number of particles is the same in each layer normalized to unity. Then the fractional resuspension rate for the domain (*L* layers) is given by

$$\Lambda_L(t) = \frac{\sum_{i=1}^{L} \Lambda_i(t)}{L} \qquad [5.13]$$

which corresponds to the resuspension fraction of an *L* layers deposit.

$$f_r(t)_L = \int_0^t \Lambda_L(t')dt' \qquad [5.14]$$

The modified R'n'R model incorporating the FY multilayer approach will be referred to as the initial multilayer model since the model will later on be extended to include the coverage effect.

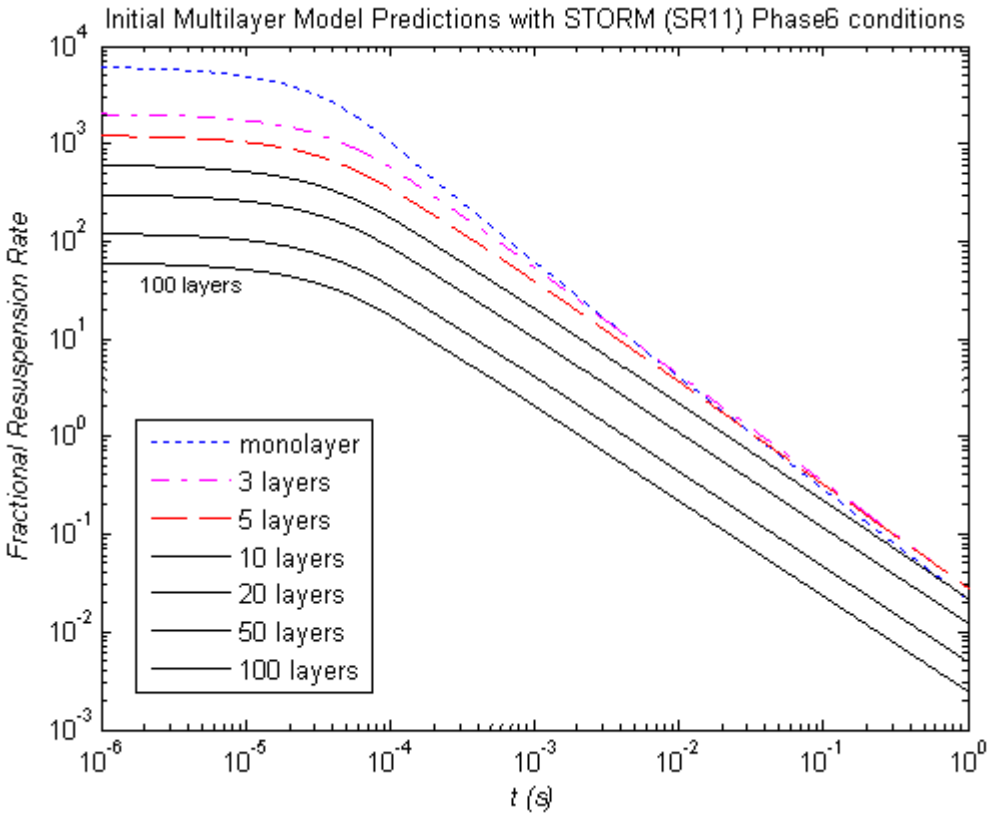

Figure 5.3 - Fractional resuspension rate comparison (particle diameter: 0.45μm)

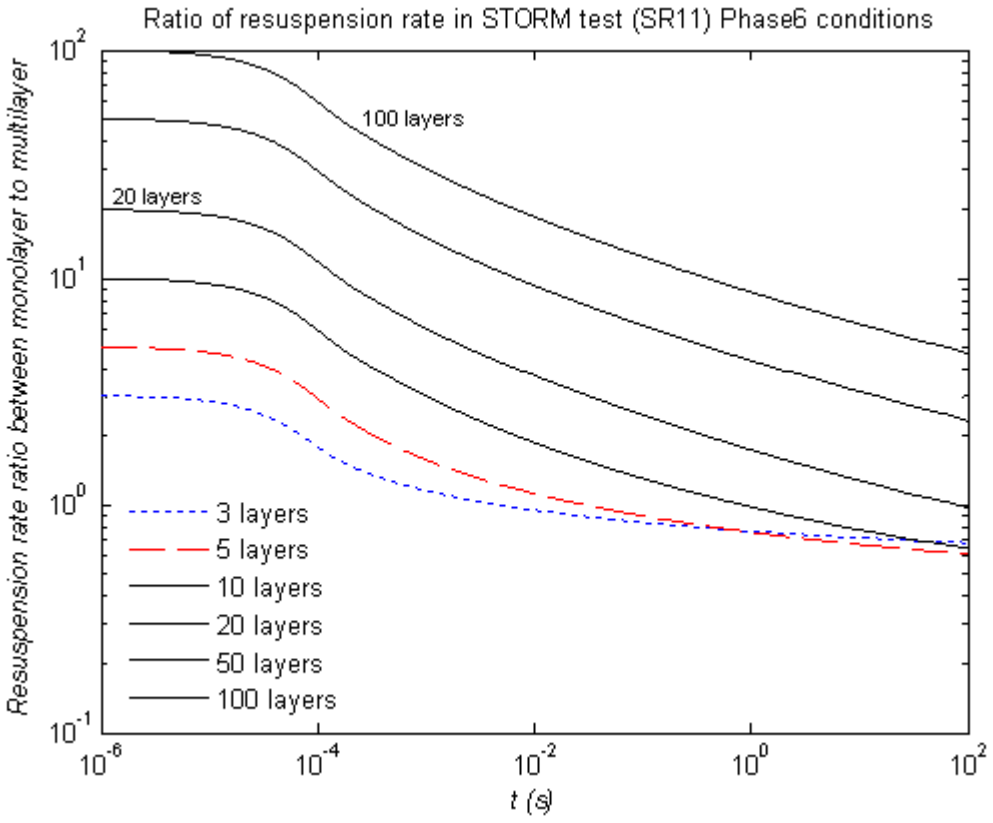

Figure 5.4 - Fractional resuspension rate ratio between monolayer and multilayer

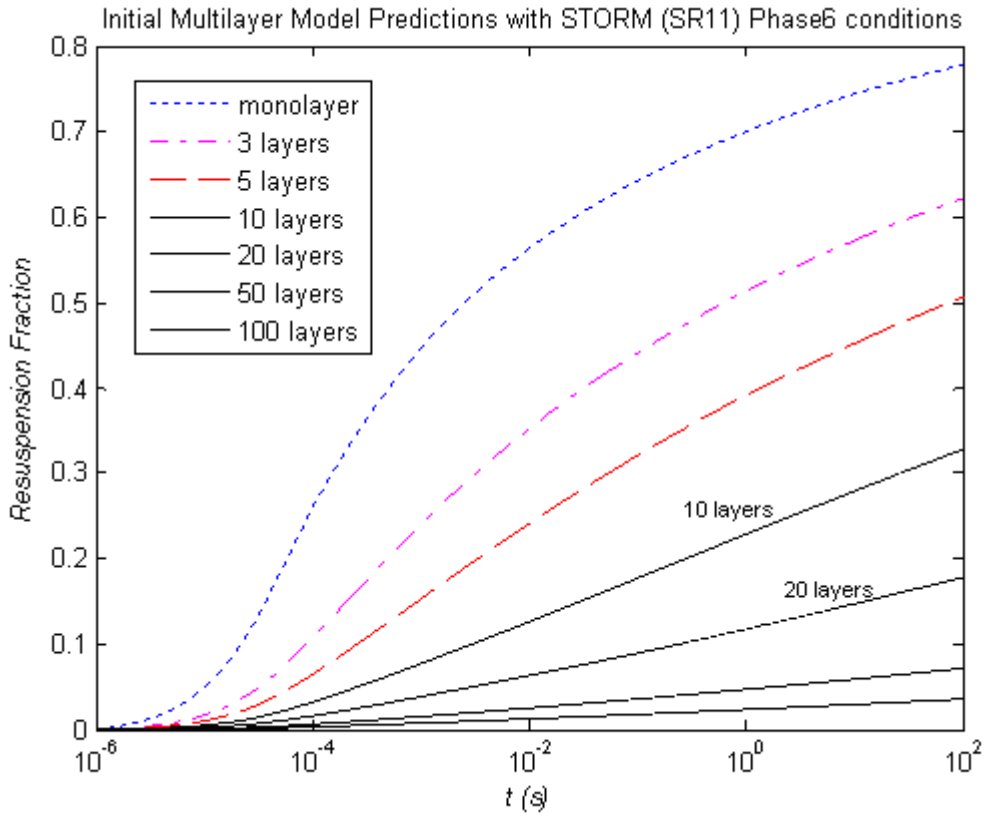

Figure 5.5 - Resuspension fraction comparison for initial multilayer model

The fractional resuspension rate is shown in Figure 5.3. The short term resuspension rate is considered finished when the exposure time t is around 10^{-4}s when as shown in the plot the long-term resuspension (approximately proportional to $1/t$) begins (we note that $1/\omega^{+}$ which corresponds to a timescale ~10^{-5}s). The initial fractional resuspension rate decreases with increasing layers when more particles tend to be removed over a longer period.

Figure 5.4 shows how much the monolayer fractional resuspension rate differs from that of the multilayer resuspension (for the same initial fraction = 1, in each case). As the layer number increases, the ratio of the resuspension rate between monolayer and multilayer increases significantly in the short term. However after a given time which increases with the value of i, the resuspension rate for a given layer eventually exceeds that for a monolayer i = 1 at the same time (the ratio < 1), and in the long-term the ratio should converge to zero (see the cases for layer i = 3 and 5 in Figure 5.2). Figure 5.5 shows the resuspension fraction of the whole deposit domain. It shows that after 100s 80% of the monolayer deposit is removed whereas only around 3% of the 100 layers deposit is resuspended.

5.1.1.1 Influence of Spread Factor on Multilayer Resuspension

Now the influence of the spread factor is considered. The geometric mean of the normalized asperity radius is fixed at 0.015. The spread factor values of 1.1, Biasi (1.817) and 4.0 are chosen for comparison (Note that the spread is the geometric standard deviation and > 1). Figure 5.6, Figure 5.7 and Figure 5.8 show the comparison of resuspension fraction for a monolayer, 10 layers and 100 layers deposits for different spread factors, respectively. We note that for a monolayer by virtue of the log normal distribution the time for 50% of the deposit is independent of the spread factor. For times smaller than this value, the largest spread factor gives the greatest fraction resuspension whereas beyond this time, the situation is reversed.

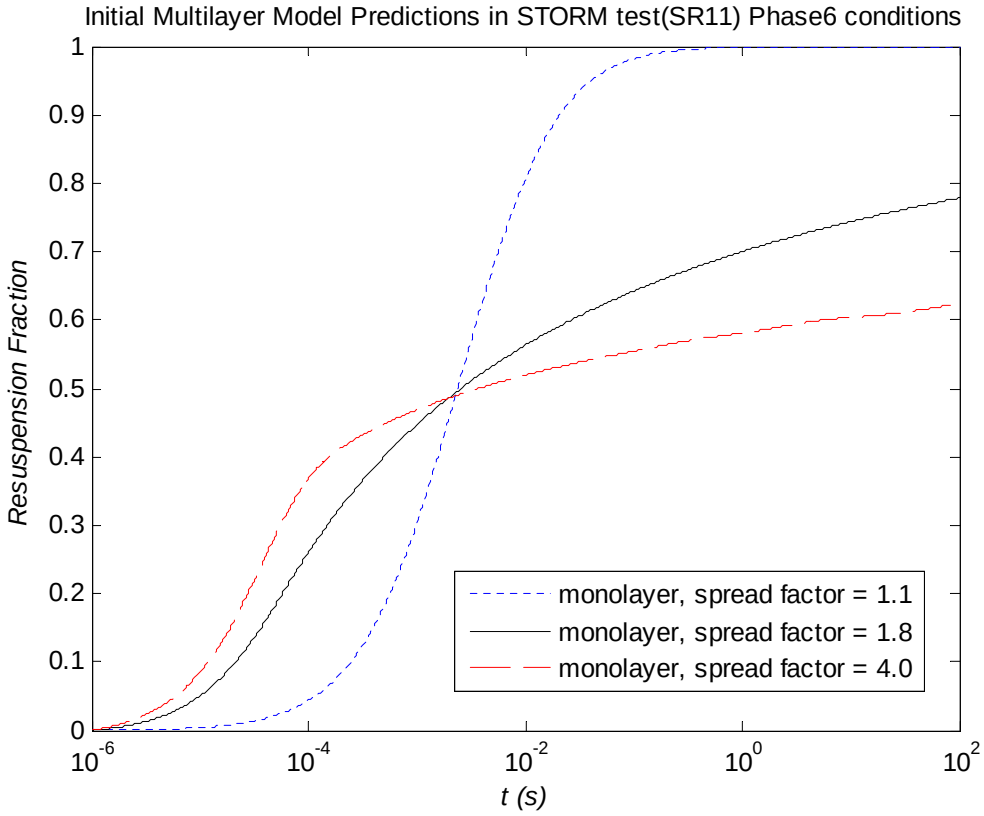

Figure 5.6 - Effect of spread factor on monolayer model (note that the exposure for 50% resuspension is the same for all spread factors)

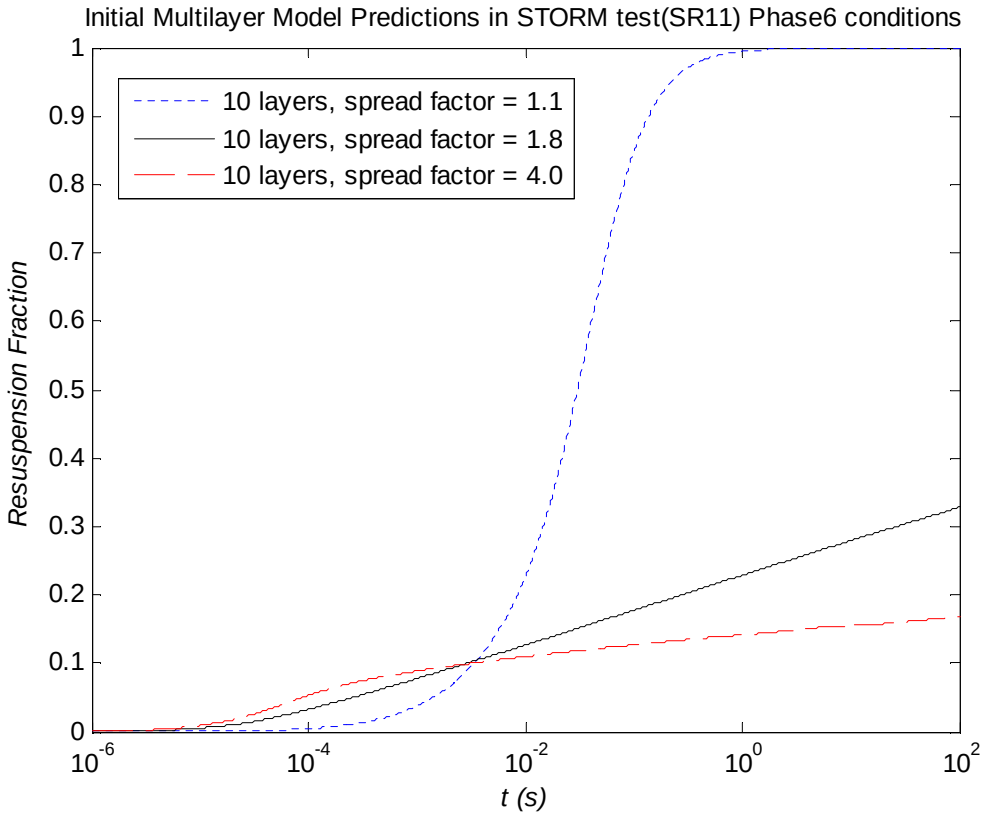

Figure 5.7 - Effect of spread factor on 10 layers model

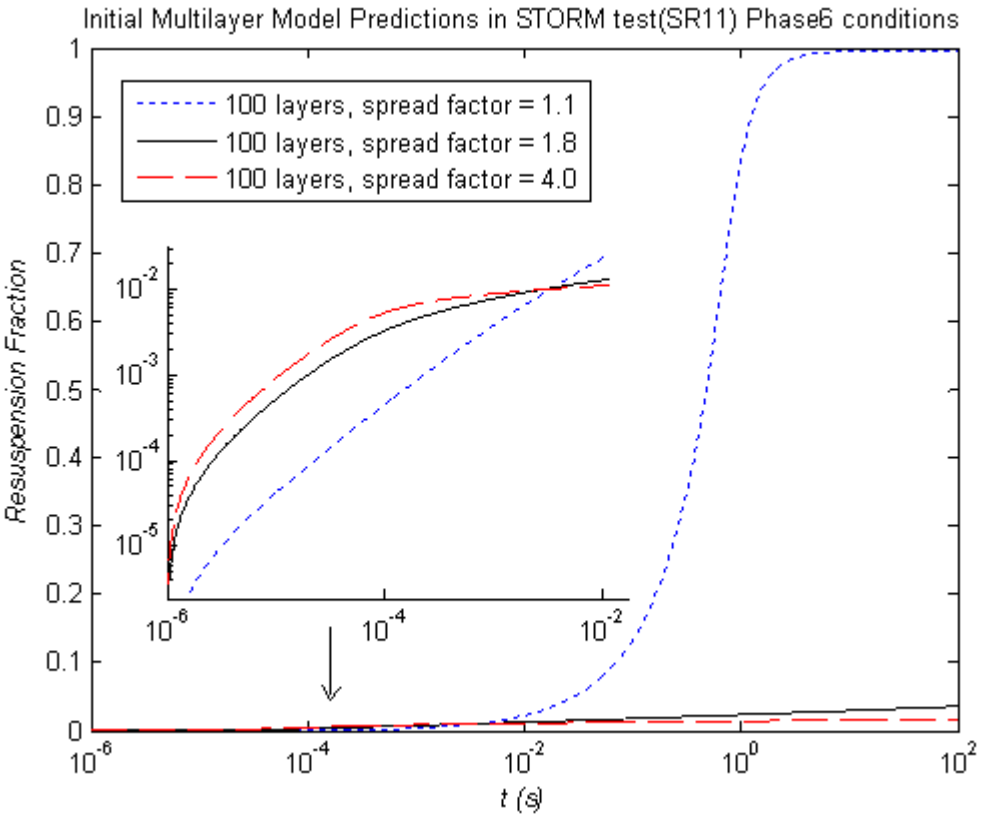

Figure 5.8 - Effect of spread factor on 100 layers model

We note that a spread of 1.1 corresponds to a very narrow distribution of adhesive forces (a value of 1.0 corresponds to zero spread) so in this case there is only a very small amount of longer term resuspension, most particles being resuspended over a period of 10^{-2}s. As the number of layers increases from 1 to 100 layers, the resuspension is still relatively sharply defined but the onset of resuspension is delayed from 10^{-4}s to 10^{-2}s, whilst occurring over a period of say 10^{-1}s. As the spread factor increases the difference between the 100 layer deposit and the monolayer is much more marked: for a spread of 4 after 1s, only 2% of the 100 layer deposit has resuspended compared with almost 100% for the monolayer deposit. There is in fact no sharp distinction between short and long-term resuspension, in fact it is really all long-term resuspension.

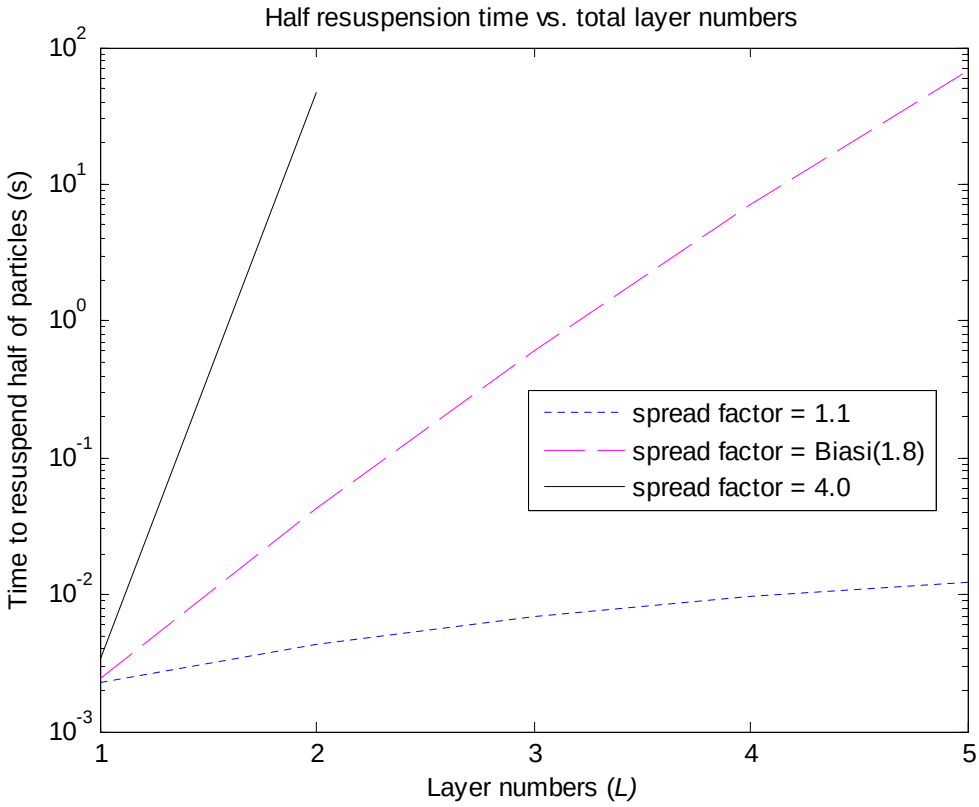

Figure 5.9 - Time to resuspend 50% particles vs. total layer numbers of deposit

Figure 5.9 showed the time to resuspend 50% particles for different spread factor. As the spread factor increased, the half resuspension time increased dramatically as the deposit became thicker.

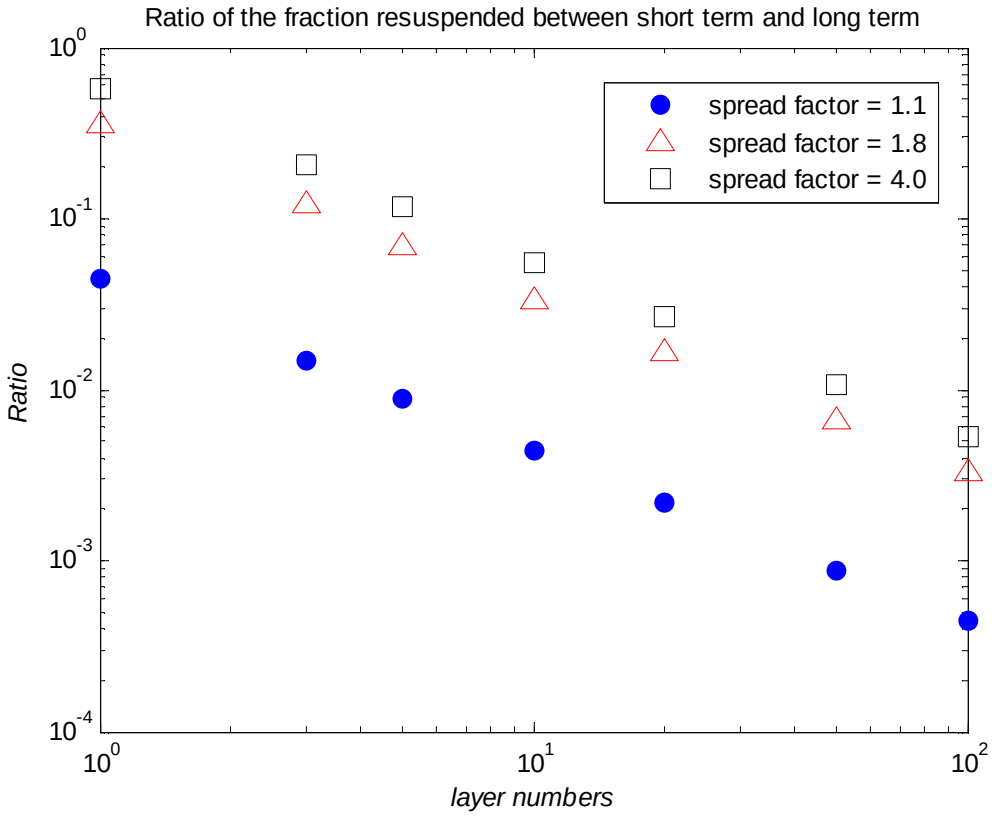

Figure 5.10 - Ratio of resuspension fraction between short term (<10^{-4} s) and long-term (note that the resuspension of long-term is 1 – the resuspension of short term)

Figure 5.10 shows the ratio of resuspension fraction between short term and long-term. The short term is considered as the period before the resuspension rate becomes approximately proportional to $1/t$. It can be observed in Figure 5.3 that after around 10^{-4} s the curves become straight lines. Therefore, short term finishes ~10^{-4} s (~12 in wall units). As the layer number increases, i.e. the deposit thickness increases the short term resuspension contributes less and less to the total resuspension since most of the particles covered are not so easily removed. For the same number of layers L, the ratio of short term and long-term resuspension fraction with a large spread factor (i.e. 4) is always higher than for a small spread factor although the difference is hardly observed when layer numbers are very large. The reason for this is due to a wide range of adhesive force, the particles with small adhesive force are more easily to be removed in the short term. However, this large range of adhesive force affects the ratio difference less and less when the layer number increases, which indicates that the thickness of the deposit is a more important factor than the spread of adhesion on resuspension. Also, Figure 5.10 indicates that the slopes are the same for the range of spread factors. It suggests that

$$\log(Ratio) = \log\left[f(\sigma_a')\right] + slope \cdot \log(L)$$
$$Ratio = f(\sigma_a') \cdot L^{slope} \qquad [5.15]$$

where the slope is very close to -1, $f(\sigma_a')$ is a function of σ_a' and is plotted in Figure 5.11.

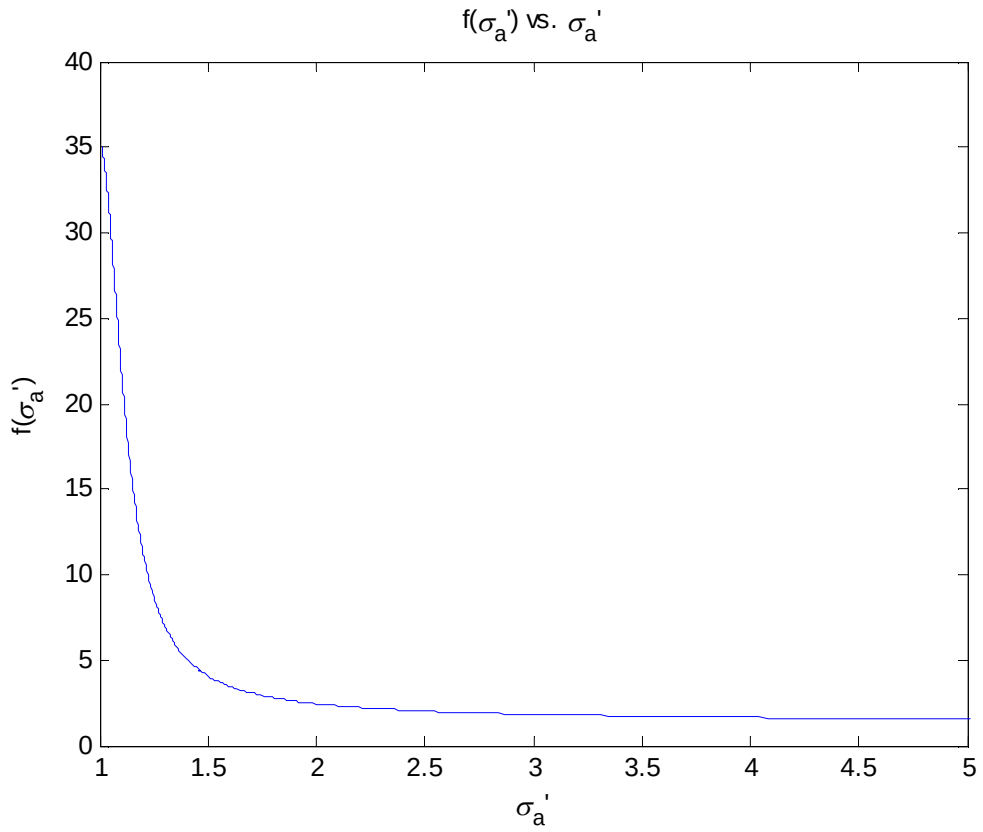

Figure 5.11 - $f(\sigma_a')$ vs. σ_a'

The function f according to Figure 5.11 is fitted to

$$f\left(\sigma_a'\right) = 34.47\sigma_a'^{-5.6} + 1.27 \qquad [5.16]$$

5.1.1.2 Comparison of Gaussian and non-Gaussian R'n'R model in Multilayer Resuspension

The major difference between Gaussian and non-Gaussian R'n'R model is from the resuspension rate constant, recall Eq.[4.12] and Eq.[4.29]: the Gaussian case

$$p = \frac{1}{2\pi}\sqrt{\frac{\langle \dot{f}^2 \rangle}{\langle f^2 \rangle}}\exp\left(-\frac{f_{dh}^{\ 2}}{2\langle f^2 \rangle}\right)\Bigg/\frac{1}{2}\left[1+erf\left(\frac{f_{dh}}{\sqrt{2\langle f^2 \rangle}}\right)\right]$$

and the non-Gaussian case

$$p = B_{fdot}\sqrt{\frac{\langle \dot{f}^2 \rangle}{\langle f^2 \rangle}}\frac{z_{dh}-A_1}{A_2^{\ 2}}\exp\left(-\frac{1}{2}\left(\frac{z_{dh}-A_1}{A_2}\right)^2\right)\Bigg/1-\exp\left(-\frac{1}{2}\left(\frac{z_{dh}-A_1}{A_2}\right)^2\right)$$

with the same assumption on the rms coefficient f_{rms} and the typical forcing frequency ω^+.

$$\sqrt{\langle f^2 \rangle} = f_{rms}\langle F \rangle \quad , \qquad \sqrt{\frac{\langle \dot{f}^2 \rangle}{\langle f^2 \rangle}} = \omega^+\left(\frac{u_\tau^{\ 2}}{\nu_f}\right)$$

The fraction resuspension of multilayer models with these two R'n'R models is calculated. In the comparison, the typical forcing frequency ω^+ and the rms coefficient f_{rms} are chosen to be the same

for both Gaussian and non-Gaussian cases (ω^+ = 0.0413 and f_{rms} = 0.2). Therefore, the difference between the curves in Figure 5.12 is only from the Gaussian and non-Gaussian distributions (the distributions of aerodynamic resultant force and its derivative) which used to derived the resuspension rate constant.

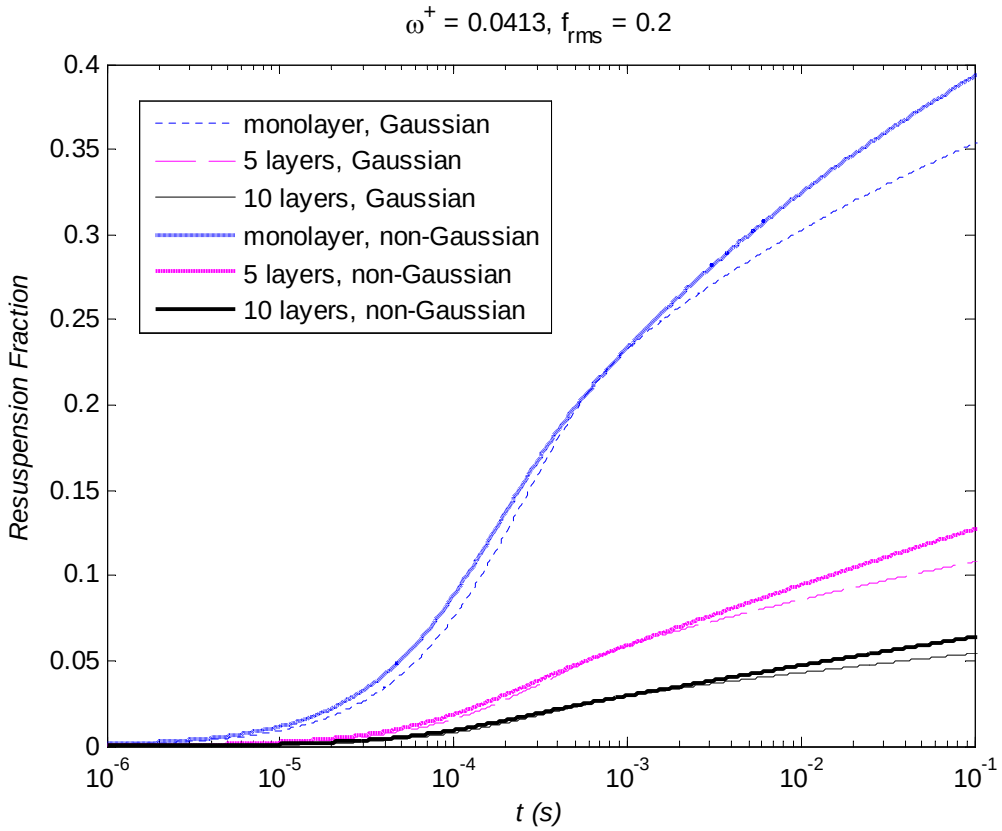

Figure 5.12 - Comparison of multilayer model with the rate constant based on Gaussian and non-Gaussian R'n'R model

Figure 5.12 shows that the non-Gaussian model always results more resuspension than the Gaussian case. As time increases, the difference becomes greater and greater. It is noted that the time of the joint point (around 10^{-3}s in the plot) depends on the wall friction velocity, typical forcing frequency and the rms coefficient; it is independent to the layer numbers.

5.1.1.3 Influence of Coverage on Multilayer Resuspension

The effect of coverage is now considered by assuming that particles are not regularly spaced as in a lattice of the FY generic model but randomly spaced with the same distribution for all layers. Thus in any given layer apart from the top layer when no particles are removed from the layer above, an area corresponding to the particles projected cross section area is revealed within which particles are exposed to the flow. Here a new parameter a_i (the coverage coefficient) is introduced to describe the number ratio of particles exposed to the flow in a given layer ($i + 1$) due to removal of particles from the layer above (i), namely

$$a_i = f_{Ai} \frac{\overline{n}_{i+1}}{\overline{n}_i} \qquad [5.17]$$

where f_{Ai} is the particle occupied area fraction (the fraction of particles projected area in horizontal plane parallel to the wall) in layer i and $\overline{n}_i$ is the initial average number of particles in the ith layer. In other words, all the particles in layer i would therefore cover $f_{Ai}\overline{n}_{i+1}$ particles in layer $i + 1$. It is noted that the average number of each layer is the same, therefore $\overline{n}_{i+1}/\overline{n}_i$ =1. Also it is assumed that the coverage coefficient is the same for all layers (use a instead of a_i). The particle occupied area fraction is defined as the total particles cross section area over the whole area of the layer.

$$f_{Ai} = \frac{\overline{A}_{pi}\overline{n}_i}{A_i} \qquad [5.18]$$

where $\overline{A}_{pi}$ is the average particle projected area (for spherical particle, it is $\pi\overline{r}_i^2$ and $\overline{r}_i$ is the average particle radius in layer i) and A_i is the total surface area of layer i.

The average number of particles in the ith layer can be determined as

$$\overline{n}_i = \frac{V_i f_{Vi}}{\overline{V}_{pi}} \qquad [5.19]$$

where V_i is the total volume of layer i. f_{Vi} is the particle volume fraction in the ith layer and $\overline{V}_{pi}$ is the average single particle volume in the ith layer. The volume fraction is related by definition to the porosity, namely considered

$$f_{Vi} = 1 - \varsigma_i \qquad [5.20]$$

It is noted that technically this porosity ought to be different for different layers. Here, it is assumed that the porosities for all the layers are the same (use ς).

The average thickness of the ith layer is assumed as the average diameter of particles in the ith layer. Therefore, the particle occupied area fraction is given by

$$f_{Ai} = \frac{\bar{A}_{pi}\bar{n}_i}{A_i} = \frac{\bar{A}_{pi}V_i f_{Vi}}{A_i \bar{V}_{pi}} = \frac{\bar{A}_{pi} 2\bar{r}_i}{\bar{V}_{pi}}(1-\varsigma) \quad [5.21]$$

It is assumed that the average number of particles in each layer is the same. Therefore, the coverage coefficient is then derived as

$$a = f_{Ai}\frac{\bar{n}_{i+1}}{\bar{n}_i} = \frac{\bar{A}_{pi} 2\bar{r}_i}{\bar{V}_{pi}}(1-\varsigma) \quad [5.22]$$

For a deposit composed by spherical particles,

$$f_{Ai} = \frac{\pi \bar{r}_i^2 \bar{n}_i}{A_i} = \frac{\pi \bar{r}_i^2 2A_i \bar{r}_i f_{Vi}}{A_i \, 4/3 \pi \bar{r}_i^3} = \frac{3}{2} f_{Vi} = \frac{3}{2}(1-\varsigma) \quad [5.23]$$

Therefore, the coverage coefficient for the deposit of spherical particles according to Eq.[5.17] and Eq.[5.23] is given by

$$a = \frac{3}{2}(1-\varsigma) \quad [5.24]$$

Note: a varies from 0 to 1.5. a = 1 means that if one particle is removed from the layer above only one particle in the layer below will be exposed to the flow. Friess and Yadigaroglu (2002) demonstrated that in STORM SR11 experiment condition, their deposition and resuspension model with the porosity between 0.62 and 0.71 gave closer results to the experimental data. Therefore, the value of a in STORM SR11 experiment condition is calculated from 0.44 to 0.57.

a is the number ratio of particles exposed to the flow of the layer below to the current layer and than it can be derived as the rate ratio since the exposure rate is approximately the number of particles multiplied by the rate constant.

$$a = f_{Ai}\frac{\bar{n}_{i+1}}{\bar{n}_i} \simeq f_{Ai}\frac{\dot{\bar{n}}_{i+1}}{\dot{\bar{n}}_i} \quad [5.25]$$

Therefore, Eq.[5.8] is redefined by including the exposure rate ratio in the source term.

$$\frac{\partial n_1(r_a', t)}{\partial t} = -p(r_a')n_1(r_a', t)$$

$$\frac{\partial n_i(r_a', t)}{\partial t} = -p(r_a')n_i(r_a', t) + a \cdot \varphi(r_a')\int_0^\infty p(\tilde{r}_a')n_{i-1}(\tilde{r}_a', t)d\tilde{r}_a' \quad (i \geq 2) \quad [5.26]$$

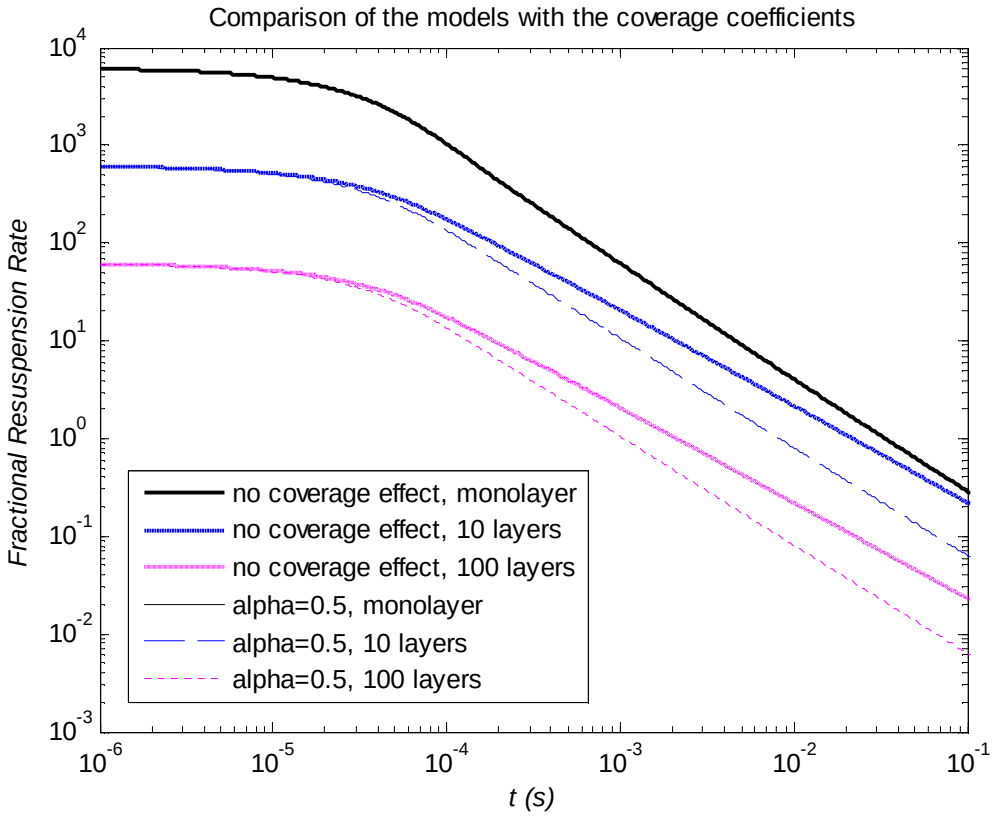

Figure 5.13 - Effect of exposure rate ratio on resuspension rate

Figure 5.13 and Figure 5.14 show the resuspension rate and fraction comparison between the initial multilayer model and the model included the coverage coefficient. As one can observe from the resuspension rate comparison, the monolayer case is unaffected by the coverage coefficient as expected and for the multilayer case (10 and 100 layers) the resuspension rate with no coverage effect (with a = 1) is very close to the resuspension with a = 0.5 in the short term $<10^{-4}$s exposure time (since this is mainly due to resuspension of the top layers where the reduced coverage effect has hardly any effect: only in the long-term $>10^{-4}$s does the coverage effect starts to dominate reducing the resuspension rate dramatically. This can also be observed in Figure 5.14 which is the comparison of resuspension fraction as a function of time. A coverage coefficient a = 0.5 reduces the fraction amount by around half after 100s. However, this coverage coefficient is determined by the porosity of each layer and in reality the porosity for each layer is different and also this porosity varies as time goes on. In the next section, this ratio constant will be replaced with a particle size distribution which will be more physically correct.

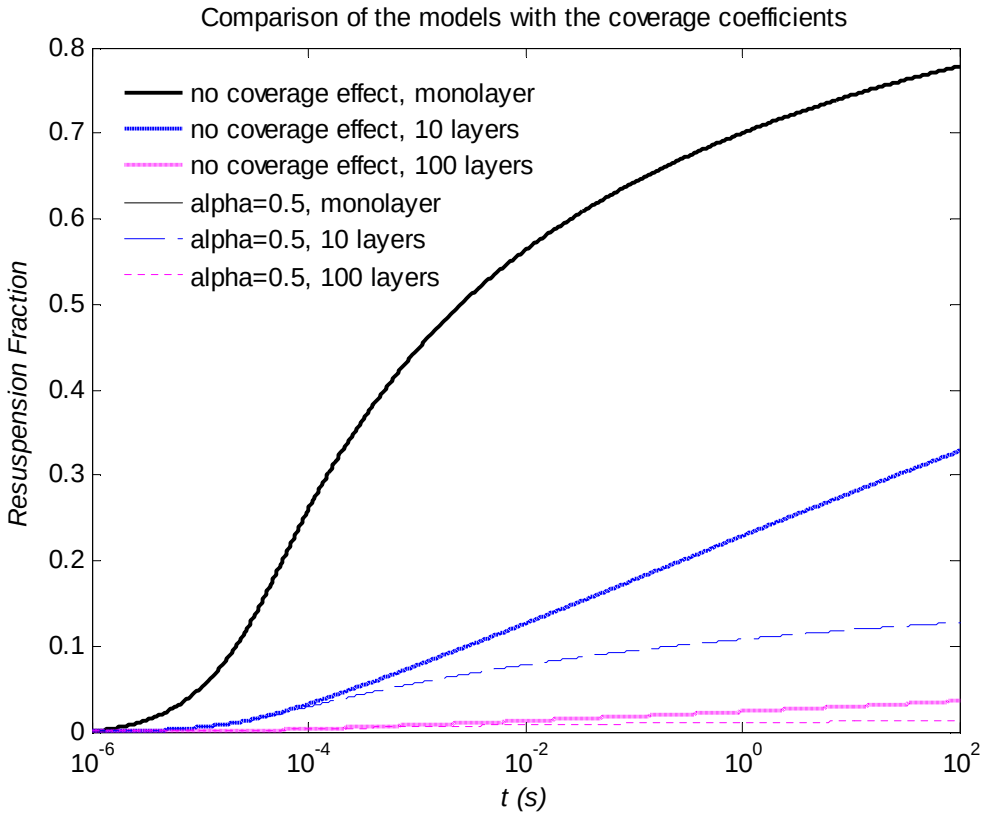

Figure 5.14 - Effect of exposure rate ratio on resuspension fraction

5.1.2 Multilayer Resuspension with Particle Size Distribution in Layer

In order to study the behaviour of deposit structure in particle resuspension, the clustering of particles within a given layer (the clustering effect) is an important consideration. However, there is not much information about the cluster and deposit structure in a bed of particles. In this section, a simple addition is introduced to the set of multilayer equations to include the influence of particle size distribution in the initial multilayer model where the clusters are considered simply as different size particles. The interaction between the particles in the same layer is not considered, but the coverage effect from the layer above to the layer below will be included.

The distribution $\psi(r)$ of the particle radius r is considered as log-normal with geometric mean $\bar{r}$ and geometric standard deviation σ_r, i.e.

$$\psi(r) = \frac{1}{\sqrt{2\pi}} \frac{1}{r} \frac{1}{\ln \sigma_r} \exp\left(-\frac{\left[\ln(r/\bar{r})\right]^2}{2(\ln \sigma_r)^2} \right) \qquad [5.27]$$

Since the resuspension rate constant p and exposure pdf n is a function of particle size, then the formula for the pdf of exposed particles (Eq.[5.8]) becomes

$$\frac{\partial n_1(r, r_a', t)}{\partial t} = -p(r, r_a') n_1(r, r_a', t)$$

$$\frac{\partial n_i(r, r_a', t)}{\partial t} = -p(r, r_a') n_i(r, r_a', t) + \psi(r) \varphi(r_a') \int_r^\infty \int_0^\infty p(\tilde{r}, \tilde{r}_a') n_{i-1}(\tilde{r}, \tilde{r}_a', t) d\tilde{r}_a' d\tilde{r} \quad (i \geq 2) \qquad [5.28]$$

Note: the integration in the source term of the second equation for particle size distribution is taken from the current particle radius r to infinity. In other words, in order to expose the current particle of radius r to the flow, the radius of the particle from the previous layer must be larger than the current particle radius. The numerical method of Eq.[5.28] is presented in Appendix 4 (p205).

Each deposit layer is assumed as the formation of a distribution of spherical particles as shown,

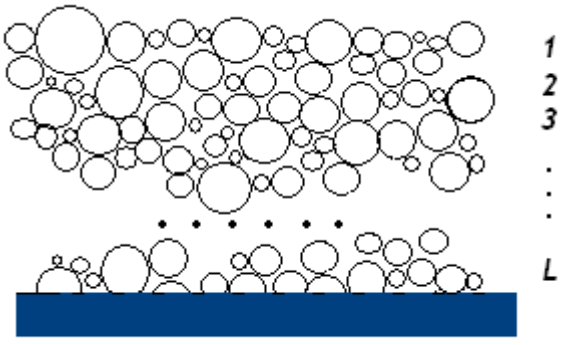

Figure 5.15 - Geometry of the multilayer system with polydisperse particles

The resuspension rate in the *i*th layer is thus defined as

$$\Lambda_i(t) = \int_0^\infty \int_0^\infty p(r, r_a') n_i(r, r_a', t) dr_a' dr \qquad [5.29]$$

The roughness condition for all the particles is assumed to be the same. The same distribution of normalized asperity radius ($\varphi(r_a')$) is used for all the particles in the domain. Layer thickness is determined by the mean particle diameter and they are assumed to be the same for every layer.

In the calculation below, the parameters from the STORM SR11 experiment Phase 6 conditions will be applied, together with Biasi's correlation for the parameters of adhesion distribution.

Average radius (μm)	Geometric standard deviation of radius	Fluid density ($kg.m^{-3}$)	Fluid kinematic viscosity ($m^2.s^{-1}$)	Wall friction velocity ($m.s^{-1}$)	Surface energy ($J.m^{-2}$)
0.227	1.7	0.5730	5.2653×10^{-5}	6.249	0.5

The average particle size and geometric standard deviation was used identical to the SOPHAEROS code (more information in Chapter 5.2.1, p184).

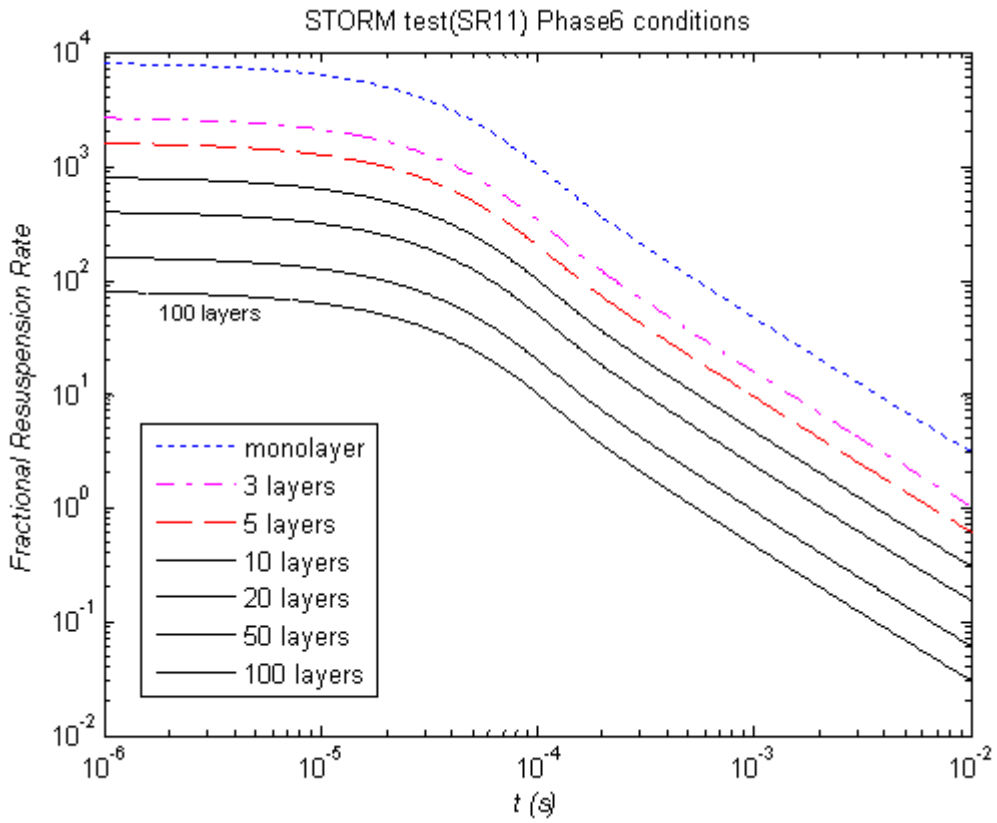

Figure 5.16 - Fractional resuspension rate vs. time for model with polydisperse particles

The fractional resuspension rate (calculated by Eq.[5.13]) for the polydisperse particles is shown in Figure 5.16. Compared to the results for the for monodisperse particles, the long-term resuspension rate in this case has decreased in a significant amount when the layer number increased which can be observed in Figure 5.17.

The comparison of the resuspension for monodisperse particles with that for polydisperse particles in each layer with the same geometric mean size Eq.[5.27] is shown below. Figure 5.17 shows the comparison of the fractional resuspension rate from which it is observed that the fractional resuspension of the polydisperse particles in the short term is greater than that for the monodisperse particles due to the fact the resuspension rate is biased towards increasing particles size. After the initial resuspension and the larger particles (> the geometric mean) have been removed, the particles left are biased towards particle sizes < geometric mean which are harder to remove than those with the geometric mean size. Note that the long-term resuspension rate of the polydisperse case is several orders of magnitude less than that of the monodisperse case.

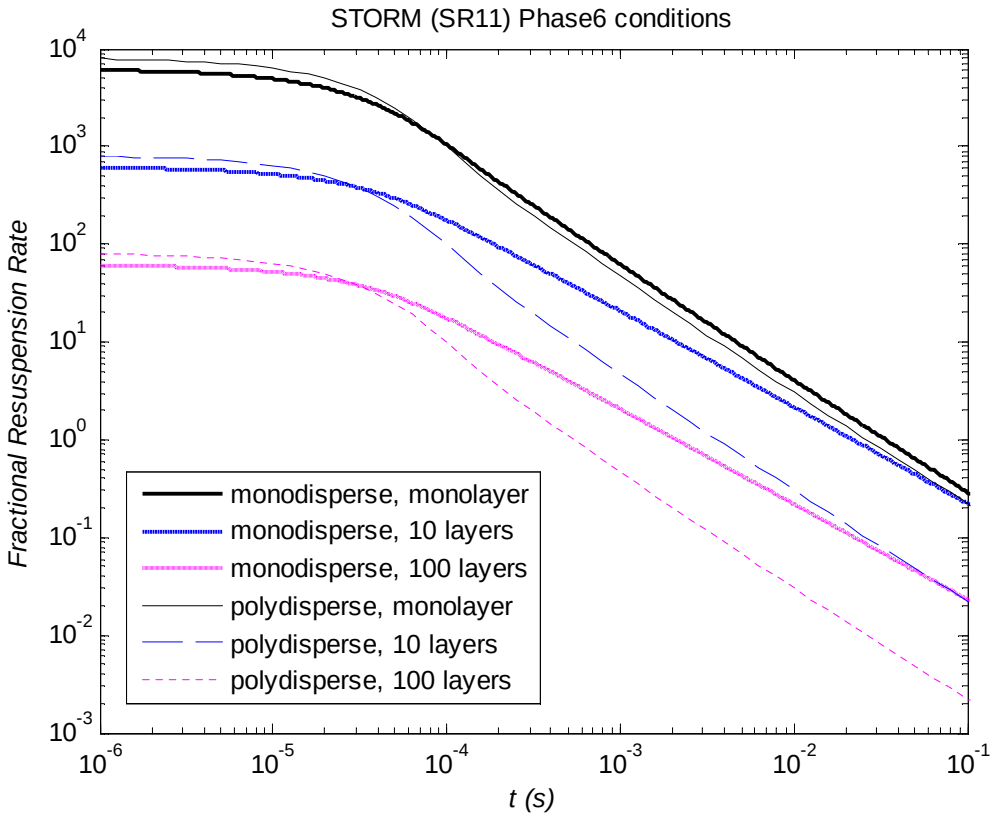

Figure 5.17 - Comparison of fractional resuspension rate vs. time for two multilayer models

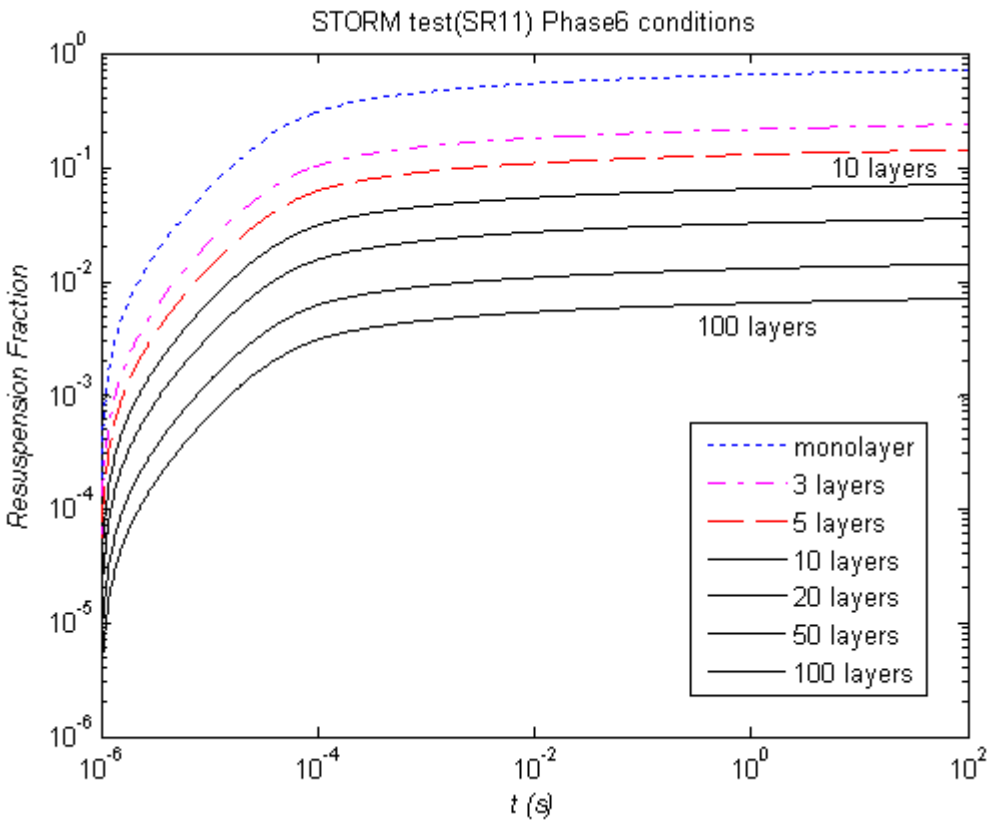

Figure 5.18 - Resuspension fraction vs. time for polydisperse particles

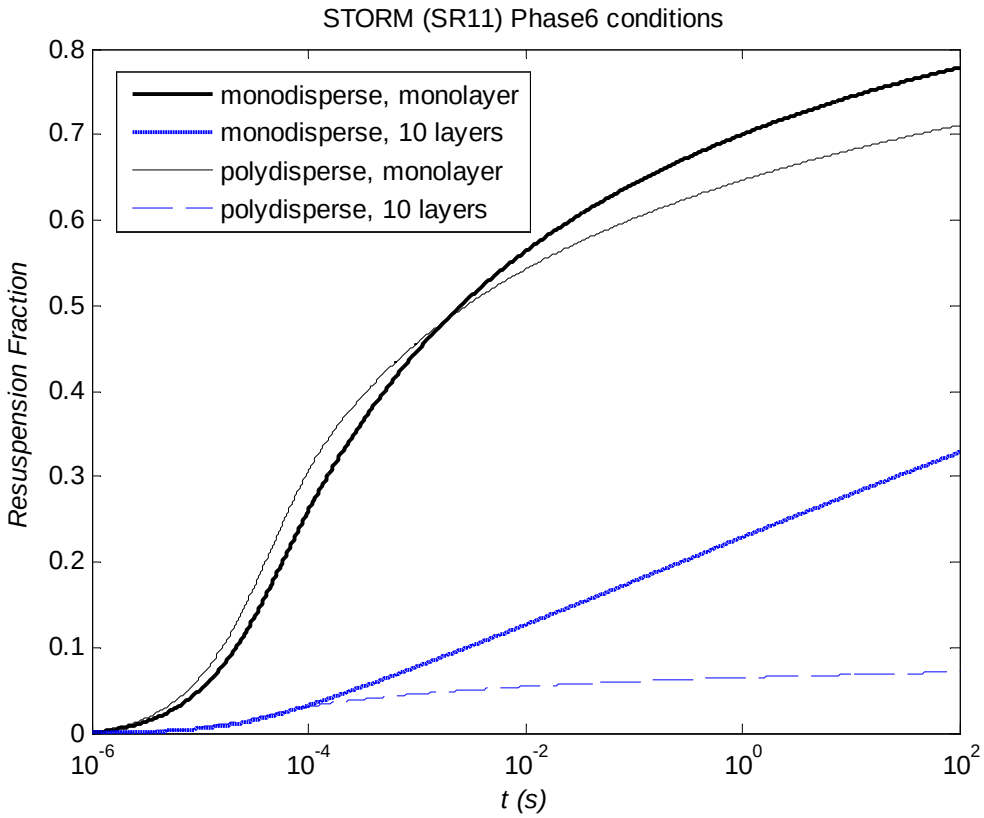

Figure 5.19 - Comparison of resuspension fraction vs. time for polydisperse particles with monodisperse particles with the same geometric mean size.

Figure 5.18 shows the resuspension fraction for different layers for the polydisperse case. It is noted that as the layer number increases to more than 10, less than 10% deposit is removed after 100s. It also shows that the resuspension fraction for each layer case is exponentially proportional to the time in the long-term after 10^{-4}s. The comparison of the resuspension fraction for the polydisperse particles and the monodisperse particles with the same geometric mean size and is shown in Figure 5.19. For the monolayer fraction resuspended, the polydisperse case gives slightly more resuspension than the monodisperse case in the short period at the beginning which is the reason of that more larger particles are considered in the polydisperse model and they are easier to be removed than smaller ones. After that period, the resuspension fraction of polydisperse particles becomes less and less compared to that of the monodisperse particles since the smaller polydisperse particles are increasingly harder to remove.

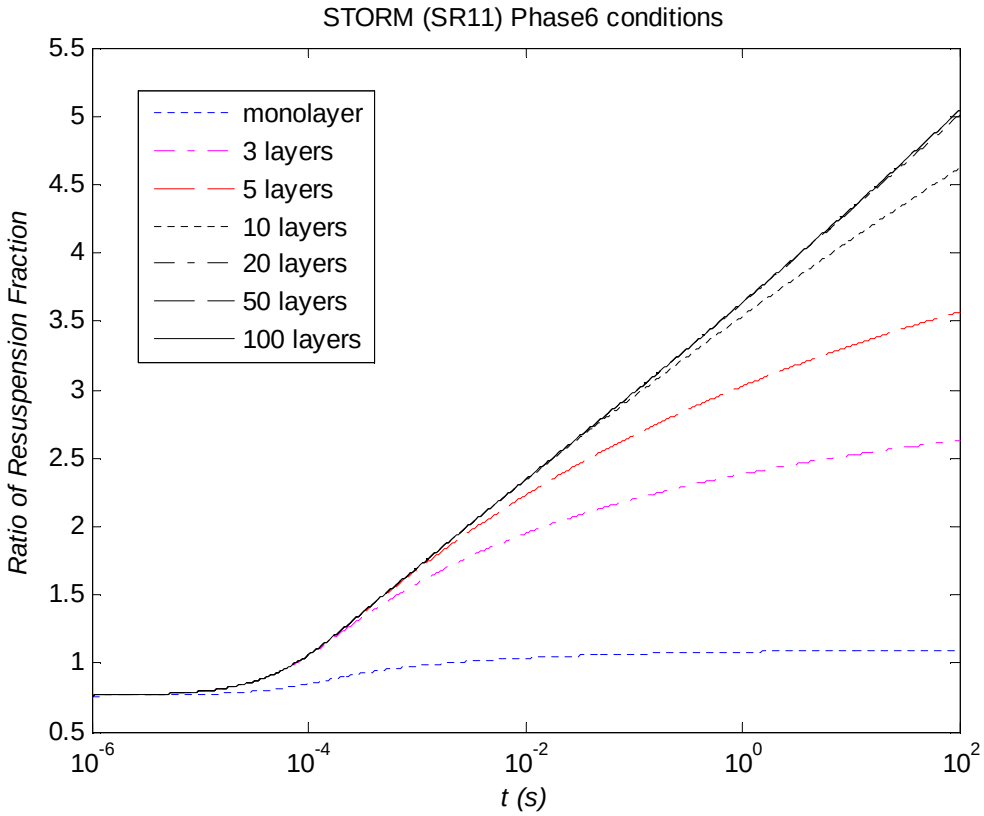

Figure 5.20 - Ratio of resuspension fraction between initial monodisperse model and model with polydisperse particles

Figure 5.20 shows the ratio of the resuspension fraction of the monodisperse particles with that of the polydisperse particles. All the curves start with similar values due to the resuspension of the top layers; also in the short term ($<10^{-4}$s) the resuspension of the polydisperse particles is greater than that of the monodisperse particles since the 50% of the polydisperse particles with sizes > that of the monodisperse particles easier to resuspend. As the layer number increases the difference between the monodisperse and polydisperse particles becomes significant. For 10 layers, the

resuspension fraction of the monodisperse particles after 100s is ~4.5 times that of polydisperse particles. And for the 100 layers case, the ratio increases to around 5 after 100s. This is all consistent with graphs for the resuspension rate comparison.

It is noted here that in the calculations of the multilayer polydisperse particles, Biasi's correlation of the parameters for the distribution of adhesive forces was used for each particle in the size distribution; so the geometric mean of normalized asperity radius and spread factor is different for every particle size.

To examine the effect of spread factor, the value of the geometric mean normalized adhesive radius is fixed at (0.015) and we consider the influence of spread factors of 1.1 (a very narrow spread), 1.817 (Biasi) and 4.0 with the same size distribution as before in Figure 5.18.

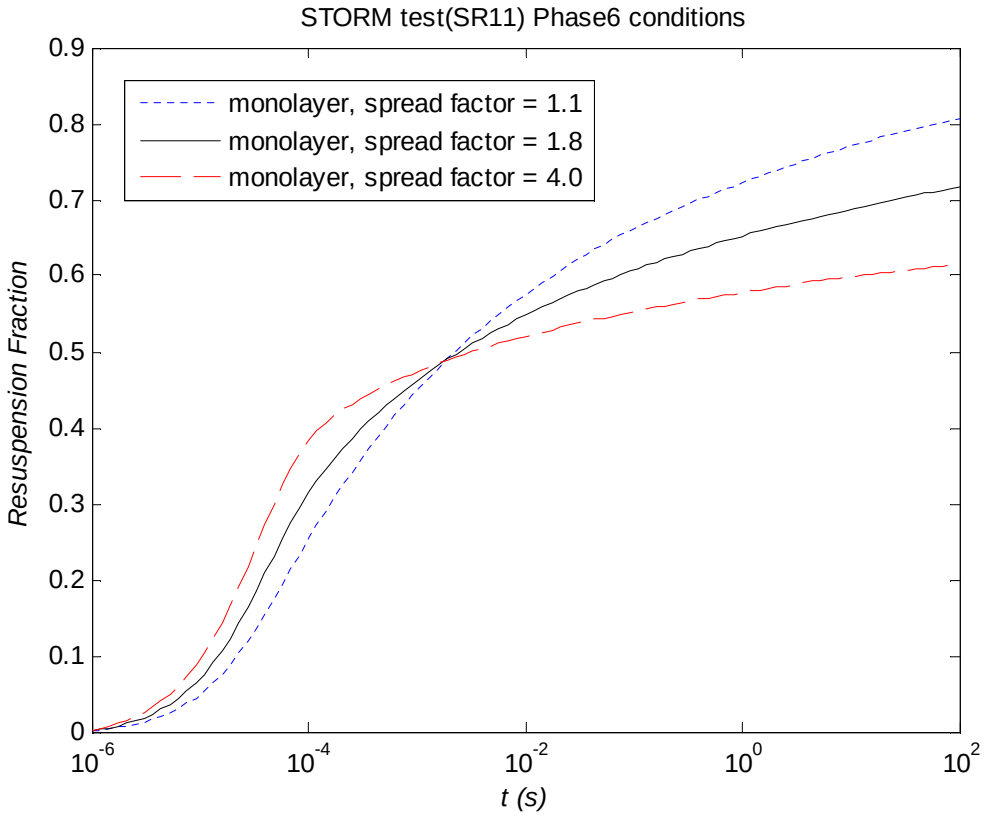

Figure 5.21 - Effect of spread factor in adhesion on monolayer resuspension for polydisperse particles

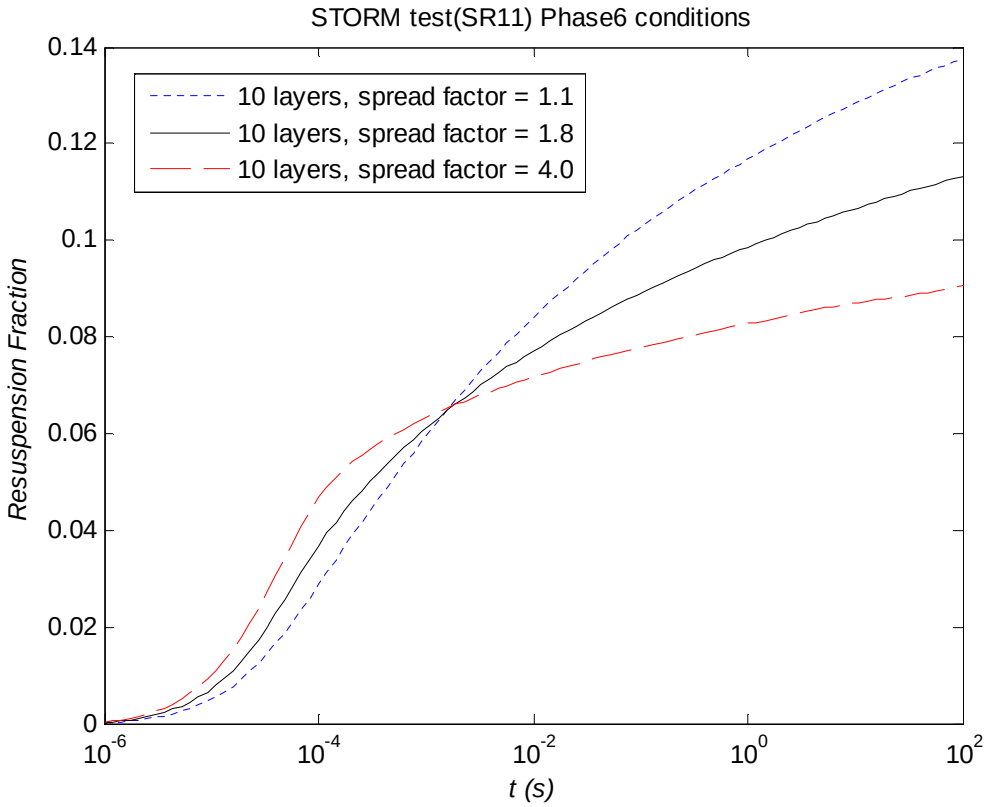

Figure 5.22 - Effect of adhesive spread factor on resuspension of polydisperse particles in a 10 layer multilayer deposit

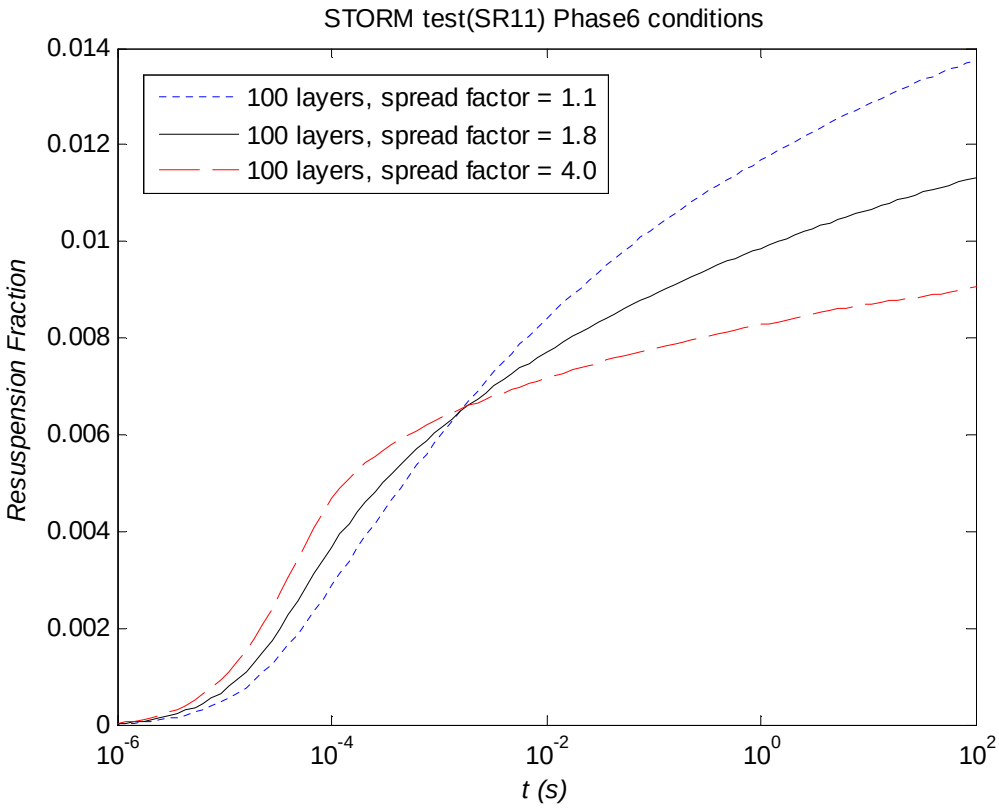

Figure 5.23 - Effect of adhesive spread factor on resuspension of polydisperse particles in 100 layer multilayer deposit

Figure 5.21, Figure 5.22 and Figure 5.23 show the effect on the fraction resuspended of spread factors for a range of layer thickness in the deposit. It is observed in Figure 5.21 that the monolayer model with larger spread initially gives more resuspension due to the fact that there is more large size particles involved in the distribution with a larger spread and they are easier to remove. After a certain period (10^{-3}s), the model with the larger adhesive spread predicts less and less resuspension because the particles left are much harder to remove. However, as the layer number increases the difference between the resuspension for different spread factors becomes less and less because the particles are harder to remove in the thicker deposit due to the coverage effect.

It is noted that in Figure 5.6, Figure 5.7 and Figure 5.8, the curves for the small adhesive spread factor (1.1) are quite different to the others with larger spread factors even for large layer numbers (the curve for small spread factor being more close to a step function). However, this phenomenon is not appeared here. The reason of this is because once a particle size distribution is considered, there would be a large probability of small particles (radius is smaller than the average radius). Therefore, no matter how small the range of adhesive force is, there are still a large amount of particles need to be removed in a much longer period.

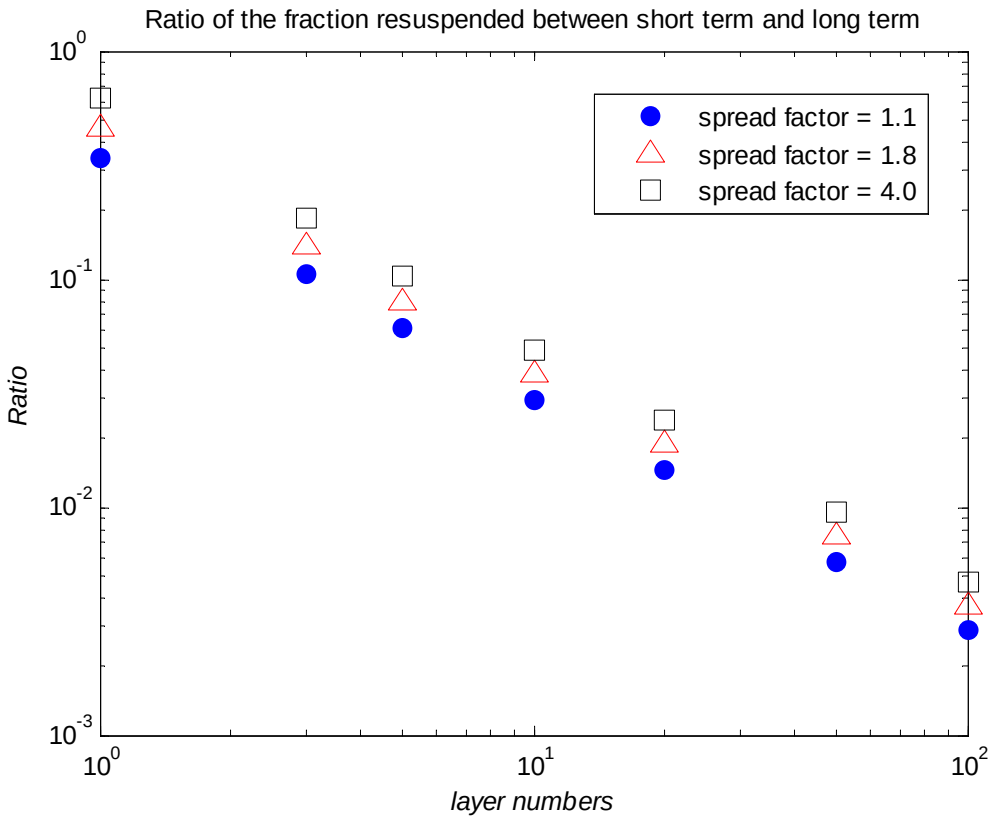

Figure 5.24 - Ratio of resuspension fraction between short term and long-term

Figure 5.24 shows the ratio of resuspension fraction between short term and long-term. The short term is considered as the period before the resuspension rate becomes approximately proportional

to 1/t. It is observed in Figure 5.16 that after around 10^{-4}s the curves become straight lines. Therefore, short term finishes around 10^{-4}s. As the layer number increases, in other words, the deposit became thicker and thicker the short term resuspension contributes less and less to the total resuspension because most of the particles were covered and not easy removed. Also, for the large spread factor (i.e. 4) the ratio of short term and long-term resuspension fraction is always higher than the model with small spread factor though the difference is hardly observed when layer numbers are very large. The reason of this is due to a wide range of adhesive force, the particles with small adhesive force being more easily removed in the short term and this affects the layers on the top more than the layers below. Also, Figure 5.24 indicates that the slopes are the same for the range of spread factors. It is noted that the slopes are close to -1.1.

5.2 Validation of Multilayer Models

In this section, model predictions are compared with the results of two experiments: the STORM SR11 test (Castelo *et al.*, 1999) and the BISE experiment (Alloul-Marmor, 2002). The former is probably the best experiment for multilayer deposit resuspension in the nuclear area and the latter is the latest experiment for multilayer resuspension for which the experimental data has been compared with R'n'R model predictions.

5.2.1 STORM SR11 Test

The STORM (Simplified Test of Resuspension Mechanism) facility was carried out by the Joint Research Centre of the European Commission (EC/JRC) at Ispra, Italy. The aerosol used throughout the tests was composed of tin oxide (SnO_2) particles produced by a laser gun. In all 13 tests were undertaken, the first 8 tests only for aerosol deposition and the rest of the tests included resuspension. SR09 (STORM Resuspension), SR10, SR11, SR12 and SR13 were the tests for aerosol resuspension (Bujan *et al.*, 2008). SR11 is also an International Standard Problem number 40 (ISP-40). It took place in April 1997 and included two distinct phases, the first concentrating on aerosol deposition mostly by thermophoresis and eddy impaction and the second on aerosol resuspension under a stepwise increasing gas flow (Castelo *et al.*, 1999).

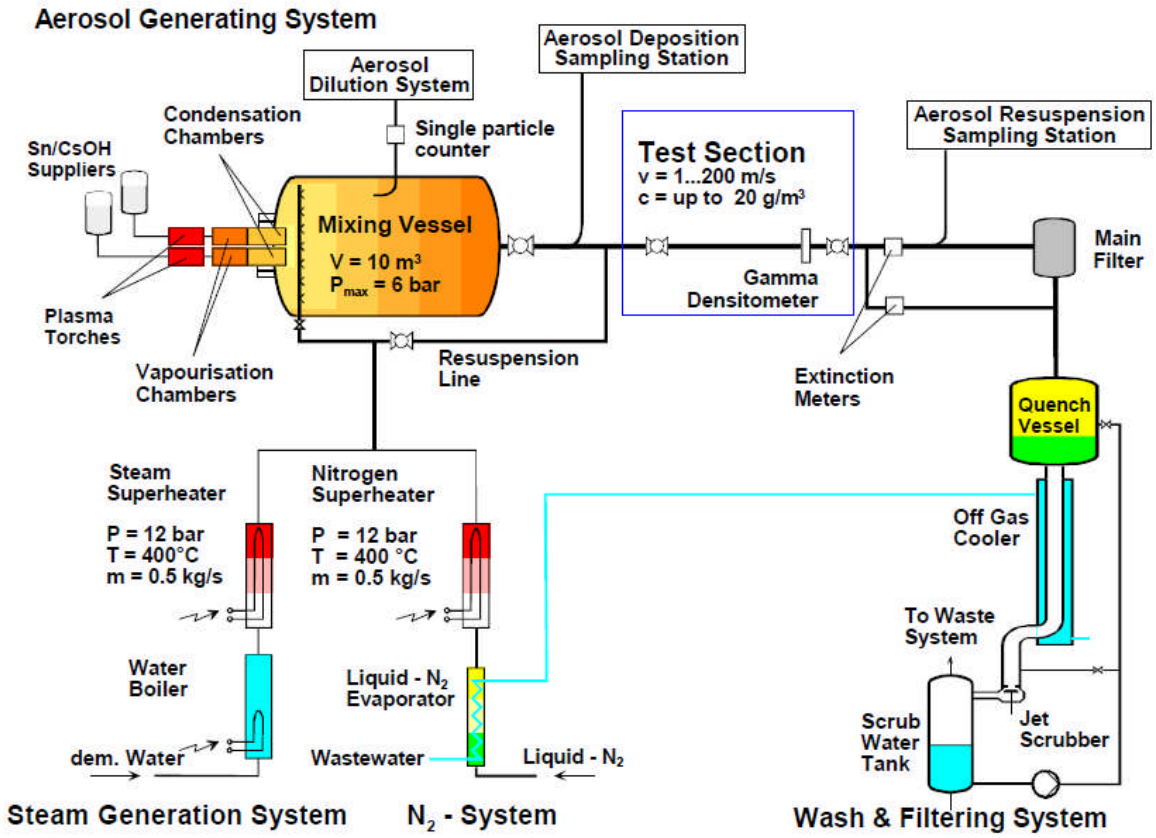

Figure 5.25 - The STORM facility (Castelo *et al.*, 1999)

The STORM test facility is shown in Figure 5.25. The test section (in the blue box) was a 5.0055m long straight pipe with 63 mm internal diameter. In the deposition phase, the carrier gas and aerosols passed through the mixing vessel followed by a straight pipe into the test section and then finally to the wash and filtering system. In the resuspension phase, the clean gas was injected through the resuspension line directly into the test section and the resuspended SnO_2 aerosols were collected in the main filter before the gas goes through the wash and filtering system (Castelo *et al.*, 1999). The resuspension phase was divided into six steps of increasing gas velocity; the carrier gas was pure nitrogen (N_2) at 370 ºC; the flow rates, fluid mean velocity, fluid density and kinematic viscosity for each step are given in the table below.

Step	Mass flow rate (kg/s)	Fluid mean velocity (m/s)	Fluid density (kg/m^3)	Fluid kinematic viscosity (m^2/s)	Wall friction velocity (m/s)
1	0.102	62.01	0.4422	6.0697×10^{-5}	2.773
2	0.126	76.87	0.5425	5.5521×10^{-5}	3.438
3	0.152	93.17	0.5480	5.5000×10^{-5}	4.167
4	0.175	107.78	0.5566	5.4204×10^{-5}	4.820
5	0.199	123.28	0.5647	5.3427×10^{-5}	5.513
6	0.224	139.74	0.5730	5.2653×10^{-5}	6.249

Table 5.1 - Conditions of STORM SR11 test

The mass flow rate was measured in the STORM SR11 test. The fluid mean velocity, density and kinematic viscosity are obtained from the SOPHAEROS code (Cousin *et al.*, 2008). (SOPHAEROS is the module of the European Integral Code ASTEC V1.3 (Accident Source Term Evaluation Code) to reproduce the experimental results of the STORM resuspension tests SR09, SR10, SR11, SR12 and SR13.) The wall friction velocity is calculated as

$$u_\tau = \sqrt{\frac{\tau_w}{\rho_f}}$$

where τ_w is the wall shear stress, whose value can be obtained from a 1-D thermal-hydraulic system code simulation, using the formula

$$\tau_w = \frac{f_{fric}}{8} \rho_f V^2 \qquad [5.30]$$

where V is the fluid mean velocity and f_{fric} is the friction factor which in the STORM case is approximately 0.016 (Komen, 2007).

The size of particles collected after deposition in the STORM test can be reproduced by a log-normal distribution and in the SOPHAEROS code the geometric mean diameter (GMD) is given as 0.454μm and the geometric standard deviation 1.7. Also in the code, the range of the particle size distribution is considered to be from 0.002μm up to 200μm (geometric mean diameter).

The SnO_2 aerosol was produced during the deposition phase. The total mass of the aerosol deposited in the test pipe was estimated to be 0.162kg. The time and mass at the end of each step and the resuspension fraction are shown in the table below.

Step	Time at the end of each step (s)	Mass at the end of each step (kg)	Fraction resuspended
1	720	0.156	0.037
2	2280	0.151	0.068
3	3300	0.124	0.235
4	4380	0.096	0.407
5	5400	0.070	0.568
6	5820	0.042	0.741

Table 5.2 - Resuspension result of STORM SR11 test

The surface energy of SnO_2 according to Yuan *et al.* (2002) varies from 0.47 J/m^2 to 0.51 J/m^2 at 370 °C. Here 0.5 J/m^2 is used for the model calculation.

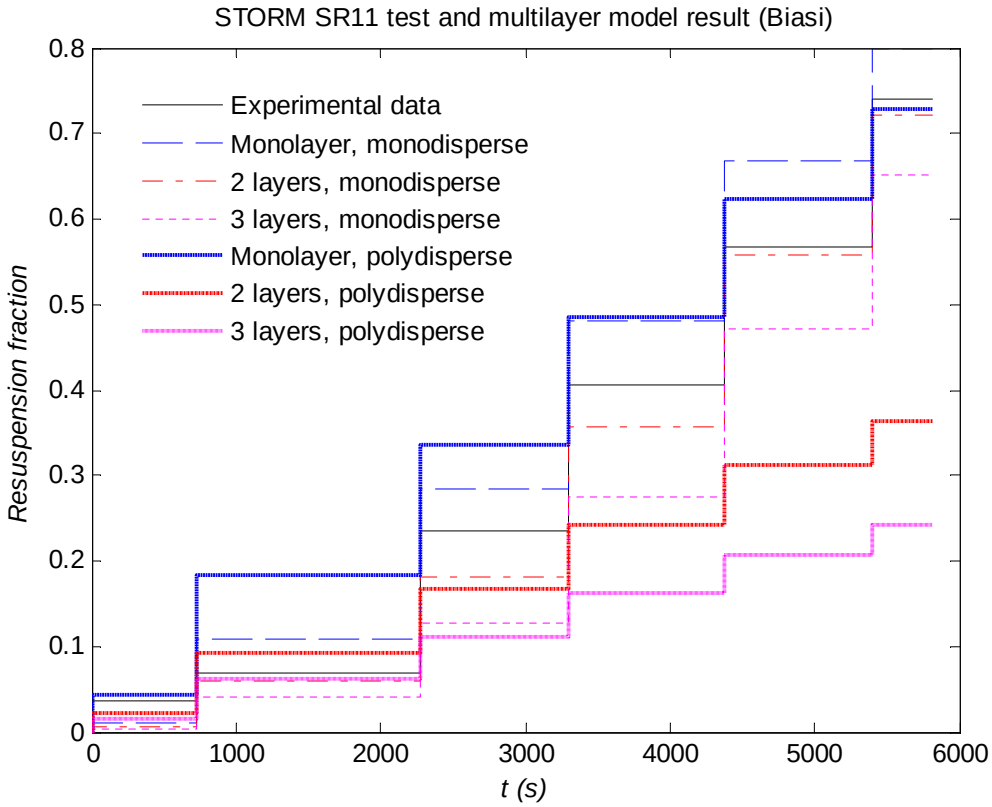

Figure 5.26 - STORM SR11 test comparison (using Biasi's correlation for the adhesive forces)

For the purposes of comparison, two multilayer models were used to calculate the fraction of particles resuspended at the end of each time step: the monodisperse multilayer model (referred to as the monodisperse case) and the polydisperse multilayer model (referred to as the polydisperse case). The values of the parameters used in the model predictions are those given in Table 5.1 and Table 5.2. Biasi's correlation for the adhesive force distribution according to each particle size was used to obtain the results shown in Figure 5.26.

Figure 5.26 shows the model comparisons of the resuspension fraction with the STORM SR11 test results. It is observed that for the monolayer resuspension both polydisperse and monodisperse cases give more resuspension than the experimental data. However, polydisperse case gives results very close to the experimental data in the first step and final step. Comparing one with another, the monodisperse case with 2 layers gives the best results of the other cases studied.

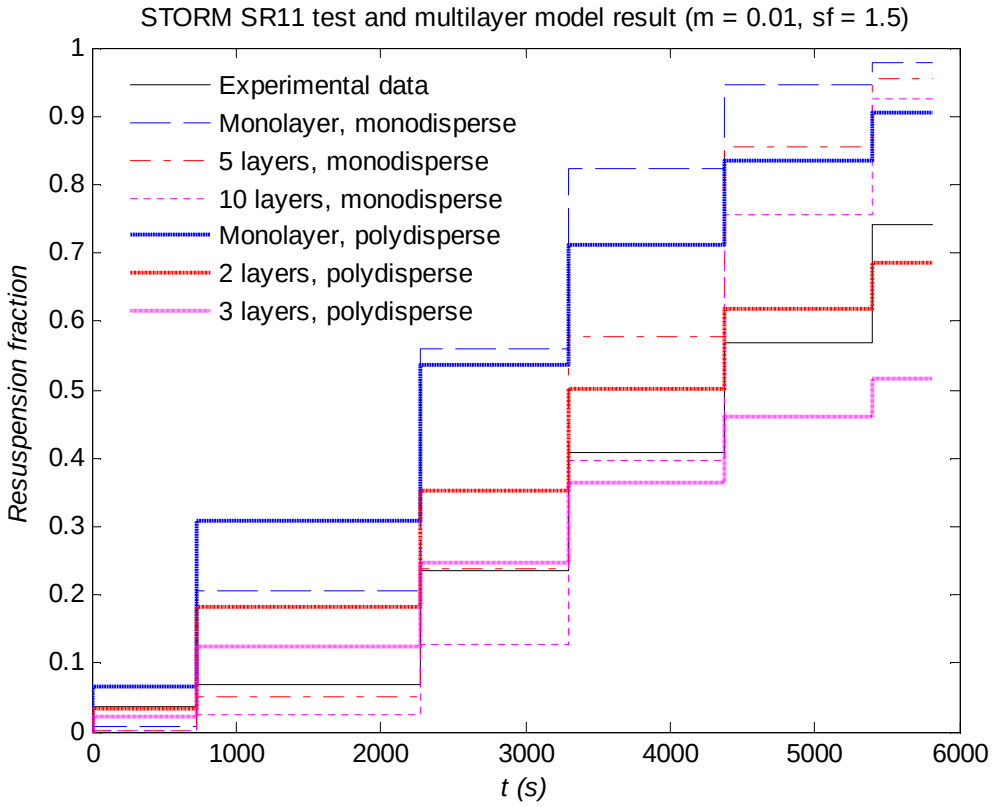

Figure 5.27 - STORM SR11 test comparison (geometric mean (reduction in adhesion) = 0.01, adhesive spread factor = 1.5)

However, it is recalled that Biasi's correlation for the adhesive forces is based on the original R'n'R model which is an isolated particle model for resuspension. Therefore, it is strictly not suited for the multilayer deposit case. In order to check the sensitivity of the resuspension to the values of the adhesion parameters, a geometric mean (reduction in adhesion) was chosen to be 0.01 according to Hall's experiment (Reeks & Hall, 2001) with two different spread factors (1.5 and 4.0) used for comparison. The small spread case is shown in Figure 5.27; one can observe that the polydisperse

case with 3 layers gives a much closer agreement with the experimental measurements than the monodisperse case.

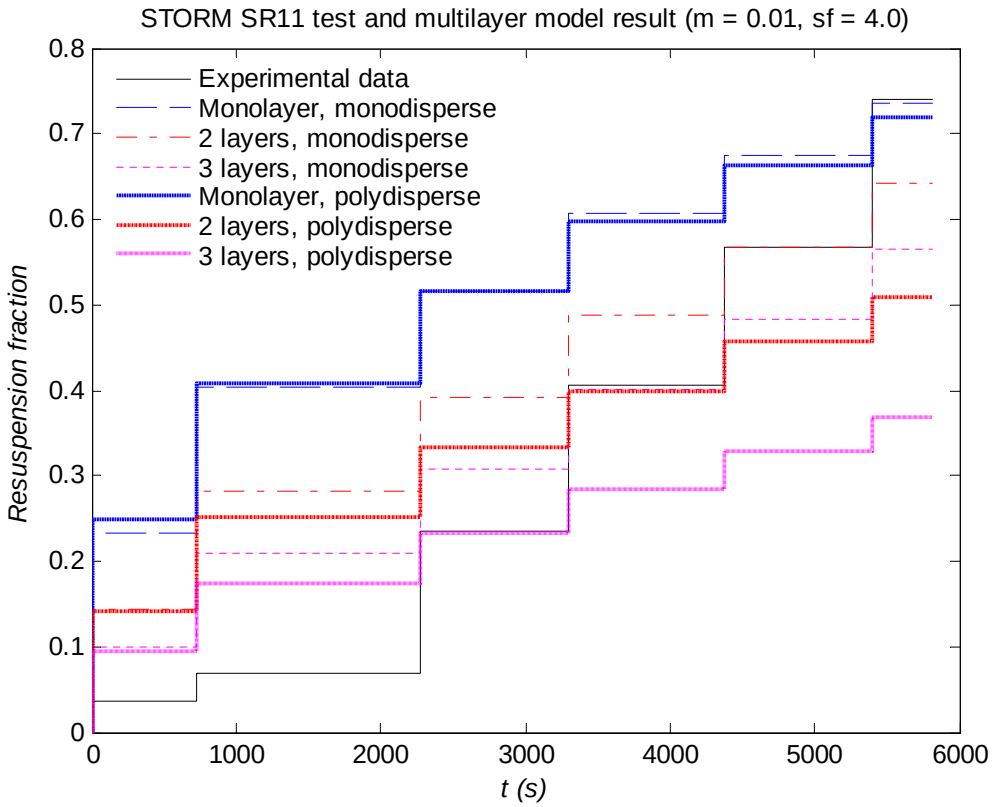

Figure 5.28 - STORM SR11 test comparison (geometric mean (reduction = 0.01, adhesive spread factor = 4.0)

In the case of the resuspension for the large spread factor (4.0), Figure 5.28 shows a poor comparison with the experimental data for both monodisperse and polydisperse cases. The trends of the curves are quite different from those of the experimental data.

5.2.2 BISE Experiment

The BISE (Banc de mIse en Suspension par Ecoulement) experiment was performed by Alloul-Marmor (2002) with the purpose of studying the resuspension of non-radioactive polydisperse particles on a surface in fully developed channel air flow.

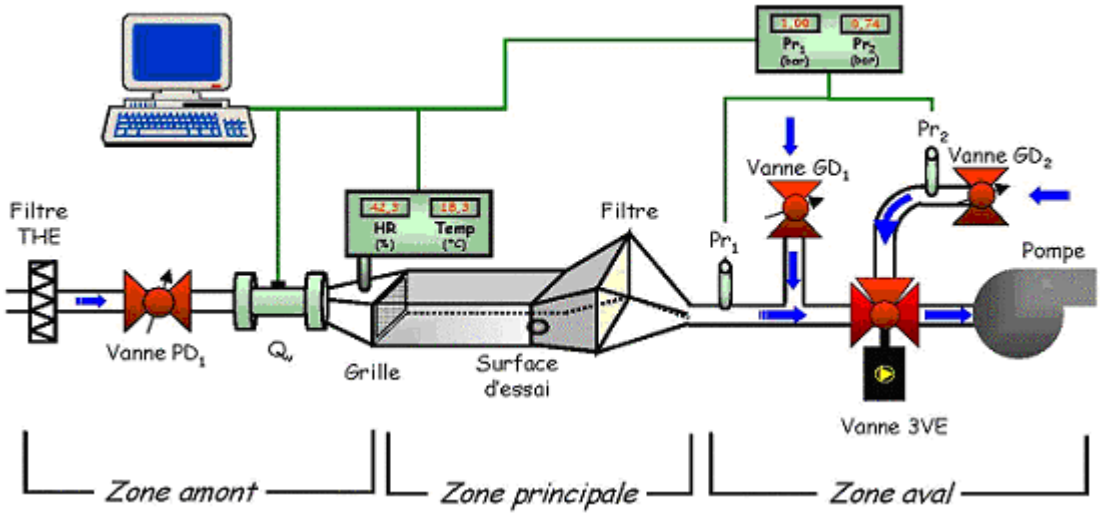

Figure 5.29 - Schema of BISE experiment facility

The principal zone of the installation is composed of two plexiglas partitions. The one on the left in Figure 5.29 is a horizontal right-angled parallelepiped conduit 40cm in length, 12cm wide and 7cm high. There was an experimental surface towards the end of the channel, as shown below. The carrier flow was dry air at room temperature with a range of mean velocities from 0.5m/s to 10m/s (friction velocities from 0.04m/s to 0.52m/s). The time interval for each experiment was 900s.

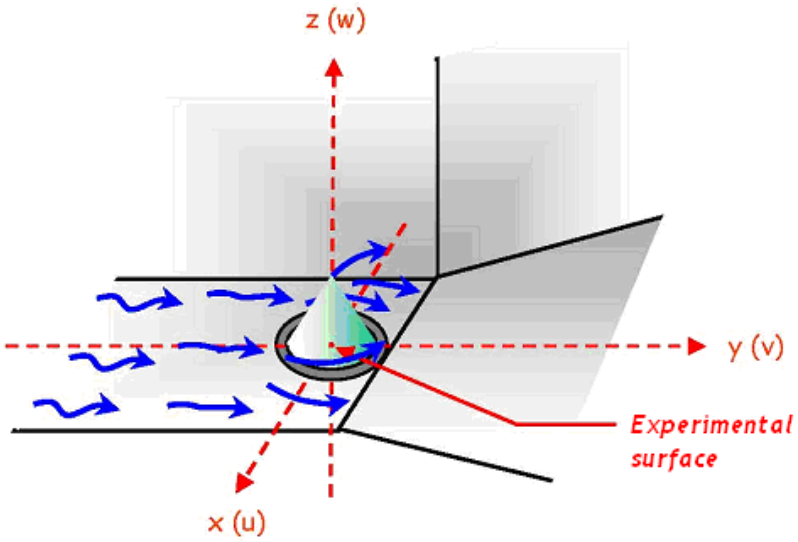

Figure 5.30 - Representation of experimental surface

Al_2O_3 spherical monodisperse particles were used in the experiment. 5 particle sizes were considered from 4.6μm to 58.7μm (MMD) and the resuspension of two of them were compared to

R'n'R model predictions. In the model comparison, only one particle size from these two has been chosen (58.7 microns) because the resuspension fraction was very small for the smaller size particles. Also the mass median diameter has been converted to geometric mean diameter, shown in the table below.

MMD (μm)	GMD (μm)	GSD
58.7	47.75	1.3

Table 5.3 - Table of particle size in BISE experiment

The values of the parameters used in the model calculation are

Average radius (μm)	Geometric standard deviation of radius	Fluid density ($kg.m^{-3}$)	Fluid kinematic viscosity ($m^2.s^{-1}$)	Surface energy ($J.m^{-2}$)
23.875	1.3	1.293	1.515×10^{-5}	0.56

It is noted that, Biasi's correlation is not appropriate for large size particles. Therefore, the geometric mean of normalized asperity radius and spread factor according to Reeks and Hall (2001) are chosen as 0.01 and 1.5, respectively.

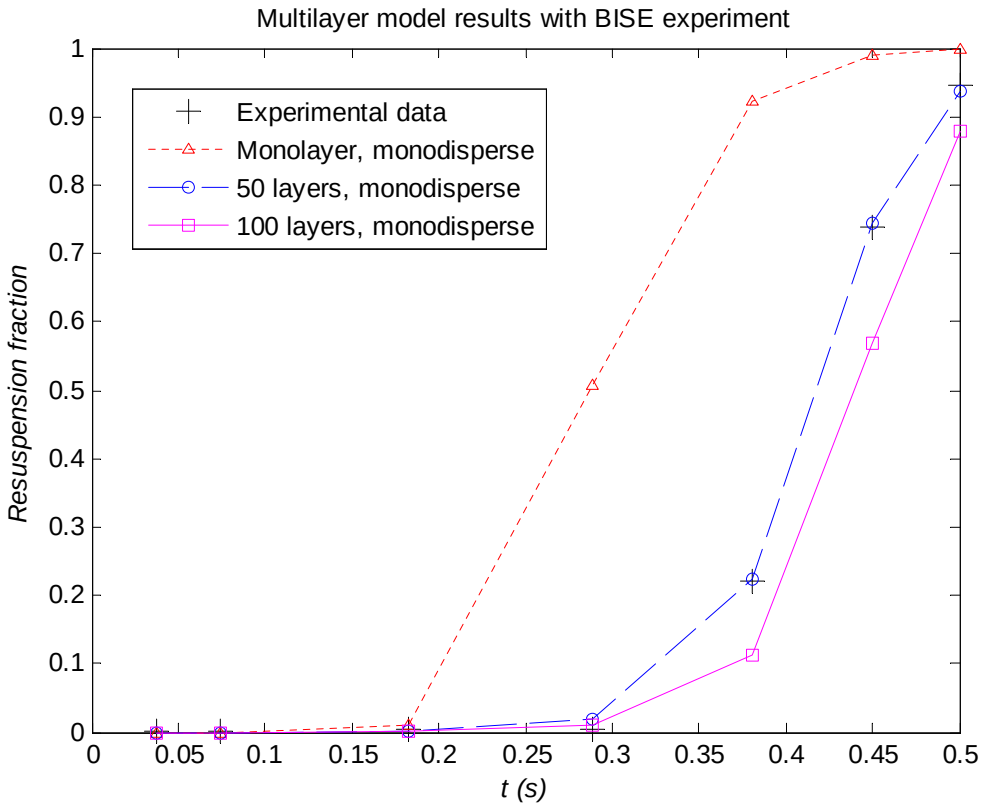

Figure 5.31 - Monodisperse multilayer resuspension predictions vs. BISE experimental results

It is clear from the comparison shown in Figure 5.31 that the monodisperse multilayer model with 50 layers gives very good results compared to the experimental data. However, when a particle size distribution is included (shown in Figure 5.32), the Polydisperse case gives quite poor comparison with the experimental data.

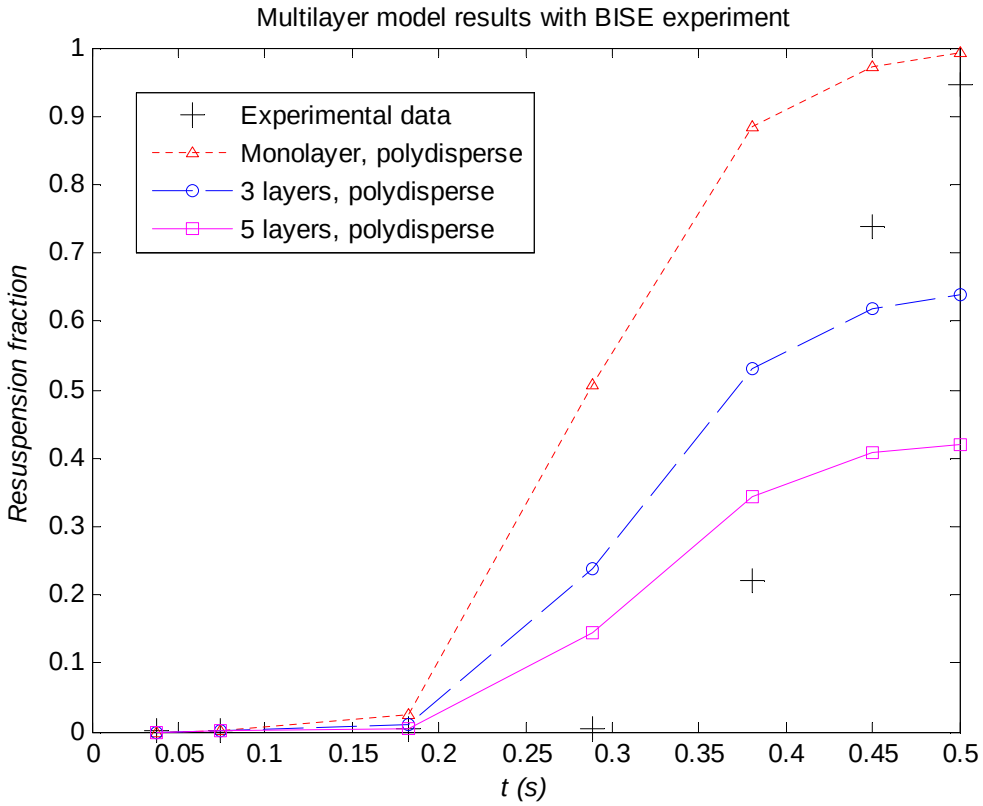

Figure 5.32 - Polydisperse multilayer resuspension predictions vs. BISE experimental results

Several conclusions can be drawn from the validation of the multilayer model:

- Both the STORM and the BISE comparisons indicate that multilayer model predictions with small adhesive spread factors give much better comparison with the experimental results. This feature was also concluded by Biasi *et al.* (2001). This may be because within a packed deposit, all the particles have similar surroundings that the spread in adhesion is reduced when there are a greater number of contacts with other particles (referred to as the co-ordination number).
- In the STORM comparison, the polydisperse case gave a better comparison with the experimental data whereas in the BISE comparison the monodisperse case gave better results. There is a marked difference between the deposit structures in the two experiments: in the STORM test the deposit is formed from a natural deposition phase in the STORM test whereas in the BISE experiment it is a compacted cone shaped deposit. This may have an influence on the coverage effect of the deposit layers. In other words, due to the fact that in BISE experiments the deposit structure is more compact, the polydisperse resuspension predictions are less applicable to this highly compacted deposit case.

- It should be noted that the adhesion parameters (reduction factor and spread factor) basically dominate the multilayer resuspension. Therefore, a better and comprehensive knowledge of these parameters is very important.

Chapter 6
Conclusions and Recommendations for Future Work

....When I wrote that only God and I knew what it meant. Now only God knows.

- Robert Browning

The work described in this thesis has been concerned with the way small particles attached to a surface are resuspended when exposed to a turbulent flow. Of practical concern has been the remobilization of radioactive particles resulting from potential nuclear accidents. In this particular case the focus is on the resuspension of small particles, < 5 microns in diameter, where the principal force holding such particles onto a surface arises from van der Waals inter-molecular forces and where the particle removal forces are generated by the turbulent shear stresses close to the surface. Given its suitable treatment of the microphysics of the attachment of small particles to rough surfaces, it was decided here to aim to develop improved versions of the Rock'n'Roll (R'n'R) model which is based on a stochastic approach to resuspension involving the rocking and rolling of a particle about surface asperities induced by the moments of the fluctuating drag forces acting on the particle close to the surface. In the process it was also decided to extend the application of resuspension of mono layers of particles to the more general case of multilayer resuspension since that is the case in a majority of resuspension experiments reported in the literature and that occurring in general in a nuclear severe accident. In the case of multilayer resuspension, a proper treatment necessitates an application of a stochastic model, force or moment balance models being inadequate and inappropriate.

The original R'n'R model makes a number of assumptions about the way particles are removed from a surface, one of the more important being that the removal forces and their time derivatives are Gaussian and statistically independent. The fluid motion close to the surface in a turbulent boundary layer consists of a random sequence of highly intermittent sweeps and ejections. The assumption that the statistics of these events are Gaussian (though the simplest and most convenient assumption to make at the time) is therefore questionable. In more recent times the

numerous DNS and LES measurements of fluid velocities in turbulent boundary layers has presented us with the opportunity to obtain more realistic distributions for the removal forces and their derivatives and in turn to develop new, more accurate and reliable models for particle resuspension. In the course of this study it has been instructive to compare the new model predictions with those of the original model. This has been done for both mono layer and multi layer resuspension for which in the latter case, this study has been of fundamental importance.

In this final Chapter we have summarised the work and conclusions of each aspect the work carried out and the impact it has upon the modelling and predictions of resuspension. The Chapter is concluded with a list of recommendations for future work

6.1 Conclusions and Discussions

6.1.1 Improvements to Force and Moment Balance Models for Resuspension

In this preliminary study we presented and discussed some improvements that have been made to the traditional force /moment balance models for particle resuspension by considering the influence of a statistical distribution of aerodynamic removal forces (moments) rather than just using their mean values. This improvement was specifically directed at the NRG4 moment balance model developed by Komen (2007) which included the influence of a spread of adhesive forces (moments) due to surface roughness. This particular model used an aerodynamic/ adhesion system of forces and moments contained in the Vainshtein model for a spherical particle in smooth contact with a surface. The influence of a combined distribution of adhesive and aerodynamic removal moments was studied as also was the sensitivity to the particular system of moments by comparing the predictions based on the Vainshtein system with that used in the R'n'R model. The general conclusion was that the inclusion of a distribution of aerodynamic forces and moments increases the resuspension but not appreciably. Greater sensitivity was reflected in the different system of moments especially for small a particles (2 microns compared to 10 microns in the case considered, see Figure 3.21 and Figure 3.22)

6.1.2 Application of LES/DNS data and the role of non-Gaussian removal forces

The LES/DNS data for the distribution of the velocities and accelerations in the viscous sub-layer of a fully-developed turbulent boundary layer and how they have been used to produce a new non-Gaussian R'n'R model for the resuspension rate constants have played a pivotal role in the work presented in this thesis. We showed specifically how these data were converted into values for the mean and fluctuating aerodynamic force f and its time derivative $\dot{f}$ (acting on a particle attached to a surface in a fully developed turbulent boundary layer). The distributions obtained for f and $\dot{f}$

were distinctly non-Gaussian, the measured distribution of f being best fitted for both sets of data by a Rayleigh distribution and similarly that of $\dot{f}$ by an SU Johnson distribution. The distribution of both these variables normalized on their rms values was found to be approximately the same for both sets of data, independent of y^+ for $y^+ < 6$ and statistically independent of one another. These distributions were used to obtain a revised formula for the resuspension rate constant in which the DNS value for the forcing frequency $\omega = \sqrt{\langle \dot{f}^2 \rangle / \langle f^2 \rangle}$ applied to the particle-surface deformation was nearly 50% higher than the equivalent LES value: by contrast the values of the ratio of the rms / mean of the aerodynamic drag force were very close to one another. By comparison with the original model the dependence of the rate constant on the adhesive force is now explicitly dependent on the Rayleigh distribution for *f* rather than a Gaussian distribution.

Resuspension predictions of this new Gaussian R'n'R model were compared with those of the original R'n'R model. This was done in 4 stages. First the difference between the Gaussian and non-Gaussian models was evaluated where the difference lies in the role of Gaussian versus non-Gaussian distributions of the fluctuating aerodynamic force and its time derivative (both with the same mean and rms). In particular it was noted that when the ratio adhesive force/ rms aerodynamic force, z_a, is large (z_a ~ 8), the ratio of resuspension rate constant based on the non-Gaussian to that of the Gaussian model ~ 30 and reflects the much slower decay of the non-Gaussian Rayleigh distribution for the aerodynamic drag force in the tails of the distribution compared to that of the Gaussian distribution. However the broad range of adhesive forces in practice significantly reduces the influence of the tails of the distribution mainly because the contribution to the total resuspension in this region of the adhesive force distribution is so small.

Secondly we considered the sensitivity of the predictions of the new model to the LES and DNS results based on the parameters in Table 4.3. The difference in the resuspension predictions naturally reflects the difference in values of ω^+ which is a natural scaling parameter for the resuspension rate and for the real time t when it occurs. It means that DNS values of the resuspension rate are not universally > LES values as the ratio of the values of ω^+ might imply. However when considering the resuspended fraction for the case of t = 1s, there is very little difference between the LES and DES predictions because for this exposure time all the short term resuspension has occurred (what is left is the fraction that resuspends over a much longer timescale).

Thirdly we compared predictions of the original Gaussian R'n'R model with those of the modified non-Gaussian R'n'R model based on the DNS results ($y^+ = 0.1$) in Table 4.3 where the difference also depends upon the different values of ω^+ and the values of f_{rms} (the ratio of the rms of the aerodynamic removal force to it is mean value). In particular we compared predictions with the experimental results in the Hall experiment (Reeks and Hall, 2001). We found that the new model gave closer results to the experimental data in the region where the friction velocity is from around

0.5m/s to 1.5m/s. Although the modified model gave more resuspension than the experimental data when friction velocity was smaller than 0.5m/s and larger than 1.5m/s, the results from the modified model still had a closer trend to the experimental data than the original R'n'R model did. It was also noted that the difference between the fraction resuspended predicted by the modified and original models could become significant when the friction velocity is small. It was concluded that the typical forcing frequency ω^+ is the crucial parameter in short term resuspension and the rms coefficient f_{rms} is the key parameter for long-term resuspension. The effect of the typical forcing frequency ω^+ on the resuspension fraction after 1s is not significant.

Finally, we examined the implications for resuspension of using the recently published formula of Lee & Balachandar (2010) (L&B) for the drag force acting on a particle on a surface (based on their DNS results for drag forces on particles on or near a surface in a turbulent boundary layer). The comparison indicated that the resuspension predictions using the L&B formula were quite close to those of the original model which uses the O'Neill formula for the drag force except in the region $-1 < z_1, z_2 < 1$ where application of O'Neill's formula gives higher values. However, this has very little effect on the resuspension rate and resuspension fraction. Therefore on the grounds of simplicity we will continue application of O'Neill's formula in our modified R'n'R model in subsequent analysis of resuspension from multilayer deposits.

6.1.3 Multilayer Resuspension Models

The ultimate model that has been developed in this work is a hybrid version of the R'n'R model adapted for application to multilayer deposits based on the Friess and Yadigaroglu multilayer approach. The deposit is modelled in several overlying layers where the coverage effect (masking) of the deposit layers has been studied; in the first instance a monodisperse deposit with a coverage ratio factor was modelled where this was subsequently replaced by the more general case of a polydisperse deposit with a particle size distribution.

The idea behind the multilayer resuspension model is that the deposited particles are removed by layers; the rate of removal of particles from any given layer depends upon the rate of removal of particles from the layer above which thus acts as a of source of uncovering and exposure of particles to the resuspending flow. This exposure depends upon the surface area exposed to the flow in any given layer and the fraction of that surface area occupied by particles (referred to as the coverage coefficient). It is assumed that when a particle is removed from the layer above only particle with sizes less than that of the particle removed can be resuspended. The influence of coverage and particle size constitutes additional features with respect to the original FY model which considered the resuspension of deposit consisting of a regular lattice array of particles of the same size (F&Y refer to this as a generic model for multilayer resuspension). As in the original FY model a lognormal distribution of adhesive forces between particles is assumed in each layer and that there is no correlation between the adhesive forces between layers. The distribution of

adhesive forces and particle-coverage coefficient need not be the same for every layer (indeed, if the layers are numbered sequentially from the top layer then there is good reason to suppose that the adhesive forces increase with increasing layer number). However in this study it is assumed that all 3 parameters are the same in each layer.

We recall that in the case of monolayer resuspension, so long as the exposure time was much greater than timescale of the aerodynamic removal forces the value of this timescale had little influence on the fraction of particles removed. In the case of multilayer resuspension, the value of this timescale is critical to the overall fraction of particles resuspended since it determines the time at which particles in any given layer are exposed to the flow and hence resuspended. In contrast to monolayer resuspension it is the fraction removed as a function of time that is important. In monolayer resuspension most of the particles that are available for resuspension will be removed in less than one second, the remainder being resuspended over much greater times. As an illustration Figure 5.2 shows the resuspension rate of particles in layers 1, 3, 5, 10 and 20 of a multilayer deposit of particles of the same size. The resuspension rate of the first layer is identical to that of the isolated particle model. For the second and subsequent layers, the initial resuspension rate starts from zero and rises to a maximum during which time most of the particles which are easily removed are resuspended from a given layer (i.e. for these particles the mean effective aerodynamic force > adhesive force), the remainder being removed on a much longer period. The time to reach a maximum may therefore be regarded as a delay time for the particles in a given layer to be exposed by removing particles from all the layers above it. This behavior results in a dramatic difference in the fraction resuspended compared with that for a monolayer for the same exposure time. Figure 5.5 shows for instance the resuspension fraction of a multilayer deposit consisting of 100 layers. It shows that after 100s, nearly 80% of the monolayer deposit is removed compared to around 3% of the 100 layers deposit.

The spread factor of the adhesive force distribution also has a great influence on multilayer resuspension. As a typical example, Figure 5.9 shows the half–life (time to resuspend 50% particles) for different spread factors. As the spread factor increased, the half life increases dramatically as the deposit became thicker. We also compared the resuspension prediction using the non-Gaussian model for the resuspension rate constant (based on the DNS results) with those based on a Gaussian model (with the same values of $\omega, f_{rms}, \langle F \rangle$). As with the case of mono-layer resuspension, Figure 5.12 shows that the non-Gaussian model always results in more resuspension than the Gaussian case but, in contrast, as time increases the difference becomes greater and greater. This difference reflects the difference in the normalized distributions for the aerodynamic drag force where the non-Gaussian distribution (used throughout this study) is significantly greater in the wings than that of the Gaussian distribution. It was noted that when both models gave the same value for the resuspension fraction (around 10^{-3}s in the plot) this value was independent of the layer thickness.

In studying the resuspension of a multilayer composed of polydispersed particles the model predictions for the resuspension fraction were compared with those of a multilayer deposit composed of monodisperse particles with the same geometric mean size. As an example, Figure 5.20 shows the ratio of the resuspension fraction of the monodisperse particles with that of the polydisperse particles as a function of layer thickness (L = 1 ~ 100) (reduction and spread factors are calculated by Biasi's correlation). All the curves start with similar values due to the dominance of resuspension of the top layers; also in the short term (<10^{-4}s) the resuspension of the polydisperse particles is greater than that of the monodisperse particles since the 50% of the polydisperse particles with sizes > that of the monodisperse particles are easier to resuspend. As the layer number increases the difference between the monodisperse and polydisperse particles becomes significant. For 10 layers, the resuspension fraction of the monodisperse particles after 100s is ~4.5 times that of polydisperse particles. And for the 100 layers case, the ratio increases to around 5 after 100s.

In comparing model predictions with the experimental results of the STORM tests and the BISE experiments, several conclusions can be made:

- Both the STORM and the BISE comparisons indicated that applying small adhesive spread factors gave much better results compared to the experiments. This result was also a conclusion of Biasi *et al*. (2001). This is because, when in a more compacted or coordinated deposit structure, all the particles have similar surrounding conditions. Therefore, the adhesion distribution should have a narrower range.
- In the STORM comparison, the polydisperse case gave a better comparison with the experimental data whereas in the BISE comparison the monodisperse case gave better results. There is a marked difference between the deposit structures in the two experiments: in the STORM test the deposit is formed from a natural deposition phase in the STORM test whereas in the BISE experiment it is a mechanically-compacted cone-shaped deposit. This may have an influence on the coverage effect of the deposit layers. In other words, due to the fact that in BISE experiments the deposit structure is more compact, the polydisperse resuspension predictions are less applicable to this highly-compacted deposit case.
- It should be noted that multilayer resuspension is most sensitive to the adhesion parameters (reduction factor and spread factor). Therefore, a better and comprehensive knowledge of these parameters is very important.

6.2 Recommendations for Future Work

Firstly, it is shown in Table 4.3 that the measured typical forcing frequency ω^+ varied with y^+. At the moment in the modified R'n'R model, the typical forcing frequency ω^+ value is a fixed value chosen from the case y^+ = 0.1 due to the fact that there are not enough simulation data to produce

the relationship between ω^+ and y^+. Therefore, the future work can be continued on studying the correlation between the typical forcing frequency ω^+ and y^+ in the viscous sublayer. The study of the correlation between the rms coefficient f_{rms} and y^+ in the viscous sublayer should also be considered. Therefore, these two presently fixed parameters will eventually be replaced by two formulas which depended on the y^+.

Secondly, it was noted that the adhesion parameters (reduction factor and spread factor) have a considerable influence on the multilayer resuspension as well as the value of ω^+. Therefore, better and comprehensive knowledge on these parameters is very important. The future work could consider tuning the correlation between the particle size and the reduction factor and spread factor for a lognormal adhesion distribution for the multilayer models (monodisperse and polydisperse models) from existing resuspension experiments, viz. Reeks & Hall (2001), Braaten (1994), STORM, ORNL ART, etc.

Thirdly, the clustering effect should be considered in the multilayer model which includes the aspects identified below.

- Particle-particle interactions in the clusters: the forces between particles should be considered; they might collide with each other and affect deposit structure and resuspension; how might this depend upon shape and packing and coordination number?
- Resuspension behaviour of a large agglomerate: we need to understand how large agglomerates resuspend; do they break up first or resuspend as an intact cluster? Is there any relationship between the sizes of resuspended agglomerates and the way the particles clustered in the deposit?
- Clustering in terms of coordination number should be considered which may be associated with the inter-particle force and particle size parameters. At the moment, coordination number is the most important parameter in defining the property of clustering.
- Distribution of clusters in the deposit layer should be studied. We might also study the distribution of coordination numbers.
- When the modified R'n'R model is applied to the clusters, there are several points that need to be reconsidered: 1. adhesive force (inter-cluster force from particle contacts); 2. aerodynamic forces (the drag force per particle comprising the cluster is probably reduced whereas lift force may become important and influence the breakup of large clusters); 3. gravity (this may not be negligible for clusters).

Appendices

1 Log-normal Distribution

Consider a random variable x which is necessarily positive; the pdf of x is denoted by $f(x)$. The arithmetic mean (μ) and variance (σ^2) of x are given by

$$\mu = \int_0^\infty x \cdot f(x)\,dx, \quad \sigma^2 = \int_0^\infty (x-\mu)^2 \cdot f(x)\,dx$$

If it is assumed that the pdf is a log-normal distribution, then

$$f(x) = \frac{1}{\sqrt{2\pi}} \frac{1}{x} \frac{1}{\ln(\sigma_1)} \exp\left\{ -\frac{\left[\ln(x) - \ln(\mu_1)\right]^2}{2\left[\ln(\sigma_1)\right]^2} \right\}$$

which indicates that the transformed variable $\ln(x)$ has a Gaussian distribution, with geometric mean μ_1 and geometric variance standard deviation σ_1.

The statistical properties of the distribution of x are related to the parameters of the lognormal distribution as follows

$$\mu_1 = \sqrt[n]{\prod_{n=1}^{N} x_n}$$

$$\mu = \exp\left\{ \ln(\mu_1) + \frac{1}{2}\left[\ln(\sigma_1)\right]^2 \right\} = \mu_1 \cdot \exp\left\{ \frac{1}{2}\left[\ln(\sigma_1)\right]^2 \right\}$$

$$\sigma = \left\{ e^{\left[\ln(\sigma_1)\right]^2} - 1 \right\} \cdot \exp\left\{ 2\ln(\mu_1) + \left[\ln(\sigma_1)\right]^2 \right\} = \mu_1^2 e^{\left[\ln(\sigma_1)\right]^2} \left\{ e^{\left[\ln(\sigma_1)\right]^2} - 1 \right\}$$

$$\text{median} = \exp\left\{ \ln(\mu_1) \right\} = \mu_1$$

$$\text{mode} = \exp\left\{ \ln(\mu_1) - \left[\ln(\sigma_1)\right]^2 \right\} = \mu_1 e^{-\left[\ln(\sigma_1)\right]^2}$$

In some simulations, the spread factor σ_1 is varied, but not the geometric mean μ_1. This means that the arithmetic mean μ changes with the spread factor σ_1 - it increases as the spread factor increases - but the median value of the distribution does not change; 50% of the particles will always be smaller than μ_1 and 50% will always be larger. The mode (the peak in the log-normal distribution) decreases as the spread factor increases.

These different effects are illustrated in Figure 3.10, which shows three different log-normal distributions, with μ_1 = 0.01 and σ_1 = 1.5, 2 and 3. So as the spread factor is increased, the modal

value - the peak in the distribution - moves towards zero, and the tail of the distribution increases slightly.

Click to return to p85.

2 Numerical Method of Modified NRG4 Models

To calculate the fraction remaining on the surface

$$f_R = \int_0^{\infty} erf\left(\frac{M_a - \langle M_D \rangle}{\sqrt{2}m_D}\right)\varphi(r_a')dr_a'$$

M_D and m_D is a function of friction velocity u_τ. M_a is a function of r_a'. Other parameters: radius r, fluid density ρ_f, fluid kinematic viscosity ν_f, surface energy γ and elastic constant κ are given. Therefore, the fraction remaining on the surface is rewritten as

$$f_R = \int_0^{\infty} erf\left(\frac{f(r_a') - g(u_\tau)}{\sqrt{2}\cdot 0.2\cdot g(u_\tau)}\right)\varphi(r_a')dr_a'$$

where $f()$ and $g()$ are known functions and $\varphi()$ is the log-normal distribution with known parameters: geometric mean $\overline{r}_a'$ and geometric standard deviation σ_a'. a is used instead for r_a' for convenience, then

$$f_R = \int_0^{\infty} erf\left(\frac{f(a) - g(u_\tau)}{0.2\sqrt{2}g(u_\tau)}\right)\varphi(a)da$$

Then divide the domain of $a \in 0, \infty$ into a set of discrete values a_k (k = 1, 2, 3, etc...) with the interval length $\Delta a_k = a_{k+1} - a_k$.

Then the fraction remaining on the surface is derived as

$$f_R = \sum_{k=1}^{\infty} erf\left(\frac{f(a_k) - g(u_\tau)}{0.2\sqrt{2}g(u_\tau)}\right)\varphi(a_k)\Delta a_k$$

Practically, the range of normalized asperity radius r_a' (a_k) is taken from $\overline{r}_a' / \sigma_a'^4$ to $\overline{r}_a' \cdot \sigma_a'^4$. The domain of asperity radius could be also divided in a log-scale range ($\log(\overline{r}_a') - 4\log(\sigma_a')$ to $\log(\overline{r}_a') + 4\log(\sigma_a')$) in order to increase the calculation efficiency.

Click to return to Eq.[3.27].

3 Derivation of Modified R'n'R Model

To calculate the resuspension rate constant, substitute Eq.[4.22], Eq.[4.24] and Eq.[4.25] to Eq.[4.10], then

$$p = \int_0^\infty \dot{f}\, P(f_{dh}, \dot{f})d\dot{f} \Big/ \int_{-\infty}^{\infty}\int_{-\infty}^{f_{dh}} P(f, \dot{f})df d\dot{f}$$

$$= \int_0^\infty \sqrt{\langle \dot{f}^2 \rangle} z_2 \frac{P(z_{dh}, z_2)}{\sqrt{\langle f^2 \rangle}\sqrt{\langle \dot{f}^2 \rangle}}\, d\dot{f} \Big/ \int_{-\infty}^{\infty}\int_{-\infty}^{f_{dh}} \frac{P(z_1, z_2)}{\sqrt{\langle f^2 \rangle}\sqrt{\langle \dot{f}^2 \rangle}} df d\dot{f}$$

$$= \int_0^\infty \sqrt{\langle \dot{f}^2 \rangle} z_2 \frac{P(z_{dh}, z_2)}{\sqrt{\langle f^2 \rangle}\sqrt{\langle \dot{f}^2 \rangle}} \sqrt{\langle \dot{f}^2 \rangle} dz_2 \Big/ \int_{-\infty}^{\infty}\int_{-\infty}^{z_{dh}} \frac{P(z_1, z_2)}{\sqrt{\langle f^2 \rangle}\sqrt{\langle \dot{f}^2 \rangle}} \sqrt{\langle f^2 \rangle} dz_1 \sqrt{\langle \dot{f}^2 \rangle} dz_2$$

$$= \frac{\sqrt{\langle \dot{f}^2 \rangle}}{\sqrt{\langle f^2 \rangle}} \int_0^\infty z_2\, P(z_{dh}, z_2)dz_2 \Big/ \int_{-\infty}^{\infty}\int_{-\infty}^{z_{dh}} P(z_1, z_2)dz_1 dz_2$$

where $z_{dh} = \frac{f_{dh}}{\sqrt{\langle f^2 \rangle}}$, f_{dh} is the fluctuating resultant force at detachment point (Eq.[4.3]).

Now calculate the top part of equation first,

$$\int_0^\infty z_2\, P(z_{dh}, z_2)dz_2$$

$$= \int_0^\infty z_2 \frac{z_{dh} + A_1}{A_2^{\,2}} \exp\left(-\frac{1}{2}\left(\frac{z_{dh} + A_1}{A_2}\right)^2\right) \cdot \frac{B_1}{B_2\sqrt{2\pi}\sqrt{z^2+1}} \exp\left(-\frac{1}{2}\left(B_3 + B_1 \ln\left(z + \sqrt{z^2+1}\right)\right)^2\right) dz_2$$

since $z = \frac{z_2 - B_4}{B_2}$, $z_2 = B_2 z + B_4$, and $dz_2 = B_2 dz$

$$= \frac{z_{dh} + A_1}{A_2^{\,2}} \exp\left(-\frac{1}{2}\left(\frac{z_{dh} + A_1}{A_2}\right)^2\right) \cdot \int_{-\frac{B_4}{B_2}}^{\infty} \frac{B_1(B_2 z + B_4)}{\sqrt{2\pi}\sqrt{z^2+1}} \exp\left(-\frac{1}{2}\left(B_3 + B_1 \ln\left(z + \sqrt{z^2+1}\right)\right)^2\right) dz$$

$$let\ B_{\dot{f}} = \int_{-\frac{B_4}{B_2}}^{\infty} \frac{B_1(B_2 z + B_4)}{\sqrt{2\pi}\sqrt{z^2+1}} \exp\left(-\frac{1}{2}\left(B_3 + B_1 \ln\left(z + \sqrt{z^2+1}\right)\right)^2\right) dz$$

B_{fdot} can be calculated numerically, which can be called as reduction factor of the derivative of the fluctuating aerodynamic resultant force. Then,

$$\int_0^\infty z_2\, P(z_{dh}, z_2)dz_2 = B_{\dot{f}} \frac{z_{dh} + A_1}{A_2^{\,2}} \exp\left(-\frac{1}{2}\left(\frac{z_{dh} + A_1}{A_2}\right)^2\right)$$

Furthermore, the bottom part is derived.

$$\int_{-\infty}^{\infty}\int_{-\infty}^{z_{dh}} P(z_1,z_2)dz_1dz_2$$

$$= \int_{-\infty}^{\infty}\int_{-\infty}^{z_{dh}} \frac{z_1+A_1}{A_2{}^2}\exp\left(-\frac{1}{2}\left(\frac{z_1+A_1}{A_2}\right)^2\right)\cdot\frac{B_1}{B_2\sqrt{2\pi}\sqrt{z^2+1}}\exp\left(-\frac{1}{2}\left(B_3+B_1\ln\left(z+\sqrt{z^2+1}\right)\right)^2\right)dz_1dz_2$$

since $dz_2 = B_2 dz$

$$= \int_{-\infty}^{\infty}\int_{-\infty}^{z_{dh}} \frac{z_1+A_1}{A_2{}^2}\exp\left(-\frac{1}{2}\left(\frac{z_1+A_1}{A_2}\right)^2\right)\cdot\frac{B_1}{\sqrt{2\pi}\sqrt{z^2+1}}\exp\left(-\frac{1}{2}\left(B_3+B_1\ln\left(z+\sqrt{z^2+1}\right)\right)^2\right)dz_1dz$$

$$= \int_{-\infty}^{z_{dh}} \frac{z_1+A_1}{A_2{}^2}\exp\left(-\frac{1}{2}\left(\frac{z_1+A_1}{A_2}\right)^2\right)dz_1\cdot\int_{-\infty}^{\infty}\frac{B_1}{\sqrt{2\pi}\sqrt{z^2+1}}\exp\left(-\frac{1}{2}\left(B_3+B_1\ln\left(z+\sqrt{z^2+1}\right)\right)^2\right)dz$$

$$= -\exp\left(-\frac{1}{2}\left(\frac{z_1+A_1}{A_2}\right)^2\right)\Bigg|_{-\infty}^{z_{dh}}\cdot\int_{-\infty}^{\infty}\frac{B_1}{\sqrt{2\pi}\sqrt{z^2+1}}\exp\left(-\frac{1}{2}\left(B_3+B_1\ln\left(z+\sqrt{z^2+1}\right)\right)^2\right)dz$$

since $\int_{-\infty}^{\infty}\frac{B_1}{\sqrt{2\pi}\sqrt{z^2+1}}\exp\left(-\frac{1}{2}\left(B_3+B_1\ln\left(z+\sqrt{z^2+1}\right)\right)^2\right)dz = 1$

Therefore,

$$\int_{-\infty}^{\infty}\int_{-\infty}^{z_{dh}} P(z_1,z_2)dz_1dz_2 = 1-\exp\left(-\frac{1}{2}\left(\frac{z_{dh}+A_1}{A_2}\right)^2\right)$$

Combine the top and the bottom part, the modified resuspension rate constant is obtained,

$$p = \sqrt{\frac{\langle \dot{f}^2\rangle}{\langle f^2\rangle}}\int_0^{\infty} z_2\,P(z_{dh},z_2)dz_2 \Big/ \int_{-\infty}^{\infty}\int_{-\infty}^{z_{dh}} P(z_1,z_2)dz_1dz_2$$

$$= B_{\dot{f}}\sqrt{\frac{\langle \dot{f}^2\rangle}{\langle f^2\rangle}}\frac{z_{dh}+A_1}{A_2{}^2}\exp\left(-\frac{1}{2}\left(\frac{z_{dh}+A_1}{A_2}\right)^2\right)\Bigg/\left(1-\exp\left(-\frac{1}{2}\left(\frac{z_{dh}+A_1}{A_2}\right)^2\right)\right)$$

Click to return to Eq.[4.26].

4 Numerical Method of Multilayer Model

Divide the domain of $r \in 0, \infty$ into a set of discrete values r_j in ascending order and numbered sequentially j = 1, 2, 3, etc... And divide the domain of $r_a' \in 0, \infty$ into a set of discrete values ξ_k (symbol ξ is used here instead of r_a' for convenience) with k = 1, 2, 3, etc... Let

$$N_{ijk}(t) = n_i(r_j, \xi_k, t)\Delta r_j \Delta \xi_k$$

where $\Delta r_j = r_{j+1} - r_j$ and $\Delta \xi_k = \xi_{k+1} - \xi_k$ are the interval length over which the resuspension rate constant $p(r, r_a')$ can be assumed constant. Thus, Eq.[5.28] becomes:

$$N_{1jk}(t) = e^{-p(r_j,\xi_k)t}\psi(r_j)\varphi(\xi_k)\Delta r_j \Delta \xi_k$$

$$\frac{\partial N_{ijk}(t)}{\partial t} = -p(r_j, \xi_k)N_{ijk}(t) + \Delta r_j \Delta \xi_k \psi(r_j)\varphi(\xi_k)\sum_{a=j}\sum_{b=1} p(r_a, \xi_b)N_{i-1ab}(t) \quad i \geq 2$$

Then dividing the time domain into a series of discrete times t_m : m = 0, 1, 2, etc. and denoting $N_{ijk}(t_m)$ by N_{ijk}^m and $p(r_j, \xi_k)$ by p_{jk}, the differential term can be replaced by

$$\frac{\partial N_{ijk}^m}{\partial t} = \frac{N_{ijk}^m - N_{ijk}^{m-1}}{\Delta t_m}$$

Therefore, N_{ijk}^m is obtained recursively in the following manner starting from

$$N_{1jk}^m = e^{-p_{jk}t_m}\psi(r_j)\varphi(\xi_k)\Delta r_j \Delta \xi_k$$

$$N_{ijk}^0 = 0 : i \geq 2$$

$$(1 + p_{jk}\Delta t_m)N_{ijk}^m = N_{ijk}^{m-1} + \Delta t_m \Delta r_j \Delta \xi_k \psi(r_j)\varphi(\xi_k)\sum_{a=j}\sum_{b=1} p_{ab}N_{i-1ab}^m \quad i \geq 2, m \geq 2$$

Then the resuspension rate (Eq.[5.29]) of the ith layer is calculated as

$$\Lambda_i = \sum_j \sum_k p_{jk}N_{ijk}^m \Delta r_j \Delta \xi_k \quad i \geq 1, m \geq 1$$

In the STORM test calculation above, the range of particle radius according to SOPHAEROS code is taken from 0.001μm to 100μm with the geometric mean 0.227μm and geometric standard deviation 1.7 (Notes: 1. due to the fact that the probability of very large size particles (r > 50μm) is very very small, the gravity effect for these large particles is neglected in this multilayer model. 2. For large size particles (r > 35μm), Biasi's correlation for spread factor is still applied, however the geometric mean in the correlation is considered as very very small). The range of normalized asperity radius is taken from $\overline{r_a'}/\sigma_a'^4$ to $\overline{r_a'} \cdot \sigma_a'^4$. The domain of asperity radius and particle size could be also divided in a log-scale range in order to increase the calculation efficiency.

Click to return to Eq.[5.28].

References

Agrati, G., Parozzi, F., Sandrelli, G., Valisi, M., Carraro, G. and Markovina, A. (1991) “STORM: SIMPLIFIED TESTS ON RESUSPENSION MECHANISMS - Preliminary description of the Project”, ENEL/DSR/CRTN Report N6/91/01/MI, June

Allelein, H. J., Auvinen, A., Ball, J., Guntay, L., Herranz, L., Hidaka, A., Jones, A. V., Kissane, M. P. Powers, D. and Weber, G. (2009) “State-of-the-art report on nuclear aerosols in reactor safety”, OECD report NEA/CSNI/R(2009)5

Alloul-Marmor, L. (2002), “Réentrainement par écoulement d’air d’une contaminationation particulaire depose sur une surface: application au cas d’un “tas” de poudre”, PhD thesis (Université Paris XII), report ISRN IRSN – 2002/28 – FR

Bagnold, R. A. (1960) “The re-entrainment of settled dusts”, *International J. of Air Pollution*, Vol.2, p357-363

Batchelor, G. K. (1967) “An Introduction to Fluid Dynamics”, Cambridge University Press

Beach, E. R., Tormoen, G. W., Drelich, J. and Han, R. (2002) “Pull-Off Force Measurements between Rough Surfaces by Atomic Force Microscopy”, Journal of Colloid and Interface Science, Vol.247(1), p84-99

Benson, G.C. and B.R. Bowsher (1988) “PHYSICAL RESUSPENSION AND REVAPORIZATION PHENOMENA IN CONTROL ROD AEROSOLS”, UKAEA-Winfrith AEEW-R2427, December

Biasi, L., de los Reyes, A., Reeks, M.W. and de Santi, G.F. (2001) "Use of a simple model for the interpretation of experimental data on particle resuspension in turbulent flows“, *Journal of Aerosol Science,* Vol.32, p1175-1200

Binnig, G. K., Quate, C. F., and Gerber, Ch. (1986) “Atomic Force Microscope”, *Phys. Rev. Lett.*, Vol.56(9), p930-933

Blackwelder, R. F. and Haritonidis, J. H. (1983) “Scaling of the bursting frequency in turbulent boundary layers”, *J. Fluid Mech.*, Vol.132, p87-103

Boehme, G., Krupp, H., Rabenhorst, H. and Sandstede, G. (1962) “Adhesion measurements involving small particles”, *Trans. Inst. Chem. Eng.*, Vol.40, p252-259

Bowling, R. A. (1988) “A theorical Review of Particles Adhesion - Particles on Surfaces 1: Detection, Adhesion, and Removal”, Edited by K. L. Mittal, Plenum Press

Braaten, D. A., Paw U, K. T. and Shaw, R. H. (1988) “Coherent structures and particle detachment in boundary layer flows”, *J. Aerosol Sci.*, Vol.19, p1183-1186

Braaten, D. A., Paw U, K. T. and Shaw, R. H. (1990) “Particle resuspension in a. turbulent boundary layer—observed and modelled”, *J Aerosol. Sci.*, Vol.21, p613–628

Braaten, D. A. (1994) "Wind tunnel experiments of large particle reentrainment-deposition and development of large particle scaling parameters", *Aerosol Science and Technology*, Vol.21, p157-169

Brockmann, J. E. (1985) “Range of possible resuspension or reentrainment of fission products during containment depressurization”, Report SAND84-0410, Vol. 2, App. G.

Buffat, M., Le Penven, L. and Cadiou, A. (2011) “An efficient spectral method based on an orthogonal decomposition of the velocity for transition analysis in wall bounded flow”, *Computers & Fluids*, Vol.42(1), p62-72

Bujan, A., Tóth, B. and Zeyen, R. (2008) “ASTEC V1.3 Code Assessment on the STORM Mechanical Resuspension Tests: A Fission Product Transport Study”, SARNET-ST-P66, EUR 23233 EN, JRC/IE Petten, The Netherlands, May

Capitão, J. A. and Sugaroni, F. (1995) “STORM Benchmarks”, Final comparison report, EUR 16281 EN

Castelo, A., Capitão, J. A. and Santi, G. (1999) “International Standard Problem 40 - Aerosol Deposition and Resuspension”, NEA/CSNI/R(99)4, EUR 18708 EN, February

Chepil, W. S. (1959) “Equilibrium of soil grains at the threshold of movement by wind”, *Soil Sci. Soc. Proc.*, Vol.23, p422–428

Cherukat P., McLaughlin J.B. (1994) “The inertial lift on a rigid sphere in a linear shear flow field near a flat wall”, *J. Fluid Mech.*, Vol.263, p1-18

Chuyanov, V. and Topilski, L. (2006) “Prevention of hydrogen and dust explosion in ITER”, *Fusion Engineering and Design*, Vol.81(8-14), p1313-1319

Ciattaglia, S. (2010) “Dust inventory control status in ITER: baseline provisions, R&D plan and first results”, 2nd Research Co-ordination Meeting of CRP on Characterization of Size, Composition and Origins of Dust in Fusion Devices, IAEA, Vienna, Austria, 21-23 June

Cleaver, J. W. and Yates, B. (1973) “Mechanism of detachment of colloidal particles from a flat substrate in a turbulent flow”, *J. of Colloid and Interface Science*, Vol.44(3), p464-474

Cleaver, J. W. and Yates, B. (1976) “The effect of re-entrainment on particle deposition”, *Chemical Engineering Science*, Vol.31(2), p147-151

Cooper, K., Gupta, A. and Beaudoin, S. (2001) “Simulation of the adhesion of particles to surfaces”, *J. Colloid Interface Sci.*, Vol.234, p284-292

Corn, M. and Stein, F. (1965) “Re-entrainment of particles from a plane surface”, *American Industrial Hygiene Association Journal*, Vol.26, p325–336

Cousin, F., Dieschbourg, K. and Jacq, F. (2008) “New capabilities of simulating fission product transport in circuits with ASTEC/SOPHAEROS v.1.3”, *Nuclear Engineering and Design*, Vol.238(9), p2430-2438

Crowe, C. T., Sommerfield, M. & Tsuji, Y. (1998) “Multiphase Flows with Droplets and Particles”, CRC Press LLC

Dandy, D. S. and Dwyer, H. A. (1990) “A sphere in shear flow at finite Reynolds number: effect of shear on particle lift, drag, and heat transfer”, *Journal of Fluid Mechanics*, Vol.216, p381-410

Deladi, S., Krijnen, G., Tas, N. and Elwenspoek, M. (2002) “Three Dimensional Adhesion Model for Arbitrary Rough Surfaces”, *International Conference on Computational Nanoscience and Nanotechnology (ICCN)*, April 22-25, San Juan, Puerto Rico, USA

Drelich, J., Tormoen, G.W. and Beach, E.R. (2004) “Determination of Solid Surface Tension from Particle-Substrate Pull-off Forces Measured with the Atomic Force Microscope”, *Journal of Colloid and Interface Science*, Vol.280, p484-497

Eckelmann, H. (1974) “The structure of viscous sublayer the adjacent wall region in a turbulent channel flow”, *J.Fluid Mech.*, Vol.65(3), p439-459

Eichenlaub, S., Gelb, A. and Beaudoin, S. (2004) “Roughness models for particle adhesion”, *Journal of colloid and interface science*, Vol.280(2), p289-298

Fairchild, C. I. and Tillery, M. I. (1982) “Wind tunnel measurements of the resuspension of ideal particles”, *Atmospheric Environment*, Vol.16, p229-238

Fauske and Associates Inc. (1984) “Resuspension of deposited aerosols following primary system or containment failure”, IDCOR Technical Report 11.6

Foucault, J. M. (1994) “Etude théorique et expérimentale des phénomènes d'envol et de saltation de particules dans une couche limite turbulente“, PhD Thesis, Université des Sciences et de Technologies de Lille, 6 october

Friedlander, S. (2000) “Smoke, Dust, and Haze”, 2nd Edition, Oxford University Press

Friess, H. and Yadigaroglu, G. (1998) “Inclusion of structural parameters in the modelling of aerosol resuspension”, *Third OECD Specialist Meeting on Nuclear Aerosols in Reactor Safety*, p15-18, Cologne, Germany

Friess, H. and Yadigaroglu, G. (2001) ”A generic model of the resuspension of multilayer aerosol deposits by turbulent flow”, *Journal of Nuclear Sci. and Eng.*, Vol.138(2), p161-176

Friess, H. and Yadigaroglu, G. (2002) “Modelling of the resuspension of particle clusters from multilayer aerosol deposits with variable porosity”, *Journal of Aerosol Science,* Vol.33, p883-906

Fromentin, A. (1989) “Particle resuspension from a multi-layer deposit by turbulent flow”, Ph.D. thesis No.8971, Swiss Federal Institute of Technology, Zurich

George, M. and Goddard, D. T. (2006) “The characterisation of rough particle contacts by atomic force microscopy”, *J. of Colloid and Interface Science*, Vol.299, p665-672

Germano, M., Piomelli, U., Moin, P. and Cabot, W. H. (1991) “A dynamic subgrid-scale eddy-viscosity model”, *Phys. Fluids*, A 3, p1760–1765

Gersten, K. and Herwig, H. (1992) “Strömungsmechanik. Grundlagen der Impuls-, Wärme- und Stoffübertragung aus asymptotischer Sicht”, Verlag Vieweg, Braunschweig, p378

Giess, P., Goddard, A. J. H., Shaw, G. and Allen, D. (1994) “Resuspension of monodisperse particles from short grass swards: a wind tunnel study”, *J. Aerosol Sci.*, Vol.25, p843-857

Giess, P., Goddard, A. J. H. and Shaw, G. (1997) “Factors affecting particle resuspension from grass swards”, *J. Aerosol Sci.*, Vol.28, p1331-1349

Goren, S.L. (1970) “The Normal Force Exerted by Creeping Row on a Small Sphere Touching a Plane”, *J. Fluid Mech.*, Vol.41(3), p619-625

Gotoh, K., Morooka, H. and Nishimura, T. (2001) “Effect of number density of deposited particles on resuspension fraction from sparse particle bed”, *J. Aerosol Sci.*, Vol.32, p559-560

Guentay S., Herranz L. E., Layly V., Routamo T. and Auvinen A. (2005) “Aerosol Behaviour in SGTR Accidents”, European Review Meeting on Severe Accident Research (ERMSAR), Aix-en-Provence, France, 14-16 November

Guingo, M. and Minier, J. P. (2008) “A new model for the simulation of particle resuspension by turbulent flows based on a stochastic description of wall roughness and adhesion forces”, *Journal of Aerosol Science*, Vol.39(11), p957-973

Hall, D. (1988) “Measurements of the mean force on a particle near a boundary in turbulent flow”, *J. Fluid Mechanics*, Vol.187, p451-466

Hall, D. (1989) “The time dependence of particle resuspension”, *J. Aerosol Sci.*, Vol.20, p907-910

Hall, D. (1994) “The resuspension of particles from flat surfaces by a turbulent flow”, Report TD/NS/REP/0056, RPTG/P(93)11, Technol. Div., Nuclear Electric, U.K

Happel, J. and Brenner, H. (1973) “Low Reynolds Number Hydrodynamics”, Noordhoff Intl. Pub., Leiden

Heames, T. J., Williams, D. A., Bixler, N. E., Grimley, A. J., Wheatley, C. J., Johns, N. A., Domagala, P., Dickson, L. W., Alexander, C. A., Osborn-Lee, I., Zawadzki, S., Rest, J., Mason, A., and Lee, R. Y. (1992) “VICTORIA: a mechanistic model of radionuclide behaviour in the reactor coolant system under severe accident conditions”, NUREG=CR-5545-Rev. 1

Hertz, H. (1896) "Miscellaneous Papers", p146-183, MacMillan and Co., London

Hocke, K., Adroguer, B., Shepherd, I. & Schatz, A. (1995) “Fission product release State-of-the-art review”, ECSC-EC-EAEC, EUR 16499 EN

Hontañón, E., de los Reyes, A. and Capitão, J. A. (2000) “The CÆSAR code for aerosol resuspension in turbulent pipe flows, Assessment against the storm experiments“, *J. Aerosol Sci*, Vol.31(9), p1061-1076

Hummel, R., Krasenbrink, A., De Santi, G. and Areia Capitao (1998) Lessons Learnt on Aerosol on Nuclear Aerosols in Reactor Safety, Cologne, Germany, 15-18 June

Ibrahim, A., Dunn, P. F. and Brach, R. M. (2003) "Microparticle Detachment from Surfaces Exposed to Turbulent Air Flow: Controlled Experiments and Modelling", *Journal of Aerosol Science*, Vol.34, p765-782

Iimura, K., Watanabe, S., Suzuki, M., Hirota, M. and Higashitani, K. (2009) "Simulation of Entrainment of Agglomerates from Plate Surfaces by Shear Flows", *Chemical Engineering Science*, Vol.64, p1455-1461

Iseli, M. (2001) “In-vessel hydrogen deflagration and detonation in ITER-FEAT”, Fusion Engineering and Design, Vol.54, p421-430

Johnson, K. L., Kendall, K. and Roberts, A. D. (1971) “Surface energy and the contact of elastic solids”, *Proc. R. Soc. London*, Vol.324, p301-313

Jurcik, B., and Wang, Hwa-Chi (1991) “Modelling of particle resuspension in turbulent flow”, *Journal of Aerosol Science*, Vol.22(1), p149-152

Kallio, G. A. and Reeks, M. W. (1989) “A numerical simulation of particle deposition in turbulent boundary layers”, *Int. J. Multiphase Flow*, Vol.15(3), p433-446

Katainen, J., Paajanen, M., Ahtola, E., Pore, V. and Lahtinen, J. (2006) “Adhesion as an Interplay between Particle Size and Surface Roughness”, *Journal of Colloid and Interface Science*, Vol.304, p524-529

Kim, H. T., Kline, S. J. and Reynolds, W. C. (1971) “The production of turbulence near a smooth wall in turbulent boundary layer”, *J. Fluid Mech.*, Vol.50(1), pp133-160

Kissane, M. P. (2008) “On the nature of aerosols produced during a severe accident of a water-cooled nuclear reactor”, *Nuclear Engineering and Design*, Vol.238(10), p2792-2800

Kissane, M. P. (2009) “A review of radionuclide behaviour in the primary system of a very-high-temperature reactor”, *Nuclear Engineering and Design*, Vol.239(12), p3076-3091

Kline, S. J., Reynolds, W. C., Schraub, F. A. and Runstadler, P. W. (1967) “The structure of turbulent boundary layers”, *J. Fluid Mech.*, Vol.30(4), p741-773

Komen, E. M. J. (2007) “Dispersion of Fission Products and Dust in Direct Cycle HTRs”, NRG report 21346/06.60264C, Revision 2, Petten

Krupp, H. (1967) "Particle Adhesion Theory and Experiment", *Advan. Colloid Interface Sci.*, Vol.1, p111-239

Laufer, J. (1954) “The structure of turbulence in fully developed pipe flow”, *NACA report 1174*

Lazaridis, M. and Drossinos, Y. (1998) “Multilayer Resuspension of Small Identical Particles by Turbulent Flow”, *Aerosol Science and Technology*, Vol.28(6), p548-560

Lazaridis, M., Drossinos, Y. and Georgopoulos, P.G. (1998) “Turbulent Resuspension of Small Nondeformable Particles”, *Journal of Colloid and Interface Science*, Vol.204(1), p24-32

Lee, H. and Balachandar, S. (2010) “Drag and lift forces on a spherical particle moving on a wall in a shear flow at finite Re”, *J. Fluid Mech.*, Vol.657, p89-125

Leighton, D.T. and Acrivos, A. (1985) “The Lift on a Small Sphere Touching a Plane in the Presence of a Simple Shear Flow”, *Journal of Applied Mathematics and Physics*, Vol.36, p174-178

Lennard-Jones, J. E. (1931) “Cohesion”, *Proceedings of the Physical Society*, Vol.43, p461-482

Matsusaka, S. and Masuda, H. (1996) “Particle Reentrainment from a fine powder layer in a Turbulent Air Flow”, *Aerosol Sci. Technol.*, Vol.24, p69-84

Miller, G.F. and Pursey, H. (1954) “The field and radiation impedance of mechanical radiators on the free surface of a semi infinite isotropic solid”, Proceedings of the Royal Society, Series A, Vol.223, p521-541

Moser, R., Moin, P. and Leonard, A. (1983) “A spectral numerical method for the Navier–Stokes equations with applications to Taylor–Couette flow”, *J. Compos. Phys.*, Vol.52, p524-544

Moser, R., Kim, J. and Mansour, N. (1999) “Direct numerical simulation of turbulent channel flow up to Ret5590”, *Phys. Fluids*, Vol.11(4), p943-945

Nicholson, K. W. (1993) “Wind Tunnel Experiments on the resuspension of particulate material”, *Atmospheric Environment*, Vol.27A(2), p181-188

Nikuradse, J. (1932) “Gesetzmässigkeiten der Turbulenten Strömung in Glatten Rohren”, Forschungsheft, No.356, VDI-Verlag GmbH, Berlin

Nikuradse, J. (1933) “Strömungsgesetze in rauhen Rohren”, Forschungsarbeiten aus dem Gebiete des Ingenieurwesens, No.361, VDI-Verlag, Berlin

O’Neill, M. E. (1968) “A sphere in contact with a plane wall in a slow linear shear flow”, *Chemical Engineering Science*, Vol.23, p1293–1297

Parozzi, F. and Masnaghetti, A. (1990) “TRAP-MELT2/ENEL 88.1”, Report no. ENEL N6/88/02/MI

Parozzi, F. (1992) “Computer models on fission product and aerosol behaviour in the LWR primary coolant system – Part II: Fission product and aerosol transport”, CEC – JRC Ispra Site, EUR 14676 EN

Parozzi, F., Alonso, A., Bolado, R., Hontanon, E., Capitão, J. A. and Drossinos, Y. (1995) “NUCLEAR SCIENCE AND TECNOLOGY: AEROSOL PHYSICAL RESUSPENSION UNDER LWR SEVERE ACCIDENT CONDITIONS”, State of the Art Review, Final Report, EUR 16505, Brussels

Parozzi, F. and Tagliaferri, L. (2000) “Improvement of the dry aerosol resuspension model of ECART code in the light of STORM results”, *CESI final report*, A0/013761

Paw U, K. T. (1982) “A universal model for entrainment processes”, *Proceedings of the fourth international conference on precipitation scavenging*, *dry deposition and resuspension*, St. Monica (California), p1111-1120

Paw U, K. T. and Braaten, D. A. (1995) “New perspectives on rebound and reentrainment processes”, *Aerosol Sci. Technol*, Vol.23, p72-79

Phares, D. J, Smedley G. T. and Flagan, R. C. (2000) “Effect of Particle Size and Material Properties on Aerodynamic Resuspension from Surfaces”, *J. Aerosol Sci.*, Vol.31(11), p1335-1353

Phillips, M. (1980) “A Force Balance Model for Particle Entrainment into a Fluid Stream”, *J. Phys. D: Appl. Phys*., Vol.13, p221-233

Prandtl, L. (1904) “Über Flüssigkeitsbewegung bei sehr kleiner Reibung”, *Verhandlungen des dritten Internationalen Mathematiker-Kongresses in Heidelberg*

Rabinovich, Y. I., Adler, J. J., Ata, A., Moudgil, B. M. & Singh, R. K. (2000) “Adhesion between nanoscale rough surfaces - I. Role of asperity geometry”, *Journal of Colloid and Interface Science*, Vol.232(1), p10-16

Rabinovich, Y. I., Adler, J. J., Ata, A., Moudgil, B. M. & Singh, R. K. (2000) “Adhesion between nanoscale rough surfaces - II. Measurement and comparison with theory”, *Journal of Colloid and Interface Science*, Vol.232(1), p17-24

Ranade, M. B. (1987) “Adhesion and Removal of Fine Particles on Surfaces”, *Aerosol Sci. Technol.*, Vol.7, p161-176

Rahn, F. J. (1988) “SUMMARY OF THE LWR AEROSOL CONTAINMENT EXPERIMENTS (LACE) PROGRAM - FINAL REPORT”, Report LACE TR-012, November

Rashidi, M. and Banerjee, S. (1990) “The effect of boundary conditions and shear rate on streak formation and breakdown in turbulent channel flow”, *Phys. Fluids A*, Vol.2(10), p1827-1838

Raunio, T. (2008) “Experimental Study on Fine Particle Resuspension in Nuclear Reactor Safety”, PhD Thesis, HELSINKI UNIVERSITY OF TECHNOLOGY, Espoo, January

Reed, J. R., and Rochowiak, P. (1988) “The adhesion of small particles to a surface”, *Proceedings of the second conference of the aerosol society* (p229), Oxford: Pergamon

Reeks, M. W. and McKee, S. (1984) “The dispersive effects of Basset history forces on particle motion in a turbulent flow”, *Phys. Fluids*, Vol.27(7), p1573-1582

Reeks, M. W., Reed, J. and Hall, D. (1985) “On the long-term resuspension of small particles by a turbulent flow”, CEGB Report, TPRD/B/0639/N85

Reeks, M. W., Reed, J. and Hall, D. (1988) “On the resuspension of small particles by a turbulent flow”, *Journal of Physics D: Applied Physics*, Vol.21(4), p574-589

Reeks, M. W. and Hall, D. (2001) “Kinetic models for particle resuspension in turbulent flows: theory and measurement”, *Journal of Aerosol Science* 2001, Vol.32(1), p1-31

Reeks, M. W. (2008) “Independent peer review of treatment of dust suspension and deposition relevant to HNB/HPB boiler tube failure safety case”, Multiphase Flow and Thermal Systems, School of Mechanical and Systems Engineering, Newcastle University

Romney, E. M. and Wallace, A. (1977) “Plutonium contamination of vegetation in dusty field environments”, Transuranics in Natural Environments, Nevada Applied Ecology Group NVO-178, National Technical Information Services, Springfield, VA, p287–302

Rubinow, S. I. and Keller, J. B. (1961) “The transverse force on spinning sphere moving in a viscous fluid”, *J. Fluid Mech*., Vol.11, p447-459

Rumpf, H. (1990) "Particle Technology", Chapman & Hall, London/New York

Saffman, P. G. (1965) “The lift on a small sphere in a slow shear flow”, *J. Fluid Mech.*, Vol.22, p385-400

Schaefer, D. M., Carpenter, M., Gady, B., Reifenberger, R., Demejo, L. P. and Rimai, D. S. (1995) “Surface roughness and its influence on particle adhesion using atomic force techniques”, *Fundamentals of Adhesion and Interfaces*, p35-48

Schewe, G. (1983) “On the Structure and Resolution of Wall-Pressure Fluctuations Associated with Turbulent Boundary-Layer Flow”, *J. Fluid Mech.*, Vol.134, p311-328

Schlichting, H. and Gersten, K. (2000) “Boundary Layer Theory”, 8th Edition, McGraw Hill

Schmidt, E. and Löffler, F. (1991) “The analysis of dust cake structures”, *Particle & Particle Systems Characterization*, Vol.8, p105-109

Sehmel, G. A. (1971) “Complexities of particle deposition and reentrainment in turbulent pipe flow”, J*. Aerosol Sci.*, Vol.2, p63-72

Sehmel, G. A. (1980) “Particle resuspension: a review”, *Environ Int.*, Vol.4, p107-127

Stempniewicz, M. and Komen, E. (2006) “Model of particle resuspension in turbulent flows”, 3rd International Topical Meeting on HTR Tech, C00000059 SA

Stempniewicz, M., Komen, E. and A. de With (2008) “Model of particle resuspension in turbulent flows”, *Nuclear Eng. & Design*, Vol.238(11), p2943-2959

Ström, L. (1986) “RESUSPENSION OF DUST DEPOSITS IN PIPES”, Studsvik - The Marviken Project, Report MXIP-11, February

Taheri, M. and Bragg, G. M. (1992) “A Study of Particle Resuspension in a Turbulent Flow Using a Preston Tube”, *Aerosol Sci. Technol.*, Vol.16, p15-20

Takase, K. (2001) “Three-dimensional numerical simulations of dust mobilization and air ingress characteristics in a fusion reactor during a LOVA event”, Fusion Engineering and Design, Vol.54, p605 -615

Taylor, N. (2007) “Incident and accident selection for ITER safety analysis”, ITER_D_26Q8NB v1.1

Townsend, A. A. (1956) “The Structure of Turbulent Shear Flow”, Cambridge University Press

Tsai, C. J., Pui, D. Y. H. and Liu, B. Y. H. (1991) “Particle detachment from disk surfaces of computer disk drives”, *J. Aerosol Sci.*, Vol.22(6), p737-746

Tsai, C. J. and Chiou, S. F. (1999) “Measurement of emission factor of road dust in a wind tunnel”, *J. Aerosol Sci.*, Vol.30, p227-228

Ueda, H. and Hinze, J. O. (1975) “Fine-structure turbulence in the wall region of a turbulent boundary layer”, *J. Fluid Mech.*, Vol.67(1), p125-143

Vainshtein, P., Ziskind, G., Fichman, M. and Gutfinger, C. (1997) “Kinetic model of particle resuspension by drag force”, *Physical Review Letters*, Vol.78(3), p551-554

Wang, H. C. (1990) “Effects of inceptive motion on particle detachment from surfaces”, *Aerosol Sci. Technol.*, Vol.13, p386-393

Weber A.P. and Friedlander S.K. (1997) "Relation between coordination number and fractal dimension of aerosol agglomerates", *J. Aerosol Sci.*, Vol.28(1), p765-766

Wen, H. Y. and Kasper, G. (1989) “On the kinetics of particle reentrainment from surfaces”, *J. Aerosol Sci.*, Vol.20, p483-498

Wen H. Y., Kasper G. and Udischas R. (1989) “Short and long-term particle release from surfaces under the influence of gas flow”, *J. Aerosol Sci.*, Vol.20, p923-926

Williams, M. and Loyalka, S. (1991) “Aerosol science theory and practice with special applications to the nuclear industry”, 1st Edition, Pergamon Press

Wright, A. L. and Pattison, W. L. (1984) Series-2 Aerosol resuspension test data summary report, Rapport NUREG/CR-ORNL/TM

Wright, A. L., Pattison, W. L. and King, J. Y. (1992) “SERIES-2 Aerosol Resuspension Test Data Summary Report”, Oak Ridge National Laboratory, Oak Ridge, TN

Wu , Y. L., Davidson, C. I. and Russel, A. G. (1992) “Controlled Wind Tunnel Experiments for Particle bounce off and Resuspension”, *Aerosol Sci. Technol.*, Vol.17, p245-262.

Yuan, Z., Mukai, K., Takagi, K., Ohtaka, M., Huang, W. and Liu, Q. (2002) ‘’Surface Tension and Its Temperature Coefficient of Molten Tin Determined with the Sessile Drop Method at Different Oxygen Partial Pressures”, *Journal of Colloid and Interface Science*, Vol.254, p338-345

Zhang, F. (2007) “Lagrangian Particle Tracking in Turbulent Boundary Layer”, MSc. Dissertation, School of Mechanical and Systems Engineering, Newcastle University, September

Zimon, A. D. (1964) “Adhesion of Dust and Powders”, Plenum Press, New York

Zimon, A. D. (1982) “Adhesion of Dust and Powder”, Second Edition, Consultants Bureau, New York

Ziskind G. (2006) “Particle resuspension from surfaces: Revisited and re-evaluated”, *Reviews in Chemical Engineering*, Vol.22(1-2), p1-123

Ziskind, G., Fichman, M. and Gutfinger, C. (1995) “Resuspension of particulates from surfaces to turbulent flows - Review and analysis”, *J. Aerosol Sci.*, Vol.26, p613-644

Ziskind, G., Fichman, M. and Gutfinger, C. (1997) “Adhesion moment model for estimating particle detachment from a surface”, *J. Aerosol Sci.*, Vol.28, p623-634

Ziskind, G., Fichman, M. and Gutfinger, C. (2000) “Particle behaviour on surfaces subjected to external excitation”, *J. Aerosol Sci.*, Vol.31, p703-719

Zoulalian, A. and Albiol, T. (1995) “Physiochemical processes at the origin of aerosol deposition”, ECSC – EC – EAEC, EUR 16508 EN